

**ENGINEERED MICROFLUIDIC PLATFORMS TO ENABLE THE
INTERROGATION OF METASTATIC EXTRAVASATION UNDER
PHYSIOLOGICALLY RELEVANT HYDRODYNAMIC FORCES**

A Dissertation
Presented to
The Academic Faculty

by

Katherine Birmingham

In Partial Fulfillment
of the Requirements for the Degree
Doctor of Philosophy in
Bioengineering

Georgia Institute of Technology
May 2020

COPYRIGHT © 2020 BY KATHERINE BIRMINGHAM

**ENGINEERED MICROFLUIDIC PLATFORMS TO ENABLE THE
INTERROGATION OF METASTATIC EXTRAVASATION UNDER
PHYSIOLOGICALLY RELEVANT HYDRODYNAMIC FORCES**

Approved by:

Dr. Susan Thomas, Advisor
School of Mechanical Engineering
Georgia Institute of Technology

Dr. John McDonald
School of Biological Sciences
Georgia Institute of Technology

Dr. Andrés Garcia
School of Mechanical Engineering
Georgia Institute of Technology

Dr. Todd Sulchek
School of Mechanical Engineering
Georgia Institute of Technology

Dr. Gregory Lesinski
Department of Hematology and Medical
Oncology
Emory University

Date Approved: April 14, 2020

ACKNOWLEDGEMENTS

First and foremost, I would like to thank my advisor, Dr. Susan Thomas, for welcoming me into her lab when I first began my graduate school journey and for her continuous scientific guidance, patience, motivation, and enthusiasm. Susan invoked my scientific curiosity and pushed me to maximize my potential as an engineer, taught me countless soft skills through her efficient management style, helped teach me how to effectively mentor younger students, inspired me with her desire to use her immense knowledge of science to help others, and showed me that it is possible to be a powerful female force in the scientific community. I have grown as a researcher, a mentor, and a person during graduate school, and I attribute much of who I am today to my advisor.

Furthermore, I would like to thank the members of the Thomas Lab, past and present, for cultivating a lab culture in which rigorous science is conducted and supported with a healthy dose of fun. The charismatic, hard-working members of the Thomas Lab provided experiment guidance and shared their expertise to help me plan and carry-out high-quality research. They were also always there to offer words of encouragement, provide comedic relief, and unwavering support. I have loved my time in graduate school and it has been some of the best years of my life, and I attribute that to my wonderful lab mates.

I would also like to express my deep gratitude to my committee members, who have provided me with invaluable guidance and insight that has help shaped my research, and for their time and energy in meeting with me and reviewing my thesis document. I would especially like to thank Dr. McDonald and Dr. Lesinski, who I had the pleasure of

collaborating with during my thesis research. I am also grateful for Dr. Garcia's support and oversight of the Bioengineering Program, which has been my home for the past four years, and to Dr. Sulchek for his exceptional insight into the microfluidic portions of my work. I would also like to thank the staff of the Parker H. Petit Institute for Bioengineering and Biosciences and the Core facilities, especially Laura Paige, Melissa Raine, Michelle Wong, Karen Ethier, Sommer Durham, Andrew Shaw, and Steve Woodward.

On a more personal note, I am grateful to have fostered new, lifelong friendships throughout graduate school. Between friendships with members of other labs, book club, tennis, and the Catholic Center, I have been constantly supported and encouraged here in Atlanta. I would especially like to thank my roommate, who never failed to make me smile, and has had a lasting positive impact on my life and has molded me into a better person. From spontaneous trips to New York, whipped cream parties during emergency room visits, puzzle nights, and sharing her love of Christ, I have cherished our time together. These friendships have contributed to unforgettable memories and provided a welcome relief to graduate school research pursuits.

Finally, I would like to thank my family for their unwavering love and support. They saw me through my best and worst of graduate school, and I would not have made it here without them. From a young age, they fostered scientific intellect, taught me the value of good education and hard work, and instilled moral values that have constantly challenged me to be a better person and contribute to make the world a better place. I am eternally grateful for their love, support, perspective, willingness to join me for a tennis game, golf match, or day out on the ski slopes, and ability to always make me laugh.

TABLE OF CONTENTS

ACKNOWLEDGEMENTS	iii
LIST OF TABLES	viii
LIST OF FIGURES	ix
LIST OF SYMBOLS AND ABBREVIATIONS	xii
SUMMARY	xv
CHAPTER 1. INTRODUCTION	1
1.1 Motivation	1
1.2 Specific Aims	4
1.3 Significance	8
CHAPTER 2. BACKGROUND AND LITERATURE REVIEW	12
2.1 Cell Adhesion in the Vasculature	12
2.1.1 Cell Adhesion under Hydrodynamic Flow	12
2.1.2 The Role of Selectins and Selectin-Ligands in the Adhesion Cascade	14
2.2 Contributions of Selectins and Their Ligands in Cancer Metastasis	16
2.2.1 Selectins in Cancer Metastasis	17
2.2.2 The Role of Selectin Ligand Expression in Cancer Cell Adhesion	19
2.2.3 Selectin Mediated Adhesion and Cancer Stem Cells	20
2.3 The Lymphatic System	21
2.4 Lymphatic Metastasis	23
2.4.1 Lymphatic Vessel Remodelling in Cancer	25
2.4.2 Subcapsular Sinus Remodelling in Cancer	25
2.5 Current Technologies to Study Cell Adhesion	27
CHAPTER 3. ANALYZING MECHANISMS OF METASTATIC CANCER CELL ADHESIVE PROPENSITY LEVERAGING A PREPARATIVE ADHESION CHROMATOGRAPHY MICROFLUIDIC	30
3.1 Introduction	30
3.2 Materials and Methods	33
3.2.1 Cell Culture	33
3.2.2 Channel Fabrication	33
3.2.3 Channel Functionalization	34
3.2.4 Perfusion Experiments	34
3.2.5 Cell Fraction Quantification and Cell Viability Analysis	35
3.2.6 Flow Cytometric Analysis	36
3.2.7 Video Analysis	36
3.2.8 Cell Pulse Location Quantification	37
3.2.9 Free Flow Elution Time Quantification	37
3.2.10 In Vivo Metastasis Model	38

3.2.11 mRNA Extraction and Sequencing	38
3.2.12 mRNA Sequencing Analysis	39
3.3 Results	39
3.3.1 Microfluidic-based Adhesion Chromatography	39
3.3.2 Adhesion Chromatography Microfluidic Enrichment of Distinct and Viable Cell Subsets of Varying In Vitro Adhesivities	45
3.3.3 Sorted Cell Fractions Exhibit Different Metastatic Potential In Vivo	49
3.3.4 Differential Selectin Ligand Expression by LS174T Cells Separated Using Adhesion Chromatography by E-selectin Adhesivity	51
3.3.5 Adhesion to E-selectin In Flow by LS174T Cells is a Transient Phenotypic Characteristic Not Associated with Significant mRNA Profile Expression Changes in Adhesive Ligand Genes	55
3.3.6 LS174T Cell E-selectin Adhesive Phenotype Association with Cancer Stem Cell Features	59
3.4 Discussion	61
3.5 Conclusion	66

CHAPTER 4. PHOTOCONVERSION AND CHROMATOGRAPHIC MICROFLUIDIC SYSTEM REVEALS DIFFERENTIAL CELLULAR PHENOTYPES OF ADHESION VELOCITY VERSUS PERSISTENCE IN SHEAR FLOW

	67
4.1 Introduction	67
4.2 Materials and Methods	70
4.2.1 Cell Culture	70
4.2.2 Channel Fabrication	71
4.2.3 Channel Functionalization	71
4.2.4 Perfusion Experiment Workflow	72
4.2.5 Confirmation of Retention of Anti-IgG Surface Functionalization after Perfusion	74
4.2.6 Elution Time Quantification	75
4.2.7 Flow Cytometric Analysis	76
4.2.8 Quantification of Adhesive Cell Behavior	76
4.2.9 Development of Standard Curve	77
4.2.10 Ligand Expression and Extent of Photoconversion	78
4.2.11 Outlier Detection and Elimination	79
4.2.12 Enzymatic Treatment	80
4.3 Results	80
4.3.1 Adherent Relative to Free Flow Cell Fractions Exhibit Greater Photoconversion Proportion and Extent	80
4.3.2 Velocity of Rolling Adhesion Magnitude on E-Selectin Correlates Differentially with Ligand Type	87
4.3.3 Slow and Fast Rolling Adhesion on E-selectin is Associated with Sialyl Lewis X Expression	95
4.3.4 Selectin Ligands Enriched in Cells Mediating Persistent but Not Non-persistent Selectin Adhesion	100
4.3.5 Screening Ligand Degrading Enzyme Effects on Adhesion Mechanisms	106
4.4 Discussion	110

4.5	Conclusion	112
CHAPTER 5. LYMPH NODE SUBCAPSULAR SINUS MICROENVIRONMENT-ON-A-CHIP TO MODEL LYMPHATIC METASTASIS AND IMMUNE CELL HOMING		114
5.1	Introduction	114
5.2	Materials and Methods	118
5.2.1	Immunohistochemistry	118
5.2.2	COMSOL Wall Shear Stress Modeling	119
5.2.3	Cell Culture	120
5.2.4	Channel Fabrication	121
5.2.5	Channel Functionalization	121
5.2.6	Perfusion Experiment Workflow	122
5.2.7	LS174T Cell and THP-1 Cell Co-perfusion Workflow	123
5.2.8	Quantification of Adhesive Cell Behavior	124
5.2.9	Quantification of Adhesive Cell Behavior	124
5.3	Results	125
5.3.1	Lymphatic metastasis, lymph node invasion, and tissue remodelling	125
5.3.2	Altered shear stress profiles within remodeled lymph node sinuses	128
5.3.3	Engineered lymph node “sinus-on-a-chip” adhesion microfluidic	131
5.3.4	Remodeling regulates cell adhesion in subcapsular sinus-mimicking flow fields	134
5.3.5	Cell adhesivity increases when co-perfused with monocytes	147
5.4	Discussion	151
5.5	Conclusion	154
CHAPTER 6. CONCLUDING REMARKS AND FUTURE DIRECTIONS		156
6.1	Conclusions	156
6.2	Contributions to the Field	159
6.2.1	Microfluidic to Interrogate Subsets of Cells with Different Average Adhesive Behavior	160
6.2.2	Integrated Microfluidic to Juxtapose Short and Long Time- and Length-Scale Adhesive Propensity	161
6.2.3	Lymph node “sinus-on-a-chip” to Elucidate Mechanisms of Lymphatic Metastasis	162
6.3	Future Directions	164
6.3.1	Interrogating the Surface Molecule Profile of Subsets of Cells with Different Long Time- and Length-Scale Adhesive Propensities to Selectins	165
6.3.2	Studying the Effects of Selective Selectin Ligand Inhibition and Qualifying Cancer Stem Cell Markers	166
6.3.3	Enhancing the Design of the Lymph Node “Sinus-on-a-Chip” to Better Recapitulate the Lymphatic Metastasis Microenvironment	167
 REFERENCES		 170

LIST OF TABLES

Table 4.1	Average rolling velocity ranges for eluting cell fractions.	87
Table 4.2	Correspondence of photoconversion integrating cell sorting microfluidic readout to adhesion persistence.	100
Table 5.1	Human and lymph node parameter reference ranges.	129
Table 5.2	Perfusion conditions for divergent channel correlated to human lymph node conditions.	131
Table 5.3	Wall shear stress ranges along the length of the divergent channel at different flow rates based on COMSOL simulations of human lymph node parameters.	135

LIST OF FIGURES

Figure 2.1	Hydrodynamic Forces Acting on Cells in the Vasculature.	12
Figure 2.2	Selectin Mediated Adhesion in the Vasculature.	14
Figure 2.3	The structure of selectin molecules.	15
Figure 2.4	Cancer Cell Expressed Selectin Ligands.	16
Figure 2.5	Anatomy of the Lymph Nodes.	23
Figure 2.6	Disseminated Tumor Cell Invasion of the Lymphatic System.	24
Figure 3.1	Engineered cell sorting adhesion chromatography microfluidic to investigate cancer metastasis <i>in vitro</i> .	43
Figure 3.2	Snapshots of Static and Continuous flow experiment videos at various timepoints.	44
Figure 3.3	Collected cell fraction analysis.	48
Figure 3.4	LS174T cells collected using adhesion chromatography in the Free flow fraction metastasize <i>in vivo</i> less than Adherent fraction.	50
Figure 3.5	LS174T cells collected using adhesion chromatography into Adherent subset after perfusion over E-selectin exhibits enhanced HECA and CD44, but not CEA, expression levels.	54
Figure 3.6	Adhesivity to E-selectin is a transient phenotype by LS174T cells not caused by mRNA expression changes.	58
Figure 3.7	CD24 expression does not differ between LS174T cells that do or do not exhibit E-selectin adhesivity.	60
Figure 3.8	Static perfusion reveals no difference between collected fractions in coexpression of CD24 and selectin-ligands.	61
Figure 4.1	Verification of anti-IgG functionalization after perfusion.	75
Figure 4.2	Comparison of interpolated standard curves.	78
Figure 4.3	Integrated photoconversion, cell sorting adhesion chromatography microfluidic for <i>in vitro</i> interrogation of metastatic cancer cell adhesive phenotypes.	81

Figure 4.4	Photoconvertible LS174T cell line and adhesive chromatography microfluidic characterization.	83
Figure 4.5	Adherent relative to free flow cell fractions exhibit increased extents of photoconversion and proportions of photoconverted cells.	86
Figure 4.6	Long and short time- and length-scale cell velocities converge when measured using photoconversion and chromatographic methodologies in combination.	88
Figure 4.7	Elution time determination for collection of multiple AD fractions.	89
Figure 4.8	Selectin ligand expression increased in cells mediating persistently slow rolling on E-selectin.	91
Figure 4.9	Magnitude of persistent, slow cell rolling mediated by E-selectin adhesive interactions inversely correlates with selectin ligand expression.	94
Figure 4.10	No correlations between ligand expression and GFP/CFP ratios among PC- cells within any collected cell fraction.	95
Figure 4.11	Cellular sLe ^x expression inversely correlated with magnitude of fast rolling adhesion on E-selectin revealed by pre-photoconversion.	97
Figure 4.12	Effects of pre-photoconversion on cells pre and post perfusion.	99
Figure 4.13	Selectin ligands sLe ^x , CD44, and CEA are enriched in cells mediating persistent slow rolling selectin adhesion in flow.	102
Figure 4.14	Opposing ligand expression correlations with rolling velocity magnitudes between persistently versus non-persistently adhesive cells.	104
Figure 4.15	No correlation between selectin ligand expression and GFP/CFP ratios among cells that remain unphotoconverted.	105
Figure 4.16	Sialyl Lewis x and CD44 correlated in highly but not lowly persistent slow rolling selectin-mediated adhesion.	108
Figure 4.17	Neuraminidase treatment effects on cell adhesion in flow to P- and L-selectin.	109
Figure 5.1	Cancer cells from primary tumors can harness the lymphatics, which remodel in states of inflammation, to form metastases.	127
Figure 5.2	Modeling lymphatic fluid flow between quiescent and remodeled lymph nodes in COMSOL.	130

Figure 5.3	Cells entering the lymph node have settled to the floor of the subcapsular sinus by the time they leave the afferent vessel.	131
Figure 5.4	Engineered divergent adhesion chromatography system to interrogate lymphatic metastatic extravasation mechanisms <i>in vitro</i> .	133
Figure 5.5	THP-1 adhesive behavior is altered with the addition of adhesion molecules.	136
Figure 5.6	Copresentation of ICAM-1 and high VCAM-1 increase the adhesive behavior of pancreatic cancer cells.	137
Figure 5.7	Enhanced expression of adhesion molecules increases the adhesivity of colon carcinoma cells.	138
Figure 5.8	Dilation of the lymphatic vessel or the subcapsular sinus decreases the distance, but not magnitude, of maximum adhesion in the subcapsular sinus.	140
Figure 5.9	Lymphatic vessel or subcapsular sinus dilation decreases the distance in the subcapsular sinus that maximum adhesion of pancreatic cancer cells occurs while minimally altering the average rolling velocity trends.	143
Figure 5.10	The location of maximum adhesion of colon carcinoma cells occurs earliest in lymph nodes with dilated subcapsular sinus.	146
Figure 5.11	Adhesive propensity of metastatic colon carcinoma cells to E-selectin increases when co-perfused with monocytes in a manner proportional to the relative percent of monocytes.	148
Figure 5.12	Colon carcinoma cells co-perfused with monocytes increases their adhesion behavior in lymph node models with enhanced adhesion molecule expression.	150

LIST OF SYMBOLS AND ABBREVIATIONS

AD	Adherent fraction
AD1/2	Adherent 1/2 fraction
AD2/2	Adherent 2/2 fraction
AD1/3	Adherent 1/3 fraction
AD2/3	Adherent 2/3 fraction
AD3/3	Adherent 3/3 fraction
APC	Allophycocyanin
BSA	Bovine serum albumin
C_{AD}	Linear regression slope of adherent fraction
C_{FF}	Linear regression slope of free flow fraction
CAM	Cell adhesion molecule
CEA	Carcinogenic antigen
CFP	Cyan fluorescent protein
CSC	Cancer stem cell
h	Channel height
H&E	Hematoxylin and eosin
D-PBS	Dulbecco's phosphate buffered saline
E	E-selectin
FBS	Fetal bovine serum
FITC	Fluorescein isothiocyanate
FF	Free flow
GFP	Green fluorescent protein

GFP/CFP	GFP to CFP ratio
ICAM-1	Intercellular adhesion molecule-1
LEC	Lymphatic endothelial cell
LN	Lymph node
LVD	Lymphatic vessel diameter
mAb	Monoclonal antibody
MFI	Mean fluorescent intensity
mRNA	Messenger RNA
NA	Neuraminidase
ns	Not significant
NSG	Nod skid gamma
PC	Photoconversion
PC+	Photoconverted positive
PC-	Photoconverted negative
PDMS	Polydimethylsiloxane
PE	Phycoerythrin
Q	Volumetric flow rate
r	Cell radius
RNA	Ribonucleic acid
SCS	Subcapsular sinus
SCS h	Subcapsular sinus height
sLe ^x	Sialyl Lewis X
τ_w	Wall shear stress
TX	Treatment
μ	Dynamic viscosity

US	Unsorted
$V_{\text{instantaneous}}$	Short time- and length-scale velocity
VCAM-1	Vascular cell adhesion molecule-1
w	Channel width
WSS	Wall shear stress

SUMMARY

Over 90% of all cancer-related deaths result from metastasis, a multistep process that occurs in the blood or lymphatic vasculature under hydrodynamic forces. During metastasis, cancer cells leave the primary tumor, intravasate into the circulatory or lymphatic system, circulate until they are able to extravasate, and eventually take up residence in a secondary location of the body to form a metastatic tumor. In order to leave the vasculature during extravasation, circulating tumor cells utilize a highly orchestrated adhesion cascade that begins with rolling adhesion to endothelial cells under a high shear environment. This process is driven by interactions between endothelial-presented selectins and glycan epitopes on selectin ligands present on the circulating cell's surface. These selectin-selectin ligand interactions have been implicated in cancer metastasis, however, an outstanding problem in the field is the lack of effective systems to study the role of wall shear stress and cellular molecular profiles in initiating and sustaining these interactions, and how this may lead to enhanced metastatic capacity of circulating tumor cells. As such, *the overall objective* of this thesis is to engineer microfluidic platforms to permit the analysis of selectin-mediated adhesion and interrogation of cellular characteristics underlying selectin-selectin ligand interactions between the endothelium and metastatic cell subsets that occur during cancer dissemination in a tumor microenvironment. My *central hypothesis* is that microfluidic systems can be engineered to mimic the hemodynamic forces of the circulatory system or hydrodynamic forces of the lymphatic system, which can be used to interrogate cellular characteristics associated with adhesion in flow or the effects of altered microenvironments on metastasis.

CHAPTER 1. INTRODUCTION

1.1 Motivation

Over 90% of all cancer-related deaths result from metastasis, a multistep process that can occur in either the lymphatics or in the blood vasculature, and these processes are related in that disseminated tumor cells move through the lumen of vessels under hydrodynamic forces. Cancer metastasis is initiated when a tumor cell leaves the primary tumor and intravasates into the circulatory or lymphatic system. The tumor cell can then circulate in the vasculature until it is able to extravasate, or leave the circulatory or lymphatic system, infiltrate a distant tissue, multiply, and form a secondary, metastatic tumor.^{1,2} In order to travel to distant sites in the body during the process of metastatic cancer extravasation, circulating tumor cells utilize a highly orchestrated adhesion cascade that begins with rolling adhesion to (lymphatic) endothelial cells under a high shear environment, in a similar manner to leukocyte homing and extravasation.³⁻⁵ Importantly, this process is driven by interactions between endothelial-presented selectins and glycan epitopes on selectin ligands present on the circulating tumor cell's surface. The interaction of selectins with their ligands slows a circulating tumor cell down and allows it to firmly adhere to (lymphatic) endothelial cells in the dynamic fluid flow environment of blood or lymphatic vessels, which can permit transmigration and the eventual formation of metastatic tumors.⁶⁻¹⁰

In the context of hematogenous metastasis, selectin-mediated adhesion has been previously recapitulated *in vitro* to elucidate the selectin-mediated adhesive behavior of metastatic cancer cells in a controlled, physiologically relevant microenvironment.¹¹⁻¹³

Furthermore, the use of such *in vitro* platforms has been extended to interrogate the correlation between short time- and length-scale selectin-mediated rolling adhesion and expression levels of selectin ligands, such as sLe^x and CEA, as well as selectin ligands that are also cancer stem cell markers, such as CD24 and CD44.¹² However, these microfluidic systems are limited in that they are unable to correlate metastatic cancer cell expression of selectin ligands and cancer stem cell markers with long time- and length-scale adhesive propensity, and they do not permit the simultaneous juxtaposition of short and long time- and length-scale adhesive behavior of metastatic cancer cells. Furthermore, these systems fail to allow the separation, collection, and post-perfusion analysis of distinct subsets of metastatic cancer cells from a heterogeneous population. Consequently, the exact cell-intrinsic mediators facilitating long time- and length-scale selectin-mediated adhesion as it relates to hematogenous metastasis are widely unknown. Collectively, therefore, there is a need for the development of new, cell-sorting microfluidic systems that can be used to interrogate the role of wall shear stress and distinct cellular molecular profiles in initiating and sustaining selectin-mediated adhesion, particularly as it relates to enhanced hematogenous metastasis potential of different adhesive phenotype subsets of circulating tumor cells. Notably, the engineering of such novel systems that allow during perfusion and post-perfusion analysis of cell subsets with different adhesive propensities can be applied to identify molecular drug targets for development as anti-cancer metastasis therapeutics or can be used as a high-throughput method of identifying various biomarkers that distinguish circulating tumor cells from malignant phenotypes.

Unlike hematogenous metastasis, which can be modeled with a constant wall shear stress, a cell which is metastasizing in the lymphatic vessels is exposed to a decreasing wall

shear stress as it moves from the entering afferent vessel toward the perimeter of the subcapsular sinus, the first point of entry into the lymph node for circulating tumor cells that have harnessed lymphatic vessels for transport.^{14,15} As a result, the hydrodynamic microenvironment under which selectin-mediated adhesion occurs is different in the lymphatics than in the blood vasculature, and, thus, the interrogation of biophysical and biomechanical mechanisms of lymphatic metastasis require a unique model system to recapitulate the distinctive fluid flow regime. Importantly, despite the central role the lymphatics play in metastasis, as lymph node status is a key indicator of cancer aggressiveness and patient prognosis, there is currently no *in vitro* system to interrogate the mechanisms of tumor cell recruitment and extravasation through selectin-mediated adhesion during lymphatic metastasis.¹⁶⁻¹⁹ Further complicating the investigation of lymphatic metastasis is tumor induced remodeling of the lymph node, such as dilation of the afferent lymphatic vessel and subcapsular sinus, which alters the fluid flow and wall shear stress that circulating tumor cells are exposed to.^{14,20-23} Taken together, due to the limited understanding of the process of lymphatic dissemination of circulating tumor cells, there exist a need to elucidate, on-chip in a high-throughput manner, the contribution of lymphatics in permitting cancer cell extravasation, and the role of the altered wall shear stress profile of the remodeled lymphatics in potentiating metastasis.

In summary, an outstanding problem in the field are the lack of effective systems to interrogate the role of hydrodynamic forces and cellular molecular profiles in initiating and sustaining increased selectin-ligand interactions, and how this may lead to enhanced extravasation and metastatic propensity of circulating tumor cells. Significantly, the development of such systems to study and better understand the interactions between

metastatic cancer cell surface selectin ligands and selectins expressed in the blood vasculature and the elucidation of cellular adhesion in the lymphatic system under hydrodynamic flow provide critical insight into the role of selectin-mediated adhesion in cancer metastasis. Of clinical relevance, these insights can serve to aid in the development of targeted drug therapies to attenuate metastasis while minimally impacting normal cell processes.^{24,25}

As such, **the overall objective** of this proposal is to engineer microfluidic platforms that will enable the interrogation of the adhesive behavior of cells under physiologically relevant hydrodynamic forces. These microfluidics will establish systems to permit analysis of selectin-mediated adhesion and interrogation of cellular characteristics underlying selectin-selectin ligand interactions between the endothelium of the blood vasculature and metastatic cell subsets that occur during cancer dissemination in a tumor microenvironment and interrogate the role of lymphatic remodeling in the presence of a tumor in altering the adhesive behavior of circulating cells entering the lymph nodes. My **central hypothesis** is that microfluidic systems can be engineered to mimic the hemodynamic forces of the circulatory system or hydrodynamic forces of the lymphatic system, which can be implemented to interrogate cellular characteristics associated with adhesion in flow or the effects of altered microenvironments on metastasis. This hypothesis will be tested using *in vitro* fluidic models in the following specific aims.

1.2 Specific Aims

Specific Aim 1: Develop an adhesion chromatography microfluidic that sorts cells based on their elution time from a selectin functionalized substrate of the flow channel to analyze attributes of cells with different adhesive phenotypes.

The *working hypothesis* of this aim is that metastatic cancer cell subsets can be functionally coenriched based on their propensity to mediate adhesive interactions with selectins in flow. To this end, an integrated, parallel-plate microfluidic device was engineered to interrogate and fractionate cells based on their adhesivity to a substrate surface functionalized with adhesive ligand in a tightly controlled flow environment to elucidate associated cell-intrinsic pathways. Wall shear stress levels and endothelial presentation of E-selectin were modeled after the inflamed vasculature microenvironment in order to simulate *in vitro* conditions under which *in vivo* hematogenous metastasis occurs. Based on elution time from the flow channel, the collection of separate fractions of cells – non-interacting and interacting – at high yields and viabilities enabled multiple post-perfusion analyses, including flow cytometry, *in vivo* metastasis modeling, and transcriptomic analysis. This platform enabled the interrogation of flow-regulated cell molecular profiles, such as (co)expression levels of natively expressed selectin ligands sLex, CD44, and carcinoembryonic antigen, and cancer stem cell marker CD24. This additionally revealed E-selectin adhesivity exhibited by metastatic human colon carcinoma cells to be a transient phenotype. Facile and rapid, this methodology for unbiased, label free sorting of large populations of cells based on their adhesion in flow represents a method of studying flow-regulated adhesion *in vitro* for the identification of molecular drug targets for development as anti-metastatic cancer therapeutics.²⁶ These results are presented in Chapter 3.

Specific Aim 2: Uncouple short time- and length-scale velocity from long time- and length-scale average velocity by integrating a photoconversion system with a cell sorting adhesion chromatography platform.

The *working hypothesis* is that an integrated photoconversion, cell sorting microfluidic platform can be designed to simultaneously quantify short and long time- and length-scale velocities of perfused cells, enabling the evaluation of whether short time- and length-scale metastatic cancer cell rolling velocities correspond to cell adhesion over long distances or time scales. To test this hypothesis, photoconvertible protein technology was incorporated with the cell sorting microfluidic system engineered in Aim 1. As such, an integrated photoconversion and cell sorting parallel-plate chromatography channel enabling the measurement of long and short time- and length-scale velocities of cells mediating adhesion in flow fields was engineered to study the mechanisms underlying adhesion to selectins by metastatic cancer cells. Through the facile enrichment of cells into subfractions of differing adhesive behaviors and a fluorescent velocity probe amenable to off-chip analysis, underlying, causal molecular profiles implicated in differing adhesive phenotypes of metastatic cancer cells could be interrogated. This analytical method revealed selectin-mediated rolling adhesion to be strongly associated with expression of selectin ligands, correlations that vary with ligand type and rolling velocity magnitude. Discrete selectin ligand expression profiles were also found to underlie persistent versus non-persistent adhesion on selectins, suggestive of divergent regulatory mechanisms. This integrated cell sorting and photoconversion microfluidic platform thus enables *in vitro* analysis and comparisons of adhesive phenotypes as they relate to mechanisms of cancer

cell metastasis in the context of selectin mediated adhesion, revealing new insights into potential cancer dissemination pathways.²⁷ These results are presented in Chapter 4.

Specific Aim 3: Engineer a lymph node “sinus-on-a-chip” adhesion microfluidic to explore the effects of WSS magnitude and dissipation on adhesion of cells, particularly as it relates to lymphatic remodeling in the presence of a tumor or inflammation.

The *working hypothesis* is that the structural changes within the sinus and afferent vessel that occur in the presence of a tumor or in states of inflammation alters the theoretical position at which cells can optimally interact within the lymph node subcapsular sinus, and these effects are further influenced by upregulation of presented adhesion receptors. To test this hypothesis, a lymph node “sinus-on-a-chip” adhesion microfluidic device that recapitulates the hemodynamic microenvironment of the lymph node subcapsular sinus was engineered to interrogate the effects of lymph node remodeling on cellular adhesion in fluid flow relevant to lymphatic metastasis and immune cell homing. Wall shear stress levels within the microfluidic channel analytically estimated and modelled after both quiescent and diseased/inflamed lymph nodes were recapitulated using this adhesion analysis device, enabling the assessment of wall shear stress magnitude and dissipation on human monocytic and metastatic cancer cell line adhesion. This methodology revealed the potential for structural changes within the lymph node sinus and afferent lymphatic vessel to reposition adhesive cells within the lymph node sinus microenvironment, effects dependent on adhesive molecule presentation context. Our results indicate that biophysical changes including wall shear stress magnitude, dissipation rate and cell transit time in flow as well as biochemical changes such as adhesion receptor expression within the sinus

lumen and the presence of lymph-borne cells synergistically contribute to the extent of adhesion. Given the tight orchestration of chemotactic cues within lymph nodes to drive optimal adaptive immune responses, these findings implicate lymph node remodeling to regulate the location at which cells can optimally interact and/or within the subcapsular sinus and therefore potential mechanism of lymph node invasion. These results are presented in Chapter 5.

1.3 Significance

The *innovation* of the work presented herein is in creating microfluidic adhesion chromatography systems that recapitulate the hydrodynamic forces and microenvironment of the areas in which metastatic extravasation occurs. While a wide distribution of adhesive phenotypes of cells has been observed upon recapitulation of the selectin-mediated adhesion process *in vitro*, the direct relationship between endogenous expression of selectin ligands on metastatic cells and their rolling adhesion behavior over selectins in both the blood vasculature and lymphatics is poorly understood.^{11,12,24} By establishing models to study cancer extravasation *in vitro*, this research develops systems to permit future interrogation of the effects of selectin ligand presentation on cell adhesion biomechanics to selectins in flow, and elucidate the poorly understood role of the lymphatics, particularly the effect of lymphatic remodeling in response to a tumor, in potentiating cancer metastasis. In the future, the knowledge gained by using these platforms may inform the development of therapeutic strategies that utilize the unique expression of glycan epitopes on selectin ligands of circulating tumor cell surfaces to develop targeted therapies that inhibit metastasis.^{24,25,28,29} Individually, each specific aim has contributed to the field of bioengineering in the following ways:

Specific Aim 1. Capacity to sort subsets of cells based on their adhesive phenotype in a physiologically relevant blood vasculature microenvironment.

Previously, there did not exist a system to sort, collect, and enrich subsets of cells based on their adhesion propensity to a selectin-functionalized substrate of a microfluidic device in a high-throughput manner. Therefore, in Specific Aim 1, we engineered a flow-based device that functions as an adhesive chromatography platform. This system, based on a widely used parallel-plate flow chamber, leverages time-averaged velocities of cells perfused as a pulse in a controlled flow field as a proxy for overall adhesion propensity to a substrate surface functionalized with adhesive ligands. The high-throughput nature of the cell adhesion chromatography system permits the analysis of a large number of cells simultaneously in an environment that, used herein, recapitulates the physiological flow of the circulatory system. Using the microfluidic analysis platform to study the behavior of cancer cells in the vascular microenvironment, and therefore relating the phenotypic characteristics of a cancer cell with their adhesive potential, can inform novel biomarkers to distinguish lowly adhesive from highly adhesive cancer cells and identify molecular pathways that can be targeted with therapeutics to prevent cancer metastasis.²⁷

Specific Aim 2. Integration of a cell sorting microfluidic and a photoconversion platform to interrogate drivers of adhesion persistence.

Previously, the photoconversion platform has been used to elucidate phenotypes underlying varying adhesive propensities at a single cell level based on short time- and length-scales, and the cell sorting platform has been used to interrogate phenotypic differences underlying varying adhesive propensities at a large, cell subset level based on average velocity.^{12,26} However, the correlation between these two readouts has not been

extensively explored or distinguished. Therefore, by combining these two platforms, we engineered an integrated system that is capable of isolating and identifying subsets of cells with different adhesive behaviors to enable associated cellular phenotypes to be discerned. Separating cells based on biophysical characteristics is a broadly used technique for probing mechanisms underlying multiple disease types, and this platform improves upon former methods by enabling both quantification of rolling adhesion velocities and assessment of their qualities, e.g. persistent versus non-persistent.^{11-13,26} Our results demonstrating divergent molecular profiles associated with various adhesive phenotypes suggests the potential for this system to be applied to identify druggable targets on distinct subsets of circulating cancer cells (tumor initiating, for example) or provide nuance to the utility of various biomarkers in distinguishing circulating cells with distinct malignant phenotypes.²⁷

Specific Aim 3. Development of a “lymph node sinus-on-a-chip” to interrogate the role of lymphatic transport in lymphatic metastasis.

While many *in vivo* models to study lymph node metastasis exist, there have been few studies that explore lymphatic metastasis in the context of cell adhesion *in vitro*, particularly as it relates to selectin-mediated adhesion and the resulting wall shear stress profile of remodeled lymphatics. There currently does not exist an effective system to model lymphatic flow from the afferent lymphatic vessel into the subcapsular sinus, which is the primary route of tumor infiltration into the lymphatics. Therefore, the exact mechanisms of tumor cell recruitment and extravasation through the lymphatics remains poorly understood. As such, we engineered an adhesion microfluidic “lymph node sinus-on-a-chip” platform to visualize and quantify the adhesive behavior of cells on a surface-

functionalized substrate. This platform permitted, for the first time, the interrogation of cancer cell metastasis as it first occurs in the lymphatics from the afferent vessel into the subcapsular sinus, and the role of the altered wall shear stress profile of remodeled lymphatics on altering the adhesive propensity of cells to further promote adhesion and extravasation. The development of a system to interrogate the pathways and intricacies of immune cell homing to the lymph nodes and lymphatic metastasis in the context of hydrodynamic forces will allow for the elucidation of the biomechanical, biophysical, and biochemical processes and regulation of circulating cell adhesion and extravasation through the lymph nodes, which can better explain the poorly understood process of lymphatic metastasis and begin to inform therapeutics that are directed at preventing lymphatic metastasis, an issue of high clinical relevance.

CHAPTER 2. BACKGROUND AND LITERATURE REVIEW

2.1 Cell Adhesion in the Vasculature

2.1.1 Cell Adhesion under Hydrodynamic Flow

In order to disseminate into distant tissues in the body, circulating tumor cells that have intravasated into a blood or lymphatic vessel must engage in a multistep adhesion cascade that slows them down amidst fluid flow, permitting them to leave the vessel and infiltrate tissues at sites far removed from the primary tumor, multiply, and form metastatic tumors.^{3,30,31} Importantly, these circulating tumor cells that have intravasated into the vasculature are exposed to hydrodynamic forces as they move through vessels (Figure 2.1).^{7,32}

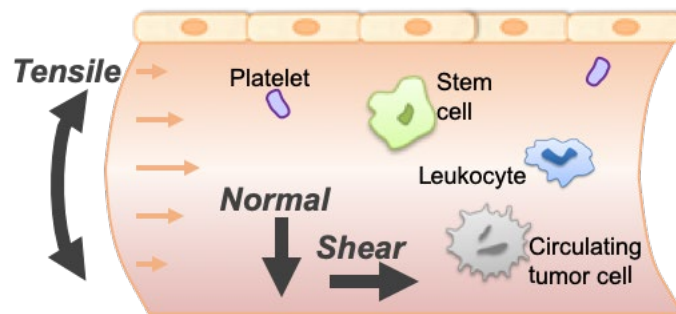


Figure 2.1 Hydrodynamic Forces Acting on Cells in the Vasculature. Cells moving through the vasculature are exposed to normal, shear, and tensile forces due to fluid flow.³³

One hydrodynamic force that has a significant effect on the adhesion of circulating tumor cells is wall shear stress, or the tangential force acting at the interface between blood or lymphatic fluid flow and endothelial cells lining the vessel, which ranges from 1-6 dyn/cm² in healthy veins to 10-70 dyn/cm² in healthy arteries.³⁴⁻³⁶ Therefore, escaping the

bloodstream or lymphatic system and forming secondary tumors requires that circulating tumor cells overcome the dispersive forces of fluid flow, including wall shear stress, by utilizing a highly orchestrated adhesion process that begins with rolling adhesion on the vascular endothelium under a high shear environment.^{3,37} This process is driven by interactions between endothelial-presented selectins and glycan epitopes on selectin ligands present on the metastatic cell's surface.^{8,9,38-41} Due to the fast binding kinetics of these interactions, which yields a high bond turnover rate, the interaction of selectins with their ligands decreases the forward velocity of the cells.⁴²⁻⁴⁵ Notably, the slower velocity of rolling cells enables the formation of integrin-cell adhesion molecule (CAM) bonds, which have a slower kinetic rate than selectin-selectin ligand bonds and allows the rolling cells to firmly adhere to the vessel wall.^{11,46-48} This firm adhesion is required before a circulating tumor cell can transmigrate across the endothelium for tissue infiltration and the formation of metastatic tumors.^{33,46,49} When selectin-mediated adhesion is recapitulated *in vitro*, a cell exhibiting rolling adhesion is defined as the cell moving with a translation velocity less than a free flowing, non-interacting cell, and a firmly adherent cell is defined as a cell that is not moving (Figure 2.2).^{11,13,33}

Notably, this multistep adhesion process is employed not only in cancer metastasis, but also in numerous other physiological and pathophysiological conditions, including the recruitment of leukocytes to sites of inflammation and the homing of stem cells.⁵⁰⁻⁵² Consequently, a better understanding of the interactions between metastatic cancer cell surface glycan epitopes and selectins as mediated by biomechanical forces from blood or lymphatic flow will aid in the development of targeted drug therapies to attenuate metastasis while minimally impacting normal cell processes.

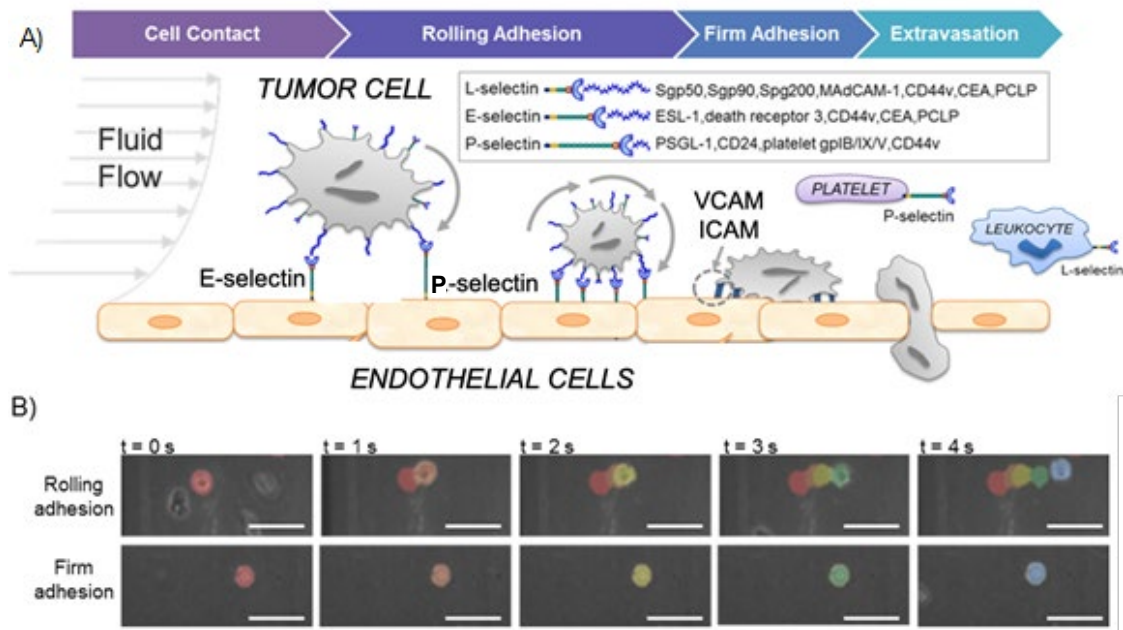


Figure 2.2 Selectin Mediated Adhesion in the Vasculature. (A) Cells extravasate by a process of selectin-mediated rolling adhesion, integrin-mediated firm adhesion, and migration across the endothelium. (B) Experimentally, two types of adhesion are observed: rolling adhesion (top row) and firm adhesion (bottom row). Colored labels indicate position of an example rolling or firmly adhered cell at successive points in time, where red represents the 0 second time point and blue represents the 4 second time point.³³

2.1.2 The Role of Selectins and Selectin-Ligands in the Adhesion Cascade

Selectins are a family of three related calcium dependent, transmembrane adhesion molecules – P-selectin, E-selectin, and L-selectin – composed of a carbohydrate binding amino-terminal, an epidermal growth factor-like domain, and a series of two to nine short, consecutive repeats between the two domains, which differentiates the selectin based on the number of repeats (Figure 2.3).^{53,54} P-selectin is found on platelets and (lymphatic) endothelial cells and since it is stored in the α -granules of platelets and Weibel-Palade bodies of endothelial cells, it can be quickly expressed on the surface of cells in response to cytokines or activating agents, such as interleukin 4 or 13.⁵⁵ (Lymphatic) endothelial cells also express E-selectin, which is transcriptionally regulated by cytokines, such a

tumor necrosis factor α and interleukin-1. Unlike P-selectin, E-selectin is not stored in the cell, and therefore, must be transcribed, translated, and transported to the cell surface de novo.⁵⁶ Finally, L-selectin is found on leukocytes, acting as a homing receptor for entry into secondary lymphoid tissue through the high endothelial venules of the vasculature.^{57–}

61

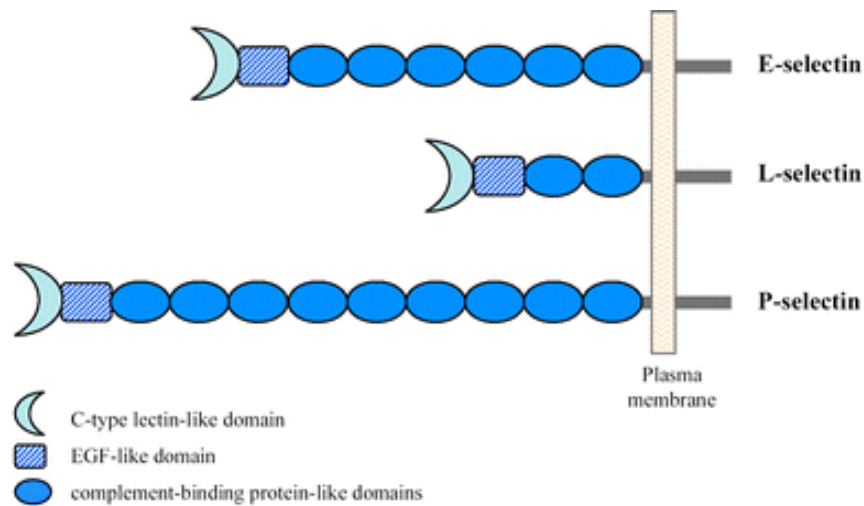


Figure 2.3. The structure of selectin molecules. Selectins are composed of a C-type lectin domain, an EGF-like domain, and consecutive repeats of complement-binding protein-like domains that vary in number and differentiate the selectins.⁶²

The propensity for cells, such as circulating cancer cells or leukocytes, to initiate interactions with selectin molecules and thereby engage in the first step of the adhesion cascade, is controlled by their expression of specific cell surface presented glycoproteins and glycolipids that act as selectin ligands.^{33,52,57,59,63} Tetrasaccharide sialyl lewis x (sLe^x), a terminal carbohydrate epitope of glycans attached to glycoproteins and glycolipids, is the most basic binding motif to all three selectins, and therefore must be expressed by a circulating cell for it to engage with selectin molecules presented by endothelial cells, platelets, and leukocytes.^{64,65} All selectins also bind PSGL-1 and it serves as the main

leukocyte ligand for adhesion to P-selectin.^{32,33} Two additional selectin ligands of particular interest in cancer biology are (1) CD44, which is a functional P- and E-selectin ligand that can be differentially spliced by metastatic cells to increase its binding avidity to P-selectin, and (2) carcinoembryonic antigen (CEA), which possesses E- and L-, but not P-selectin, ligand activity (Figure 2.4).^{57,66} Although selectins and some of their ligands are well studied, the understanding of the correlation between selectin-mediated adhesion in flow and the corresponding (co)expression of selectin ligands, and the molecular mechanisms that underlie this behavior, is currently deficient, particularly as it relates to extravasation of circulating tumor cells.

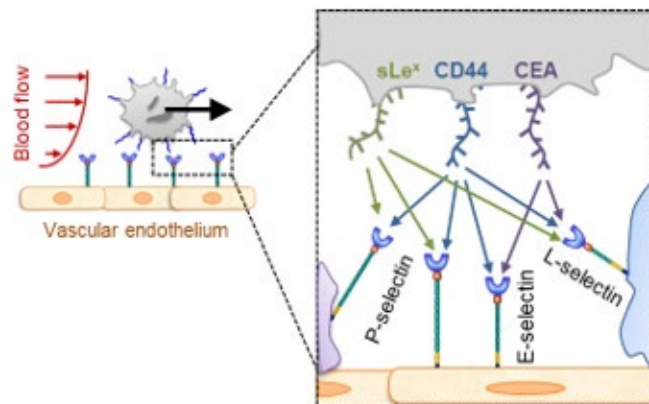


Figure 2.4. Cancer Cell Expressed Selectin Ligands. Circulating cancer cells can escape from the vasculature amidst hydrodynamic forces to establish secondary tumors through cell-cell interactions mediated by selectins presented on the vascular endothelium or circulating host cells and the selectin ligands on the circulating tumor cell.¹²

2.2 Contributions of Selectins and Their Ligands in Cancer Metastasis

Numerous studies have implicated selectin-mediated adhesion in facilitating hematogenous dissemination of tumor cells in a process that mirrors leukocyte extravasation.^{9,11–13,40} E- and P-selectin has been shown involved directly in the adhesion

of circulating tumor cells to the vascular endothelium. Conversely, L-selectin, and in some cases P-selectin, has been shown to have an indirect role in metastatic extravasation.^{62,67} Together, E-, P-, and L-selectin, in combination with additional cell adhesion molecules expressed by cells in vessels forming bonds with adhesion ligands present on the surface of cancer cells are hypothesized to allow a circulating tumor cell that has escaped into the blood or lymphatic system to slow down against fluid flow, adhere to the vessel wall, and extravasate.^{39,62,68}

2.2.1 *Selectins in Cancer Metastasis*

E-selectin, which is expressed by both endothelial cells and lymphatic endothelial cells, mediates slow, persistent rolling adhesion, and has been found to be upregulated in metastatic cancer.^{11,13,57} Therefore, interactions between circulating tumor cells and E-selectin are of particular interest when elucidating extravasation. Expectedly, the involvement of E-selectin in the formation of metastases *in vivo* has been interrogated by multiple groups. One study found that E-selectin knock-out mice have a drastically reduced capacity to form metastatic tumors compared to wild-type controls. In colon carcinoma, there is a direct association between the expression levels of numerous E-selectin ligands and metastatic phenotype characteristics, including enhanced adhesion to the endothelium of the blood vasculature.⁶⁹ Further substantiating these observations is a study that showed transgenic mice overexpressing E-selectin in the liver are able to form liver metastases when injected with E-selectin expressing melanoma cells, whereas wild-type mice did not form any metastatic tumors.⁷⁰ Despite this evidence that E-selectin is implicated in cancer metastasis, the mechanism underlying interactions between E-selectin and metastatic

cancer cells under flow, both in hematogenous and lymphatic microenvironments, has yet to be fully explored and explained *in vitro*.

Endothelial cells and inflamed lymphatic endothelial cells also express P-selectin, and therefore, P-selectin is also conjectured to have a direct role in permitting circulating tumor cells adhesion to the endothelial cell-lined blood vessel walls or inflamed lymphatic vessel and lymph node walls.^{71,72} However, unlike E-selectin, P-selectin mediates nonpersistent adhesion of metastatic cancer cells with intermediate rolling velocities.^{11,13} Finally, L-selectin is expressed by leukocytes, and mediates fast, nonpersistent tethering of metastatic cancer cells indirectly through secondary capture to form clusters of cells that are able to evade immune detection and overcome the dispersive forces created by hydrodynamic flow in vessels.^{11,13,64,73} Notably, P-selectin, which is expressed not only by (lymphatic) endothelial cells but also platelets, can also contribute indirectly to dissemination of circulating tumor cells in a manner similar to L-selectin through secondary tethering of circulating tumor cells to endothelial walls with platelets acting as an intermediary.⁵⁸ Although the characteristics of P- and L-selectin mediated adhesion of cancer cells is different than that of E-selectin, expression of P- and L-selectin is also correlated with increased metastases *in vivo*. For example, P-selectin deficient mice and L-selectin deficient mice, as well as P-/L-selectin double deficient mice, exhibit decreased metastatic potential compared to untreated mice.⁷⁴ Moreover, silencing of L-selectin on macrophages attenuates the occurrence of lymphatic metastases when mice are injected with lymphoma cells.⁷⁵ Collectively, there is sufficient evidence to implicate E-, P-, and L-selectin in directly and/or indirectly facilitating metastasis, and thus, after expounding the mechanisms by which selectin-mediated recruitment of disseminated tumor cells occurs,

drugs targeting specific molecules or mechanisms of this process may serve as promising anti-cancer metastasis therapeutics.^{25,28}

2.2.2 *The Role of Selectin Ligand Expression in Cancer Cell Adhesion*

Since selectins have been shown to play an important role in cancer metastasis, the selectin ligands expressed by circulating cancer cells are also implicated as key regulators of the metastatic cascade.^{11–13,69,70,74} One hallmark of cancer cells is aberrant glycosylation, which is marked not only by changes in cell surface glycosylation between healthy and cancerous cells, but also continuation of alterations in cell surface glycosylation as the cancer progresses.¹³ Notably, one observed change in glycosylation is hypersialylation – the overexpression of sialic acid residues on the surface of cancer cells – which may enhance the metastatic potential of cancer cells by increasing the ability of circulating tumor cells being able to interact with, adhere to, and transmigrate across endothelial cells lining the blood or lymphatic vessel.^{76,77} Most of the cancer cells that interact with selectins express several selectin ligands, some of which are canonical ligands that are also expressed by leukocytes, such as CD44, while others are non-canonical ligands unique to cancer cells, such as CEA.^{78–80} Functionally, increased expression of selectin-ligands has been found to be directly and proportionally correlated with increased adhesion.^{11–13,78,81,82} Notably, a series of *in vitro* studies interrogating extent of rolling adhesion of metastatic colon carcinoma cells on P-, E-, and L-selectin found that increased expression of sLe^x, the most basic binding motif for all selectins, conferred slower short time- and length-scale rolling velocities on all selectins. Furthermore, this same study noted that enhanced expression of CD44 was correlated with slower short time- and length-scale rolling velocities on E- and L-selectin, and enhanced expression of CEA conferred slower short

time- and length-scale rolling velocities on E-selectin.¹² Clinically, expression levels of selectin ligand PSGL-1 is correlated with increased disease progression in myeloma, and E-selectin ligands expressions are increased in the tumor cells of acute myeloid leukemia patients with metastatic disease compared to patients with only primary tumors.^{83,84}

Taken together, selectin ligands may individually or synergistically contribute to circulating tumor cell adhesion in the microvasculature. However, there remains a deficiency of understanding of the direct relationship between endogenous expression of selectin ligands on metastatic cells and adhesivity, especially at long time- and length-scales.

2.2.3 Selectin Mediated Adhesion and Cancer Stem Cells

Cancer stem cells (CSCs) represent a unique subset of cells that are characterized by their stem cell-like ability to self-renew, proliferate unlimitedly, and differentiate into multiple lineages, which grants them an enhanced capacity to form metastatic tumors.^{85,86} There is accumulating evidence that the capacity of CSCs to self-renew indefinitely and differentiate into a heterogeneous population of cells is responsible for the resistance of many cancers to chemotherapeutics and cytotoxic agents.⁸⁷⁻⁸⁹ Notably, some markers of CSCs, such as CD44 and CD24, are also functional selectin ligands on metastatic cancer cells, suggesting that CSCs may also exhibit an enhanced ability to engage in selectin-selectin ligand interactions under hydrodynamic flow that are necessary to initiate adhesion and extravasation through the vasculature for the eventual formation of metastatic tumors.^{80,90-92} However, there is some ambiguity in CSC markers among different cancers, as some ligands, such as CD24, are observed to be CSC markers in only a subset of cancers,

and even within particular cancers, there is a heterogeneous expression level of CSC ligands.^{91,93–95} Furthermore, the exact correlation between expression levels of CSC markers and a metastatic cancer cell's adhesive propensity is unclear, as there is conflicting literature regarding the expression of selectin ligand markers and metastatic potential as it relates to CSC subsets.^{96–98} Relevant to studies in this thesis, one group found that knockdown of CD44 on metastatic colon cancer cells resulted in decreased metastases *in vivo*, despite CD44's known role as both a CSC marker in colorectal cancer as well as a mediator of slow rolling behavior of metastatic colorectal cancer cells to P- and E-selectin *in vitro*.⁹⁹ Further compounding these contradictory roles of CD44 is a study that colabeled metastatic cancer cells for two CSC markers – CD44 and CD24 – and analyzed the short time- and length-scale adhesion of these cells *in vitro*, and found that CD44^{hi}/CD24^{hi}, but not CD44^{low}/CD24^{hi} subsets of cells, had significantly greater proportion of slow rolling cells compared to fast rolling cells, suggesting that knocking-out CD44 .¹²

Taken together, due to the potentially enhanced capability of CSCs to evade destruction by current cancer therapeutics, there is a clear need to engineer systems that can permit further interrogation of the existence of a relationship between expression levels of CSC markers and increased metastatic potential, as it can serve to reconcile conflicting reports regarding the adhesive propensity of cancer stem cells, provide more clarity to molecular underpinnings of cancer metastasis, and improve current cancer treatments or identify new drug targets.

2.3 The Lymphatic System

The lymphatic system, like the circulatory system, is responsible for the movement of fluid throughout the body. There are two main components of the lymphatic system – (1) the lymphatic vessels, which are responsible for transporting interstitial fluid, soluble proteins, and immune cells; and (2) the lymph nodes (LNs), which are responsible for filtering the components of lymphatic fluid before returning it to the blood.^{100–103} Together, there are over 500 LNs in the human body, which are all interconnected by a vast network of lymphatic vessels.¹⁰⁴ These lymphatic vessels are made up of highly permeable initial lymphatic capillaries that combine to form larger collecting lymphatic vessels. These collecting lymphatic vessels drain directly into the LNs via afferent vessels, permitting the contents contained within the lymphatic fluid to gain access into the lymph node.^{105–107} The first point of entry from the afferent vessel into the LN is the subcapsular sinus (SCS), which is lined by a layer of lymphatic endothelial cells (LECs) on top of a layer of SCS macrophages.^{108–111} After entering the SCS, lymphatic fluid drains through the trabecular sinus, into the medullary sinus, and finally out of the LN through the efferent lymphatic vessel (Figure 2.5A).^{103,104,112} Notably, the endothelial lining of the SCS basement acts as a crucial gatekeeper into the deeper regions of the LN, as penetration through the SCS permits access to the deeper LN cortex (Figure 2.5B).^{112–114}

Collectively, the lymphatic system is a series of interconnected lymphatic vessels and lymph nodes that provide cells with a route of transport throughout the body, and also play a crucial role in protecting host immunity by transporting antigen and antigen presenting cells to the LNs in order to initiate an adaptive immune response.^{101,102,106,112,114,115}

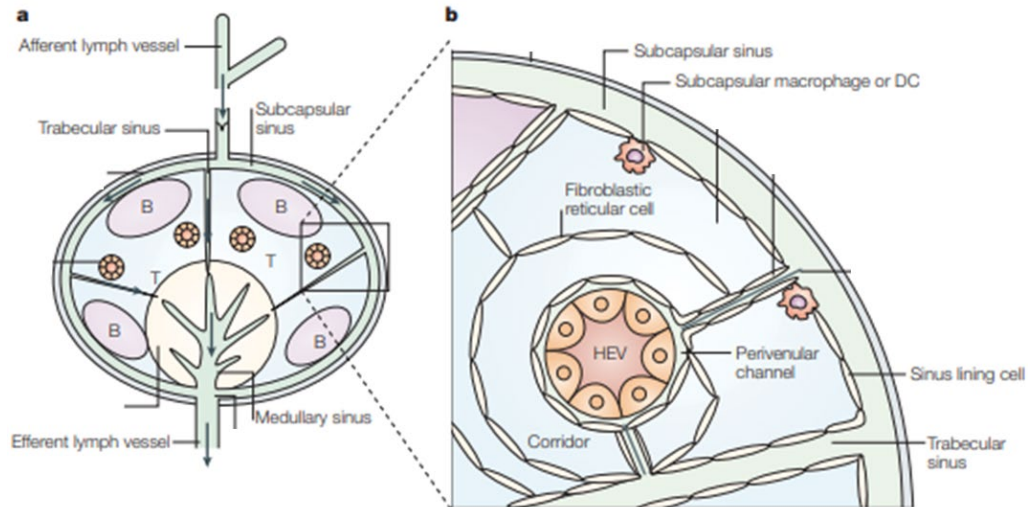


Figure 2.5. Anatomy of the Lymph Nodes. (A) Lymphatic fluid enters the lymph node from the afferent vessel, travels through the subcapsular sinus, trabecular sinus, medullary sinus, and leaves the lymph node by the efferent vessel. (B) Penetration through the subcapsular sinus allows access to the deeper cortex of the lymph node.¹¹²

2.4 Lymphatic Metastasis

Although direct hematogenous metastasis can occur, the lymphatics have also been found to play a central role in cancer metastasis, as the LNs provide efficient access to distant organs and an expanded network of local lymphatics by draining directly into the circulatory system or through the thoracic duct. Consequently, through a sequential sequence of events, a cancer cell that leaves the site of a primary tumor by intravasation can be rapidly carried to the LN afferent vessel and into the SCS of the sentinel LN via the natural route of lymphatic fluid flow.^{116–121} Once the disseminated tumor cell has entered the lymph node, it can: (1) Actively migrate through the endothelial lining of the sinus, multiply, and form a metastatic tumor within the LN; (2) Continue moving through the lymphatic network via the thoracic duct and take up residence in more distant lymph nodes; or (3) Drain into the circulatory system and begin the process of hematogenous metastasis.

There is direct evidence of the spread of metastatic tumor cells from the sentinel LNs to distant organs through lymphatic vessels, and, due to the multifaceted pathway of dissemination, the involvement of the LNs in the metastatic cascade is thought to allow the formation of numerous, simultaneously occurring secondary tumors originating from a single primary tumor, in addition to the formation of tumors within the lymph nodes themselves (Figure 2.6).^{122–125}

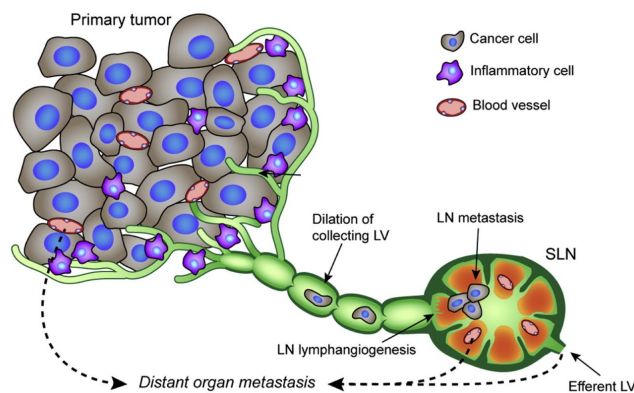


Figure 2.6. Disseminated Tumor Cell Invasion of the Lymphatic System. Tumor cells can intravasate into the lymphatic system and gain access to the subcapsular sinus through the afferent vessel. Once a circulating tumor cell has entered the lymph node, it can form a metastatic tumor within the lymph node or use the lymphatics to travel to other sites in the body to form distant organ metastases.¹²⁵

Substantiating the involvement of the LNs in cancer metastasis are numerous reports that have interrelated the existence of circulating tumor cells in the LNs to a poorer disease prognosis, with a negative correlation between a positive LN status and patient survival.^{17,126–132} For example, the five year survival rate for colorectal cancer patients diagnosed with LN positive cancer is over 30% less than patients with LN negative cancer, and the five year survival rate for LN positive pancreatic cancer patients is a mere 12%.^{17,126,130} Furthermore, there are numerous *in vivo* reports of lymphatic metastases among cell lines from various cancers, including 4T1 breast cancer cell line, B16F10

melanoma cell line, LS174T colon adenocarcinoma cell line, and PANC-1 pancreatic cancer cell line.^{133–136} Despite the clinical and experimental evidence of lymphatic involvement in cancer metastasis, the mechanisms of lymphatic metastasis and the roles circulating tumor cell adhesion ligand – lymphatic endothelial cell adhesion molecule interactions remain widely unknown.

2.4.1 Lymphatic Vessel Remodelling in Cancer

The presence of a primary tumor can lead to dynamic remodeling of the LNs, including lymphangiogenesis, lymphatic vessel diameter dilation, SCS dilation, and an upregulation of cellular adhesion molecules.^{137–142} Lymphangiogenesis involves the proliferation, sprouting, migration, and tube formation of new lymphatic vessels from existing lymphatics, and is driven by lymphatic endothelial cells migrating and proliferating at the site of the primary tumor to form sprouting lymphatic vessels that connect the tumor to the lymphatic system. Therefore, lymphangiogenesis can provide cancer cells increased access to the LNs, facilitating the infiltration of the lymphatic system with disseminated tumor cells.^{137,142,143} Also promoting the entry of cancer cells into the LNs is the enlargement of collecting lymphatics that is commonly observed in cancer patients. Although lymphatic vessel enlargement does not result in the formation of additional vessels, it can facilitate invasion simply by increasing the amount of drainage from the primary tumor to the sentinel LN, which leads to more efficient delivery of cancer cells to distant sites in the body through the LN.^{133,140,144}

2.4.2 Subcapsular Sinus Remodelling in Cancer

In addition to dilation of the collecting lymphatics, remodeled LNs in the presence of a tumor also exhibit dilation of the SCS, which results in an increase in the size of the LNs, including the height of the SCS.^{14,139,145-147} This remodeling may create an transformed microenvironment that supports cancer metastasis by altering the fluid flow through the SCS and increasing the number of disseminated tumor cells that can be contained within the SCS.^{138,139,141} Additionally, the lymphatic endothelial cells lining the walls of the subcapsular sinus exhibit an increase in adhesion molecule presentation, including the upregulation of two molecules implicated in the metastatic extravasation adhesion cascade, ICAM-1 and VCAM-1, in response to inflammation, including inflammation created by the tumor microenvironment.¹⁴⁸⁻¹⁵² Importantly, this enhanced ICAM-1 and VCAM-1 expression is directly correlated with increased LN metastases and poorer patient survival in clinical oral tongue squamous cell carcinoma patients.¹⁵⁰ *In vivo*, one study found that less than one-third of mice injected with B16F1 cells with low affinity for VCAM-1 developed LN metastases. Conversely, over two-thirds of mice injected with B16F1 cells with high affinity for VCAM-1 developed LN metastases.¹⁵³ Given the role of VCAM-1 in the process of tumor cell dissemination, these studies suggest that increased expression of VCAM-1 on lymphatic endothelial cells may have the functional consequence of increasing the ability of circulating tumors cells contained within the SCS to adhere and transmigrate across the basement of the SCS, however, this has yet to be shown experimentally.

Bridging the effects of shear stress and the enhanced expression of cellular adhesion molecules on lymphatic endothelial cells of remodeled LNs is a hypothesis that ICAM-1 upregulation on lymphatic endothelial cells is due, at least in part, to increased shear force

from lymphatic fluid flow in the SCS of LNs that have altered in response to the tumor microenvironment.^{149,152} Kawai *et al.* isolated lymphatic endothelial cells from sentinel LNs of breast cancer patients and stimulated them with high levels of shear stress. Quantification of ICAM-1 expression showed that both mRNA and protein levels increased upon stimulation, and this stimulation induced ICAM-1 upregulation was sufficient to increase the adhesion of breast cancer cells to lymphatic endothelial cells *in vitro*.¹⁴⁹ These observations were substantiated by Miteva *et al.*, who also found that fluid flow induces an upregulation of ICAM-1 expression on lymphatic endothelial cells in both *in vitro* and *in vivo* models.¹⁵²

Together, lymphatic structure changes that occur in response to a tumor may further facilitate metastases by altering the fluid flow into the LNs and altering the wall shear stress profile within the SCS. The effect of lymphatic remodeling, however, remains widely unexplored as it relates to mechanisms of cancer extravasation, particularly the biophysics of cell adhesion in the context of lymphatic fluid flow.

2.5 Current Technologies to Study Cell Adhesion

To enable both the interrogation of biomechanical effects on metastasis and to better comprehend the mechanisms of adhesion, engineered microfluidic systems are frequently implemented to model metastasis *in vitro*.^{11,13} Despite being highly simplified systems relative to *in vivo* models, they have the advantage of enabling experimentation under defined cellular, molecular, and/or biophysical conditions.¹⁵⁴ Using videomicroscopy-based imaging integrated with microfluidics to monitor the extent of adhesion in simulated flow fields that exhibit forces similar to those experienced in the microvasculature, many

thousands of cells can be analyzed in a single experiment, enabling high sampling volumes in individual or parallelized experiments. Biochemical, biomolecular, and transcriptomic manipulations of analyzed cells can also be performed to interrogate biomolecular mechanisms contributing to metastatic adhesive phenotypes.^{11,12,44,154–156} The capacity to probe the attributes intrinsic to cancer cells that confer adhesion in an unperturbed manner, however, is not feasible using these interventional type approaches without a priori knowledge. Imaging based analyses alone provide limited insight into biomolecular mechanisms and also does not allow subsets of cells to be collected and assayed in an unbiased manner based on their phenotypes of adhesion.¹⁵⁷

Further, most flow-based microfluidic platforms that are currently used for cell adhesion assays do not have the capacity to interrogate long time- and length-scale adhesive behavior of cells, and instead analyze short time- and length-scale adhesion.^{11–13,156} The ability to interrogate long time- and length-scale adhesion of cells or juxtapose short and long time- and length-scale adhesion of cells and analyze biological difference that underlie subsets of cells with different adhesion propensities is currently deficient. There is a need to elucidate different time- and length-scale adhesive propensity of metastatic cancer cells, as it has been previously noted that short time- and length-scale rolling behavior of cells over selectins does not predict average rolling behavior of cells. This phenomena, termed reduced “adhesion persistence”, may implicate specific subsets of cells in enhanced metastatic potential, and therefore a better understanding of observation can serve to improve anti-cancer metastasis therapeutics.^{11,13}

Outstandingly, sufficient *in vitro* models to study the mechanisms of lymphatic metastasis are even more lacking than microfluidic platforms to study hematogenous

metastasis, and the wall shear stress conditions under which tumor cells in the LNs are exposed to is rarely incorporated into such *in vitro* LN models. Previously, hydrodynamic flow in the LNs has been simulated through computer programming, but the results have not been incorporated into the design of a microfluidic system to model extravasation, since most LN metastasis models focus on exploring the role of cell proliferation and chemoattractant agents in promoting metastasis as opposed to the effects of altered fluid flow.^{44,158–160}

To this end, the development of new microfluidic platforms to interrogate adhesion of dissemination tumor cells in varied context is needed to facilitate a greater breadth of understanding of the mechanisms of metastatic extravasation, and give key insights into how differential expression of cell surface ligands or lymphatic remodeling may affect cellular adhesion.

CHAPTER 3. ANALYZING MECHANISMS OF METASTATIC CANCER CELL ADHESIVE PROPENSITY LEVERAGING A PREPARATIVE ADHESION CHROMATOGRAPHY MICROFLUIDIC

3.1 Introduction

Over 90% of all cancer-related deaths result from metastasis, a multistep process in which cancer cells leave the primary tumor, intravasate into the blood stream, circulate in the vasculature until they are able to extravasate, and eventually take up residence in a secondary location in the body to form a metastatic tumor.^{1,40} Extravasation occurs in the presence of hemodynamic force, necessitating processes to overcome its dispersive effects. Amongst multiple implicated mechanisms, adhesive interactions with endothelial presented receptors such as E-selectin amongst others, act to slow down circulating cancer cells, leading to eventual cell arrest and extravasation.^{1,32,38,39,161} Despite the correlation between a cell's propensity to exhibit selectin-mediated adhesion and metastatic potential, the cancer cell-intrinsic mediators facilitating the process are poorly understood.^{68,162-165} Given that cancer is one of the largest public health burdens facing the U.S. today, afflicting over 14.5 million with nearly 1.7 million new diagnoses each year, a better understanding of the mechanisms underlying cancer metastasis and identification of relevant biomarkers or therapeutic targets is crucial for developing anti-metastatic cancer therapies and to monitor patient responses to therapy.^{29,81,82,166,167}

To enable both the interrogation of biomechanical effects on metastasis as well as the elucidation of mechanisms of adhesion, engineered microfluidic systems are frequently implemented to model metastasis *in vitro*.^{12,164} Despite being highly simplified systems relative to *in vivo* mouse models, they have the advantage of enabling experimentation under defined cellular, molecular, and/or biophysical conditions. Using video microscopy-based imaging to monitor the extent of adhesion in simulated flow fields that exhibit forces on par with those experienced in the microvasculature, many thousands of cells can be analyzed in a single experiment, enabling high sampling volumes in individual or parallelized experiments. Biochemical, biomolecular, and transcriptomic manipulations of analyzed cells can also be performed to interrogate biomolecular mechanisms contributing to metastatic adhesive phenotypes.^{81,82,161,165,168,169} The capacity to probe the attributes intrinsic to cancer cells that confer adhesion in an unperturbed manner, however, is not feasible using these interventional type approaches without *a priori* knowledge. Imaging based analyses alone also provide limited insight into biomolecular mechanisms and also do not allow for subsets of cells to be collected and assayed in an unbiased manner based on their phenotypes of adhesion.

To overcome the existing limitations but leverage the advantages of such *in vitro* microfluidic systems in the investigation of metastasis, we engineered a flow-based device that functions as an adhesive chromatography platform. This system, based on a widely used parallel-plate flow chamber, leverages the time-averaged velocities of cells perfused as a pulse and dispersed in perfusion media in a controlled flow field as a proxy for overall adhesion propensity to a substrate with or without surface functionalization with adhesive ligands (Figure 3.1a). The high-throughput nature of the cell adhesion chromatography

system permits the analysis of a large number of cells simultaneously in an environment that, used herein, recapitulates the physiological flow of the circulatory system. Using residence time theory, cells with lowly versus highly adhesive phenotypes can be separately enriched and collected at sufficient yields amenable to off-chip analyses, allowing further investigation of cell subsets expression profiles, metastatic potential, and molecular characteristics. Using this methodology, cell subsets exhibiting distinct adhesive behaviors within a population of genomically identical metastatic human colon carcinoma cells that nevertheless exhibit heterogeneous profiles of adhesion to E-selectin in flow were interrogated to reveal how expression and transcriptomic mechanisms associated with this transient metastatic phenotype are regulated by flow.

3.2 Materials and Methods

3.2.1 Cell Culture

Human colorectal adenocarcinoma LS174T cells and mouse melanoma B16F10 cells were cultured in Dulbecco's Modified Eagle Medium supplemented with 10% heat inactivated fetal bovine serum (FBS) and 1% penicillin-streptomycin-amphotericin (Life Technologies). The cells were harvested via mild trypsinization with 0.25% trypsin EDTA and 0.05% trypsin EDTA respectively, centrifuged at 400 X G for 5 min, and resuspended in culture medium. Cells were either used for perfusion experiments or diluted into tissue culture treated cell flasks for subculture. Prior to use in perfusion experiments, the LS174T cells were incubated in suspension for 2 hr at 37°C to allow cell surface glycoprotein regeneration. Quantification of cell confluency was performed by analyzing the area of adherent cell cultures compared to the total surface area of the well surface bottom using ImageJ (National Institutes of Health). The confluency at various time points was normalized to that at the time of seeding the cells.

3.2.2 Channel Fabrication

Microfluidic channels were fabricated as detailed previously.¹⁷⁰ Concisely, the microfluidic channels were made using 100 um thick double-sided adhesive tape (3M) backed with a release liner into which a U-shaped channel of two parallel 2 cm wide by 14 cm long sections connected by a 2 cm wide by 1.5 cm long section was cut using a craft cutter (Silhouette America). The adhesive channels were then affixed to Polydimethylsiloxane (PDMS) (Ellsworth Adhesives), which was previously cured by mixing PDMS base with curing agent at a ratio of 9:1 and curing for 3 hr at 90°C in a Pyrex

dish. To finish fabrication, an inlet hole was punched into channel using a biopsy punch, and assembly was attached to a non-tissue culture treated polystyrene plates where an outlet hole was drilled.

3.2.3 *Channel Functionalization*

The channel was functionalized by incubating with $2.5 \mu\text{g mL}^{-1}$ Fc specific goat anti-human IgG (R&D Systems) in Dulbecco's Phosphate Buffered Saline (D-PBS) without calcium and magnesium at 4°C overnight, blocking with 1% BSA in D-PBS at room temperature for 1 hr, incubating with $2.5 \mu\text{g mL}^{-1}$ of recombinant human E-Selectin Fc chimera protein (R&D Systems) in D-PBS with calcium and magnesium at room temperature for 2 hr, and finally, blocking the entire device with 1% BSA in D-PBS at room temperature for 1 hr. In between each step, the channel was washed three times with 1 mL of D-PBS with calcium and magnesium. For Static flow experiments, the channel was functionalized from the outlet up to 1 cm from the inlet. For Continuous flow experiments, only the straight portion nearest the outlet was functionalized.

3.2.4 *Perfusion Experiments*

An inlet syringe coupled to tubing, which was filled with perfusion media (0.1 % BSA in D-PBS), were connected to a syringe pump (PhD Ultra Harvard Apparatus). The syringe pump was used to withdraw a cell pulse of 250,000 cells diluted in 200 μL of perfusion media into the inlet tubing at a rate of 0.5 mL min^{-1} . The tubing-syringe pump was inserted into the inlet hole of the channel and a 5 mL test tube was connected to the bottom of the outlet hole as the cell collection reservoir. The entire apparatus was placed on an Eclipse TI optical microscope (Nikon) with an objective magnification of 10X and

linked to NIS-Elements software (Nikon) to acquire videos at 0.281 μ s and a frame rate of 25 frames per sec. To begin perfusion, the syringe pump was set to a flow rate to achieve the desired wall shear stress to initiate inflow from the syringe-tubing assembly. In Static flow experiments, perfusion was paused after two min of inflow to allow the cells to settle to the bottom of the channel and interact with the functionalized surface. After five min of stopped flow had transpired, flow was restarted for the predetermined free flow elution time of the cells (the time it takes for 95% of the cell pulse to elute out of an unfunctionalized channel), after which perfusion was stopped and the test tube containing the cell solution collected during perfusion was removed and a new test tube was attached. Finally, the syringe with inlet tubing was replaced with a new syringe-inlet tubing apparatus filled with only perfusion media and used to eject the cell solution out of the channel and into the second collection tube. In Continuous flow experiments, perfusion was stopped after the free flow elution time had been reached. At the end of the experiment, the number of cells and nonviable cells were counted, then analyzed using a BD LSRII flow cytometer (BD Biosciences) for expression of various ligands or put back into cell culture.

3.2.5 Cell Fraction Quantification and Cell Viability Analysis

The collected cell fractions were centrifuged at 400 X G for 5 min, the supernatant was decanted, and the cell pellet resuspended in 200 μ L of perfusion media. Trypan Blue 0.4% (Life Technologies) was diluted 1:1 with D-PBS. The 0.2% solution was mixed with collected cells in a 1:1 ratio and incubated at room temperature for 2 min. A sample of the cell-trypan solution was then loaded onto a hemocytometer and viewed under a microscope

to count the total number of cells collected in each fraction as well as the fraction of non-viable cells and the viable cells.

3.2.6 *Flow Cytometric Analysis*

The cell solution was centrifuged at 400 X G for 5 min and resuspended in diluted antibody solutions on ice for 45 min, washed with D-PBS two times, and resuspended in perfusion media for analysis on the flow cytometer. The antibodies (BD Biosciences) were diluted in D-PBS in the following ratios – 1:20 for PE CD44 and PE CEA, 1:40 for APC or PE HECA452, and 1:10 for APC CD24. Obtained flow cytometric data was analyzed using FlowJo software (Treestar Inc.).

3.2.7 *Video Analysis*

The mean distance of the cells from the channel bottom at any given time was experimentally determined and calculated as previously described.¹³ Briefly, a cell pulse followed by perfusion media was perfused into an unfunctionalized channel and five min videos were taken with the focal plane set to the channel bottom at nine evenly spaced positions across the channel length. The videos were subsequently analyzed using an OpenCV-based Traffic Flow Analyzer cell tracking software that is able to detect cell edges and their x and y position, and consequently determine the cell velocity according to Equation 1. The metric $y_{vel}/0.5(r_x+r_y)$ was used to represent the distance of a cell from the channel bottom based on its horizontal velocity.

$$v_x = \frac{\tau_{wall}}{h\mu_{medium}} \left(\frac{h^2}{4} - y_{vel}^2 \right) \quad (1)$$

3.2.8 *Cell Pulse Location Quantification*

To determine the location of the cell pulse when perfusion is paused during static flow experiments, inflow of a 200 μL cell pulse at 1.25×10^6 cells mL^{-1} followed by perfusion media into an unfunctionalized channel was started for two min, stopped, then images were taken at evenly spaced positions along the length of the channel and the number of cells at each position were counted. Alike, the number of interacting cells in functionalized channels was quantified by taking 30 sec videos across nine evenly spaced length positions in the channel and three evenly spaced width positions at each length position after steady flow had been reached, and previously described metrics were used to distinguish interacting from non-interacting cells.¹⁷¹ Briefly, in perfusion experiments, a cell that paused within imaging field of view or translated substantially slower than the free flow velocity was defined as an “interacting” cell, whereas a “non-interacting” cell was defined as one that which did not mediate contact with the channel bottom during observation.¹³

3.2.9 *Free Flow Elution Time Quantification*

The free flow elution time of the cells was determined by modifying a procedure previously used to find the residence time of cells in a microfluidic channel.¹³ 30 min videos of 250,000 cells perfused as a 200 μL cell pulse at a flow rate corresponding to the desired wall shear stress were taking 0.5 cm from the channel outlet. The aforementioned cell tracker code set to threshold of 4 and a blurring factor of 7 was used to identify objects that had a diameter between 12-18 μm that had traveled more than 400 μm during the course of the video and record the time it took the object to leave the field of view after

perfusion had begun. The values were put into Prism (GraphPad Software Inc) to create cumulative frequency plots. The elution time of free flow cells was defined as the time at which 95% of the tracked cells had left the field of view.

3.2.10 In Vivo Metastasis Model

10^4 LS174T cells, either from the unsorted parental population or fractionated using the adhesion chromatography system, were suspended in 100 μ L of sterile saline and each fraction was injected intravenously via the tail vein into six week old female NSG mice under isoflurane anesthesia (Jackson Labs). After 7 or 14 d, mice were sacrificed by CO₂ asphyxiation, lungs dissected, and metastatic foci counted. Afterwards, the lungs were flash frozen in optimal cutting temperature (OCT) gel in a bath of 2'-methylbutane cooled in a bath of liquid nitrogen then maintained in a freezer at -80°C until cryosectioning into 10 μ m slices, staining with hematoxylin and eosin (H&E), and imaging with a Nanozoomer microscope (Hamamatsu Photonics). Cell densities were quantified as previously described.¹⁷⁰ Briefly, H&E stained histology images were imported into ImageJ using the NDPI tools plugin¹⁷² and thresholded using identical parameters across all images to quantify the percent area above the thresholded background to quantify the cell density of each cryosection. All protocols for animal procedures were approved by the Institutional Animal Care and Use Committee at Georgia Institute of Technology.

3.2.11 mRNA Extraction and Sequencing

The cell samples used to for mRNA extraction were flash frozen using liquid nitrogen either immediately after perfusion or after 48 hr of culture. Total RNA was isolated by the RNeasy Micro Kit (Qiagen) according to the manufacturer's instructions. Briefly, frozen

cell pellets (3^5 cells per pellet) were immediately suspended in RLT Plus lysis buffer in the presence of beta-mercaptoethanol. Lysates were homogenized via centrifugation (at maximum speed for 2 min) using Qiashredder columns. One volume of 70% ethanol was added to the lysate, and mixed via pipetting. The samples were transferred to RNeasy MinElute spin columns and centrifuged for 15 sec at 8000 X G. After washing column with RW1 buffer, on column DNase digestion was performed. After on-column washing steps, columns were dried via centrifugation at full speed for 5 min. RNA was eluted in 50 μ L of RNase-free water. RNA concentration and purity were determined via a NanoDrop spectrophotometer. Once the mRNA was extracted, The New England Biolabs (NEB) mRNA isolation kit was used to pull down mRNA using poly T beads. Next, the NEB Ultra II RNA directional kit was used to convert the mRNA to double stranded cDNA, utilizing illumine adapters, which were added to each fragment in order to sequence the mRNA.

3.2.12 mRNA Sequencing Analysis

In preparing the RNA-Seq data from 6 LS174T samples for the differential gene expression analysis, quality control was performed on 12 raw FASTQ files using FastQC (Babraham Informatics) and Trimmomatic (Usadel Lab) to ensure the quality of the data. The quantification of the gene expression levels for the 6 LS174T samples was performed using Salmon.¹⁷³ The gene counts were imported using a R package to prepare a count matrix for the downstream exploratory and gene-level analysis.¹⁷³ For the analysis involving the single replicates, GFOLD was used to observe changes in gene expression.

3.3 Results

3.3.1 Microfluidic-based Adhesion Chromatography

We constructed from polydimethylsiloxane (PDMS), a polystyrene tissue culture plate, and an adhesive gasket a parallel plate flow chamber device whose inlet is connected to a syringe pump to vary the wall shear stress to mimic a range of physiologically relevant shear stresses (Figure 3.1b,c). Easy to rapidly construct and assemble, and amenable to high speed video microscopy imaging of perfusion experimentation throughout the flow channel (Figure 3.1b), cells perfused as a suspension into this device in perfusion media are subjected to a roughly uniform wall shear stress level across >90% of the channel width and can be collected into an interchangeable cell reservoir at the outlet (Figure 3.1c). Experimentation performed under “Continuous” flow conditions (no cessation of flow during experimentation, Figure 3.1d, 3.2a) necessitated a so-called settling region within the flow channel to ensure all perfused cells were in contact with an adhesive substrate for uniform distances, given the time, which in the context of flow translates to distance, necessary for all perfused cells to settle to the inferior channel substrate (Figure 3.1e).^[11,19] Channels were thus functionalized only within the last third of the total channel length (channel positions 7-9, Figure 3.1d), where cells were uniformly in contact with the substrate as defined by being within one cell radii from the interior channel wall as experimentally validated by measurement of cell velocity and size (Figure 3.1e). In unfunctionalized channels passivated by blocking with bovine serum albumin (BSA), the time at which 95% of the infused cell pulse had eluted through the channel was defined as commencing the sorting phase of the experiment (Figure 3.1f). In the presence of E-selectin, this resulted in extensive adhesion by selectin-binding LS174T cells as quantified by video image analysis that was restricted to and homogeneously distributed along only the functionalized straight portion of the channel nearest the outlet (channel positions 7-9

but not 1-6, Figure 3.1g), extents unaffected by channel width position (Figure 3.1h). Adhesive LS174T cells also translated in rolling adhesion at similar velocities at various distances from the outside edge of the channel (Figure 3.1h), thus indicating good spatial control and uniformity of functionalization. Overall, given the exact size of this channel, the surface area of functionalization, wall shear stress level, and a minimum surface area density to prevent cell-cell interactions, adhesion chromatography experiments could be performed to a maximal loading capacity of approximately 10^6 cells, a number that can be tuned by parameters of channel configuration and flow.

As a point of comparison given the capacity of force to regulate the initiation of rolling adhesion, we also established a workflow for evaluating cell adhesion initiated in the absence of force but presence of flow during de-adhesion, so called “Static” experimentation. During these experiments, after loading of the cell pulse into the channel, cells were allowed to settle and interact with the substrate for 5 min (Figure 3.2b), a time experimentally determined as sufficient for cells to settle in static conditions, after which time fluid flow was reinitiated to start the sorting phase of experimentation (Figure 3.1i, 3.2c).^{13,174} Perfused again as a pulse, cells could be loaded into the device and distribute amongst the channel length (Figure 3.1j). When assessed by video microscopy, at times soon after 95% of cells had eluted from an unfunctionalized channel after reinitiation of flow (Figure 3.1k), the extent of adhesion by LS174T cells to E-selectin was substantial throughout the channel length (Figure 3.1l). Notably, the highest number of interacting cells were located at the middle length of the channel (Figure 3.1l), implying that interacting cells roll slowly and do not have time to reach the end of the channel by the end of perfusion. The extent and velocity of rolling adhesion did not vary significantly with

channel width position (Figure 3.1m). Approximately $5E10^5$ cells could be loaded into the device for experimentation, a number that again could be tweaked based on channel and flow parameters.

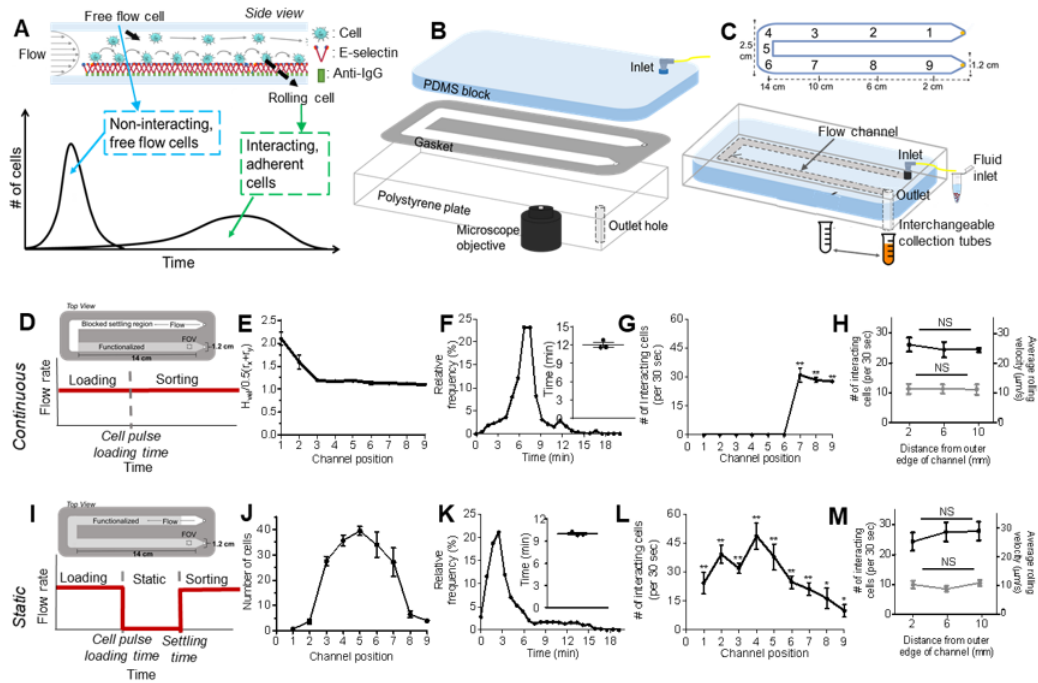


Figure 3.1 Engineered cell sorting adhesion chromatography microfluidic to investigate cancer metastasis *in vitro*. (A) Elution profiles of LS174T metastatic colon carcinoma cell populations when perfused over E-selectin, demonstrating the early elution of free flow cells followed by subsequent elution of adherent cells. (B) Hemodynamic microenvironment-mimicking, parallel-plate microfluidic fabrication, into which (C, bottom) metastatic cancer cells are infused into the E-selectin functionalized channel, visualized via an integrated high speed videomicroscopy, and collected into collection tubes based on channel residence time. (D-H) Continuous perfusion experiments, (I-M) Static perfusion experiments. (D,I) Channel functionalization schematic and perfusion workflow diagram. (E) Distance of individual perfused cells from the channel bottom calculated based on measured individual cell velocity and size decreases from the inlet (channel position 1) until reaching channel position 3 after which it is uniform throughout the remaining channel length. Data represent mean \pm s.e.m. (F,K) Representative relative frequency distribution of elution time of the infused cell pulse with the inset showing the mean time at which 95% of the cell pulse has eluted \pm s.e.m. (G,L) Number of interacting cells along the length of the channel during the sorting phase. Data represent mean \pm s.e.m. (H,M) Number of interacting cells along the width of the channel (black) and average velocity of rolling cells along the width of the channel (gray). Data represent mean \pm s.e.m. (J) Location of cell pulse during static phase of Static perfusion experiments (E-H,J-M) Each point represents the mean \pm s.e.m. of $n \geq 5$ independently run experiments. Cell pulse of LS174T colon carcinoma cells perfused at 1 dyn cm^{-2} over (E,G,I,K) 2.5 ug mL^{-1} E-selectin or (F,J) unfunctionalized channels. * $p < 0.05$ ** $p < 0.01$ compared to unfunctionalized channel (no interacting cells) by one-sample t-test.

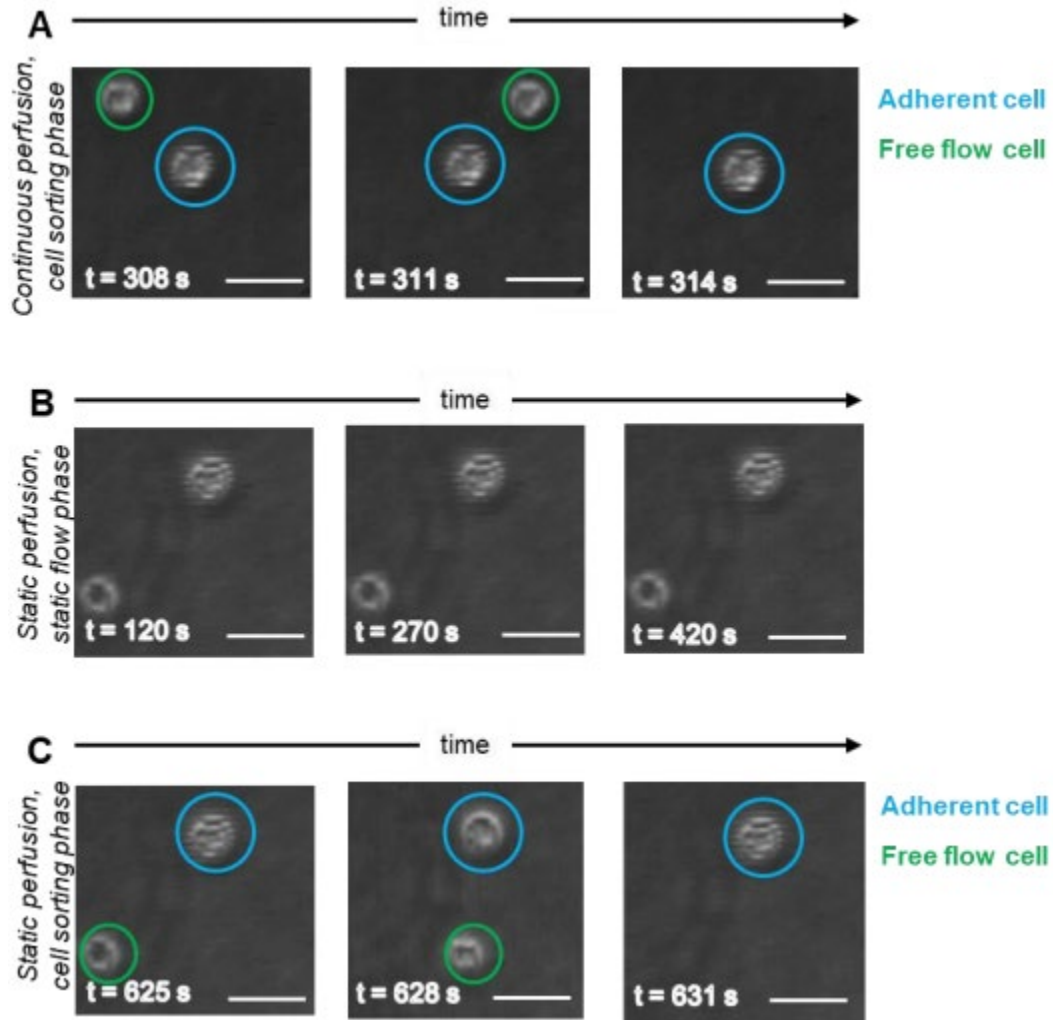


Figure 3.2. Snapshots of Static and Continuous flow experiment videos at various timepoints. (A) Frames from a Continuous perfusion video showing the time-lapse of a free flow and adherent cell during the cell sorting phase. (B) Frames from a Static perfusion video showing the lack of movement of cells during the static flow cell settling phase when flow is stopped. (C) Frames from a Static perfusion video showing the time-lapse of a free flow and adherent cell after flow is restarted in the cell sorting phase following the 5 minute static flow cell settling period. (A-C) Perfusion of an LS174T cell pulse of 250,000 cells over $2.5 \mu\text{g mL}^{-1}$ E-selectin at 1 dyn cm^{-2} . Scale bar represents $15 \mu\text{m}$.

3.3.2 *Adhesion Chromatography Microfluidic Enrichment of Distinct and Viable Cell Subsets of Varying In Vitro Adhesivities*

Experiments were performed under both Continuous and Static conditions to interrogate the effect of force on initiation of E-selectin-mediated adhesion and whether the extent and quality of experimentally observed adhesion to E-selectin differed between experimental flow types. A cell pulse of E-selectin-binding LS174T cancer cells and perfusion media was perfused through the channel surface functionalized with $2.5 \mu\text{g mL}^{-1}$ E-selectin at a predetermined flow rates corresponding to physiological levels of wall shear stress where selectin-mediated adhesion occurs, ranging from 0.5 to 5 dyn cm^{-2} .¹⁷⁴ Unsurprisingly, the extent of LS174T cell adhesion to E-selectin decreased with increasing wall shear stress level (Figure 3.3a). The velocity with which cells mediated adhesion also increased as the wall shear stress increased (Figure 3.3b).^{82,82,171} Strikingly, the velocity of rolling adhesion by LS174T cells on E-selectin did not differ between Continuous and Static experimentation at all wall shear stress levels tested, with the exception of the highest of 5 dyn cm^{-2} , where the rolling velocity of cells of adherent cells in Continuous experiments was significantly greater than that in Static experiments (Figure 3.3a-b). Non-E-selectin ligand expressing B16F10 melanoma cells were also separately perfused through the channel in a cell pulse under both Static and Continuous conditions.¹⁷⁵ Expectedly, there were minimal interacting B16F10 cells at all tested wall shear stresses levels (Figure 3.3a).

The difference in elution times from an flow channel that result from differential ability of cells to mediate adhesion was leveraged to quantify the fraction of total cells capable of mediating adhesion to E-selectin in flow – with non-interacting, free flow cells

exiting the channel before interacting, adherent cells (Figure 3.1a).^{13,171} Cells that eluted prior to the predetermined “non-interacting cell elution time” were collected as the “Free flow” fraction. Subsequently, the cell collection reservoir was changed and the cell subset remaining within the microfluidic device removed by escalating the flow to 5 dyn cm⁻² for 5 min was collected labeled as the “Adherent” fraction (Figure 3.3c).

Using this workflow and using a wall shear stress of at 1 dyn cm⁻² and 2.5 μg mL⁻¹ E-selectin, >70% of cells (either LS174T or B16F10) were recovered during experimentation, levels unchanged by channel functionalization (Figure 3.3d). Of the cells recovered, ~60% of LS174T cells eluted in the adherent population (Figure 3.3e), extents at levels nearing those seen for Static experimentation (Figure 3.3a). Conversely, nearly all of B16F10 cells eluted into the non-interacting, Free flow fraction when perfused in either Static or Continuous flow set-ups, consistent with B16F10 cells, which lack E-selectin ligands failing to mediate adhesion to E-selectin in flow (Figure 3.3a).¹⁷⁵ However, ~10% of perfused B16F10 cells were recovered in the Adherent fraction, a proportion similar in magnitude to the amount of LS174T cells recovered from unfunctionalized channels (Figure 3.3e) indicating a small extent of contamination within the enriched adherent cell subset. Nevertheless, the fraction of LS174T cells comprising the adherent fraction was substantially larger than for B16F10 cells. Of the collected cells of each clone type, over 95% were viable in collected cell fractions, and viability was not affected by perfusion, channel functionalization, nor the adhesion propensity of the cell (Figure 3.3f). Furthermore, fractionated LS174T cell subsets cultured for 72 hr showed no differences in the ability to proliferate (Figure 3.3g) or grow (Figure 3.3h) in culture, indicating that the system is able to collect viable cells for further expansion and post-perfusion analysis.

When varying wall shear stress level to emulate the range of physiologically relevant flow conditions of the microenvironment a circulating metastatic cell may be exposed to, perfusion of selectin-ligand expressing LS174T cancer cells over E-selectin functionalized surfaces resulted in collection of a decreasing fraction of total perfused cells (Figure 3.3i). At 0.5 and 1.0 dyn cm⁻², experiments performed under Continuous flow conditions resulted in slightly but significantly lower levels of cell recovery compared to Static experiments (Figure 3.3i). Taken together, these results indicate that this adhesion chromatography device is capable of not only separating cells based on adhesion propensity to the functionalized substrates in a manner regulated by hemodynamic force, but also that sorted cells can be retained and/or expanded for further phenotypic, genotypic, and molecular analysis post perfusion.

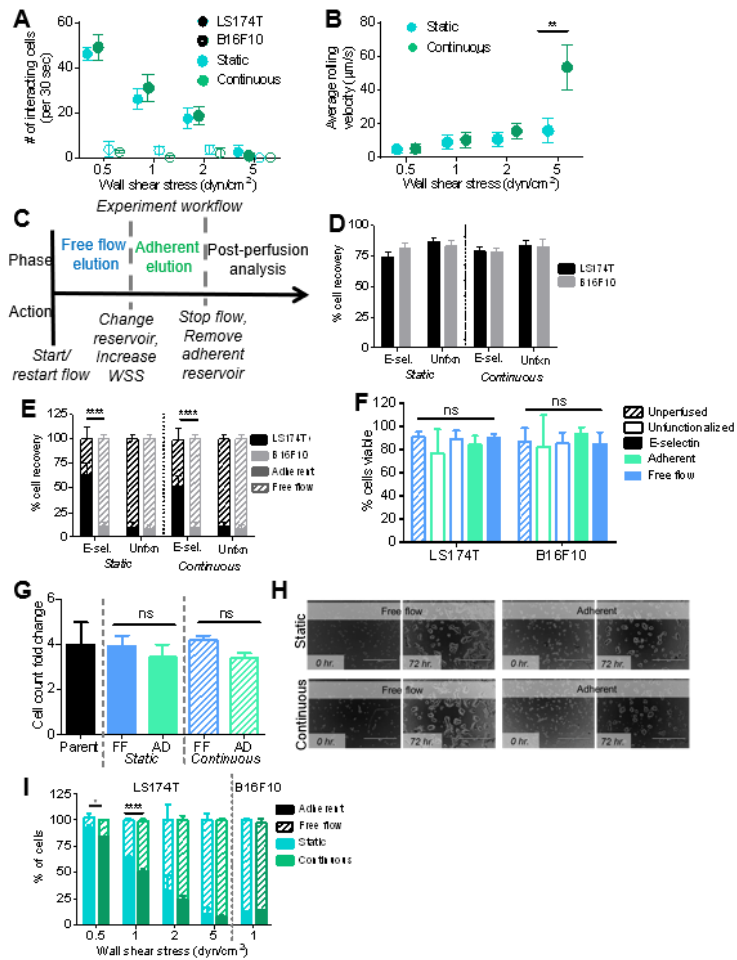


Figure 3.3 Collected cell fraction analysis. (A) Number of interacting cells during the sorting phase of perfusion. (B) Rolling velocity of interacting cells during the sorting phase of perfusion. $n \geq 20$. (A-B) Either static or continuous flow at 0.5, 1, 2, or 5 dyn cm^{-2} . Each point represents the mean \pm s.e.m. of $n \geq 3$ independently run experiments. (C) Experiment workflow diagram of static and continuous flow experiments. (D) Percent of total cells recovered from infused pulse of 250,000 cells after perfusion on either a functionalized or unfunctionalized channel. (E) Percent of cells collected in either the free flow or adherent cell fraction after either Static or Continuous flow on an unfunctionalized channel or a functionalized channel. (F) Percent of cells that are viable prior to perfusion or in each fraction after perfusion on either a functionalized or unfunctionalized channel. (G) Increase in cell number of cultured unsorted cells or collected cell fractions after 72 hr normalized to initial cell culture seeding number. FF: free flow, AD: adherent. (H) Representative brightfield images of cultured cells in a well of a 96 well plate at time of initial seeding (0 hr.) or after 72 hr. Scale bar represents 400 μm . (I) Percent of LS174T or B16F10 cells collected in each fraction after perfusion under either Static or Continuous flow (D-G, I) Perfusion experiments were at 1 dyn cm^{-2} . Functionalized experiments were over $2.5 \mu\text{g mL}^{-1}$ E-selectin. Each bar represents the mean \pm s.e.m. of $n \geq 3$ independently run experiments. (E, I) * $p < 0.05$, ** $p < 0.01$, ** $p < 0.0001$ by t-test comparing sizes of adherent cell fractions.**

3.3.3 Sorted Cell Fractions Exhibit Different Metastatic Potential *In Vivo*

We sought to explore the relationship between propensity to mediate adhesion to E-selectin, using channel residence time as a proxy, and metastatic potential *in vivo*. As such, using an E-selectin functionalized channel, a cell pulse of LS174T cells were perfused through the channel at 1.0 dyn cm^{-2} and sorted based on elution time into free flow and adherent populations, and 10^5 cells from sorted fractions were subsequently injected intravenously via the tail vein into NSG mice. Markedly, the cells from the adherent subset, enriched in the adhesion chromatography device based on their enhanced ability to interact with E-selectin *in vitro*, exhibited greater lung metastatic tumor bearing potential than the cells from the free flow subset *in vivo* 7 and 14 d post injection as quantified by counting the total number of lung metastases in each mouse (Figure 3.4a-b). Further, when normalizing the number of metastasis in each lung 7 d post injection to the unsorted, parental population, the injected free flow cell group exhibited a decreased number of metastases, further elucidating the less metastatic nature of the free flow fraction (Figure 3.4c). Quantification of hematoxylin and eosin histology sections confirmed these results, as injection of cells from the free flow fraction resulted in a lower cell density within lung cryosections than injection of cells from either the adherent fraction or unsorted, parental population (Figure 3.4d). These results demonstrate the utility of this adhesion chromatography device in enriching cells with differential metastatic potentials based on their E-selectin binding capabilities.

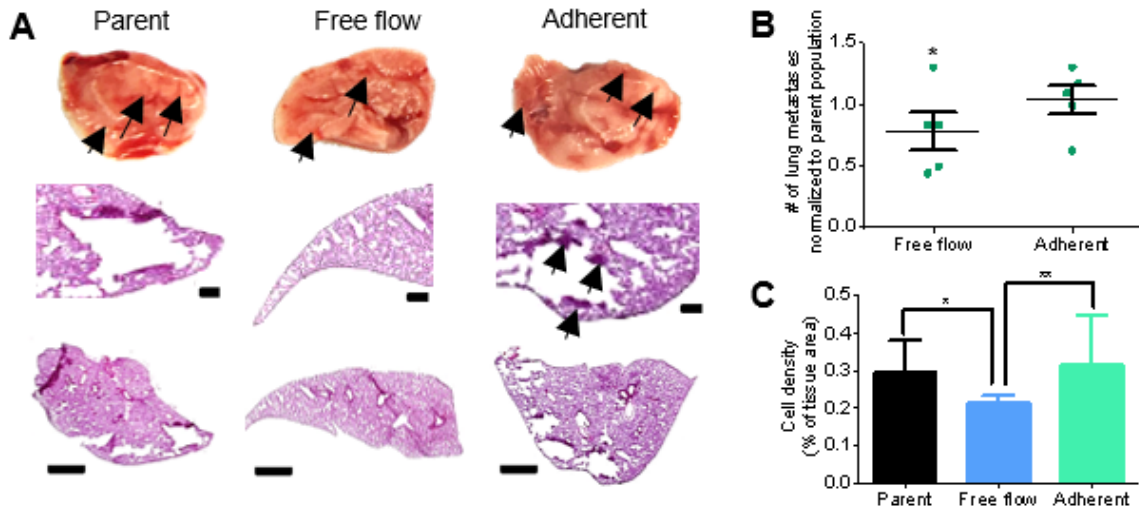


Figure 3.4 LS174T cells collected using adhesion chromatography in the Free flow fraction metastasize *in vivo* less than Adherent fraction. (A) Representative bright field and chromogenic images of NSG mouse whole lobes and lung sections and 7 d post intravenous (i.v.) infusion of parent (unsorted) or sorted free flow or adherent LS174T cells. Arrows indicate metastatic tumors. Scale bars, 100 μm or 1 mm in regions of interest and whole lobe images, respectively. (B) Count of lung metastases in either the free flow group or the adherent group normalized to the mean number of lung metastases per NSG mouse in the parent (unsorted) group 7 d post i.v. infusion. (C) Quantification of hematoxylin and eosin staining for each group. (A-C) Perfusion and separation of an LS174T cell pulse of 250,000 cells was over $2.5 \mu\text{g mL}^{-1}$ E-selectin at 1 dyn cm^{-2} . NSG mice were injected i.v. with 10^5 LS174T cells. (B) Each point represents an individual mouse lung. (C) Bars represent mean \pm s.e.m. of $n \geq 5$ individual mice. Statistical test by (B) t-test $H_0: \mu = 1$ * $p < 0.05$ or (C) one-way ANOVA with post hoc t-test with Bonferonni corrections for multiple comparisons * $p < 0.05$ ** $p < 0.01$

3.3.4 *Differential Selectin Ligand Expression by LS174T Cells Separated Using Adhesion Chromatography by E-selectin Adhesivity*

Selectin ligand glycan epitope and glycoprotein expression levels in LS174T cell populations sorted for their enriched adhesive potential on E-selectin were measured. Sialofucosylated tetrasaccharides sialyl Lewis x (sLe^x) ligand expression, as measured by anti-sLe^{x/a} binding antibody HECA-452, on sLe^a-negative LS174T cells collected in the adherent versus free flow fractions, was assessed flow cytometrically. In both Static and Continuous flow experiments, the Free flow LS174T subset (the cells that did not interact with the E-selectin during perfusion through the microfluidic device) had significantly less HECA452 immunoreactivity relative to the cells that exhibited adhesion to E-selectin (Figure 3.5a,b). Furthermore, when binned into high and low HECA452 stained populations based on the highest 10% and lowest 10% of the unsorted parent populations (HECA^{hi} and HECA^{lo}, respectively), the adherent fraction had significantly more cells HECA^{hi} (sLe^{x hi} expressing) cells whereas the free flow cell population had significantly more HECA^{lo} (sLe^{x lo} expressing) cells (Figure 3.5c). Jointly, these results substantiate the finding that increasing sLe^x expression is associated with enhanced LS174T cell adhesivity to E-selectin in flow.^{13,171}

Relationships between LS174T cells' capacity to mediate adhesion to E-selectin in flow and expression of CD44 and carcinoembryonic antigen (CEA), two previously identified selectin ligand glycoproteins, was also determined. Experiments performed under both Static flow and Continuous flow conditions revealed increased levels of CD44 expression on cells collected in the interacting, adherent cell fractions (Figure 3.5d-e).^{13,29,161} Despite differences in CD44 expression levels among collected fractions in both

perfusion methods, only an increase in CD44^{lo} cells in the free flow subset and an increase in CD44^{hi} cells in the adherent subset collected after continuous flow (Figure 3.5f) with high and low CD44 stained populations defined on the highest 10% and lowest 10% of the unsorted parent populations (CD44^{hi} and CD44^{lo}, respectively). Contrastingly, CEA expression levels among the two fractions did not differ (Figure 3.5g-h), and this lack of difference was also reflected in no change in the frequencies of the sorted populations within the high and low CEA stained populations defined on the highest 10% and lowest 10% of the unsorted parent populations (CEA^{hi} and CEA^{lo}, respectively) (Figure 3.5i). Together, these results implicate a flow-regulated role for CD44 in E-selectin mediated adhesion and suggest a redundant role of E-selectin ligand CEA, as has been previously suggested.⁸²

Sorted cells were next costained to interrogate any relative co-enrichment of CD44/HECA(sLe^x) or CEA/HECA(sLe^x) expression by flow cytometry. Using mean fluorescence intensity of HECA452 as a proxy, sLe^x expression in CD44^{hi} and CD44^{lo} LS174T subset (Figure 3.5j) was found to be enhanced in the CD44^{hi} subset in both Static and Continuous experimentation (Figure 3.5k). Dissimilarly, when employing the same gating strategy to analyze CEA and HECA coexpression, there was no difference found in sLe^x expression between the cell subset with either high or low CEA expression (Figure 3.5l). Collectively, these findings elucidate the interrelation between the adhesion propensity of LS174T cells and their ligand expression, further demonstrating the importance of concurrent high expression of sLe^x and CD44 in enhancing LS174T cell interaction with E-selectin in flow. Moreover, they illustrate the utility of this platform in

probing complex relations between adhesion cell adhesive phenotypes and profiles of ligand expression.

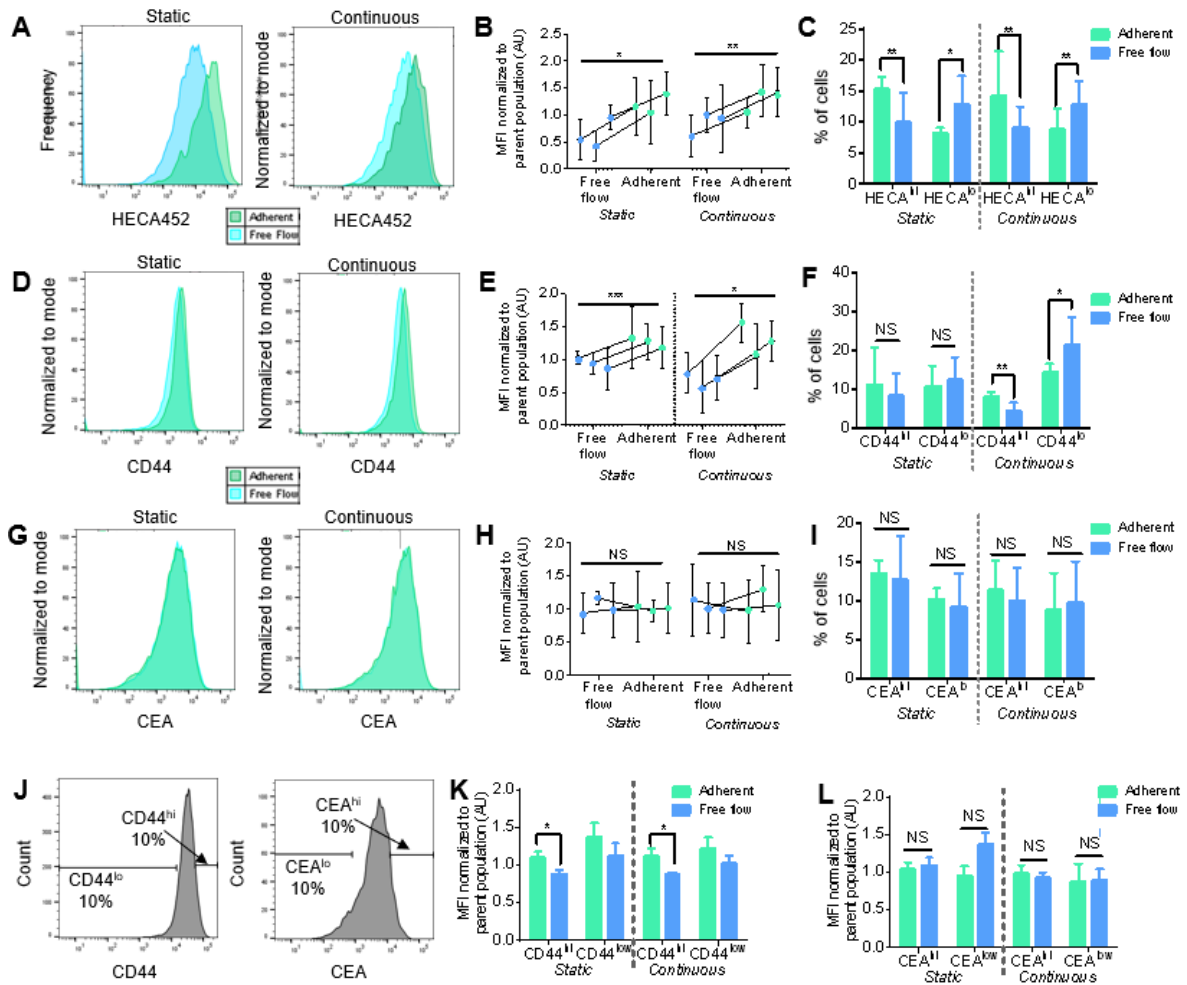


Figure 3.5 LS174T cells collected using adhesion chromatography into Adherent subset after perfusion over E-selectin exhibits enhanced HECA and CD44, but not CEA, expression levels. (A,D,G) Representative flow cytometric histograms of sLe^x (HECA452), CD44, or CEA expression. (B,E,H) sLe^x (HECA452), CD44, or CEA expression normalized to the parent population between cells in the collected free flow fraction and adherent fraction. Each point represents the mean fluorescent intensity of analyzed cells \pm s.e.m. (C,F,I) Percent of cells in each fraction that are in the top 10% or bottom 10% of sLe^x (HECA), CD44, or CEA expressing cells. Each bar represents the mean \pm s.e.m. of $n \geq 3$ individually run experiments. (J) Representative flow cytometry gating and analysis strategy for (K,L) sLe^x (HECA452) expression levels normalized to the unsorted parent LS174T cell population in either high (top 10%) or low (bottom 10%) expressing subset of (K) CD44 or (L) CEA. Each bar represents the mean \pm s.e.m. of $n \geq 3$ individually run experiments. Perfusion and separation of an LS174T cell pulse of 250,000 cells was over $2.5 \mu\text{g mL}^{-1}$ E-selectin at 1 dyn cm^{-2} . * $p < 0.05$ ** $p < 0.01$ *** $p < 0.001$ by paired t-test.

3.3.5 Adhesion to E-selectin In Flow by LS174T Cells is a Transient Phenotypic Characteristic Not Associated with Significant mRNA Profile Expression Changes in Adhesive Ligand Genes

In order to elucidate the drivers of invasive cancer metastasis, metastatic potential is often studied by probing genotypic differences among the various subsets of metastatic cancer cell populations.^{11,12} To interrogate the ability of LS174T cells to retain their metastatic selectin adhesion characteristics for subsequent study, LS174T cells were perfused in Continuous flow experiments and collected into Adherent or Free flow fractions. The subsets were either reperfused immediately to confirm enrichment based on adhesivity or placed in culture for 72 hr before analysis in subsequent perfusion experiments. Expectedly, immediate reperfusion resulted in the reperfused Free flow cells showing a decreased adhesion, as indicated by significantly more cells eluting into the Free flow fraction than the other two subsets. Correspondingly, the reperfused Adherent cells showed a greater adhesive propensity, and the cells also had a greater expression of sLe^x than the reperfused free flow cells (Figure 3.6a-b). When the cultured subsets were reperfused under Continuous conditions, however, there was no difference in the relative size of the collected interacting and non-interacting fractions between subsets, and HECA452 staining revealed no difference in expression levels (Figure 3.6a-b). These results reveal E-selectin adhesivity to be a phenotypic characteristic of LS174T that is not sustained.¹²

To investigate the mechanisms underlying this transient metastatic phenotype of LS174T cells, mRNA sequencing was performed and gene expression profiles among various cell subset were quantified and compared. Specifically, parental populations of

LS174T colon carcinoma cells were perfused in Continuous flow at 1 dyn cm^{-2} over $2.5 \mu\text{g mL}^{-1}$ and sorted into Free flow and Adherent fractions based on elution time. A subset of each fraction was immediately processed for mRNA extraction and analysis, and the remaining cells from each fraction were cultured separately for 48 hr prior to transcriptome analysis. Additionally, a time-matched, perfused but unsorted population of parental LS174T cells were either immediately or cultured for 48 hr before processing for transcriptome analysis to serve as a control. Subsequently, the LS174T cells sorted in the adhesion chromatography system using E-selectin under Continuous flow conditions were analyzed and the sorted fractions were compared to each other as well as to that of the untreated parental cells.

We hypothesized that since adhesivity is not a retained characteristic of LS174T cells but rather a transient phenotype, the sorted subsets of cells analyzed immediately after perfusion would exhibit different expression levels of genes, particularly those related to adhesion, the actin/cytoskeleton structure, and/or cell growth phase, compared to each other, as well as compared to that of the unsorted populations and sorted populations that were analyzed after 48 hr in culture – all of which we expected to all exhibit similar expression levels. Surprisingly, mRNA expression data for all samples showed minimal differences between subsets, and hierarchical clustering grouped the samples not by their respective fraction, but rather by the time at which they were analyzed after perfusion (0 versus 48 hr), which is likely a growth phase related artifact (Figure 3.6c). Given these unexpected results, we analyzed changes in genes regulating sLe^x, CD44, and CEA expression but again found no significant differences between any group, and the hierarchical grouping still clustering samples by time rather than sorting (Figure 3.6d).

Further, interrogation of fold change of the genes of interest revealed only minor fold changes between all combinations, with a majority of the differences clustering at a fold change of nearly zero (Figure 3.6e-g). Finally, because changes in the actin cytoskeleton structure and cell cycle stage have been implicated in cancer metastasis, we probed the mRNA profile of those pathways, which again informed similar mRNA expression among all six samples and consistent clustering as to what was seen previously (Figure 3.6h-i). Taken together, these results indicate that the transient adhesive phenotypes of metastatic LS174T subsets is not reflected in changes mRNA profile of genes controlling adhesive ligand presentation, despite measured differences of both functional adhesive propensity on E-selectin and surface presented sLe^x and CD44 ligand expression. Notably, due to the lack of measurable changes in expression of pathways we hypothesized would control cell adhesivity to E-selectin, biological replicates were not conducted, and transcriptome analysis was not performed.

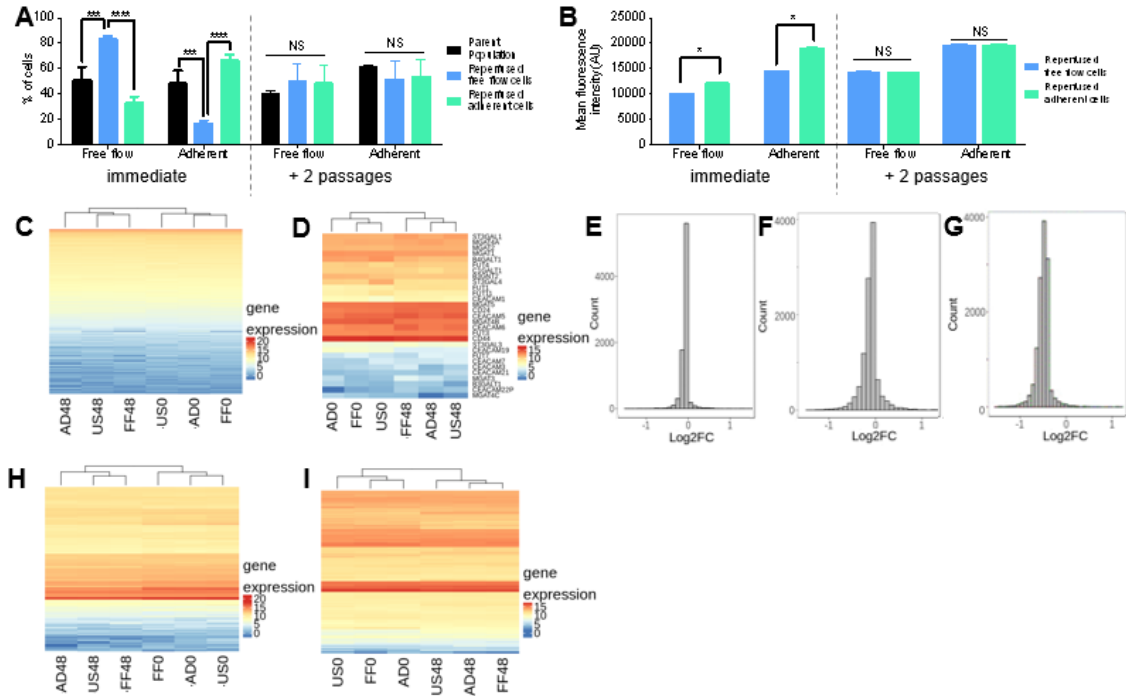


Figure 3.6 Adhesivity to E-selectin is a transient phenotype by LS174T cells not caused by mRNA expression changes. (A) Percent of LS174T cells collected in either the free flow or adherent fraction of the parent (unsorted) population or reperused cell subsets either immediately after perfusion or after 2 passages. Each bar represents the mean \pm s.e.m. of $n \geq 3$ individually run experiments. **(B)** Quantification of sLe^x expression of cells in each collected cell fraction. **(C,D,H,I)** mRNA expression heatmaps of **(C)** all analyzed mRNA, **(D)** genes regulating CEA, CD44, and sLe^x presentation, **(H)** actin-cytoskeleton structure, and **(I)** cell cycle stage. US0/FF0/AD0: unsorted/free flow/adherent, flash frozen at 0 hr; US48/FF84/AD48: unsorted/free flow/adherent, flash frozen at 48 hr. **(E-G)** Histograms of log2 fold change at 0 hr of genes regulating CEA, CD44, and sLe^x presentation of **(E)** free flow compared to adherent, **(F)** free flow compared to unsorted, and **(G)** adherent compared to unsorted. **(A-C)** Perfusion and separation of an LS174T cell pulse of 250,000 cells was over $2.5 \mu\text{g mL}^{-1}$ E-selectin at 1 dyn cm^{-2} . * $p < 0.05$ *** $p < 0.001$ **** $p < 0.0001$ by **(A)** One way ANOVA with post-hoc t-test or **(B)** t-test.

3.3.6 *LS174T Cell E-selectin Adhesive Phenotype Association with Cancer Stem Cell Features*

The relationship between a molecular marker of cancer stem cells and adhesive phenotype on E-selectin in flow for LS174T cells were investigated through costaining sorted populations with CD24 and either HECA452, CD44, or CEA (Figure 3.7a-c). Upon evaluation of the expression of E-selectin ligands and cancer stem cell marker CD24, the highest 10% of HECA (sLe^x) and CEA expressing cells were found to exhibit higher levels of CD24 expression (Figure 3.7c,e).¹⁷⁶ Contrastingly, the lowest 10% of CD44 expressing cells correlated with higher levels of CD24 expression (Figure 3.7b). Using the adhesion chromatography system to enrich cells on 2.5 $\mu\text{g mL}^{-1}$ E-selectin at 1.0 dyn cm^{-2} , the effect of E-selectin adhesivity on the frequencies of CD24 expressing cells within adhesive versus non-adhesive (free flow) subsets was measured. Irrespective of perfusion type (Continuous or Static), CD24 expression levels did not differ with adhesive phenotype (Figure 3.7d, Figure 3.8a), nor was there a difference in the frequency of CD24^{hi} and CD24^{lo} cells in either fraction (Figure 3.7e, Figure 3.8). When assessed as coexpression relationships via quadrant analysis, no differences in HECA452, CD44, or CEA with CD24 were observed for Static experiments (Figure 3.8c-e). However, under Continuous flow conditions, frequencies of HECA^{lo}/CD24^{lo} were increased for cells exhibiting a lowly adhesive phenotype (Figure 3.7f). Adherent LS174T cell subsets also exhibited decreased frequencies of CD44^{lo}/CD24^{hi} cells (Figure 3.7g) and increased levels of both CD44^{hi}/CD24^{hi} and CEA^{lo}/CD24^{lo} cells (Figure 3.7g,h).

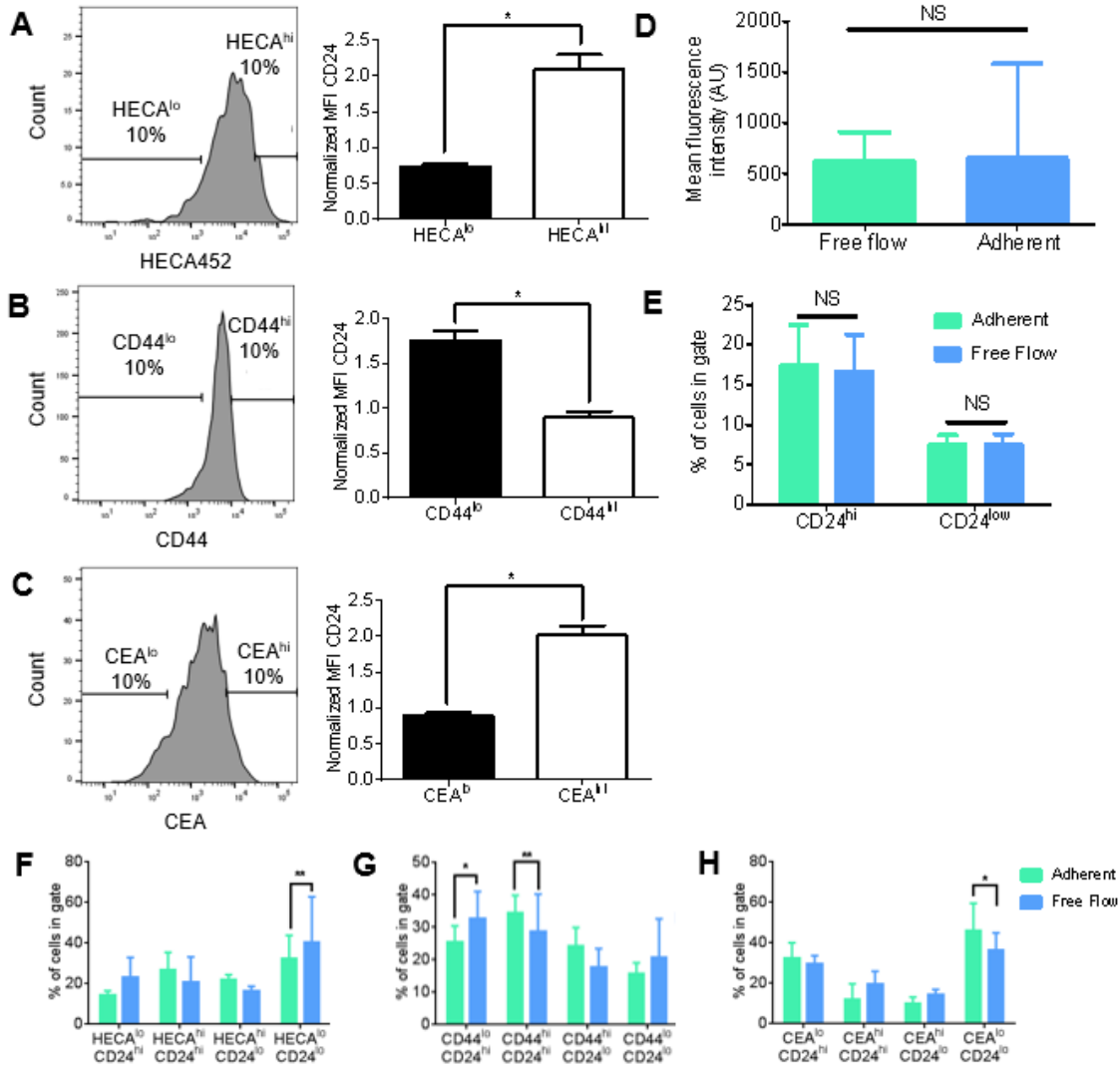


Figure 3.7 CD24 expression does not differ between LS174T cells that do or do not exhibit E-selectin adhesivity. (A-C) Representative flow cytometric histograms of sLe^x (HECA452), CD44, or CEA expression indicating gating for the top and bottom 10% percent of cells expressing the respective ligand and the CD24 MFI in the highest versus lowest 10% of HECA, CD44, or CEA expressing cells. (D) Average mean fluorescent intensity of cells obtained from the free flow and adherent fractions in continuous flow. (E) Percentage of cells in the top or bottom 10% of CD24 expressing cells after continuous flow. (D,E) Each bar represents the mean \pm s.e.m. of $n \geq 3$ individually run experiments. (F-H) Comparisons between frequencies of cells in low versus high selectin ligand expression derived from costaining. (A-C, F-H) Each bar represents the mean \pm s.e.m. of $n \geq 3$ individually run experiments. Perfusion and separation of an LS174T cell pulse of 250,000 cells was over $2.5 \mu\text{g mL}^{-1}$ E-selectin at 1 dyn cm^{-2} . * $p < 0.05$ ** $p < 0.01$ by paired t-test.

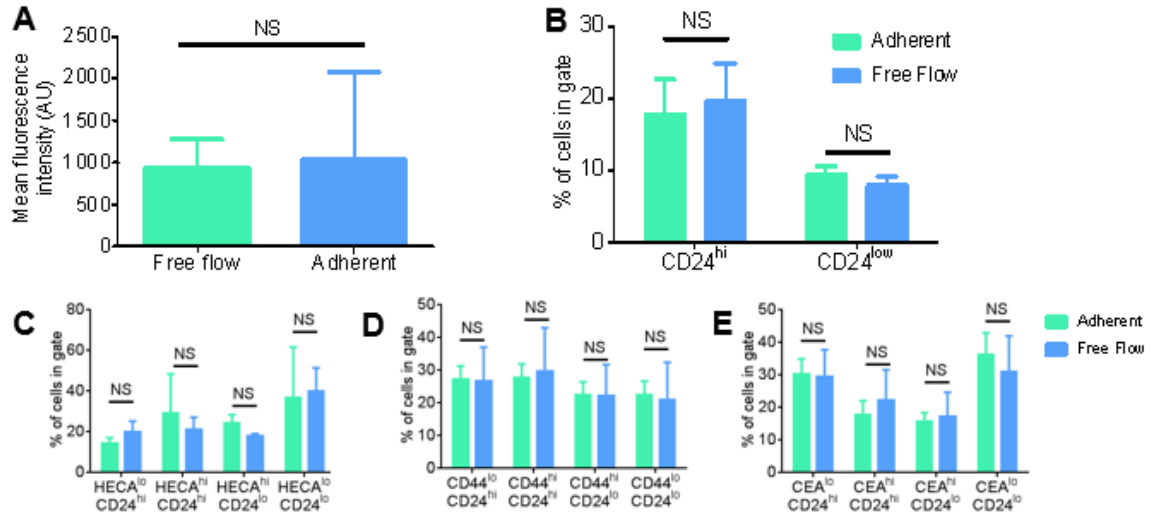


Figure 3.8 Static perfusion reveals no difference between collected fractions in coexpression of CD24 and selectin-ligands. (A) Average mean fluorescent intensity of cells obtained from the free flow and adherent fractions in static flow. (B) Percentage of cells in the top or bottom 10% of CD24 expressing cells after static flow. (D,E) Each bar represents the mean \pm s.e.m. of $n \geq 3$ individually run experiments. (F-H) Comparisons between frequencies of cells in low versus high selectin ligand expression derived from costaining. (C-E) Comparisons between frequencies of cells in low versus high selectin ligand expression derived from costaining in static perfusion. (A-E) Each bar represents the mean \pm s.e.m. of $n \geq 3$ individually run experiments. Perfusion and separation of an LS174T cell pulse of 250,000 cells. * $p < 0.05$ ** $p < 0.01$ by paired t-test.

3.4 Discussion

We demonstrate the ability to rapidly sort in an unbiased, label free manner large populations of cells based on their adhesion propensity in flow through the use of an engineered, microfluidic based adhesion chromatography platform. Using residence time as a proxy for time-averaged cell adhesive behavior to collect two distinct fractions of cells – adhesive (interacting) and free flow (non-interacting), this platform - enables not only real-time visualization of cellular adhesion under hemodynamic force, but also allows post perfusion phenotypic analysis and *in vivo* modeling of the fractionated cell subsets under defined flow conditions. Noting that increased adhesion *in vitro* correlated with enhanced

metastatic potential *in vivo* by LS174T colon carcinoma cells, we demonstrate this sorting platform can be implemented to better understand the complex process of cancer metastasis by probing interactions between selectins and glycosylated ligands expressed by metastatic cells. We furthermore demonstrate the utility of this system in the interrogation of phenotypic attributes associated with E-selectin adhesion transiently exhibited by metastatic LS174T cells, noting that the observed phenotypic differences are likely not due to mRNA expression profile changes.

This cell adhesion chromatography system permitted the interrogation of attributes shared within populations of cells that exhibit similar adhesion phenotypes. Notably, sLe^x and CD44, but not CEA, were found to have enhanced expression on LS174T cells that were able to mediate adhesive interactions with E-selectin in flow. With respect to endogenous sLe^x expression, this finding is consistent with the existing literature.¹² CEA was also not found to be enriched in either collected subset of cells, which is supported by knockdown of CEA expression in LS174T cells failing to alter adhesive behavior on E-selectin in flow.⁹⁹ Previous reports, on the other hand, have demonstrated a correlation between CD44 expression and selectin-mediated adhesion over P- and L-, but not E-selectin, which is in contrast with our findings of CD44 expression being enhanced with increased E-selectin adhesivity.¹¹ However, this noted positive correlation between adhesion propensity on E-selectin in flow and CD44 expression is in direct agreement with previous reports that also found higher levels of rolling behavior over E-selectin in cells with enhanced CD44 as well as sLe^x expression.^{12,81} Our findings highlight the advantages of our cell-sorting microfluidic platform over systems used in previous reports for our integrated system permits the analysis of the relationship between multiple cell parameters

(adhesive phenotype and ligand expression levels) of unperturbed, distinct metastatic subsets based on population averages without the need for cumbersome cell knockdown studies, limitations of single level cell measurements, or repeated sorting of cells as a result of the ability to permit rapid interrogation of a large number of cells in a relatively short period of time.

The apparent discrepancy between the lack of differential mRNA profiles and observed functional changes in adhesive propensity and E-selectin ligand presentation among sorted cell populations suggest that the protein expression changes result from post-transcriptional and/or post-translational regulatory processes.¹⁷⁷ One hypothesis is that the functional changes are a result of post-transcriptional alterations in microRNA (miRNA), which were not measured in this work. These results are consistent with previous reports that have noted only half of all protein expression changes are correlation with mRNA expression changes and post-translational repression of E-selectin ligand presentation on metastatic colon cancer cells via miRNA being implicated in regulating E-selectin mediated adhesion.¹⁷⁸⁻¹⁸⁰ Therefore, further analysis of the genomic profile of the sorted and unsorted cell fractions transcriptomally analyzed either immediately or cultured for 48 hr by analyzing and comparing miRNA expression levels, and subsequently knocking-out any identified miRNA and quantifying adhesivity alterations using our microfluidic platform, may provide further insight into the phenotypic changes causing functional adhesive differences between subsets and corroborate our proposed explanation for the reported discrepancies in mRNA expression and adhesive ligand protein expression. In addition to unexplored potential post-translational differences, additional potential post-

transcriptional changes include alterations in the length of proteins or untranslated regions of mRNA.¹⁷⁷

Correlations between adhesive phenotype and cancer stem cell markers were assessed in LS174T cells by analyzing the cell subsets fractionated for adhesion to E-selectin under flow for CD24 expression, a cancer stem cell marker whose expression is implicated in increased tumor progression, motility, and metastatic potential.^{81,170,172,176} We found that CD44 expression was inversely proportional to CD24 expression, noting the enrichment of CD24^{hi} cells in a CD44^{lo} subset, generally. This observation may give further insight into reports that demonstrate *in vivo* CD44-knockdown experiments lead to increased lung metastasis, despite our finding that high CD44 expression is linked with increased levels of adhesion on E-selectin, as the CD44 knockdown cells are subsequently augmenting a cancer stem cell subset.^{12,93,99}

Together, the noted increase in a CD44^{hi}/CD24^{hi} subset among adherent cells and increase in a CD44^{lo}/CD24^{hi} subset among free flow cells suggest that CD44 alone is predictive of adhesive phenotype, suggesting that there is no direct correlation between CD24 expression and adhesion on E-selectin under flow. Notably, these results conflict with what we recently measured for these cells when analyzed for E-selectin adhesion potential, however, those results were at a single cell, rather than population, level and obtained at 0.5 dyn cm⁻¹, under which conditions a significantly higher fractions of cells mediate adhesion in flow (by ~50%, Figure 3.3i), which may explain the discrepancy. Furthermore, despite a lack of expression level differences between CEA in sorted populations, we found an increased CEA^{lo}/CD24^{lo} subset in the Adherent subset.¹² Interestingly, although CEA expression may not be correlated with adhesive differences

on E-selectin, CEA^{lo} cells have been found to have increased cancer stem cell like properties, enhanced levels of sphere formation *in vitro*, and enhanced metastatic potential *in vivo*.¹⁸¹ Therefore, using our cell sorting platform, we are inadvertently able to enrich for this population. Low adhesive potential has previously been correlated with increased cancer stem properties in melanoma and breast cancer.¹⁸² Together our results indicate a lack of correlation between cancer stem cell marker CD24 and adhesion propensity on E-selectin in LS174T colon carcinoma cells.

Our results suggest a unique capacity for physiological force from fluid flow in influencing mechanisms of metastatic dissemination. Specifically, cell fractions collected via the Continuous perfusion method exhibited significant differences in ligand expression and coexpression between subsets that were not found in cell fractions collected via the Static perfusion method (Figure 3.5 and 3.7). We hypothesize that this is a result of forced contact between cell-expressed selectin ligands and the functionalized substrate in static flow experiments allowing a greater number of low affinity receptor-ligand interactions to occur in the free flow fraction that are not able to form in continuous flow experiments with a constantly applied shear stress. Thus, despite not changing the approximate frequency of adhesive cells of the total population, subtle differences in the collected cell subfractions were diluted in the absence of the dispersive effects of flow. Due to the continuous nature of fluid flow through the vasculature microenvironment in which cancer extravasation occurs, Continuous perfusion could be considered a more physiologically relevant experimental method for future investigations elaborating the mechanisms and biology of cancer metastasis.

3.5 Conclusion

In conclusion, we have engineered an integrated, parallel-plate microfluidic device to fractionate cells based on their elution time from a flow channel as a proxy for cell adhesivity to a substrate surface functionalized with adhesive ligand to investigate the pathway of cancer extravasation. Used here, wall shear stress-levels were modeled after hemodynamic flow of the vasculature microenvironment in order to simulate conditions under which *in vivo* metastasis occurs *in vitro*. By separately collecting two fractions of cancer cells - non-interacting and interacting – the cellular populations can be subsequently analyzed, reperfused, or modeled *in vivo* after perfusion, allowing interrogation of a large number of cells in a tightly controlled flow environment. This platform enabled the interrogation of cell molecular profiles, such as (co)expression levels of natively expressed selectin ligands (sLe^x, CD44, and CEA) and cancer stem cell marker CD24 on circulating cancer cells, as it relates to adhesive phenotype on a subset level based on adhesive propensity, thereby probing differences that may underlie varying adhesive phenotypes of a heterogeneous metastatic cancer cell population. Using the microfluidic analysis platform to study the behavior of cancer cells in the vascular microenvironment, and therefore relating the phenotypic characteristics of a cancer cell with their adhesive potential, will inform novel biomarkers that can be used to identify cancer cells and identify molecular pathways that can be targeted with therapeutics to prevent cancer metastasis.

CHAPTER 4. PHOTOCONVERSION AND CHROMATOGRAPHIC MICROFLUIDIC SYSTEM REVEALS DIFFERENTIAL CELLULAR PHENOTYPES OF ADHESION VELOCITY VERSUS PERSISTENCE IN SHEAR FLOW

4.1 Introduction

Systemic metastasis—a multistep progression in which cancerous cells disassociate from the primary tumor, infiltrate the circulatory system, leave the vasculature, and establish metastatic tumors in secondary tissues—is the cause of over 90% of all cancer-related deaths.^{10,32,183} In order to travel to distant sites in the body during the process of metastatic cancer extravasation, circulating tumor cells utilize a highly orchestrated adhesion cascade that, like leukocytes, can involve slow rolling interactions with endothelial cells under hemodynamic forces.^{6–9,162} This process is mediated by interactions between endothelial-presented selectins and selectin ligands [such as sialofucosylated CD44 variants and carcinoembryonic antigen (CEA)] present on the tumor cell's surface.^{68,163,164} The interaction of selectins with their ligands slows the cells to allow cell-cell signaling or firm adhesion to occur within in the dynamic fluid flow environment of the circulatory system, and thus represents a critical regulatory step leading to subsequent cell transmigration and eventual formation of distant metastatic tumors.^{9,12,26,68,81,82} Identification of cellular attributes and/or pathways contributing to metastatic dissemination in the context of selectin-mediated adhesion are therefore of high interest for its potential to identify cancer cell-selective drug targets inhibiting cancer's spread.^{28,184,185}

Although they are highly simplified compared to *in vivo* mouse models, engineered *in vitro* systems that mimic the *in vivo* microenvironment offer numerous advantages for the investigation of mechanisms underlying malignant progression in a highly controlled manner.^{12,186} The application of microfluidics to such problems allows the interrogation of biomechanical effects on metastatic cell transport under defined cellular, molecular, and biophysical conditions.^{24,81,187,188} For example, *in vitro* systems have been used to sense morphological cell changes in a hypoxic tumor microenvironment, to probe force interactions between cells and the extracellular matrix, and to elucidate the impact of hemodynamic flow induced shear stress on regulating mechanotransduction mechanisms of circulating cancer cells.^{189,190} Further, and relevant to this work, they can be designed to recapitulate selectin-mediated cell adhesion in flow, permitting the examination of adhesion mechanisms, and when coupled with high speed video microscopy, can be used to visualize the adhesive behavior of cells in flow fields that simulate the microenvironment of the vasculature.^{11-13,26} Despite their numerous advantages, approaches to date have been limited to indirect analysis of perturbation of associated pathways or drugs on measured adhesion quantity and quality. Few approaches have been described that allow cells to be recovered and analyzed, fewer still that enable high content analysis of metastatic cancer cell adhesion and expression phenotypes to enable mechanistic disease and drug response modeling.

To fill this technical gap, a cell sorting microfluidic was previously engineered by our group to fractionate cells based on their residence time in a selectin functionalized channel as a proxy for average velocity. This platform permits the separation and enrichment of subsets of cells exhibiting little to no adhesion versus those that are highly

adhesive based on their elution time through the functionalized microfluidic for interrogation of their metastatic potential in vivo and profiling of cellular molecular profiles.²⁶ This approach solely separated cells into fractions of cells exhibiting any adhesion versus that did not. A natural extension of this proof-of-principle would be to perform such analyses with finer resolution in elution times (e.g. fast versus slow rolling adhesion). The persistence of adhesion by metastatic colon cancer cells to selectins in shear flow is highly variable, however, complicating interpretation of elution time alone as a readout of cell adhesion phenotype^{11,13} and the application of the cell adhesion chromatography system to analyze complex or even subtle adhesive mechanisms.

To establish a methodology to analyze cellular phenotypes associated with different quantities and qualities of adhesion in flow, we sought to reconcile and address the potential confounding effects of sustained versus diminished adhesion persistence on fractionating and profiling cell subsets with differing adhesive phenotypes among a heterogeneous population of metastatic cancer cells. To do so, a fluorescence-based velocity probe recently reported by our group as enabling the off-chip analysis of velocities with which cells move through spatially defined shedding areas of photoconverting light was incorporated into the cell adhesion chromatography microfluidic system.¹² Individually, the cell sorting microfluidic quantifies adhesion in flow over long time- and length-scales on a large, subset basis. Conversely, the photoconversion technique quantifies velocities of rolling adhesion in flow over short time- and length-scales on a single cell basis. The integration of the cell sorting and photoconversion systems thus permits the simultaneous evaluation of cellular properties associated with long versus short time- and length-scale adhesion behaviors of metastatic tumor cells. Using this

methodology, analysis of persistent adhesion via photoconversion and adhesion chromatography converged to yield the same analyzed cellular velocities and phenotypes associated with rolling adhesion by human LS174T metastatic colon carcinoma cells that are frequently used to model selectin-mediated tumor dissemination.^{82,191–193} This analytical method also revealed rolling adhesion on E-selectin to be strongly associated with expression of E-selectin ligands, correlations that vary with ligand type and rolling velocity magnitude. Further, discrete selectin ligand expression profiles were found to underlie persistent versus non-persistent adhesion by LS174T cells to E-, P-, versus L-selectin in flow, suggestive of divergent regulatory mechanisms. This integrated cell sorting and photoconversion microfluidic platform thus enables *in vitro* analysis and comparisons of adhesive phenotypes as they relate to mechanisms of cancer cell metastasis in the context of selectin mediated adhesion to reveal new insights into potential cancer dissemination pathways.

4.2 Materials and Methods

4.2.1 Cell Culture

Human colorectal adenocarcinoma LS174T cells (both parental and those transfected to stably express Phamret14) were cultured in Dulbecco's Modified Eagle Medium supplemented with 10% heat inactivated fetal bovine serum (FBS) and 1% penicillin-streptomycin-amphotericin (Life Technologies). Cells were harvested via mild trypsinization with 0.25% trypsin EDTA, centrifuged at 400 X G for 5 min, and resuspended in culture medium. Prior to use in perfusion experiments, the cells were

incubated in suspension for 2 h at 37°C to allow regeneration of adhesive cell surface ligands. All cells were obtained from American Type Culture Collection.

4.2.2 *Channel Fabrication*

Microfluidic channels were fabricated as detailed previously.²⁶ Briefly, the microfluidic channels were made using 100 µm thick double-sided adhesive tape (3M) backed with a release liner into which a U-shaped channel was cut, using a craft cutter (Silhouette America), consisting of two parallel 14 cm long by 2 cm wide sections connected by a 1.5 cm long by 2 cm wide straight portion of adhesive tape. The channel was designed as a U-shape to optimize the size of the platform for ease of use with the spatial constraints of the high speed videomicroscopy, while permitting settling of the cell pulse before reaching the functionalized portion of the channel, as experimentally and quantitatively validated previously.²⁶ The adhesive channels were then affixed to PDMS (Ellsworth Adhesives), which was previously cured by mixing PDMS base with curing agent at a ratio of 9:1 and curing at 90°C for 3 h in a Pyrex dish. To complete fabrication, an inlet hole was punched into the end of one of the long, straight portions of the channel using a 3 mm biopsy punch. The platform was attached to a non-tissue culture treated polystyrene plate into which an outlet hole was drilled prior to assembly to permit the collection of the cell fractions into easily interchangeable reservoirs without disturbing flow, as described previously.²⁶

4.2.3 *Channel Functionalization*

The long, straight portion of the channel nearest the outlet was functionalized through the following steps: incubating at 4°C overnight with Fc specific goat anti-human

IgG (R&D Systems) diluted in Dulbecco's Phosphate Buffered Saline (D-PBS) without calcium and magnesium to a concentration of $2.5 \mu\text{g mL}^{-1}$ for E-selectin experiments or $25 \mu\text{g mL}^{-1}$ for P- and L-selectin experiments, which is non-specifically adsorbed onto the surface of the polystyrene plate; blocking for 1 h at room temperature with 1% BSA in D-PBS; incubating for 2 h at room temperature with either $2.5 \mu\text{g mL}^{-1}$ of recombinant human E-Selectin Fc chimera protein (R&D Systems), $25 \mu\text{g mL}^{-1}$ of recombinant human P-Selectin Fc chimera protein (R&D Systems), or $25 \mu\text{g mL}^{-1}$ of recombinant human L-Selectin Fc chimera protein (R&D Systems), all of which were diluted in D-PBS with calcium and magnesium; and finally, blocking the entire device for 1 h at room temperature with 1% BSA in D-PBS at room temperature. In between each step, the channel was washed three times with 1 mL of D-PBS with calcium and magnesium. Only the straight portion nearest the outlet was functionalized by pipetting 200 μL of goat anti-human IgG Fc specific, 1% BSA and selectin solutions into the drilled outlet hole which, by virtue of this volume covering only the terminal straight channel portion, prevented functionalization of the rest of the channel. In so doing, cells that had all settled to the bottom of the channel prior to reaching the functionalized portion of the channel were ensured to experience a uniform channel length with which to mediate adhesive interactions.²⁶

4.2.4 Perfusion Experiment Workflow

Perfusion experiments were performed in a similar manner to that formerly described.²⁶ An inlet syringe connected to tubing filled with perfusion media (0.1 % BSA in D-PBS), was connected to a syringe pump (PhD Ultra Harvard Apparatus) and used to withdraw a cell pulse of 250,000 cells diluted in 200 μL of perfusion media into the inlet

tubing at a rate of 0.5 mL min⁻¹. The tubing connected to the syringe was inserted into the inlet hole of the channel. An outlet reservoir was made by connecting a 5 mL test tube to the bottom of the drilled outlet hole on the polystyrene plate. The assembled platform was placed on an Eclipse TI optical microscope (Nikon) with an objective magnification of 10X and linked to NIS-Elements software (Nikon) to acquire videos at a frame rate of 25 frames per second at an exposure time of 0.281 μs and 2x2 binning of a 500 by 376 pixels. To complete the set-up, the system was integrated with a 405 nm light source was placed under the channel, directly upstream of the microscope objective, at the beginning of the functionalized portion of the channel. To ensure a short time- and length-scale velocity was ascribed to the cells, a mask that is placed atop the laser and has a rectangular cutout 1.2 cm wide by 1 cm long to permit light exposure across the entire width of the channel but only 1 cm down the length of the channel in the direction of flow to occlude light exposure outside the defined window.

To begin perfusion, the 405 nm was turned on at maximum power and the syringe pump was set to a flow rate of 1 dyn cm⁻² for E-selectin experiments or 0.5 dyn cm⁻² for P-selectin and L-selectin experiments to initiate inflow from the syringe-tubing assembly. The flow rate to achieve desired wall shear stresses was determined from Equation 2, with the assumption that the apparent viscosity of the perfusion media was 0.009 P.

$$Q = \frac{\tau_w * h^2 * w}{6 * \mu} \quad (2)$$

Perfusion was continued for 10 min for experiments conducted at 1 dyn cm⁻² or 20 min for experiments conducted at 0.5 dyn cm⁻², as these were the predetermined elution

times for the free flow cells to elute through the channel (as measured previously)^{13,26}, after which perfusion was stopped and the test tube containing the cell solution collected during perfusion was removed and a new test tube was attached. Finally, the syringe with inlet tubing was replaced with a new syringe-inlet tubing apparatus filled with only perfusion media and used to eject the cell solution out of the channel and into the second collection tube for experiments in which only one adherent (AD) fraction was collected. For experiments in which two AD fractions were collected, after the predetermined free flow cell elution time, the cell collection reservoir was changed, perfusion was continued for an additional 10 min (the time required for 50% of the adherent cells to elute). For experiments in which three adherent fractions were collected, after the predetermined free flow cell elution time, another fraction was collected after 28 min, the time for 66% of adherent cells to elute, to collect Adherent 2/3.

In experiments where cells were statically pre-photoconverted and photoconverted with perfusion, the cell pulse of 250,000 Phamret LS174T cells diluted in 200 μL of 0.1% BSA perfusion media were first statically photoconverted for 4 or 8 min in 96 well plate prior to perfusion through an E-selectin functionalized channel as described above.

4.2.5 Confirmation of Retention of Fc Specific Goat Anti-human IgG Surface Functionalization after Perfusion

Retention of Fc specific goat anti-human IgG adsorption was verified by functionalizing dishes with either 2.5 $\mu\text{g mL}^{-1}$ or 25 $\mu\text{g mL}^{-1}$ of FITC labelled Fc specific goat anti-human IgG. The channels were then blocked with 1% BSA for 1 h, and subsequently, perfusion experiments were conducted at either 1 dyn cm^{-2} for 28 min (the

longest time experiments are performed at 1 dyn cm^{-2}) or 0.5 dyn cm^{-2} for 20 min (the longest time experiments are performed at 0.5 dyn cm^{-2}). During the experiments, the perfusion media was collected, and the mean fluorescent intensity (MFI) of the perfusion media was measured using a plate reader. The MFI of the collected perfusion media was correlated to an Fc specific goat anti-human IgG concentration using a standard curve. The perfusion media was found to contain a negligible amount of Fc specific goat anti-human IgG (anti-IgG) (Figure 4.1).

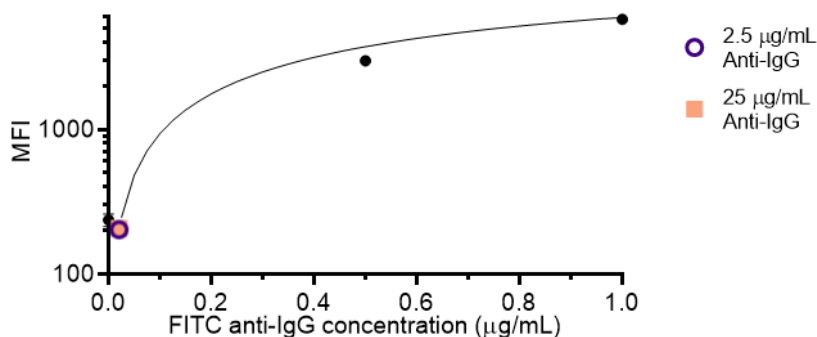


Figure 4.1 Verification of Fc specific goat anti-human IgG functionalization after perfusion. (A) Standard curve of mean fluorescence intensity (MFI) of FITC labeled Fc specific goat anti-human IgG (anti-IgG) at different concentrations with MFI of perfusion media collected after either functionalization and perfusion with $2.5 \mu\text{g/mL}$ Fc specific goat anti-human IgG (anti-IgG) at 1 dyn cm^{-2} for 28 minutes (purple circle) or $25 \mu\text{g/mL}$ Fc specific goat anti-human IgG (anti-IgG) at 0.5 dyn cm^{-2} for 20 minutes (orange square).

4.2.6 Elution Time Quantification

Similar to previous work²⁶, 2 hour videos of 250,000 cells perfused as a $200 \mu\text{L}$ cell pulse at a flow rate corresponding to a wall shear stress of 1 dyn cm^{-2} were taken 0.5 cm from the channel outlet. Our custom written cell tracker code was used to analyze collected videos, setting to threshold of 4 and a blurring factor of 7 to identify objects that had a diameter between $12\text{-}18 \mu\text{m}$ that had traveled more than $400 \mu\text{m}$ during the course

of the video and record the time it took the object to leave the field of view after perfusion had begun. Cumulative frequency plots generated in Prism (GraphPad Software Inc) based on the elution time of each cell quantified using cell tracking software. For experiments where 2 AD fractions were collected, the elution time of the adherent 1/2 (AD1/2) fraction was 10 min after the free flow cells had eluted. For experiments where 3 adherent fractions were collected, the elution time of the adherent 1/3 (AD1/3) fraction was 8 min after the free flow cells had eluted and the elution time of the adherent 2/3 (AD2/3) fraction was 10 min after the AD1/3 cells had eluted.

4.2.7 Flow Cytometric Analysis

Collected cell solution fractions were centrifuged at 400 X G for 5 min and resuspended in diluted antibody solutions on ice for 45 min, washed with D-PBS with calcium and magnesium two times, and resuspended in 0.1% BSA perfusion media for analysis on the flow cytometer. The antibodies (BD Biosciences) were diluted in D-PBS with calcium and magnesium in the following ratios – 1:20 for PE CD44 and PE CEA, 1:40 for APC HECA452, and 1:10 for APC CD24. Obtained flow cytometry data was analyzed using FlowJo software (Treestar Inc.).

4.2.8 Quantification of Adhesive Cell Behavior

Cell adhesive phenotypes were characterized based on both their long and short time- and length-scale velocities of rolling adhesion in flow when perfused over a selectin functionalized substrate. The short time- and length-scale velocity of perfused cells was quantified by their green fluorescent protein to cyan fluorescent protein (GFP/CFP) ratio compared to an unphotoconverted control and converted to velocity using a

photoconversion standard curve. Average cell velocities were quantified based on their population average residence times in the functionalized channels.²⁶

4.2.9 Development of Standard Curve

Channels were blocked with 1% BSA (diluted with D-PBS with calcium and magnesium) to inhibit any non-specific cell interaction with the polystyrene dish during perfusion. The light source was set to maximum power and masked, as described above, to allow light only on 1 cm of the channel in the direction of flow. By varying the flow rate within the channel and, therefore, the velocity of cells, the residence time of cells exposed to the 10 mm window of light from the light source can be controlled. Using this setup, cells were perfused in the channels at differing flow rates which corresponded to desired velocities of cells, as derived previously¹³, and desired residence times of cells exposed to light source according to Equations 3 and 4, where the cell radius is assumed to be 8 μm and medium viscosity 0.009 P.

$$v_{instantaneous} = \frac{\text{mask length}}{\text{residence time in channel}} \quad (3)$$

$$v_{instantaneous} = \frac{\tau_w}{h * \mu} * \left[\frac{h}{4} - r^2 \right] \quad (4)$$

Each perfusion was allowed to run for the duration of the time experimentally determined necessary for the cell pulse to traverse the light source window. After which, the cells and perfusion media was expelled from the channel at high flow rates into the reservoir. The cells and perfusion media in the reservoir were collected, centrifuged at 400 X G, and resuspended in FACS buffer (0.1% BSA diluted in D-PBS with calcium and

magnesium) for flow cytometry analysis of extent of photoconversion. Data from flow cytometry was collected and analyzed using FlowJo (Treestar Inc). Graphing the relationship between the extent of photoconversion—as given by ratio of GFP to CFP, normalized to a control sample perfused with the light source off—and velocity of cells at different flow rates using Prism (GraphPad Software Inc), a nonlinear regression was fit to the data. This was done for Phamret LS174T cells of different passage age and different cell thaws to ensure the standard curve was broadly applicable (Figure 4.2).

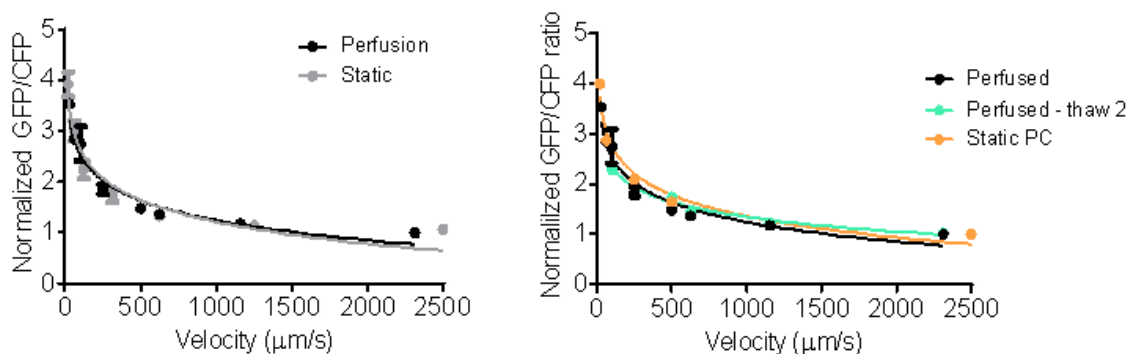


Figure 4.2 Comparison of interpolated standard curves. (A) Overlay of photoconversion standard curves created either by statically photoconverting 250,000 Phamret-expressing LS174T cells for various amounts of time (gray line) or perfusing a cell pulse of 250,000 Phamret-expressing LS174T cells in an unfunctionalized channel at various flow rates (black line). (B) Static standard curve (orange) and perfusion standard curve (black) from (A) overlaid with a perfusion standard curve from a population of Phamret-expressing LS174T cells (teal) thawed at a different time than the cells used to create the standard curves from (A).

4.2.10 Ligand Expression and Extent of Photoconversion

FlowJo (Treestar Inc) and Prism (GraphPad Software Inc) were used for gating and subsequent analysis of flow cytometry data. For all experiments, collected events from the BD LSR II Flow Cytometer were gated for live cells. The live cell population was then gated into photoconverted and unphotoconverted populations, and coefficients of correlation in linear models were quantified as previously described.¹² Briefly, after an

unphotoconverted sample of LS174T Phamret cells were analyzed on the flow cytometer and gated to include only live cells, logarithmic plots of GFP versus CFP signal were made using FlowJo, and the resultant population was used gate the photoconverted negative population, likewise, any cells with a greater GFP/CFP ratio as compared to the unphotoconverted cells were gated as photoconverted positive. In order to determine correlation coefficients of the linear, the photoconverted negative or photoconverted positive cells, which were labeled with a PE- or APC-conjugated antibody for the ligand of interest, from each collected fraction were subsequently analyzed on the flow cytometer at the single cell level for fluorescent intensity of PE or APC, GFP, and CFP. The resulting data points were then pooled and divided into four equal subgates based on their extent of photoconversion, as quantified by the GFP/CFP ratio such that the center of each subgate was the mode of the cell population. The range for each quartile was determined by a perfused, photoconverted, but unsorted control that was conducted on each day for each experimental condition. This was done each time an experiment was performed to account for inherent variability between cells. For each subgate, the mean PE or APC fluorescent intensity and GFP/CFP ratio was calculated. Finally, Prism was used to fit a linear regression model to the data, as well as perform post-hoc tests for non-zero slopes and differences between slopes.

4.2.11 Outlier Detection and Elimination

ROUT outlier tests with criteria $Q = 1$ were conducted on all data sets used for linear regression models. Recognized outliers were removed from the data sets prior to model fitting.

4.2.12 Enzymatic Treatment

Prior to perfusion in functional adhesion experiments with enzymatic treatment, Phamret LS174T cell suspensions at 1×10^7 cells mL^{-1} were incubated with or without 0.1 U mL^{-1} *Vibrio Cholerae* Neuraminidase (Roche Applied Science) at 37°C for 1 hr, as described previously.^{81,194} After treatment, cells were washed to remove the enzyme and resuspended in 0.1% BSA diluted in D-PBS with calcium and magnesium for perfusion. To confirm complete digestion, cells were stained with a fluorescent mAb HECA452 (which recognizes LS174T expressed sialic-acid-bearing epitope sialyl Lewis x) and analyzed on a flow cytometer.

4.3 Results

4.3.1 Adherent Relative to Free Flow Cell Fractions Exhibit Greater Photoconversion Proportion and Extent

A previously engineered cell sorting microfluidic platform based on a parallel plate flow chamber configuration was modified by adding a 405 nm laser to the beginning of the selectin functionalized portion of the channel (Figure 4.3A,B).²⁶ The start of the functionalized channel portion was intentionally chosen as the light exposure location in order to standardize when cells would be exposed to light during experimentation, thus minimizing potential variance in when cells were light exposed (e.g. after different times of adhesion) that may confound interpretation of experimental results. Note that by virtue of the upstream settling feature, all cells perfused through the device were within ~10% of a cell radius from the inferior substrate, ensuring all cells had the opportunity to mediate adhesive contacts.^{13,26} Metastatic human colon carcinoma LS174T cells of epithelial origin

and approximately 14 cell μm diameter were used as the model cell line, as they have been extensively studied in adhesion assays and for interrogation of mechanisms underlying colon cancer metastasis.^{9,11-13,26,81,195,196} LS174T cells that stably expressed Phamret, a photoconvertible fluorescent protein formed from fusion of photoactivatable green fluorescent protein (GFP) with cyan fluorescent protein (CFP), exhibited no difference in adhesion behavior compared to untransfected parental cells (Figure 4.4A,B). Use of this engineered cell line thus enabled a readout of short time- and length-scale velocity to be ascribed individually to each cell in proportion to their transit time through the illuminated region during perfusion, as previously described and quantified by an increase in GFP signal relative to an unchanged CFP signal resulting in an increased GFP/CFP ratio (Figure 4.3A, 4.5A).^{12,197,198}

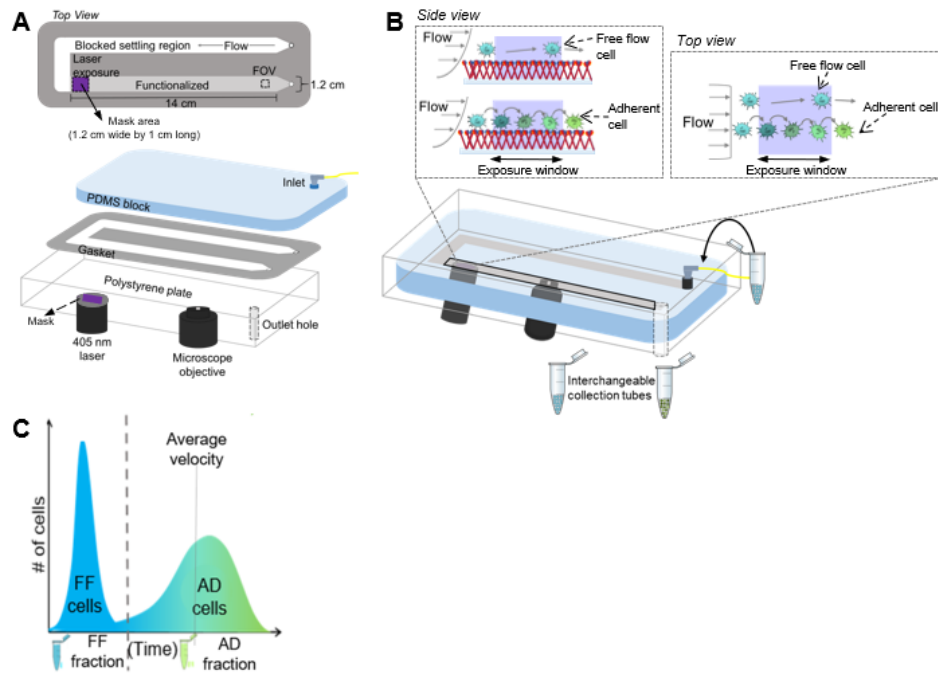


Figure 4.3 Integrated photoconversion, cell sorting adhesion chromatography microfluidic for *in vitro* interrogation of metastatic cancer cell adhesive phenotypes. (A) The short and long time- and length-scale velocity of an infused cell pulse can be

simultaneously quantified by utilizing a 405 nm laser to photoconvert Phamret-expressing cells to ascribe an short time- and length-scale velocity and interchangeable cell fraction tubes to ascribe an average velocity in a (B) hemodynamic microenvironment-mimicking, parallel-plate microfluidic device, into which metastatic cancer cells are infused into the selectin functionalized channel and visualized via integrated high speed videomicroscopy. (C) LS174T cells perfused over a functionalized channel were sorted into a free flow (FF) and adherent (AD) fraction based on their elution time from the cell sorting system.

As selectins mediate cell adhesion over a wide range of rolling velocities (order of 1-100 $\mu\text{m}/\text{sec}$) and efficiencies,¹¹ parameters under which this device was implemented to interrogate mechanisms underlying of long- versus short- scale adhesive interactions by LS174T cells to E-, P-, and L-selectin were adjusted in order for the collected cell population sizes to be roughly similar amongst selectins and sufficiently large to enable subfractionation and fluorescent labeling analyses described below. Specifically, all experiments were performed at concentrations of 2.5 versus 25 $\mu\text{g mL}^{-1}$ and 1.0 dyn cm^{-2} versus 0.5 dyn cm^{-2} for E- versus P- and L-selectin, respectively, and cells sorted over 20 min into Free flow (FF) versus Adherent (AD) fractions (Figure 4.3A) for analysis (Figure 4.4C-E). The chosen wall shear stresses of 0.5 and 1 dyn cm^{-2} recapitulate the low venular shear stresses under which metastatic circulating tumor cell recruitment occurs.^{11,199,200}

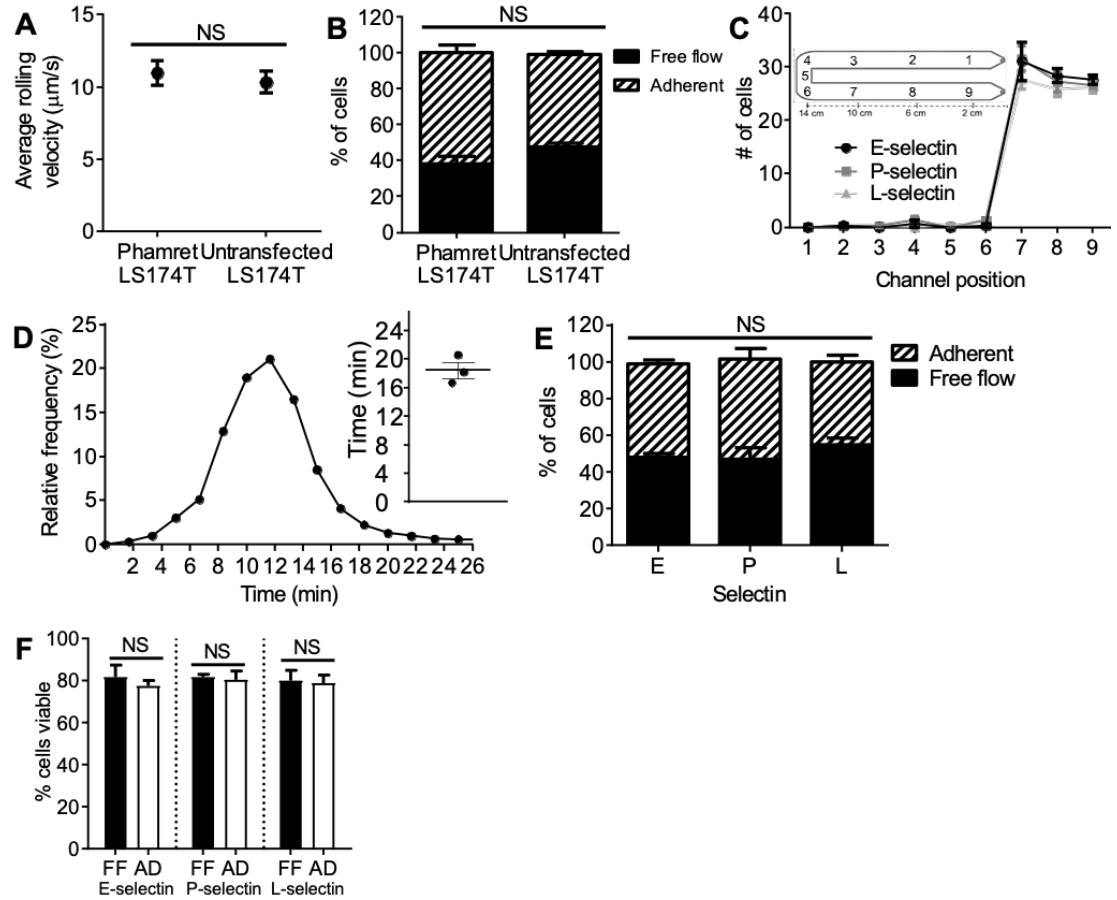


Figure 4.4 Photoconvertible LS174T cell line and adhesive chromatography microfluidic characterization. (A,B) Comparison of (A) average rolling velocity and (B) percent of cells collected in each fraction from a cell pulse of either 250,000 control LS174T cells or Phamret-expressing LS174T cells over $2.5 \mu\text{g mL}^{-1}$ E-selectin at 1 dyn cm^{-2} . (C) Number of interacting cells along the length of the channel during the sorting phase in an E-, P-, or L-selectin functionalized channel. (D) Representative relative frequency distribution of elution time of a cell pulse infused at 0.5 dyn cm^{-2} . Inset depicts the mean time at which 95% of the cell pulse has eluted \pm s.e.m. (E) Percent of cells collected in each fraction after perfusion in an E-, P-, or L-selectin functionalized channel. (F) Viability of cells in each collected Free flow or Adherent fraction. (C-F) Perfusion and separation of a Phamret-expressing LS174T cell pulse of 250,000 cells over $2.5 \mu\text{g mL}^{-1}$ E-selectin at 1 dyn cm^{-2} or $25 \mu\text{g mL}^{-1}$ L- or P-selectin at 0.5 dyn cm^{-2} . (A-E) Each dot or bar represents the mean \pm s.e.m. of $n \geq 3$ individually run experiments. Statistical analysis (A,B,F) by paired t-test or (E) one-way ANOVA with post hoc t-test with Bonferroni corrections for multiple comparisons.

Within each collected subfraction, the extent and proportion of total cells that were photoconverted was measured based on unphotoconverted control cells (Figure 4.5B,C). Expectedly, the extent of photoconversion (GFP/CFP ratio) was significantly greater for the AD relative to FF subset, though not to a statistically significant extent on P-selectin (Figure 4.5D), potentially due to the wider range of velocities typically observed for cells mediating adhesion to P-selectin^{11,13} and diminished adhesion persistence¹¹ resulting in cells not mediating adhesion within the photoconversion window eluting into the AD fraction or vice versa. Additionally, measured ratios in the FF fraction were not statistically different from unphotoconverted cells when perfused over E- and P-selectin (Figure 4.5E). However, a small increase was measured over L-selectin (Figure 4.5D), in line with the tethering type interaction mediated by L-selectin and very low adhesion persistence mediated by LS174T cells on L-selectin.¹¹ The frequency of photoconversion positive (PC+) cells (Figure 4.5E) was also increased in AD relative to FF fractions after perfusion, though again not to a statistically significant extent on P-selectin (Figure 4.5E), changes not associated with differences in cell viability (Figure 4.4F). Notably, the frequencies of PC+ cells were significantly non-zero in the FF fraction (Figure 4.5E). Thus, despite high (>220 $\mu\text{m}/\text{sec}$) average velocities indicated by their elution into the FF fraction, a low but substantial fraction of cells within the FF fraction did exhibit some level of photoconversion above background. Consistent with previous reports,¹¹ a subfraction of cells thus exhibit non-persistent adhesion which in this case is captured by a subfraction of cells that elute into the FF fraction but have been photoconverted as a result of adhesion within the light exposure window that slows them down to some level below minimum detectable short time- and length-scale velocity (Figure 4.5F). In its capacity to identify

and measure different adhesion qualities (persistent versus non-persistent adhesion), this system also substantiates previous results that a higher proportion of LS174T cells exhibit diminished adhesion persistence on P- and L- relative to E-selectin (Figure 4.5E).

In an effort to further quantify differences short time- and length-scale velocity magnitudes exhibited by FF versus AD cells, the extent of photoconversion was assessed by subdividing the PC+ cells into GFP/CFP ratio quantile bins based on perfused and photoconverted but unsorted cells (Figure 4.5G). The proportion of cells exhibiting high extents of photoconversion (bin 4) corresponding to low short time- and length-scale cell velocities was substantially higher in AD but not FF cells collected on all three selectin types (Figure 4.5H-J). This integrated system can thus assess both the quantity (frequency of AD versus FF and PC+ cells of total) as well as quality [persistent (PC+ in AD) versus non-persistent (PC+ in FF)] of rolling adhesion by cells in shear flow.

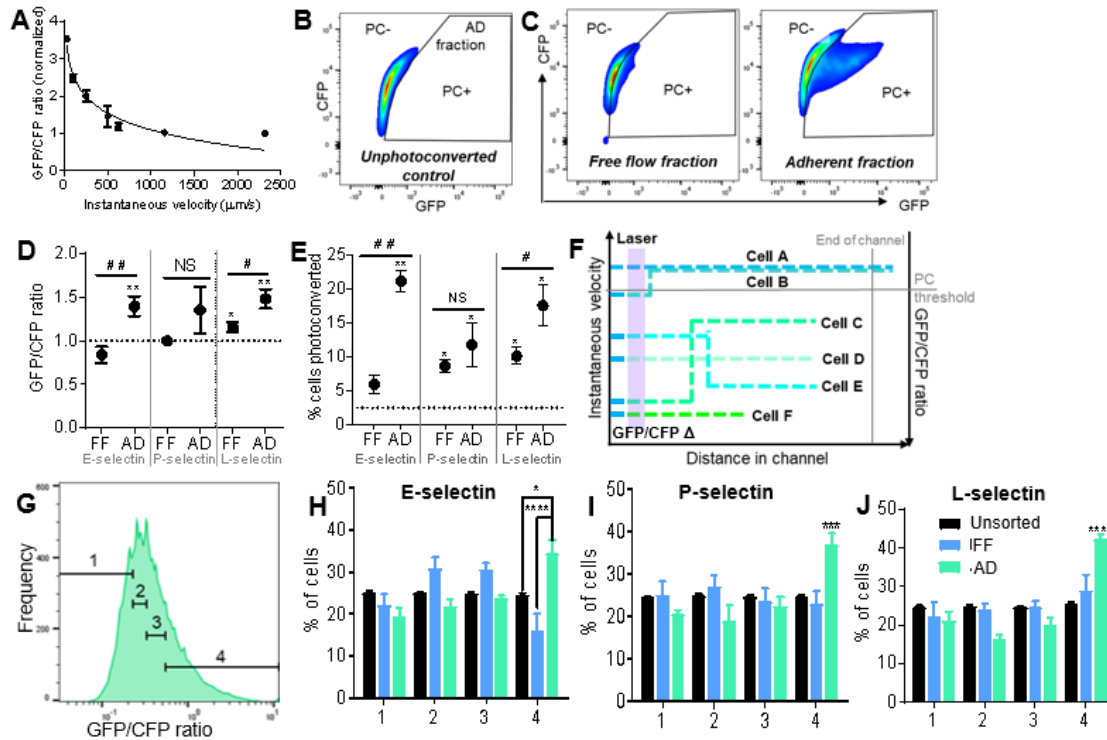


Figure 4.5 Adherent relative to free flow cell fractions exhibit increased extents of photoconversion and proportions of photoconverted cells. (A) Photoconversion standard curve relating cell velocity and GFP/CFP ratio normalized to an unphotoconverted control. **(B)** Flow cytometry scatter plot gating of photoconverted (PC+) and unphotoconverted (PC-) Phamret-expressing LS174T cells based on unphotoconverted control population. **(C)** Representative flow cytometry plots of the extent of photoconversion from cells collected in the FF (left) or AD fractions (right). **(D)** GFP/CFP ratio measured by flow cytometry and **(E)** percent of PC+ cells from collected fractions after perfusion, photoconversion, and separation over E-, P-, or L-selectin. Intercept of d dashed line: E, 1; F, 2.5%. **(F)** Schematic depicting persistent versus non-persistent adhesion along adhesive ligand-functionalized substrate. Cell A represents a free flow cell, while cell B represents a lowly persistent, photoconverted cell that would elute into the FF fraction. Cell C and cell E are also lowly persistent cells. Cell D is a fast rolling highly persistent cell, whereas cell F is a slow rolling highly persistent cell. **(G)** PC+ cells from a perfused and photoconverted, but unsorted, cell pulse used to create four extents of photoconversion quantile bins. **(H-J)** Percent of PC+ cells from collected fractions contained within each bin after perfusion, photoconversion, and separation over **(H)** E-, **(I)** P-, or **(J)** L-selectin. **(D,E,H-J)** Each dot or bar represents the mean \pm s.e.m. of $n \geq 3$ individually run experiments. * $p < 0.05$, ** $p < 0.01$, *** $p < 0.001$, **** $p < 0.0001$ by **(D,E)** one sample t-test (*) with **(D)** $h_0 = 1$ or **(E)** $h_0 = 2.25\%$ or paired t-test (#). **(I-K)** One-way ANOVA with post hoc t-test with Bonferroni corrections for multiple comparisons.

4.3.2 *Velocity of Rolling Adhesion Magnitude on E-Selectin Correlates Differentially with Ligand Type*

The expression of selectin ligands within subfractions/subsets of perfused cells was assessed in the context of E-selectin adhesion, which is highly persistent (Figure 4.5D-F).¹³ Thus, enrichment of specific selectin ligands over differing rolling velocity magnitudes was measured and results between chromatography versus photoconversion methodologies was compared.

First, the fractionation resolution was increased to further elucidate phenotypic differences amongst late and early eluting cells within the AD fraction. Specifically, collection of either two fractions of interacting cells (Figure 4.6A, 4.7A,B) – the first and later 50% of interacting cells to elute (AD 1/2 and 2/2, corresponding to average velocities of 83 – 220 and <83 $\mu\text{m/s}$, respectively) – or three fractions of interacting cells (Figure 4.6B, 4.7A,C) – the first, middle, and last third of interacting cells to elute (AD 1/3, 2/3, and 3/3, corresponding to average velocities of 90 – 220, 60 – 90, and <60 $\mu\text{m/s}$, respectively) was performed (Table 4.1).

Table 4.1 Average rolling velocity ranges for eluting cell fractions.

Cell fraction	Average rolling velocity ($\mu\text{m/s}$)
Free flow (AD)	> 220
Adherent 1/2 (AD 1/2)	83-220
Adherent 2/2 (AD 2/2)	< 83
Adherent 1/3 (AD 1/3)	90 - 220
Adherent 2/3 (AD 2/3)	60 - 90
Adherent 3/3 (AD 3/3)	< 60

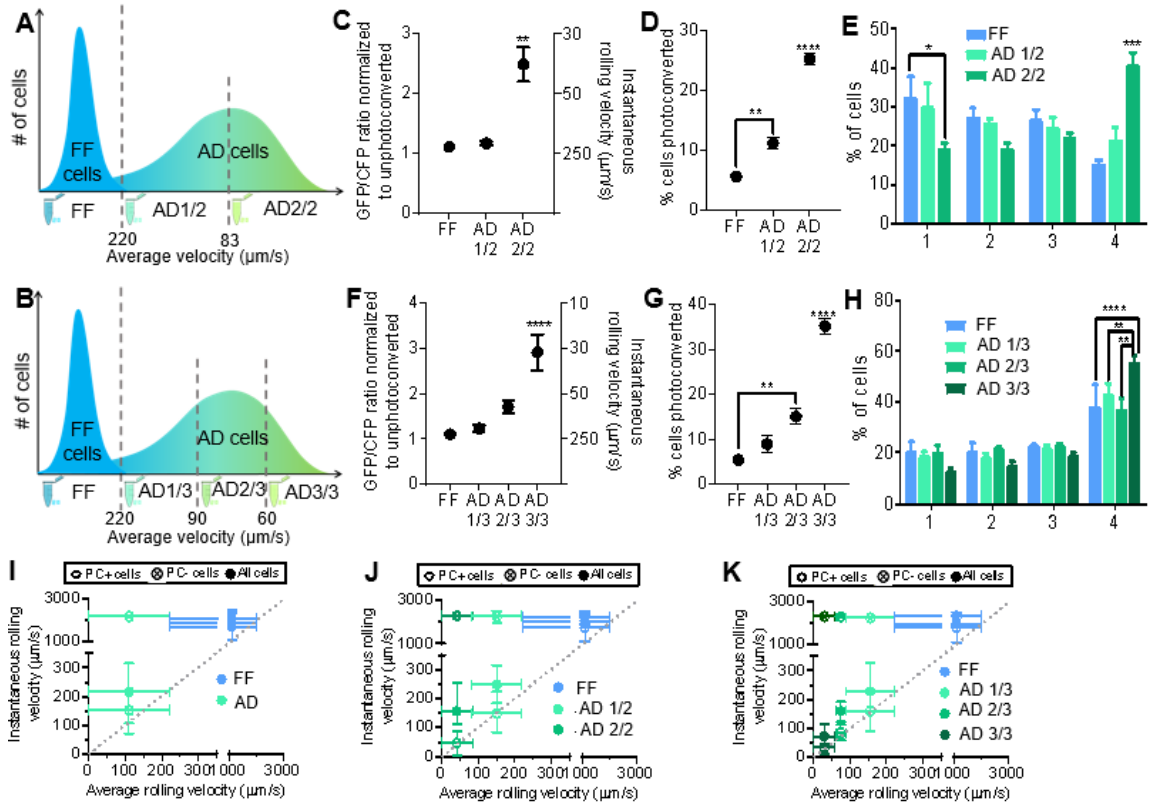


Figure 4.6 Long and short time- and length-scale cell velocities converge when measured using photoconversion and chromatographic methodologies in combination. Phamret-expressing LS174T cells perfused over $2.5 \mu\text{g mL}^{-1}$ E-selectin at 1 dyn cm^{-2} were sorted into (A) two or (B) three AD fractions based on their elution time from the selectin functionalized integrated photoconversion and cell sorting system. (C-H) Extent of photoconversion measured by flow cytometry (C,F) and percent of PC+ cells (D,G) within each fraction normalized to the unphotoconverted control population when either (C,D) two or (F,G) three AD fractions were collected. FF denotes free flow, AD denotes adherent. (E,H) Binning and analysis of PC+ cells from each fraction based on extent of photoconversion measured by flow cytometry normalized to the unphotoconverted control after collection of (E) two or (I) three AD fractions. (I-K) Short time- and length-scale velocity \pm s.e.m and average velocity \pm s.e.m among cells in each fraction when (I) one, (J) two, or (K) three AD fractions were collected. (C-K) Each dot or bar represents the mean \pm s.e.m. of $n \geq 3$ individually run experiments. Perfusion, photoconversion, and separation of a Phamret-expressing LS174T cell pulse of 250,000 cells over $2.5 \mu\text{g mL}^{-1}$ E-selectin at 1 dyn cm^{-2} . * $p < 0.05$, ** $p < 0.01$, *** $p < 0.001$, **** $p < 0.0001$ by one-way ANOVA with post hoc t-test with Bonferroni corrections for multiple comparisons.

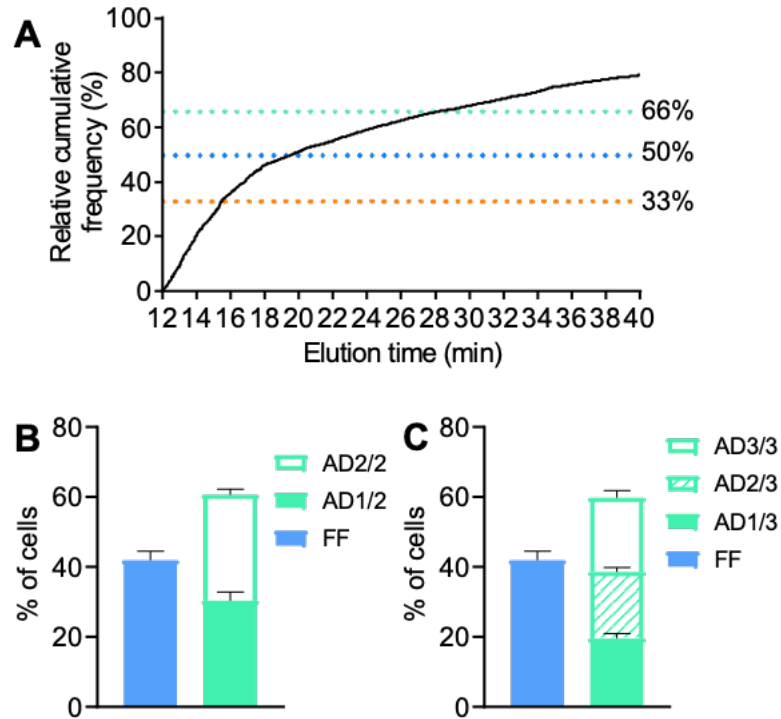


Figure 4.7 Elution time determination for collection of multiple AD fractions. (A) Relative cumulative frequency of elution time of the interacting cells in a perfused cell pulse. Orange, blue, and green lines represent elution of 33%, 50%, and 66% of the interacting cells, respectively. (B,C) Percent of cells in each fraction when either (B) 2 or (C) 3 Adherent fractions are collected. (A-C) Perfusion of 250,000 Phamret-expressing LS174T cells over $2.5 \mu\text{g mL}^{-1}$ E-selectin at 1 dyn cm^{-2} . (B,C) Each bar represents the mean \pm s.e.m. of $n \geq 3$ individually run experiments.

In so doing, the extent of photoconversion for cells in AD 2/2 but not AD 1/2 was found to be greater than that of FF (Figure 4.6C) with a greater percentage of AD 2/2 cells being photoconverted, specifically to high extents (Figure 4.6D,E fourth quartile) as would be expected given the upper limit of photoconversion measurable velocities (Figure 4.5A). Similarly, when the perfused cells were fractionated into three adherent subsets, again, only the latest eluting fraction (AD 3/3) had significantly greater extents of photoconversion (Figure 4.6F) and greater percent of cell photoconverted (Figure 4.6G,H fourth quartile) compared to the FF cells and earlier eluting adherent cells (AD 1/3 and AD 2/3). In converting these photoconversion extents to velocities, analysis of all collected cells in

PC+ fractions demonstrated rolling behavior over E-selectin that was in alignment at both long and short time and length scales (e.g. long and short time- and length-scale rolling velocity, respectively), in contrast to all cells (PC+ and PC-) that exhibited short time- and length-scale velocities higher than those predicted by their elution time (Figure 4.6I-K).

Expression levels of selectin ligands among the AD fractions were next assessed by flow cytometric analysis post sorting (Figure 4.8A). PC+ cell populations eluting in the latest fractions demonstrated the most pronounced enhancements in sLe^x and CD44 expression compared to the non-interacting (PC- and FF) and early eluting AD cells (Figure 4.8B,C,E,F). CEA ligand expression was also enriched in the latest fraction of eluting AD cells compared to levels measured for FF cells (Figure 4.8D,G), a trend not seen when only one AD fraction was collected.²⁶ Notably, no differences were observed between adhesive ligand expression on E-selectin among PC- cells (Figure 4.8B-G).

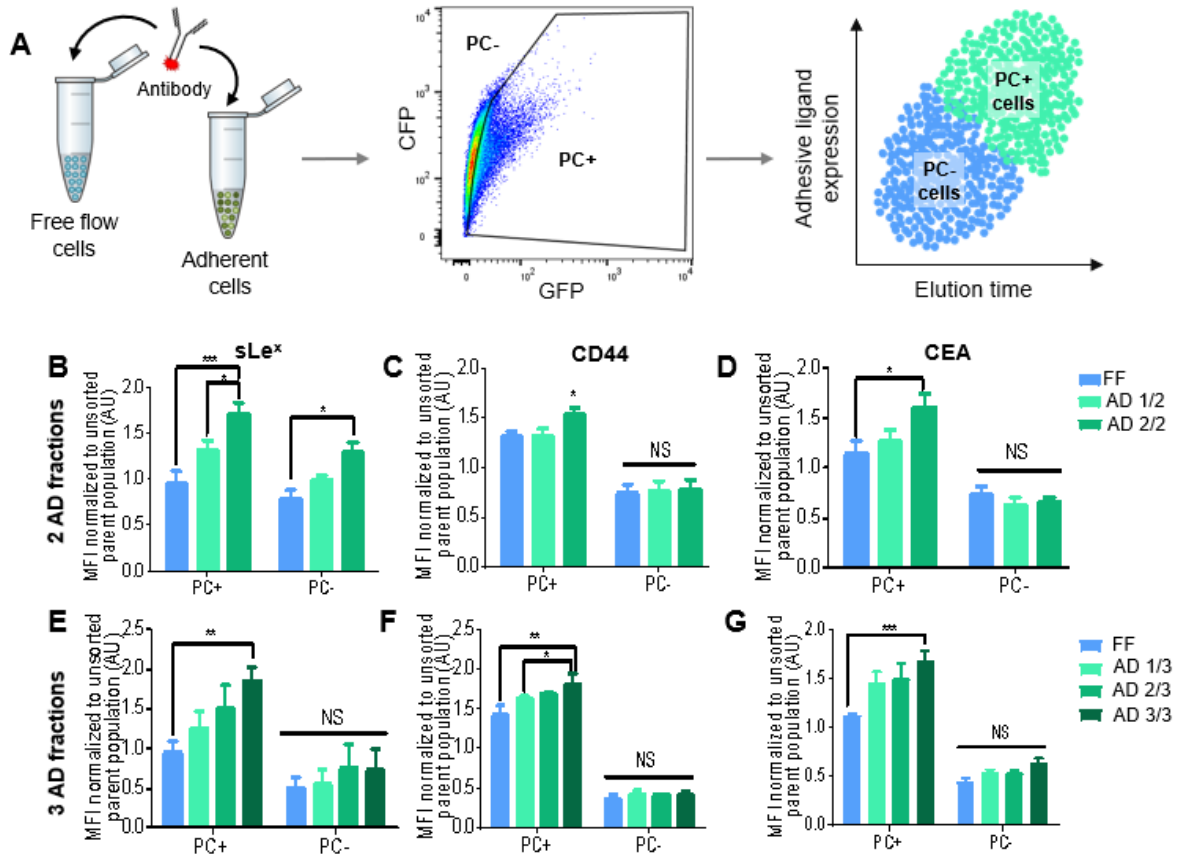


Figure 4.8 Selectin ligand expression increased in cells mediating persistently slow rolling on E-selectin. (A) Phamret-expressing LS174T colon carcinoma cells perfused over selectin-functionalized channels, photoconverted in a manner proportional to short time- and length-scale velocity, sorted into fractions based on average velocity, and gated using flow cytometry into photoconverted (PC+) and unphotoconverted (PC-) populations. Cells collected in each fraction are stained with fluorescently tagged antibodies, allowing correlations between ligand expression, elution time, and photoconversion to be elucidated. **(B-G)** Perfused, photoconverted, and sorted Phamret-expressing LS174T cells were collected into **(B-D)** two or **(E-G)** three AD fractions fluorescently labeled for **(B,E)** sLe^x, **(C,F)** CD44, or **(D,G)** CEA to measure ligand expression levels among PC+ or PC- cells between the collected fractions. MFI denotes mean fluorescent intensity. **(B-G)** Each bar represents the mean \pm s.e.m. of $n \geq 3$ individually run experiments. Perfusion, photoconversion, and separation of a Phamret-expressing LS174T cell pulse of 250,000 cells over $2.5 \mu\text{g mL}^{-1}$ E-selectin at 1 dyn cm^{-2} . * $p < 0.05$, ** $p < 0.01$, *** $p < 0.001$ by one-way ANOVA with post hoc t-test with Bonferroni corrections for multiple comparisons.

Relationships between adhesive ligand expression with short time- and length-scale velocity magnitude, as measured by a cell's mean GFP/CFP ratio, in various fractions were next assessed. After further dividing the PC⁺ and PC⁻ subsets of cells separately based on GFP versus CFP expression into four evenly distributed bins (quantiles with respect to the frequency of an unphotoconverted parent population of Phamret LS174T cells, Figure 4.9A) to quantify the GFP/CFP ratio spread among the cells, mean ligand expression levels were quantified for each bin in the FF and AD fraction of PC⁺ or PC⁻ cell populations. In so doing, the relative correlations (when statistically non-zero) between adhesion molecule expression and cellular velocity was quantified, with greater slope differences between subfractions indicating different relative roles for each ligand in mediating selectin adhesion within each fraction, e.g. slow (PC⁺ in AD 2/2 and AD 3/3) versus fast (PC⁺ in AD 1/2, AD 1/3, and AD 2/3) rolling adhesion.

Regression analyses comparing ligand expression levels amongst PC⁺ cells within various AD fractions revealed sLe^x and CD44 expression being proportional to the GFP/CFP ratio of PC⁺ cells perfused, photoconverted, and sorted into either two (Figure 4.9B,C) or three (Figure 4.9E,F) adherent fractions on E-selectin in flow. These relationships were more pronounced with increasing the number of collected AD fractions. Notably, significant correlations with CEA expression were also found, a relationship not observed when only one AD fraction was analyzed²⁶ but consistent with results using photoconversion methodology alone (Figure 4.9D,G).¹² No correlations were seen between ligand expression and velocity among PC⁻ cells (Figure 4.10). Overall, these data demonstrate that increased expression of adhesive ligands sLe^x and CD44 to be inversely correlated with slower rolling on E-selectin over a broad range of velocity magnitudes,

whereas CEA expression is associated with E-selectin adhesion in the context of slow rolling only.

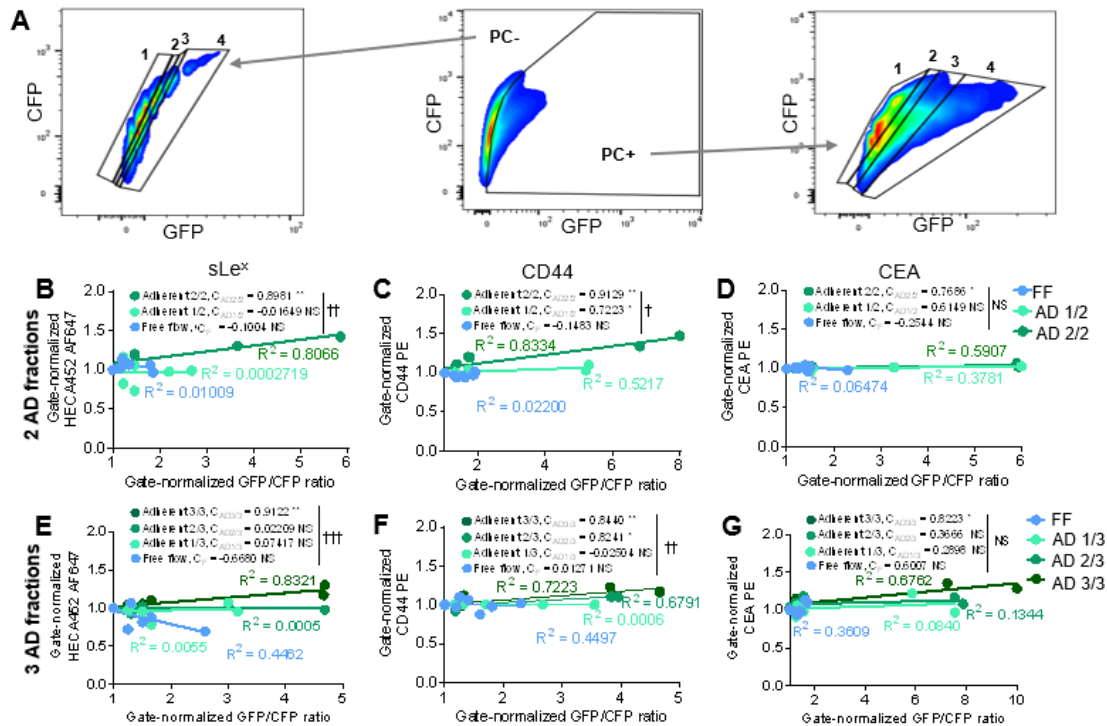


Figure 4.9 Magnitude of persistent, slow cell rolling mediated by E-selectin adhesive interactions inversely correlates with selectin ligand expression. (A) PC+ and PC- cells from the photoconverted but unsorted cell fraction (A, middle) binned into four equal gates (left/right) based on their extent of photoconversion after perfusion over $2.5 \mu\text{g mL}^{-1}$ E-selectin at 1 dyn cm^{-2} or $25 \mu\text{g mL}^{-1}$ L- or P-selectin at 0.5 dyn cm^{-2} . The extent of photoconversion (GFP/CFP ratio) of FF PC- cells and (B-D) two or (E-G) three fractions of AD PC+ cells related to the expression of (B,E) sLe^x reactive HECA452, (C,F) CD44, and (D,G) CEA. (B-G) Binned, flow cytometry data of PC+ cells was pooled from independent experiments and plotted with corresponding linear fits; C_{AD} and C_F represent the regression slope of the PC+ cells in the AD and FF fractions, respectively, * denotes non-zero slopes of the linear fit, † denotes significance of comparison between the C_{AD} values and C_F . * $p < 0.05$, ** $p < 0.01$. Outlier tests with criteria $Q = 1$ were conducted on all data sets, and outliers were removed prior to regression and statistical analysis. Perfusion, photoconversion, and separation of a Phamret-expressing LS174T cell pulse of 250,000 cell over $2.5 \mu\text{g mL}^{-1}$ E-selectin at 1 dyn cm^{-2} .

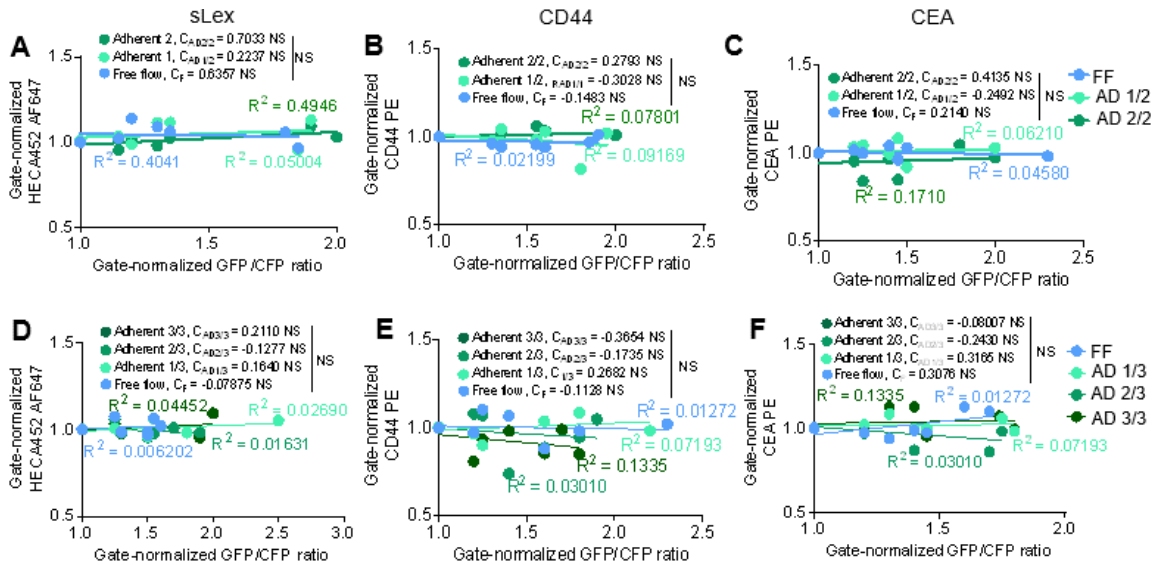


Figure 4.10 No correlations between ligand expression and GFP/CFP ratios among PC- cells within any collected cell fraction. (A-E) The extent of photoconversion (GFP/CFP ratio) of FF PC- cells and (A-C) 2 or (D-E) 3 AD fractions related to the expression of (A,D) sLe^x reactive HECA452, (B,E) CD44, and (C,F) CEA. (A-F) Binned, flow cytometry data of PC- cells was pooled from independent experiments and plotted with corresponding linear fits; C_F and C_{AD} represent the regression slope of the PC- cells in the Adherent and Free flow fractions, respectively. Outlier tests with criteria $Q = 1$ were conducted on all data sets, and outliers were removed prior to regression and statistical analysis. Perfusion, photoconversion, and separation of a Phamret-expressing LS174T cell pulse of 250,000 cell over 2.5 μmL^{-1} E-selectin at 1 dyn cm^{-2} .

4.3.3 Slow and Fast Rolling Adhesion on E-selectin is Associated with Sialyl Lewis X Expression

Within the experimental configuration described so far, only fractions that exhibit velocities within the dynamic range of the photoconversion system are measurable via photoconversion (Figure 4.11A). Under all fractionation conditions, the latest eluting cells, and therefore the cells with the slowest average rolling velocities, exhibited the most significant correlations between increasing extent of photoconversion and adhesive molecule presentation (Figure 4.9B-G). However, with the photoconversion methodology, velocities above $\sim 200 \mu\text{m/s}$ are poorly discernible (Figure 4.5A). As such, although the

photoconversion methodology reduces noise within subfractionated populations to reveal subtle trends, it is limited to the direct analysis of cells interacting with slow short time- and length-scale velocities only (Figure 4.11A).

To expand the working parameters and versatility of the system to elucidate expression relationships for cells exhibiting higher velocities of rolling adhesion, photoconversion of cells prior to perfusion was performed (Figure 4.11B). In so doing, GFP/CFP ratios were increased for all cells depending on the time of light pre-exposure (Figure 4.12A). As a result, different fractions of cells are adjusted to GFP/CFP levels within the working dynamic range of the fluorometric velocity measurement technique based on pre-exposure time length (Figure 4.11A), broadening the range of adhesive phenotypes (in this case to include on average fast rolling cells) over which expression correlations can be quantified using this photoconversion method. For example, with pre-exposure for 4 min, nearly all cells were PC⁺ when fractionated on E-selectin into two AD fractions (Figure 4.11C), with minimal differences in viability amongst collected fractions (Figure 4.12B). However, photoconversion extent varied widely with GFP/CFP ratio of AD 1/2 within the photoconversion dynamic range (Figure 4.11A). Regression analysis revealed sLe^x expression positively correlated with photoconversion extent for not only AD 1/2 but also the AD 2/2 fraction with 4 min pre-photoconversion (Figure 4.11D,E), in contrast to analyses performed on fractions that were not pre-photoconverted (Figure 4.9B).

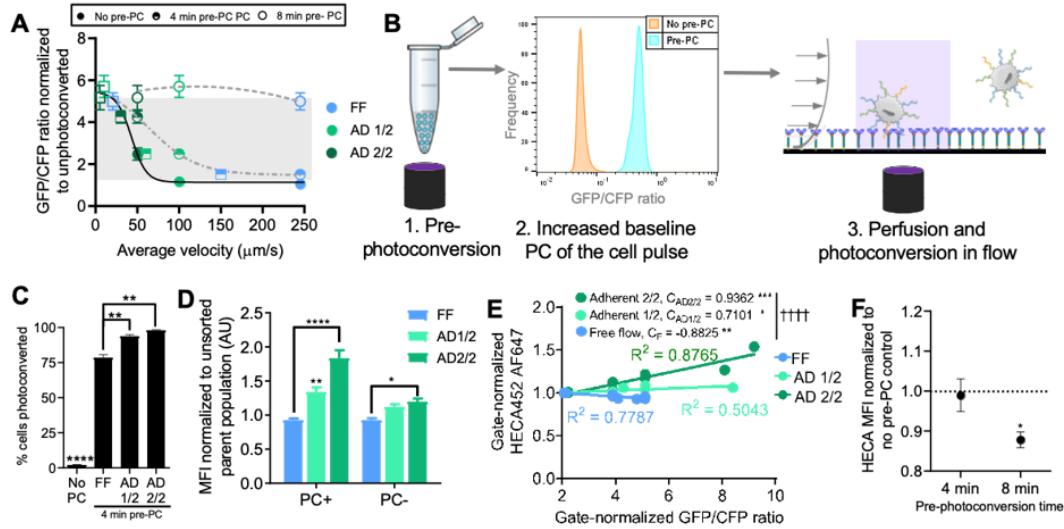


Figure 4.11 Cellular sLe^x expression inversely correlated with magnitude of fast rolling adhesion on E-selectin revealed by pre-photoconversion. (A) Measured GFP/CFP ratios and average velocities (calculated by elution time) of collected cell fractions. Circles, measured average velocities; Squares, average velocities adjusted based on pre-photoconversion time and measured average velocities. (B) Experiment workflow depicting static photoconversion of cells pre-perfusion to increases the baseline photoconversion of the cell pulse, followed by perfusion and photoconversion over an E-selectin functionalized channel in order to maximally photoconvert late eluting adherent cells. (C) Percent of Phamret-expressing LS174T cells photoconverted after exposure to the 405 nm laser for 4 min of pre-photoconversion. FF denotes free flow, AD denotes adherent. PC denotes photoconversion. (D) Quantification of mean fluorescent intensity of sLe^x reactive HECA452 in each collected fraction of either PC+ or PC- subsets. (E) The extent of photoconversion (GFP/CFP ratio) of PC+ cells within the FF and 2 AD fractions related to the expression of sLe^x (HECA452). Binned, flow cytometry data of PC+ cells was pooled from independent experiments and plotted with corresponding linear fits; $C_{AD1/2}$, $C_{AD2/2}$, and C_F represent the regression slope of the PC+ cells in the AD 1/2, AD 2/2, and FF fractions, respectively, * denotes non-zero slopes of the linear fit, † denotes significance of comparison between $C_{AD1/2}$, $C_{AD2/2}$, and C_F . Outlier tests with criteria $Q = 1$ were conducted on all data sets, and outliers were removed prior to regression and statistical analysis. (F) Quantification of mean fluorescent intensity of sLe^x expression normalized to a perfused, but not pre-photoconverted control after 4 or 8 min of pre-photoconversion. (C-F) 4 min of pre-photoconversion followed by perfusion, photoconversion, and (C-E) fractionation of a Phamret-expressing LS174T cell pulse of $250,000$ cell over $2.5 \mu\text{g mL}^{-1}$ E-selectin at 1 dyn cm^{-2} . (A,C-F) Each dot or bar represents the mean \pm s.e.m. of $n \geq 3$ individually run experiments. * $p < 0.05$, ** $p < 0.01$, *** $p < 0.001$ **** $p < 0.0001$ by (C-E) one-way ANOVA with post hoc t-test with Bonferroni corrections for multiple comparisons or (F) one sample t-test with $h_0 = 1$. Dashed line at 1.

Of note, overexposure to photoconverting light results in loss of cell viability (Figure 4.12A). When using a light pre-exposure time that results maximal photoconversion but 50% cell loss (8 min, Figure 4.11A, 4.12A), perfusion over E-selectin resulted in loss of cell viability. In the context of collection into multiple fractions, nearly half of the free flow cells (FF) and 40% of early eluting, adhesive cells (AD 1/2) remained viable, whereas only about 20% of the late eluting adhesive cells (AD 2/2) were viable (Figure 4.12C). Notably, pre-photoconversion does not affect the adhesive behavior of cells in the channel, as the percent of pre-photoconverted cells that elute into the FF, AD1/2, and AD2/2 fractions after perfusion through the channel without photoconversion during perfusion is not statistically different than the percent of cells that elute into the aforementioned fractions without pre-photoconversion (Figure 4.12D,E). Without subfractionation, expression of sLe^x by viable cells post perfusion was lower in cells pre-exposed to the photoconverting light for 8 min versus those without pre-photoconversion (Figure 4.11F). This supports sLe^x enabling adhesive interactions to E-selectin in flow as the viability of cells exhibiting the most extensive adhesive interactions would be compromised. Findings using this pre-photoconversion technique thus confirm inverse correlations between sLe^x expression and velocity of rolling adhesion across a broad range of velocity magnitudes.

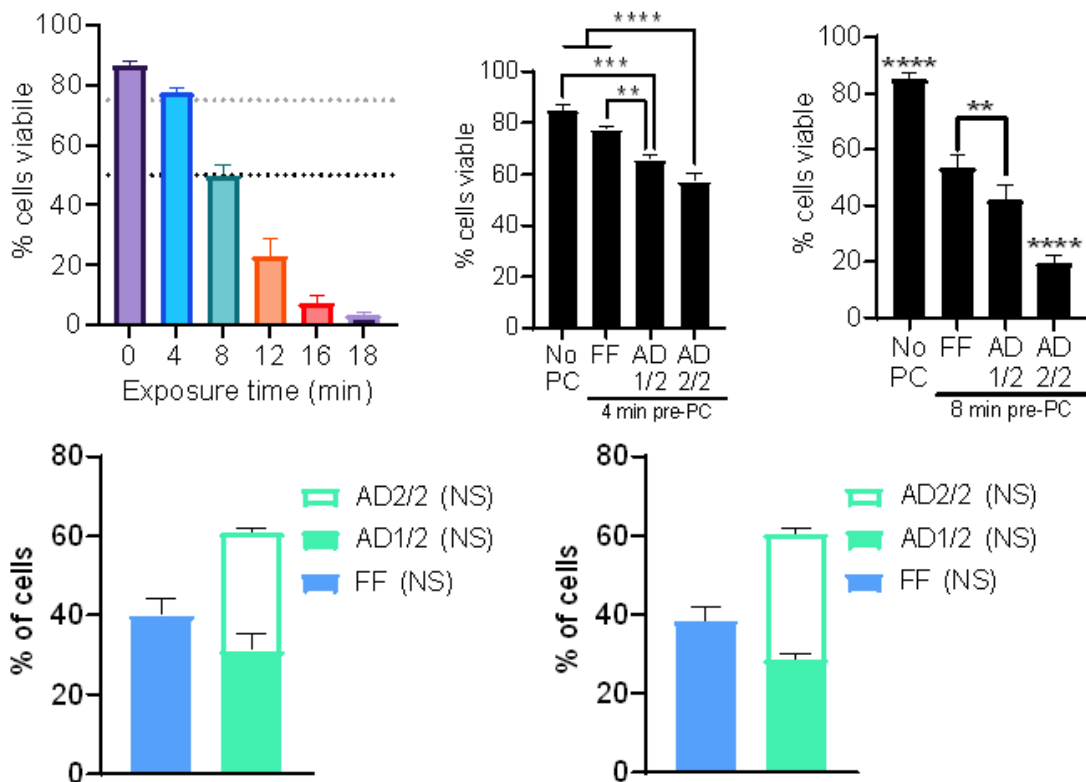


Figure 4.12 Effects of pre-photoconversion on cells pre and post perfusion. (A) Percent of viable Phamret-expressing LS174T cells after exposure to the 405 nm laser for different lengths of static pre-photoconversion time. Gray line represents 75% cell viability, black line represents 50% cell viability. (B,C) Percent of cells viable (B) 4 or (C) 8 min of pre-photoconversion. FF denotes Free flow, AD denotes Adherent. PC denotes photoconversion. (D,E) Percent of cells collected in each fraction after either (D) 4 or (E) 8 minutes of static photoconversion, followed by perfusion without photoconversion and fractionation. (A-E) Pre-photoconversion and perfusion of a Phamret-expressing LS174T cell pulse of 250,000 cell over $2.5 \mu\text{g mL}^{-1}$ E-selectin at 1 dyn cm^{-2} . (A-E) Each bar represents the mean \pm s.e.m. of $n \geq 3$ individually run experiments. (B,C) ** $p < 0.01$, * $p < 0.001$, **** $p < 0.0001$ by one-way ANOVA with post hoc t-test with Bonferroni corrections for multiple comparisons. (D,E) Two sample t-test comparing percent of cells in each fraction compared to percent of cells in each fraction when cells are not pre-photoconverted. NS denotes no significance.**

4.3.4 *Selectin Ligands Enriched in Cells Mediating Persistent but Not Non-persistent Selectin Adhesion*

The capacity of this system to differentiate subsets of LS174T cells in persistent versus non-persistent adhesion with selectins was next leveraged in order to interrogate mechanisms underpinning these different qualities of selectin adhesion (Table 4.2). Ligand expression levels amongst subfractions were compared and relationships between measured short time- and length-scale velocities evaluated. Specifically, a subset of non-persistent cells (e.g. those within the PC+ subset of the FF fraction) were compared to those of the PC+ cells within the AD fraction, which exhibit sustained rolling adhesion, the caveat being for reasons described above that the latter is limited to only slow rolling cells (<200 $\mu\text{m/s}$) for fractionation experiments performed without pre-photoconversion.

Table 4.2 Correspondence of photoconversion integrating cell sorting microfluidic readout to adhesion persistence.

Fraction	Photoconversion	Adhesion persistence
Free flow	PC-	No adhesion
Free flow	PC+	Non-persistent
Adherent	PC-	Non-persistent
Adherent	PC+	Persistent

Within fractions collected on selectin functionalized substrates of AD cells only, expression of sLe^x and CD44 was increased in PC+ subset (Figure 4.13A,B). Expression of sLe^x was also increased in PC- cells collected on P-, but not E- or L-, selectin (Figure 4.13A). No other correlations were found between velocity and selectin ligand expression among cells that remain unphotoconverted (PC-, Figure 4.13A-C). Additionally, CEA

expression was found to be increased in PC⁺ AD but not FF subset on P- and L-, but not E-, selectin (Figure 4.13C), a surprising trend given CEA's function as an E- but not P-selectin ligand in these cells. These data demonstrate sLe^x but not CD44 to be enriched in LS174T cells mediating not only persistent but also non-persistent slow rolling adhesive interactions with P-selectin in shear flow and CEA is associated with persistent adhesive phenotype on P- and L-selectin.

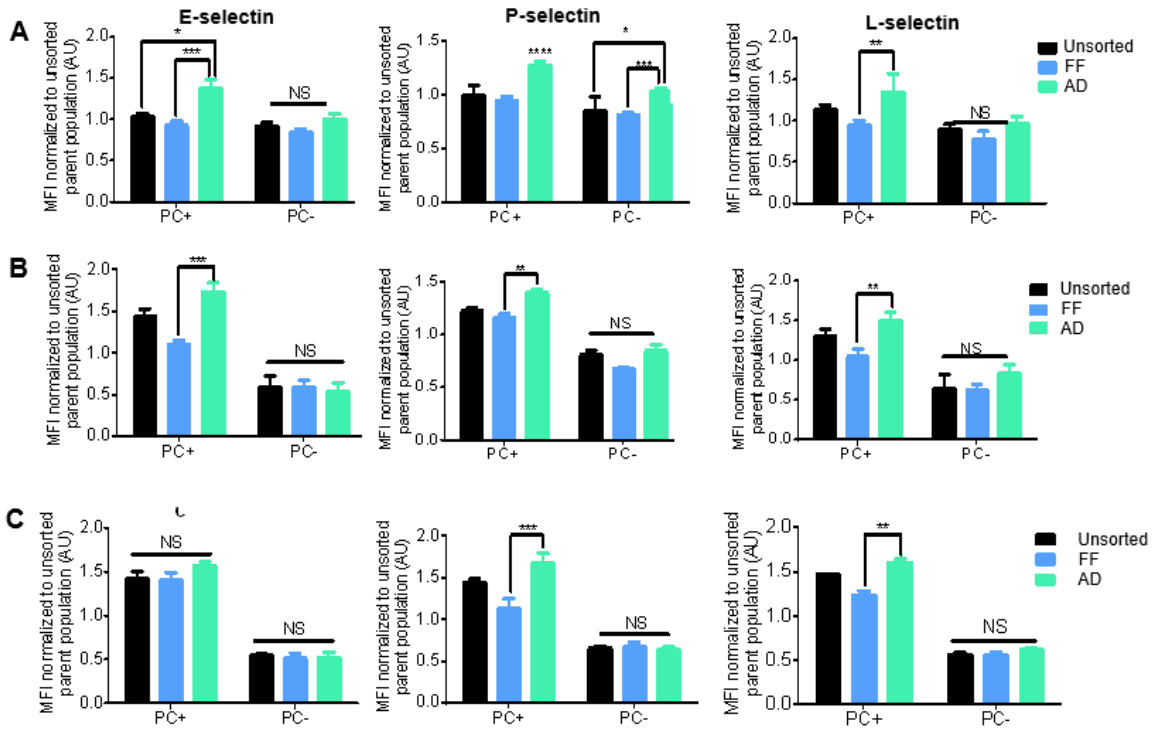


Figure 4.13 Selectin ligands sLe^x, CD44, and CEA are enriched in cells mediating persistent slow rolling selectin adhesion in flow. (A-C) Expression levels of selectin ligands (A) sLe^x, (B) CD44, and (C) CEA among PC⁺ and PC⁻ cell subsets collected after exposure to a 405 nm light during perfusion of a cell pulse of 250,000 Phamret-expressing LS174T cells over 2.5 μg mL⁻¹ E-selectin at 1 dyn cm⁻² or 25 μg mL⁻¹ L- or P-selectin at 0.5 dyn cm⁻². Each bar represents the mean ± s.e.m. of n≥3 individually run experiments. * p < 0.05, ** p < 0.01, *** p < 0.001, **** p < 0.0001 by one-way ANOVA with post hoc t-test with Bonferroni corrections for multiple comparisons.

Regression analyses revealed sLe^x and CD44 expression to vary directly versus inversely with cell velocity magnitude (measured by GFP/CFP ratio) on E-selectin in the context of persistent (PC⁺ cells in AD fraction) versus non-persistent (PC⁺ cells in FF fraction) adhesion, respectively (left panels, Figure 4.14A,B). No correlations direct or otherwise were seen for CEA expression (Figure 4.14C, left panel). In the context of P- and L-selectin adhesion, sLe^x and CEA but not CD44 expression correlated directly with GFP/CFP ratio for persistent adhesion (middle and right panels, Figure 4.14A-C). Contrastingly, inverse correlations in expression of all three ligands with GFP/CFP ratio were found in the context of non-persistent adhesion (PC⁻, Figure 4.14D). Consistent with results from the collection of multiple adherent fractions, no correlations are observed in PC⁻ cells subsets (Figure 4.15). Together, these results demonstrate the differential overall expression levels of selectin ligands and associations with velocity magnitudes between cells mediating persistent versus non-persistent adhesion. For example, although CD44 expression overall is enriched in cells in cells exhibiting persistent adhesion to P-selectin, its expression does not correlate with slower rolling velocities. Furthermore, although sLe^x expression is increased in cells mediating slow rolling P-selectin non-persistently, its expression is associated with increased, not decreased, velocity magnitudes. This integrated analysis platform can thus reveal complex interdependent relationships in cellular phenotypes associated with both rolling adhesion quantity (e.g. velocity) and quality (e.g. persistence).

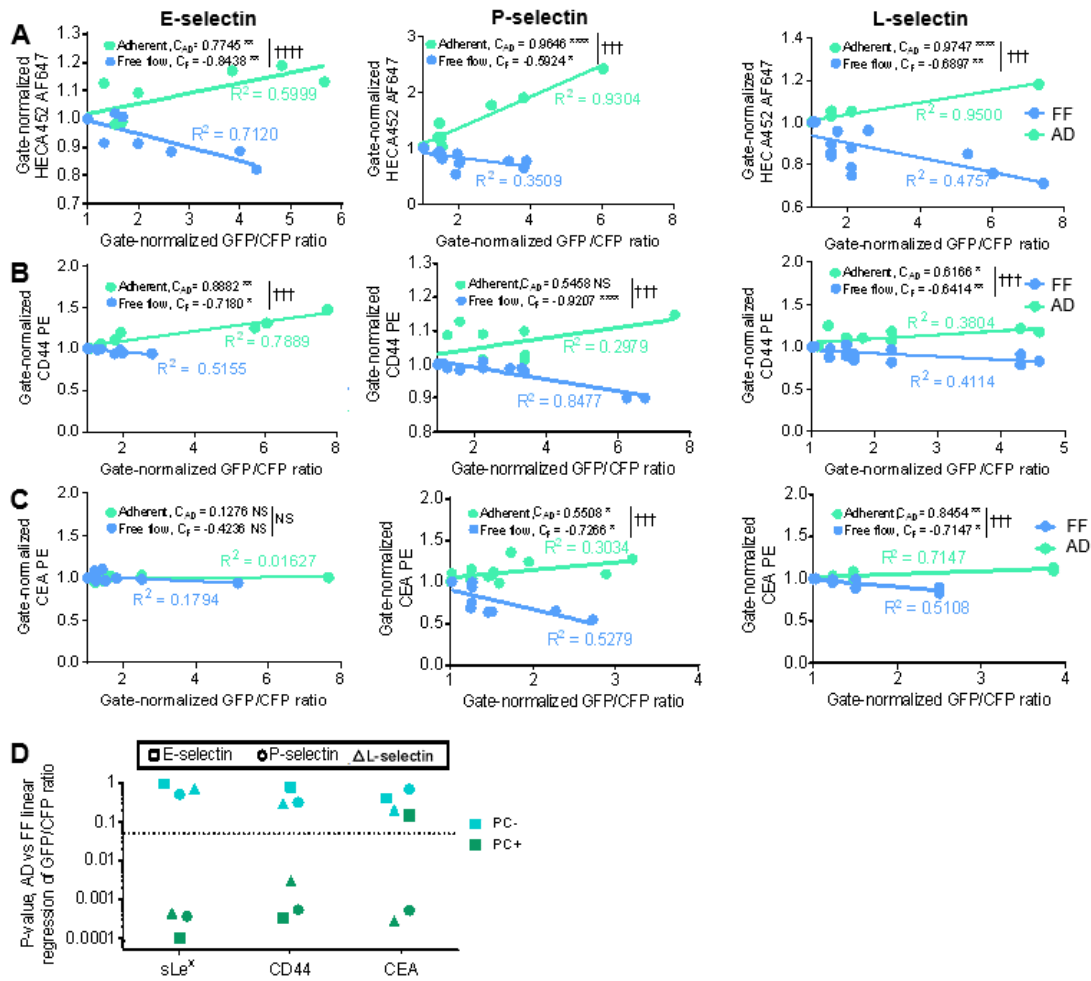


Figure 4.14 Opposing ligand expression correlations with rolling velocity magnitudes between persistently versus non-persistently adhesive cells. Sorted cell fractions labeled with fluorescently tagged antibodies for (A) sLe^x, (B) CD44, and (C) CEA, then applying the photoconversion gates and binning allowed the extent of photoconversion and elution time to be correlated to the relative ligand expression. Binned, flow cytometry data of cells was pooled from independent experiments and plotted with corresponding linear fits; C_{AD} and C_F represent the regression slope of the PC+ cells in the Adherent and or PC- cells in the Free flow fractions, respectively, * denotes non-zero slopes of the linear fit, † denotes significance of comparison between C_{AD} and C_F . * $p < 0.05$, ** $p < 0.01$, *** $p < 0.001$, **** $p < 0.0001$. Outlier tests with criteria $Q = 1$ were conducted on all data sets, and outliers were removed prior to regression and statistical analysis. Perfusion, photoconversion, and separation of a Phamret-expressing LS174T cell pulse of 250,000 cells over either $2.5 \mu\text{g mL}^{-1}$ E-selectin at 1 dyn cm^{-2} or $25 \mu\text{g mL}^{-1}$ L- or P-selectin at 0.5 dyn cm^{-2} . (D) Summary of P-values of comparisons between the slopes of the linear relationships for interrogated ligands cells in the Adherent (C_{AD}) versus Free flow (C_F) fractions; dashed line represents $p=0.05$.

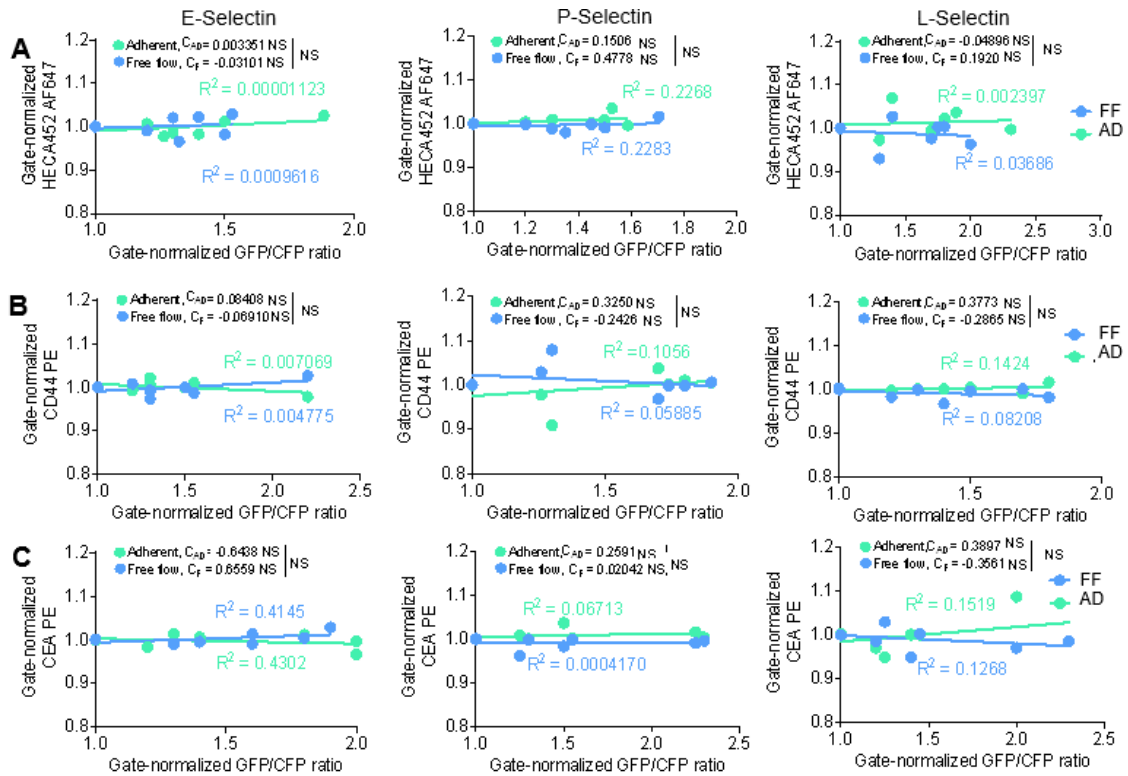


Figure 4.15 No correlation between selectin ligand expression and GFP/CFP ratios among cells that remain unphotoconverted. The extent of photoconversion (GFP/CFP ratio) of PC- cells within FF and AD fractions related to the expression of (A) sLe^x (HECA452), (B) CD44, and (C) CEA sorted over E-, P-, or L-selectin. (A-C) Binned, flow cytometry data of PC- cells was pooled from independent experiments and plotted with corresponding linear fits; C_{AD} and C_F represent the regression slope of the PC- cells in the AD and FF fractions, respectively. Outlier tests with criteria $Q = 1$ were conducted on all data sets, and outliers were removed prior to regression and statistical analysis. Perfusion, photoconversion, and separation of a Phamret-expressing LS174T cell pulse of 250,000 cell over $2.5 \mu\text{g mL}^{-1}$ E-selectin at 1 dyn cm^{-2} or $25 \mu\text{g mL}^{-1}$ P- or L-selectin at 0.5 dyn cm^{-2} .

4.3.5 Screening Ligand Degrading Enzyme Effects on Adhesion Mechanisms

To demonstrate the versatility of this microfluidic approach to assess drug treatment effects on cell adhesion extent and mechanism, cells were treated with neuraminidase (NA), a sialidase that cleaves the terminal sialic acid residues on sLe^x epitopes,^{81,201,202 203–205} and cell adhesion to selectin-functionalized surfaces analyzed via the integrated microfluidic and photoconversion based approach (Figure 4.16A). With NA treatment, sLe^x expression was completely lost (Figure 4.16B), while surface expression levels of CD44 and CEA ligands remained unchanged compared to untreated cells (Figure 4.16C,D) in all collected cell fractions. As previously reported,^{81,82,168} NA treated LS174T cells retained the ability to mediate adhesion to E-, but not P- or L-, selectin (Figure 4.16E-F, 4.17). When fractionated on E-selectin, approximately 25% of perfused cells eluted into the AD fraction (Figure 4.16E). With respect to the extent of photoconversion, GFP/CFP ratios were diminished for AD but slightly increased for FF fractions as a result of NA (Figure 4.16F). Although the proportion of PC⁺ cells in AD fraction was also strikingly decreased as a result of NA, the proportion was strongly increased for FF (Figure 4.16G), suggestive of NA treatment diminishing LS174T adhesion persistence and velocity of rolling adhesion on E-selectin. The overall relative frequency of PC⁺ cells in the AD compared to FF fraction remained increased, however, though the relative difference much reduced (Figure 4.16H).

As CD44 expression has a strong inverse correlation with E-selectin rolling velocities by LS174T cells that holds across velocity magnitudes (Figure 4.8,4.9,4.11), effects of NA treatment on regression trends with CD44 were assessed. As expected given the role of sialylfucosylated CD44 variants in mediating E-selectin adhesion by these

cells^{12,26}, NA treatment eliminated correlations between CD44 and extent of photoconversion within PC+ subsets of cells collected into AD cell fractions on E-selectin (Figure 4.16I). The lack of correlation of CEA expression was also sustained (Figure 4.16J). No changes were seen in correlations were seen in treated cells that eluted into the FF fraction, as they continued to show a lack of correlation between selectin-ligand expression and rolling velocity (Figure 4.16I,J). Together, these data suggest that sialylated CD44 mediates sustained adhesion to E-selectin and non-persistent adhesion that results from NA treatment is mediated by another herein unexplored selectin ligand.

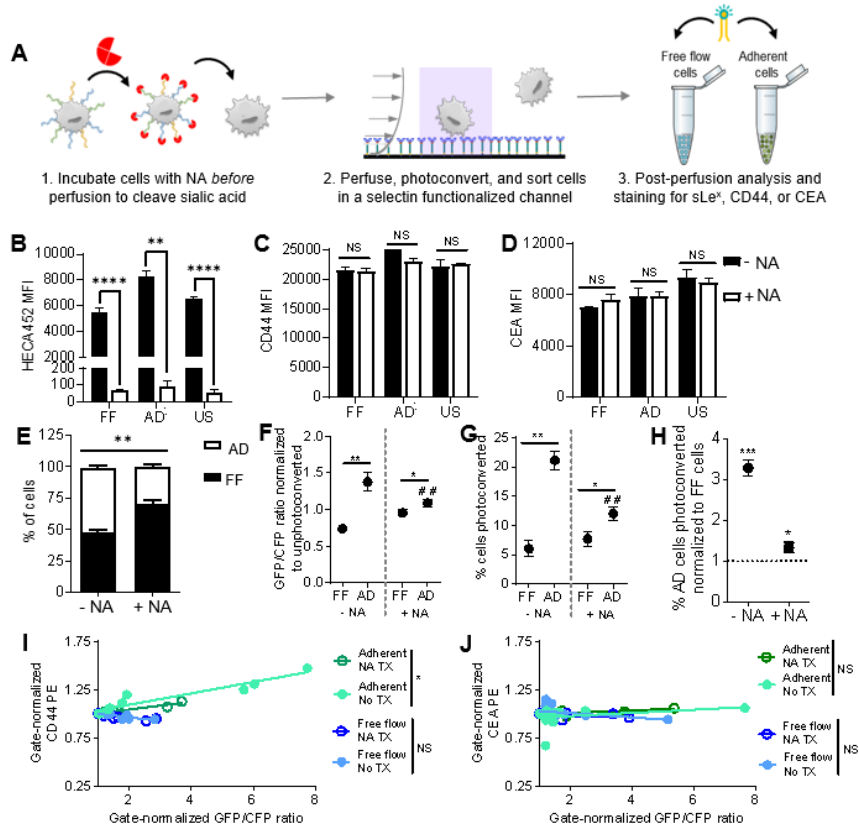


Figure 4.16 Sialyl Lewis x and CD44 correlated in highly but not lowly persistent slow rolling selectin-mediated adhesion. (A) Experimental workflow for neuraminidase (NA) treatment perfusion experiments. (B-D) quantification of mean fluorescent intensity of (B) sLe^x, (C) CD44, or (D) CEA expression after treatment with/without NA and perfusion over E-selectin. FF denotes the Free flow, AD denotes Adherent, US denotes an unsorted group. (E) Percent of cells collected in the AD and FF fractions, (F) Mean GFP/CFP ratio after perfusion over E-selectin, (G) percent of cells photoconverted, and (H) percent of cells photoconverted in the AD fraction normalized to the FF fraction with/without NA treatment. (I,J) The extent of photoconversion (GFP/CFP ratio) of PC- cells within the Free flow fraction or PC+ cells within the AD fraction related to the expression of (I) CD44 or (J) CEA sorted over E-selectin. Binned flow cytometry data of cells was pooled from independent experiments and plotted with corresponding linear fits after perfusion over E-selectin with/without NA treatment. Outlier tests with criteria $Q = 1$ were conducted on all data sets, and outliers were removed prior to regression and statistical analysis. (B-J) Perfusion, photoconversion, and separation of a Phamret-expressing LS174T cell pulse of 250,000 cells over $2.5 \mu\text{g mL}^{-1}$ E-selectin at 1 dyn cm^{-2} . (E-J) Each dot or bar represents the mean \pm s.e.m. of $n \geq 3$ individually run experiments. (B-J) * $p < 0.05$, ** $p < 0.01$, **** $p < 0.0001$ by (B-K) paired t-test or (J) one sample t-test with $h_0 = 1$; dashed line at $y=1$. (G) # denotes difference between -NA AD group and +NA AD group by paired t-test.

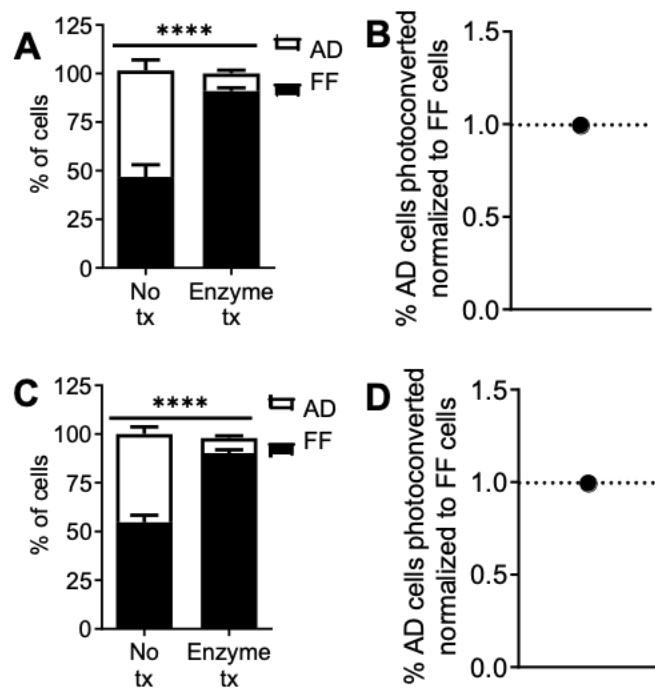


Figure 4.17 Neuraminidase treatment effects on cell adhesion in flow to P- and L-selectin. (A,C) Percent of cells collected in the FF and AD fractions. (B,D) Percent of cells photoconverted in the AD fraction normalized to the FF fraction after perfusion of a cell pulse of 250,000 Phamret-expressing LS174T cells over $25 \mu\text{g mL}^{-1}$ (A,B) P- or (C,D) L-selectin at 0.5 dyn cm^{-2} . FF denotes Each dot or bar represents the mean \pm s.e.m. of $n \geq 3$ individually run experiments. **** $p < 0.0001$ by (A,C) one-way ANOVA with post hoc t-test with Bonferroni corrections for multiple comparisons or (B,D) one sample t-test with $h_0 = 1$; dashed line at $y = 1$.

4.4 Discussion

The ability to evaluate within a heterogeneous population the cellular features associated with different qualities of rolling adhesion using a novel, integrated cell sorting and photoconversion adhesive chromatography microfluidic platform was demonstrated here through the juxtaposition of measured long and short time- and length-scale adhesive rolling behaviors. Building off of a previously designed cell sorting system that fractionates subsets of cells based on their time-averaged cell adhesive behavior,²⁶ a 405 nm laser was added to photoconvert cells in a manner directly proportional to their velocity under the small window of light exposure,¹² thereby “labeling” the cells with their short time- and length-scale velocity. Cells with slow rolling velocities within the light exposure window could thus be compared across elution times, i.e. adhesive versus non-adhesive fractions. Furthermore, cellular features could be analyzed using this preparative technique to distinguish expression pattern differences between cells with different adhesion phenotypes, as was explored here using flow cytometry.

First, the photoconversion readout allowed ligand expression signal in measured population subfractions to be filtered to exclude those that were exhibited non-persistent adhesion (and were thus PC-). In so doing, expression of CEA was found to be enriched in cell subfractions mediating adhesion to E-selectin, increases not seen without photoconversion.²⁶ Even low levels of diminished persistence thus diluted signal and photoconversion could distinguish CEA expression by cells mediating slow, persistent rolling adhesion on E-selectin (Figure 4.8). Additionally, pre-photoconversion as well as increasing the number of collected adhesive subfractions allowed trends to be explored across rolling adhesion magnitudes (Figures 4.6,4.8,4.9,4.11). These techniques revealed

adhesive ligands sLe^x and CD44 to be inversely correlated with slower rolling on E-selectin over a broad range of velocity magnitudes, whereas CEA expression is associated with E-selectin adhesion in the context of slow rolling only.

Concurrent measurement of short and long time- and length-scale velocities also permitted the elucidation of cellular molecular phenotypes related to different adhesion persistence phenotypes. We previously reported colon carcinoma cells to exhibit in their interactions with P- and L- but not E-selectin diminished adhesion persistence,^{11,13} defined as the capacity for cells to sustain adhesion and this case rolling adhesion over time and distance. In the instance of highly persistent adhesion, cells would mediate the same adhesive behavior along the entire channel length. Thus, so long as rolling velocities are below the threshold detectable by photoconversion, AD fractions would contain PC+ cells. Cells exhibiting low adhesion persistence on the other hand would interact for only portions of their transit time through the channel. Cells eluting into the FF fraction that are PC+ would thus be considered very lowly persistent as they were mediating adhesion within the light exposure window but deadhered. It should be noted that PC- cells cannot be assigned as either persistent or non-persistent, as they may have not photoconverted as a result of lack of adhesion or their rolling adhesion velocity being higher than the maximum velocity detectable by photoconversion.

This photoconversion and chromatographic method confirmed previous results using videomicroscopy only^{11,13} that LS174T cells exhibit a persistent phenotype over E-, but not P- or L-selectin (Figure 4.5). Concurrent cellular phenotyping also revealed that although CD44 expression overall is enriched in cells in persistent P-selectin adhesion, its expression does not correlate with slower rolling velocities. Furthermore, although sLe^x expression is

increased in cells mediating slow rolling P-selectin non-persistently, its expression is associated with increased, not decreased, velocity magnitudes. CEA expression was also associated with persistent adhesive phenotype on both P- and L-selectin (Figure 4.13), despite not serving as a ligand for the former.⁸² Correlations in selectin ligand expression with rolling velocity magnitude were also found to be inverted between persistently versus non-persistently adhesive cells on all selectins (Figure 4.14). Furthermore, enzymatic digestion of sialofucosylated epitopes also reduced persistent but not non-persistent adhesion by LS174T cells to E-selectin in flow (Figure 4.15), the latter presumably mediated by another selectin ligand unexplored herein. Molecular expression characteristics thus vary by adhesion quality amongst selectin types, which has ramifications for the potential contribution of adhesion types and molecular pathways in dissemination mechanisms. This integrated analysis platform can thus reveal complex interdependent relationships in cellular phenotypes associated with both rolling adhesion quantity (e.g. velocity) and quality (e.g. persistence) as well as drug effects on the molecular mechanisms underpinning such processes.

4.5 Conclusion

In closing, this integrated system is capable of isolating and identifying subsets of cells with different adhesive behaviors to enable associated cellular phenotypes to be discerned. Separating cells based on biophysical characteristics is a broadly used technique for probing mechanisms underlying multiple disease types, and this platform improves upon former methods by enabling both quantification of rolling adhesion velocities and assessment of their qualities, e.g. persistent versus non-persistent. Our results demonstrating divergent molecular profiles associated with various adhesive phenotypes

suggests the potential for this system to be applied to identify druggable targets on distinct subsets of circulating cancer cells (tumor initiating, for example) or provide nuance to the utility of various biomarkers in distinguishing circulating cells with distinct malignant phenotypes.

CHAPTER 5. LYMPH NODE SUBCAPSULAR SINUS MICROENVIRONMENT-ON-A-CHIP TO MODEL LYMPHATIC METASTASIS AND IMMUNE CELL HOMING

5.1 Introduction

Lymph node status negatively correlates with patient survival in many cancers.^{206–210} Though still debated,^{145,211–214} the general hypothesis underlying how lymph node metastasis occurs is that the lymphatic vasculature provides a conduit for invasive cancer cells to move towards lymph nodes driven by both chemotactic cues and fluid flows driven by lymph propulsion. Once in lymph nodes, metastatic cells have the opportunity to undergo extensive interactions with resident immune cells that can influence their metastatic behavior. In particular, it is known that immune tolerance is associated with metastatic spread as well as drug resistance.^{215,216} Understanding interactions of metastatic cells within this anatomical location, which has been widely implicated in influencing anti-tumor immunity and response to therapy, is thus of high relevance in the current era of cancer immunotherapy. Additionally, a therapeutic window has been proposed wherein systemic dissemination of metastatic disease can be therapeutically ameliorated.^{217–219} In such a context, understanding the biology underlying lymphatic metastasis has the potential to identify unique druggable targets for lymph node positive, but not systemic, disease.

Transit via the lymphatic system has the potential to provide access to lymph-borne cells to the systemic circulation in two manners, the first by virtue of lymphatic vessels returning lymph to blood at the thoracic duct.²²⁰ Numerous reports have demonstrated the

potential for a second, perhaps more likely, dissemination route via invasion within the local lymph node microenvironment and access to lymph node parenchyma-resident cancer cells to access the circulatory system through lymph node capillaries.^{23,212,213,221} Thus, the ability to arrest in lymph nodes despite lymph flow and then transmigrate into the lymph node parenchyma may be a contributing factor in metastatic dissemination through the lymphatic route. Notably, numerous reports have documented evidence of the accumulation of circulating tumor cells within the subcapsular sinus, whose invasion into the lymph node parenchyma can be blocked by inhibition of adhesion receptors^{222–225} or chemotactic cues.^{14,22,145,226–228} Together, the involvement of the lymph nodes in the multifaceted progression of the metastatic cascade is thought to allow the formation of numerous, simultaneously occurring secondary tumors originating from a single primary tumor, however, the mechanisms by which this occurs remain widely unknown.

As in the hematogenous context, metastasis by lymph-borne cells occurs within luminal flow fields, which in the context of lymphatic vessels is driven by propulsive lymph flow.^{211,229} The resulting hydrodynamic forces are known to play essential roles in regulating adhesion relevant to metastatic extravasation.^{41,220,230} Specifically, the dispersive effects of hydrodynamic force must be overcome by adhesive interactions in order to enable receptor signaling and chemotaxis.^{41,231–233} Although volumetric flow rates of lymph are far lower than that in blood, the stress levels experienced within vessels are not dissimilar.²³⁴ Thus, it could be expected that adhesive processes involved in cell homing and metastasis through the blood vasculature may be involved in regulating lymphatic dissemination. Indeed, this is supported by observations of cell adhesion molecules E- and P-selectin as well as ICAM and VCAM by lymphatic endothelial cells

that form the interior of the lymphatic vessel lumen and within the lymph node sinus, whose expression of which has been reported to change in states of inflammation.^{235–239}

Concurrent with stromal cell and lymphocyte responses disease and/or inflammation, lymph nodes are widely reported to structurally remodel. A hallmark of metastatic disease is lymphadenopathy, i.e. swollen lymph nodes.²⁴⁰ Concurrently, tissue stiffening has been reported,^{241,242} which is most often attributed to metastatic colonization but an effect that has also been reported in lymph nodes prior to metastasis.^{241,243,244} In addition to expansion of the lymph node parenchyma-localized fibroblastic reticulum²⁴⁵ and high endothelial venules,²⁴⁶ both afferent (lymph node-entering) lymphatic vessels and the subcapsular sinus are known to dilate in contexts of human disease,^{247–249} effects that are also recapitulated in mouse models.^{235–239} How these changes have the potential to synergistically influence cell dissemination to lymph nodes has not been systemically explored. This however is hampered in large part by the reliance on mouse models, which differ subtly in their structures^{250,251} as well as the inability in mouse systems to uncouple biomolecular versus biophysical changes that often occur concurrently in states of disease.

To fill this critical gap, we sought to bring to bear *in vitro* tools long employed in the context of studying neutrophil adhesion and blood-borne metastasis to the problem of analyzing mechanisms of lymph node metastasis. Although *in vivo* mouse models are more complex, these microfluidic systems offer the advantage of enabling high-throughput experimentation under defined molecular, cellular, and/or biophysical conditions.^{11,13,165,252–254} Furthermore, coupling these microfluidic devices with high-speed videomicroscopy permits rapid and facile visualization and quantification of the adhesive behavior of thousands of cells in a single experiment largely infeasible even with the most

advanced intravital imaging systems.^{11,13,26,27,255} In particular, we applied a parallel plate flow chamber technology adapted to recapitulate the dissipating wall shear stress (WSS) experienced within the lymph node subcapsular sinus as a result of the radially dispersed flow after lymph entry into the lymph node via the afferent vessel. Using this lymph node “sinus-on-a-chip” adhesive microfluidic platform, we explored the effects of WSS magnitude and dissipation on adhesion by human monocytic and metastatic cancer cell lines, both of which are known to disseminate to lymph nodes via the lymphatic vasculature. Monocytes home to the lymph node via the afferent vessel into the subcapsular sinus and play a crucial role in mounting an immune response against disease.^{256–258} Pertinently, previous research has found that monocytes can mediate and increase the adhesive behavior of cancer cells under flow, and it has been shown *in vitro* that monocytes can promote colon cancer extravasation and the formation of metastases in the lungs.^{259,260} We also chose to focus on metastatic pancreatic cancer and colon adenocarcinoma cells due to the high clinical relevance of lymphatic metastasis in these diseases, as 89% pancreatic cancer patients have disseminated tumor cells within their lymph nodes and 45% of colon cancer patients have lymph node involvement.^{261,262} This analytical method revealed that cell adhesion within dissipating fields of WSS is regulated by both WSS magnitude and the time of cell in transit. As a result, structural changes within the sinus and afferent vessel alters the potential position at which cells can optimally interact and/or within the lymph node subcapsular sinus, effects also influenced by presented adhesion receptors. Metastatic cell co-perfusion with monocytes also increases the extent of cell adhesion, implicating inflammation and mobilization of lymph borne immune cells as regulating lymphatic metastasis. Given the defined chemotactic programs that drive lymphocyte and myeloid

cell migration in lymph nodes from lymph, our results implicate the biophysical effects of lymph node remodeling and their influence on directing adhesion within the subcapsular sinus space as a potential axis that can regulate the mechanisms driving lymph node invasion.

5.2 Materials and Methods

5.2.1 Immunohistochemistry

Whole mouse lymph nodes were collected, embedded in optimum cutting temperature embedding medium, and stored at -80° C. Whole lymph nodes were sliced using a cryostat into 10 µm thick tissue sections, mounted onto histological slides, and stored at -20° C until slicing. Prior to staining, the slides were fixed in acetone for 20 min at -20° C, blocked with 10% goat serum diluted in Dulbecco's Phosphate Buffered Saline (D-PBS) with calcium and magnesium for 1 h at room temperature, then incubated overnight at 4° C with the following primary antibodies: (1) rabbit anti-mouse LYVE-1 (1:200, Invitrogen, PA1-16635), (2) chicken anti-mouse CD62E (1:100, Novus Biologicals, AF575), and (3) hamster anti-mouse CD54 (1:100, Novus Biologicals, NBP2-22540) or rat anti-mouse CD106 (1:50, Novus Biologicals, NB100-77474). The following day, the slides were incubated for 1 h at room temperature with the following fluorophore conjugated secondary antibodies: (1) goat anti-rabbit Alexa Flour 633 (1:300, Invitrogen, A-21070), (2) goat anti-chicken Alexa Flour 488 (1:200, Invitrogen, A-11039), and (3) goat anti-hamster DyLight 550 (1:1000, Novus Biologicals, NBP1-71730R) or goat anti-rat DyLight 550 (1:100, Invitrogen, SA5-10019). Finally, the slides were mounted using Vectashield mounting medium with DAPI and microscopic images were taken using a

Zeiss 710 confocal microscope. In between each step, the slides were washed three times with gentle agitation in 0.1% Tween 20 diluted in D-PBS with calcium and magnesium.

5.2.2 COMSOL Wall Shear Stress Modeling

The wall shear stress profile along the floor of the subcapsular sinus was simulated using COMSOL Multiphysics Software version 5.4. An idealized lymph node sinus was designed in SolidWorks, modeling the afferent vessel as a cylinder leading into a thin disk, which was used to model the subcapsular sinus (Figure 5.2B). Different dimensions for quiescent or remodeled lymph node afferent lymphatic vessel diameter (LVD) and subcapsular sinus height (SCS h) were used to construct three variations of the lymph node geometry (Figure 5.2B,3D), while the upper limit of the subcapsular sinus radius was maintained at 5 m, which was chosen based on the average size of a human lymph node, yielding a physiologically relevant slope of wall shear stress decrease.^{15,263,264} The geometry was exported as a .STL file and imported into COMSOL. Within COMSOL, the fluid material was defined as a Newtonian, incompressible fluid with a dynamic viscosity of 1200 Pa s and a density of 1009 kg m⁻³, which were chosen on literature cited values.²²⁰ The fluid flow was set to laminar flow with a constant volumetric flow rate of 1.45E-10 m³ s⁻¹, which is within the range of flow rates measured in humans.²⁶⁵ The boundary walls were chosen to be the outer surface of the liquid domain, the inlet was defined as the top of the afferent vessel cylinder, and the outlet was defined to be the circumferential side wall of the subcapsular sinus thin disc. Finally, the cut plane where the wall shear stress values were quantified was defined as the bottom of the thin disc, representing the floor of the lymph node subcapsular sinus.

The Particle Tracing for Fluid Flow module of COMSOL Multiphysics Software version 5.4 was used to simulate the trajectory of a cell as it moved from the afferent vessel into the subcapsular sinus and determine the point at which the cell had settled to the floor of the subcapsular sinus. The particle properties were modeled after that of a cancer cell, with a diameter of 14 μm and a mass density of 1032 kg m^{-3} .²²⁰ The same inlet, outlet, flow rate, fluid properties, and boundary walls as used in the wall shear stress modeling were used. For each simulation, a particle (modeling a cell) began its flow trajectory through the geometry at the top of the afferent vessel (height 2.5 mm) in a randomly selected radial position (less than or equal to one half the diameter of the afferent vessel), and the height and radial position of the particle was tracked until it reached the periphery of the subcapsular sinus. The particle was defined as settled on the subcapsular sinus floor when the center of the particle was at a height of 7 μm , the radius of the particle. For each lymph node condition (Figure 5.4D) five cell simulations were plotted.

5.2.3 Cell Culture

THP-1 monocytes were cultured every three days via 1:5 dilution in Roswell Park Memorial Institute 1650 supplemented with 10% FBS and 1% PSA. PANC-1 cells, graciously provided by Dr. Gregory Lesinski, were cultured in DMEM supplemented with 10% FBS, 1% PSA, and 1% Glutamax. Human colorectal adenocarcinoma LS174T cells and Phamret-expressing LS174T cells, stably transfected as described previously¹², were cultured in Dulbecco's Modified Eagle Medium (DMEM) supplemented with 10% heat inactivated fetal bovine serum (FBS) and 1% penicillin-streptomycin-amphotericin. LS174T cells and PANC-1 cells were harvested via mild trypsinization with 0.25% trypsin EDTA, centrifuged at 400 X G for 5 min, resuspended in culture medium, and either diluted

into tissue culture flasks for subculture or incubated in suspension for 2 h at 37°C to allow regeneration of adhesive cell surface ligands.

5.2.4 *Channel Fabrication*

Microfluidic channels were fabricated in a manner similar to that as detailed previously.^{12,26,182} Briefly, using a craft cutter, the adhesive microfluidic channel, which consisted of a straight 10 cm long by 0.2 cm wide section connected to a 4 cm long divergent section that increased in width from 0.2 cm to 1.2 cm, was cut from sheet of 125 μm thick double-sided adhesive tape backed with a release liner. The channel was then affixed to polydimethylsiloxane (PDMS), which was previously cured by mixing PDMS base with curing agent at a ratio of 9:1 and curing at 90°C for 3 h in a Pyrex dish prior to being cut to the outer dimensions of the channel shape. To complete fabrication, an inlet hole was punched into the beginning of the long, straight portion of the channel using a 3 mm biopsy punch, and platform was attached to a non-tissue culture treated polystyrene plates into which an outlet hole was drilled prior to assembly.

5.2.5 *Channel Functionalization*

The short, divergent portion of the channel nearest the outlet was functionalized through the following steps: incubating at 4°C overnight with Fc specific goat anti-human IgG in D-PBS without calcium and magnesium to a concentration of 2.5 $\mu\text{g mL}^{-1}$ for E-selectin experiments, 5 $\mu\text{g mL}^{-1}$ for E-selectin + 2.5 $\mu\text{g mL}^{-1}$ ICAM and E-selectin + 2.5 $\mu\text{g mL}^{-1}$ VCAM experiments, or 12.5 $\mu\text{g mL}^{-1}$ for E-selectin + 10 $\mu\text{g mL}^{-1}$ VCAM experiments; blocking for 1 h at room temperature with 1% Bovine serum albumin (BSA) in D-PBS with calcium and magnesium; incubating for 2 h at room temperature with 2.5

$\mu\text{g mL}^{-1}$ of recombinant human E-Selectin Fc chimera protein, plus the addition of $2.5 \mu\text{g mL}^{-1}$ of recombinant human ICAM-1/CD54 Fc chimera protein, $2.5 \mu\text{g mL}^{-1}$ of recombinant human VCAM-1/CD106 Fc chimera protein or $10 \mu\text{g mL}^{-1}$ of recombinant human VCAM-1/CD106 Fc chimera protein for some experiments, all of which were diluted in D-PBS with calcium and magnesium. Finally, the entire channel was blocked for 1 h at room temperature with 1% BSA in D-PBS with calcium and magnesium at room temperature. In between each step, the channel was washed three times with 1 mL of D-PBS with calcium and magnesium.

5.2.6 Perfusion Experiment Workflow

Perfusion experiments were performed in a similar manner to that formerly described.²⁶ Succinctly, an inlet syringe connected to tubing filled with perfusion media (0.1 % BSA in D-PBS with calcium and magnesium) was connected to a syringe pump and used to withdraw a cell pulse into the inlet tubing at a rate of 0.5 mL min^{-1} . For single cell perfusion experiments, the cell pulse was 200,000 THP-1 monocytes, PANC-1 cells, or LS174T cells diluted in $125 \mu\text{L}$ of perfusion media. The tubing and syringe assembly was inserted into the inlet hole of the channel and an outlet reservoir was made by connecting a 5 mL test tube to the bottom of the drilled outlet hole on the polystyrene plate. The assembled platform was placed on an Eclipse TI optical microscope with an objective magnification of 10X and linked to NIS-Elements software to acquire videos at a frame rate of 25 frames per second at an exposure time of $0.281 \mu\text{s}$ and 2x2 binning of 500 by 376 pixels.

To begin perfusion, the syringe pump was set to a constant flow rate, based on desired wall shear stress ranges of different lymph node models derived from COMSOL simulations, to initiate inflow into the channel from the syringe-tubing assembly. A flow rate of $34.7 \mu\text{L min}^{-1}$ was used to model a quiescent lymph node, a flow rate of $27.4 \mu\text{L min}^{-1}$ was used to model a lymph node with a dilated lymphatic vessel diameter, and a flow rate of $9.7 \mu\text{L min}^{-1}$ was used to model a lymph node with a dilated subcapsular sinus. Perfusion was continued until all cells, except those that firmly adhered to the functionalized portion of the channel, eluted from the device. Once the cells reached the divergent portion of the channel during perfusion, 30 sec videos were taken along the center of the channel at 0.5 cm increments to quantify the number of interacting cells and average rolling velocity of interacting cells at different wall shear stresses.

5.2.7 LS174T Cell and THP-1 Cell Co-perfusion Workflow

For co-perfusion experiments, a mixed cell pulse of 125 μL was made by adding 100,000 Phamret-expressing LS174T cells to either 33,333, 100,000, or 300,000 THP-1 monocytes immediately before perfusion to establish ratios of LS174T to THP-1 cells: 75:25; 50:50; 25:75, respectively. The Phamret LS174T only cell pulse contained 100,000 cells diluted in 125 μL of perfusion media. The perfusion workflow and quantification of adhesive cell behavior was the same as described above, however, in order to distinguish the Phamret-expressing LS174T cells from the THP-1 monocytes, the Phamret-expressing LS174T cells in the channel were imaged using a fluorescein isothiocyanate filter (excitation bandpass 475-492 nm, emission bandpass 505-535 nm) with a Chroma

Technology 100W PhotoFluor mercury lamp with same microscope settings as described above, save for an exposure time of 200 ms.

5.2.8 *Quantification of Adhesive Cell Behavior*

Cell adhesive behavior was characterized based on the number of interacting cells and the velocities of rolling adhesion of interacting cells in flow when perfused over an E-selectin +/- ICAM or VCAM functionalized substrate. An adhering cell was defined as one that was seen to exhibit horizontal translation at a velocity substantially slower than the non-interacting cells, which were cells that did not mediate specific adhesive contact with the substrate of the channel during observation and whose velocity magnitude is known based on calculated velocity profiles as well as cell velocities through unfunctionalized channels. The number of interacting cells at various wall shear stresses was quantified by counting the number of interacting cells in 30 sec videos taken at 0.5 cm increments along the divergent portion of the channel. Individual cell velocities were measured quantitatively using ImageJ with a manual particle tracking plugin. The location of maximum adhesion for each lymph node microfluidic model and functionalization scheme (Figure 5.8-5.10S) was defined as the distance in the divergent channel where the greatest number of interacting cells per 30 seconds was observed, calculated by finding the mean of five perfusion experiments for every mode at each channel location or wall shear stress.

5.2.9 *Quantification of Adhesive Cell Behavior*

For pairwise comparisons (Figures 5.5-5.12), every combination of two points at every wall shear stress or channel location where a measurement was taken was statistically analyzed using an unpaired t-tests, defining statistically significant differences as a $p <$

0.05, as noted by a *, #, or \$. When analyzing statistical differences among different lymph node conditions as a function of wall shear stress (Figures 5.8G-R,5.9G-R,5.10G-R), the nonlinear regression best fit line was compared between the overlapping wall shear stress range of healthy LN versus dilated LVD (0.62 – 0.16 dyn/cm²), healthy LN versus dilated SCS (0.28 – 0.16 dyn/cm²), and dilated LVD versus dilated SCS (0.28 – 0.11 dyn/cm²). Statistical significance was determined by the extra sum-of-squares F-test to determine if one curve adequately both sets of data with a $p < 0.05$, noted by †.

5.3 Results

5.3.1 *Lymphatic metastasis, lymph node invasion, and tissue remodelling*

Lymphatic metastasis is a multistep process (Figure 5.1A), which includes invasion of lymph-borne metastatic cells into lymph nodes through invasion through the subcapsular sinus, which results in formation of lymph node tumors seen in humans^{212,213,266} as well as metastatic mouse tumor models.^{267–270} Multiple structural features of lymph nodes influence flow paths and thus the movement of lymph-borne cells, including transition of fluid and cells from the lymphatic vessels into the lymph-filled sinus which in general moves flow orthogonally to lymph in flow (Figure 5.1B). This results in the radial distribution of lymph around the lymph node parenchyma.^{15,220} In the context of disease or inflammation, the structure of lymph nodes is altered,^{235–239} including dilation of both the lymphatic vessel^{23,271–273} as well as subcapsular sinus.^{14,274,275} There is less consensus on the effects of disease and inflammation on measured lymphatic flow rates and these effects are less widely reported, though both increases and decreases have been reported in the context of cancer, inflammation, and other diseases such as lymphedema or

obesity.^{133,220,276-278} Alterations in sinus-presented adhesion molecules have also been reported¹⁴⁸⁻¹⁵² and expression of adhesion receptors by lymphatic endothelial cells, which line the subcapsular sinus, is known to be altered by shear stress and exposure to other inflammatory mediators. Indeed, in mouse lymph nodes, remodeling induced by tumor growth in the downstream results in altered adhesion receptor expression relative to naïve animals (Figure 5.1C-D). The concerted effects of these biophysical (structural, flow) and biochemical (adhesion molecule expression) changes on cell adhesion within the context of lymph flow through the lymph node sinus has yet to be explored.

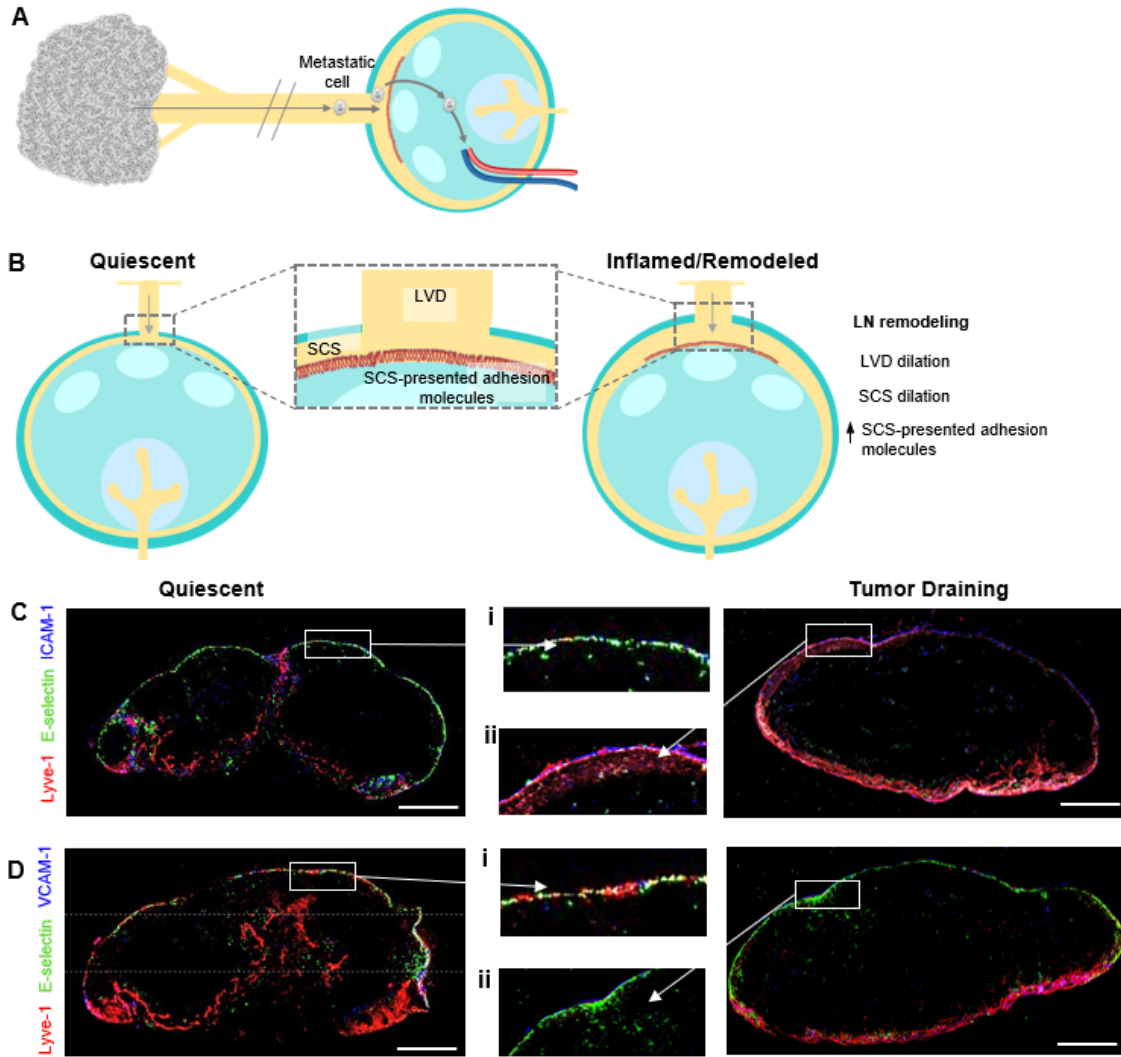


Figure 5.1. Cancer cells from primary tumors can harness the lymphatics, which remodel in states of inflammation, to form metastases. (A) Cancer cells can leave the site of a primary tumor, enter the lymphatic system, and gain access to the lymph nodes to form metastatic tumors. (B) In the presence of a tumor or in states of inflammation, lymph nodes remodel through dilation of the subcapsular sinus height, dilation of the lymphatic vessel diameter, and increased expression of adhesion molecules, such as intracellular adhesion molecule-1 and vascular cellular adhesion molecule-1 on the surface of sinus lining lymphatic endothelial cells. (C,D) Immunohistochemistry images of quiescent (left panel, i) or B16F10 tumor draining (right panel, ii) lymph nodes stained for lymphatic endothelial cells (Lyve-1, red), E-selectin (green), and either (C) ICAM-1 (blue) or (D) VCAM-1 (blue). (C,D) Scale bar is 400 μ m. LVD denotes lymphatic vessel diameter, SCS denotes subcapsular sinus.

5.3.2 *Altered shear stress profiles within remodeled lymph node sinuses*

In order to analyze the effects of lymph node biophysical remodeling (Figure 5.2A) on fluid flow profiles through the lymph node subcapsular sinus,^{14,257,279,280} lymphatic fluid flow that disperses radially after reaching a planar (e.g. Figure 5.2D, neglecting curvature) lymph node capsule was modeled (Figure 5.2B).^{14,257,279,280} First, the solution to this fluid velocity profile predicts a wall shear stress (WSS, τ in the equation below) profile that decays with radial position (Figure 5.2C, Equation 4).²⁸¹

$$\tau = \frac{3\mu Q}{\pi h^2 r} \quad (4)$$

The magnitude of shear stresses experienced by cells at the inferior sinus surface are thus highly sensitive to changes in sinus height (h) and volumetric flow rate (Q), though to a lesser extent. The magnitude of the peak WSS within the sinus region is also a function of lymphatic vessel diameter (LVD), with the peak value decreasing with increasing diameter. When considering these geometries of mouse and human lymph nodes (Table 5.1) but leaving Q fixed given its pulsatile nature as well as less well characterized magnitudes, a range of WSS values would be predicted to be experienced within the lymph node sinus region (Figure 5.2D-E).

Table 5.1. Human and lymph node parameter reference ranges.

<i>Reference parameters</i>	Human			Mouse		
	LVD (mm)	SCS h (μm)	Lymphatic transit rate (cm/min)	LVD (μm)	SCS h (μm)	Volumetric flow rate ($\mu\text{L/hr}$)
Quiescent	0.2 – 2 ¹ 1 – 2 ² 0.7 – 1.3 ³	40 – 80 ⁴	0.98 – 4.23 ⁵	50 – 80 ⁶ 90 ⁷	13.9 ⁸ 15 – 20 ⁹ 4.5 – 13 ¹⁰	0.3 – 4 ¹¹
Inflamed/ remodeled	1 – 2 ¹² 1 – 3 ¹³	80 – 120 ¹⁴	0.95 – 4.33 ⁵	120 – 300 ¹⁴	20 – 57 ¹⁶ 50 – 100 ¹⁷	

The effects of redistribution of fluid flow from the lymphatic vessel into the sinus on shear stress profiles were also modeled using COMSOL (Figure 5.2C, F-G). Importantly, the wall shear stress ranges calculated using the COMSOL simulations closely agreed with those derived from the analytical solution. In so doing, alterations in lymph node geometries were found to minimally influence the likelihood of cells being in contact with the inferior sinus floor upon entry into the lymph node sinus region (Figure 5.3). Supporting the suitability of our original assumptions, curvature of the lymph node sinus was also found to negligibly influence these WSS profiles at most geometric confirmations (data not shown).

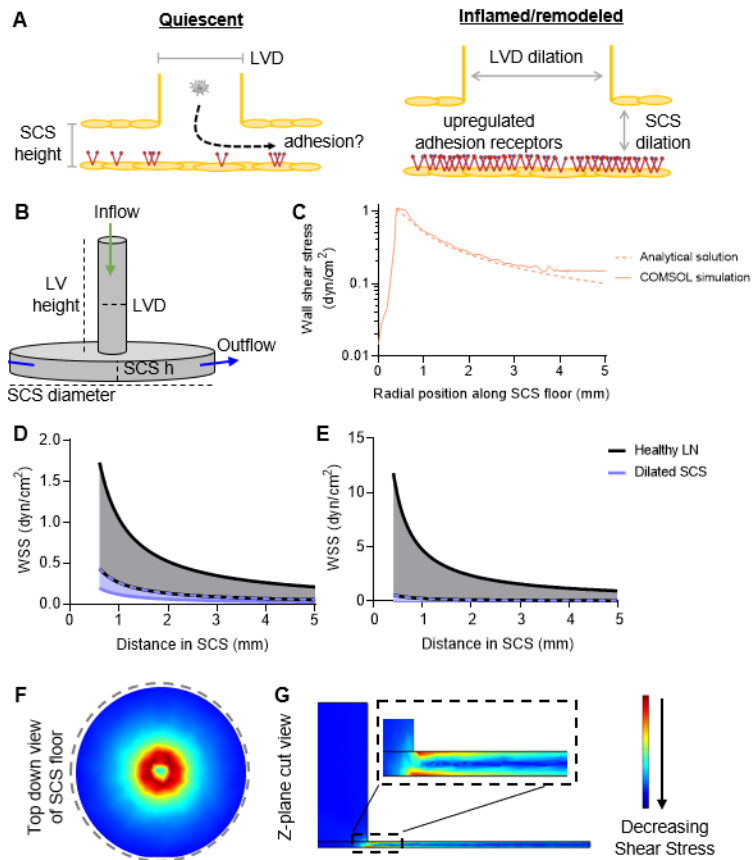


Figure 5.2. Modeling lymphatic fluid flow between quiescent and remodeled lymph nodes in COMSOL. To computationally model (A) the effect of lymphatic remodeling or inflammation on the ability of a circulating cell to adhere to the lymphatic endothelial cells lining the subcapsular sinus floor, we (B) made a simplified model of an afferent lymphatic vessel leading into the subcapsular sinus in SolidWorks and (C) imported it into COMSOL to perform fluid flow simulations to quantify the wall shear stress along the subcapsular sinus floor (solid line) and also calculated the analytical solution (dashed line). Given the variability in lymph node parameters in human and mice, (D,E) the range of resulting wall shear stresses was calculated using the analytical solution for (D) human or (E) mouse lymph nodes based on maximum and minimum literature cited parameters for subcapsular sinus height. Lymph viscosity was assumed to be $1.2\text{E-}3 \text{ Pa}\cdot\text{s}$, the volumetric flow rate was assumed to be (D) $1.45\text{E-}10 \text{ m}^3/\text{s}$ or (E) $8.33\text{E-}13 \text{ m}^3/\text{s}$, and the subcapsular sinus radius was assumed to be (D) 5 mm or (E) 500 μm . WSS denotes wall shear stress. SCS denotes subcapsular sinus. LVD denotes lymphatic vessel diameter. LV denotes lymphatic vessel. H denotes height. (F,G) COMSOL shear stress simulation plots along the (F) floor of the subcapsular sinus and (G) center of the z-plane in the idealized lymph node afferent vessel and subcapsular sinus model based on healthy human lymph node parameters.

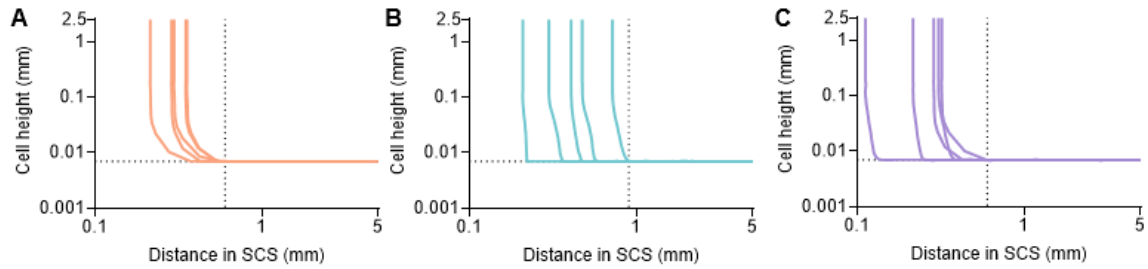


Figure 5.3. Cells entering the lymph node have settled to the floor of the subcapsular sinus by the time they leave the afferent vessel. (A-C) COMSOL cell trajectory simulations using human lymph node parameters showing the position of the center of a cell of diameter $14\ \mu\text{m}$ as it moves from the afferent lymphatic vessel into the subcapsular sinus. Each colored line represents the trajectory of a single cell with a randomized radial starting location at the top of the afferent vessel. Dashed line on y-axis at a height of $7\ \mu\text{m}$, indicating the cell has settled to the bottom of the subcapsular sinus floor. Dashed line on x-axis represent afferent vessel radius of (A,C) $0.6\ \text{mm}$ (healthy afferent vessel diameter) or (B) $0.9\ \text{mm}$ (dilated lymphatic vessel diameter).

5.3.3 Engineered lymph node “sinus-on-a-chip” adhesion microfluidic

We engineered a lymph node “sinus-on-a-chip” parallel plate adhesion flow chamber that can be configured to mimic the hydrodynamic microenvironment of a quiescent or remodeled lymph node, and specifically here the WSS experienced within the lymph node sinus (Figure 5.4A). The device, which is easy and rapid to fabricate, is constructed from a sheet of polydimethylsiloxane and a polystyrene tissue culture plate between which is a $125\ \mu\text{m}$ adhesive gasket. The microfluidic is connected to high speed videomicroscopy to permit the visualization and quantification of cell adhesion of an infused cell pulse along the length of the divergent portion of the channel (Figure 5.4A,E). The divergent portion of the microfluidic channel was also functionalized with adhesion receptors^{13,255,282,283} within the divergent channel portion to recapitulate their expression on the lymphatic endothelium-lined subcapsular sinus floor (Figure 5.4B). The channel was also designed with a $10\ \text{cm}$ long unfunctionalized straight portion (Figure 5.4C) sufficient in length to allow perfused cells to be uniformly in contact with the substrate,²⁸³ as the cells

entering the lymph nodes would be expected to be immediately settled to the subcapsular sinus floor upon arrival from the afferent vessel in all lymph node conditions based on our analyses (Figure 5.3). The simulated magnitude and rate of WSS dissipation predicted for quiescent or diseased human lymph nodes (Figure 5.4D,F)^{14,15,133,144,237,267,271,284–286} could be recapitulated within this perfusion system wherein a 4 cm long functionalized divergent portion that increases linearly in width from 0.2 cm to 1.2 cm (Figure 5.4C) by simply varying the volumetric flow rate of fluid perfusion through the system using the inline pump system. Specific conditions tested in the microfluidic system herein (Figure 5.4G) were chosen to recapitulate consensus parameters from the literature on human lymph nodes (Table 5.2).

Table 5.2. Perfusion conditions for divergent channel correlated to human lymph node conditions.

Microfluidic lymph node model	Perfusion flow rate (ml/min)	WSS range (dyn/cm ²)	Model LVD (μm)	Model SCS H (μm)
Healthy LN	0.03472	1 – 0.167	1.2	50
Dilated LVD	0.02153	0.62 – 0.11	1.2	100
Dilated SCS	0.00972	0.28 – 0.04	1.8	50

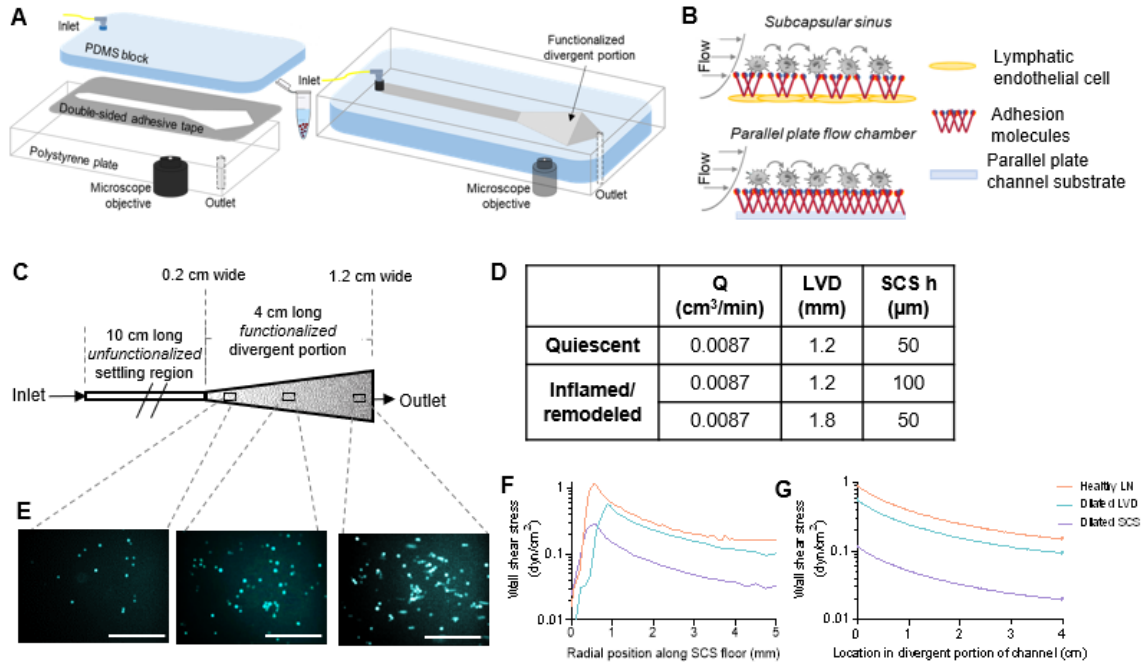


Figure 5.4. Engineered divergent adhesion chromatography system to interrogate lymphatic metastatic extravasation mechanisms *in vitro*. Motivated by the wall shear stress profile of COMSOL human lymph node models, (A) we designed a subcapsular sinus microenvironment-mimicking, divergent parallel-plate microfluidic. (B) To recapitulate the microenvironment of the lymph node subcapsular sinus and adhesion cascade of immune or cancer cells, the divergent portion of the channel is functionalized with adhesion molecules. (C) The channel is designed with an unfunctionalized settling portion settling portion connected to a functionalized, divergent portion with an increasing width, which was modeled after fluid flow through (D) quiescent and healthy human lymph nodes. Cell adhesion in the channel can be (E) visualized via integrated high speed videomicroscopy. The divergent shape of the channel was designed (F) based on COMSOL simulations of the wall shear stress profile of healthy and dilated human lymph nodes which very closely (G) recapitulates the decreasing wall shear stress profiles of the idealized human lymph node models. (E) Scale bar is 200 μm.

5.3.4 *Remodeling regulates cell adhesion in subcapsular sinus-mimicking flow fields*

The adhesive behavior of monocytes, which migrate to the lymph nodes via the afferent vessel and into the subcapsular sinus during states of inflammation and disease,^{287–289} as well as metastatic pancreatic and colon cancer cells in different lymph node sinus flow models was assessed in order to elucidate effects of lymph node remodeling on these behaviors.^{287,290–292} To this end, 200,000 THP-1 monocytic cells as well as PANC-1 and LS174T cells, which are commonly used cell lines used to investigate cell adhesive behavior^{255,282,283,293,294} with the latter two being commonly used metastatic cancer cell lines known to exhibit lymphatic metastasis in xenograft tumor models,^{295,296} were perfused at varying flow rates through the microfluidic system. These channels were functionalized within the divergent portion of the microfluidic device with various combinations of adhesion receptors. Specifically, four different functionalization schemes were used: 2.5 µg/mL E-selectin alone (1) or in combination with 2.5 µg/mL ICAM (2), 2.5 µg/mL VCAM (3), or 10 µg/mL VCAM (4). These molecules were chosen given their widely appreciated roles in mediating cell adhesion in fluid flow,^{11,47,153,226,297,298} expression by subcapsular sinus lining cells,²⁹⁹ and reported changes in expression in this anatomical location in response inflammation.^{226,300,301} Cell adhesion was then quantified within the perfusion system by counting the number of interacting cells and quantification of the average rolling velocity of the interacting cells at 0.5 cm increments along the center of the functionalized, divergent portion of the flow channel (left column, Figures S2-S4, 4-6). As each measurement location corresponds to a different wall shear stress acting on the cells (Table 5.3), comparisons between extent of adhesion and rolling velocity at similar and WSS level were also be made (middle and right columns, Figures 5.5-5.10).

Overall, whereas neither THP-1, PANC-1, nor LS174T cells mediated adhesion to ICAM or VCAM under flow, co-presentation of adhesion receptors with E-selectin increased cell adhesion in all tested conditions, though effects were channel location and/or shear stress dependent (Figures 5.5-5.7). This is unsurprising given E-selectin's well-established role in mediating fast rolling adhesion^{13,283} to enable slower adhesive interactions, such as those mediated by integrins.^{153,302,303}

Table 5.3. Wall shear stress ranges along the length of the divergent channel at different flow rates based on COMSOL simulations of human lymph node parameters.

Channel position (cm)	0	0.5	1	1.5	2	2.5	3	3.5	4
Microfluidic lymph node model	Wall Shear Stress (dyn/cm²)								
Healthy LN	1.000	0.545	0.437	0.305	0.278	0.212	0.205	0.184	0.167
Dilated LVD	0.620	0.338	0.244	0.189	0.157	0.132	0.115	0.112	0.110
Dilated SCS	0.280	0.153	0.110	0.085	0.071	0.060	0.052	0.046	0.040

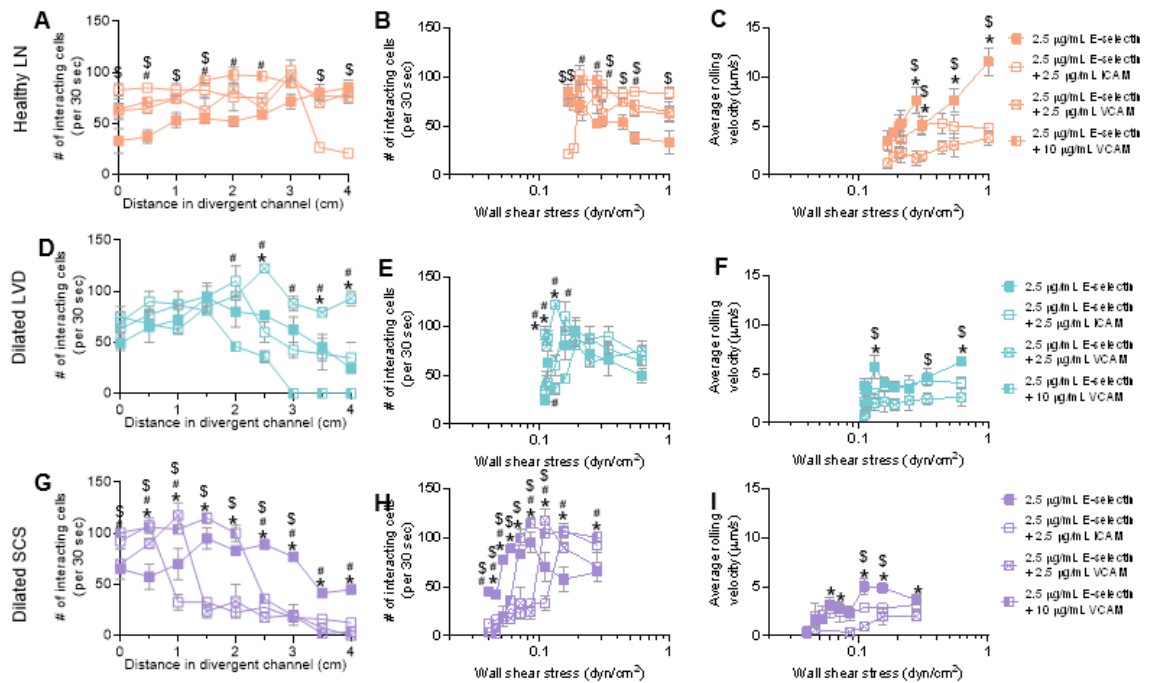


Figure 5.5. THP-1 adhesive behavior is altered with the addition of adhesion molecules. The (A,B,D,E,G,H) number of interacting cells and (C,F,I) average rolling velocity of interacting cells in a (A-C) healthy lymph node, (D-F) LN with a dilated lymphatic vessel diameter, or (G-I) lymph node with a dilated subcapsular sinus. (A-D) Statistical analysis by unpaired t-tests between points at each wall shear stress. $p < 0.05$ between: \$ E-selectin vs. E-selectin + 2.5 $\mu\text{g}/\text{mL}$ ICAM, * E-selectin vs. E-selectin + 2.5 $\mu\text{g}/\text{mL}$ VCAM, and # E-selectin vs. E-selectin + 2.5 $\mu\text{g}/\text{mL}$ ICAM. LN denotes lymph node, LVD denotes lymphatic vessel diameter, SCS denotes subcapsular sinus.

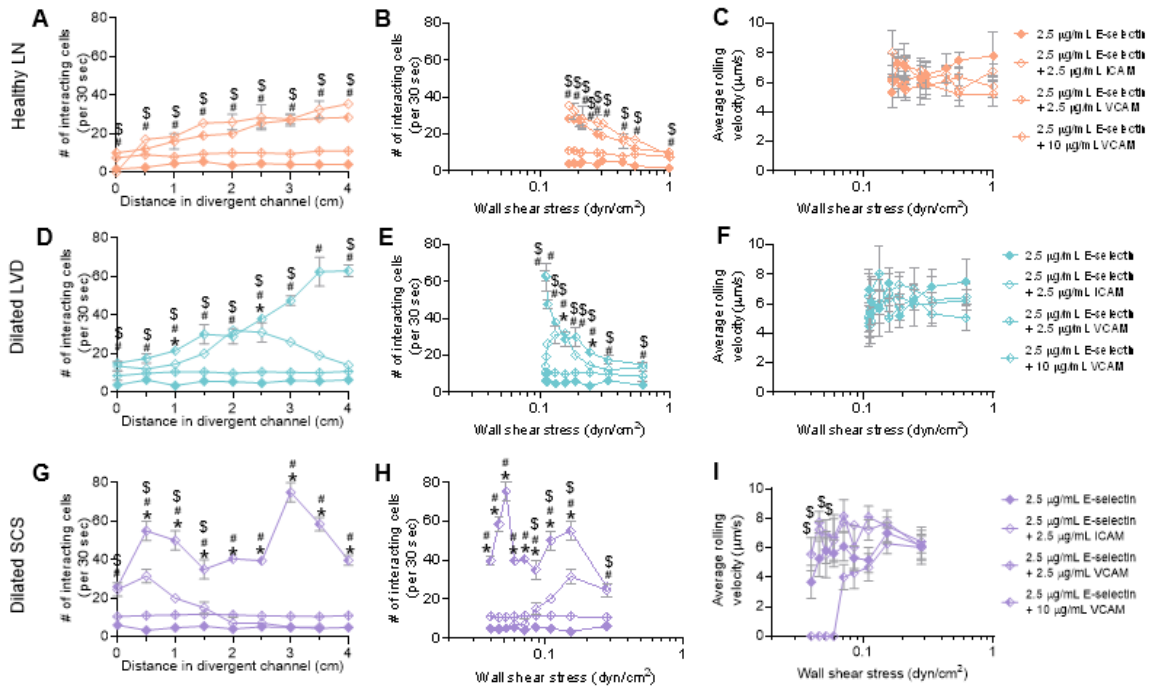


Figure 5.6. Copresentation of ICAM-1 and high VCAM-1 increase the adhesive behavior of pancreatic cancer cells. The (A,B,D,E,G,H) number of interacting cells and (C,F,I) average rolling velocity of interacting cells in a (A-C) healthy lymph node, (D-F) LN with a dilated lymphatic vessel diameter, or (G-I) lymph node with a dilated subcapsular sinus. (A-I) Statistical analysis by unpaired t-tests between points at each wall shear stress. $p < 0.05$ between: \$ E-selectin vs. E-selectin + 2.5 $\mu\text{g}/\text{mL}$ ICAM, * E-selectin vs. E-selectin + 2.5 $\mu\text{g}/\text{mL}$ VCAM, and # E-selectin vs. E-selectin + 2.5 $\mu\text{g}/\text{mL}$ ICAM. LN denotes lymph node, LVD denotes lymphatic vessel diameter, SCS denotes subcapsular sinus.

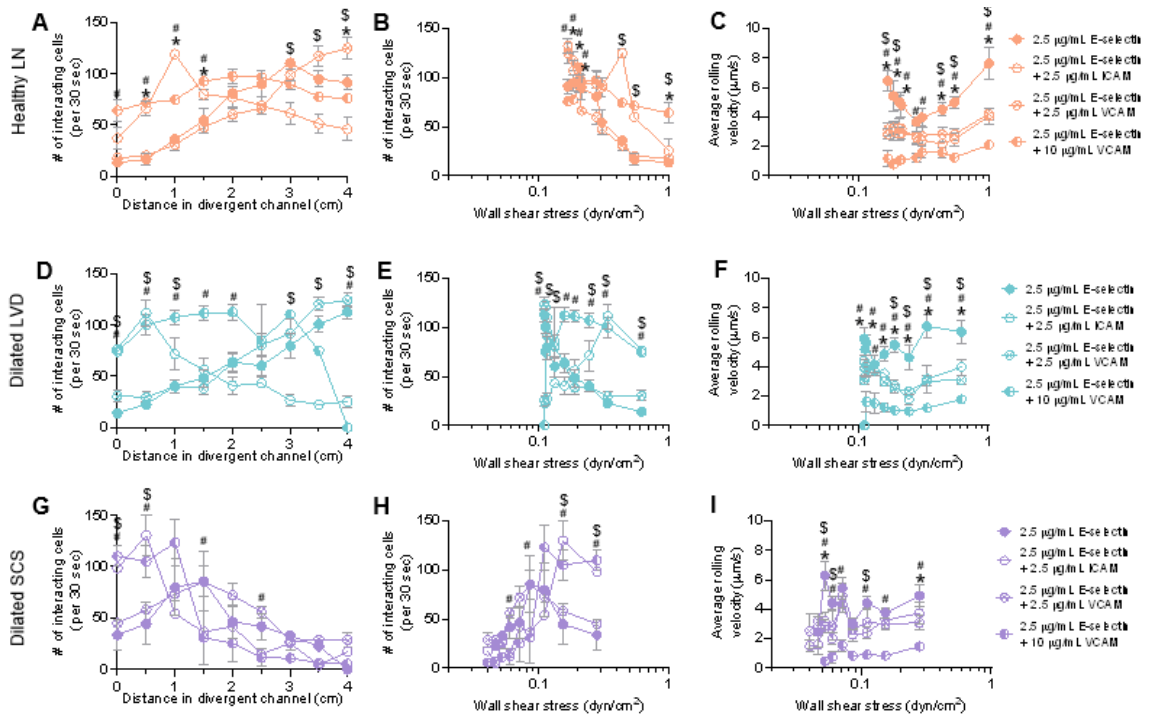


Figure 5.7. Enhanced expression of adhesion molecules increases the adhesivity of colon carcinoma cells. The (A,B,D,E,G,H) number of interacting cells and (C,F,I) average rolling velocity of interacting cells in a (A-C) healthy lymph node, (D-F) LN with a dilated lymphatic vessel diameter, or (G-I) lymph node with a dilated subcapsular sinus. (A-I) Statistical analysis by unpaired t-tests between points at each wall shear stress. $p < 0.05$ between: \$ E-selectin vs. E-selectin + 2.5 $\mu\text{g}/\text{mL}$ ICAM, * E-selectin vs. E-selectin + 2.5 $\mu\text{g}/\text{mL}$ VCAM, and # E-selectin vs. E-selectin + 2.5 $\mu\text{g}/\text{mL}$ ICAM. LN denotes lymph node, LVD denotes lymphatic vessel diameter, SCS denotes subcapsular sinus.

When considering the influence of hydrodynamic flow environment, perfusion parameters recapitulating lymph nodes with dilated afferent lymphatic vessels and subcapsular sinuses had the greatest effect on altering the adhesive behavior of perfused monocytes along the length of the divergent channel functionalized with E-selectin alone or in combination with ICAM or VCAM. Specifically, conditions mimicking a dilated lymph node sinus resulted in maximal THP-1 cell adhesion at lower WSS levels when co-perfused on E-selectin co-functionalized with ICAM or 2.5 ug/ml of VCAM (Figure 5.8G,I,K,L), corresponding to cells accumulating at locations earlier in the channel (Figure 5.8A,C,E,F). This would suggest that these WSS regimes may result in THP-1 cell arrest at locations within the lymph node subcapsular sinus that are more proximal to the afferent vessel (Figure 5.8S), perhaps a result from the low cell rolling velocities of adhesion at these WSS levels, which notably did not vary appreciably between perfusion condition (Figure 5.8M,O,P,R). Seemingly similar effects were seen for THP-1 adhesion on E-selectin alone or E-selectin co-functionalized with 10 ug/ml VCAM (Figure 5.8B,L). However, we note the nearly identical or highly similar profile of adhesion with respect to channel position (Figure 5.8A,F), implicating effects of time in flow/transit rather than WSS directly on THP-1 cells as influencing adhesion within these contexts.

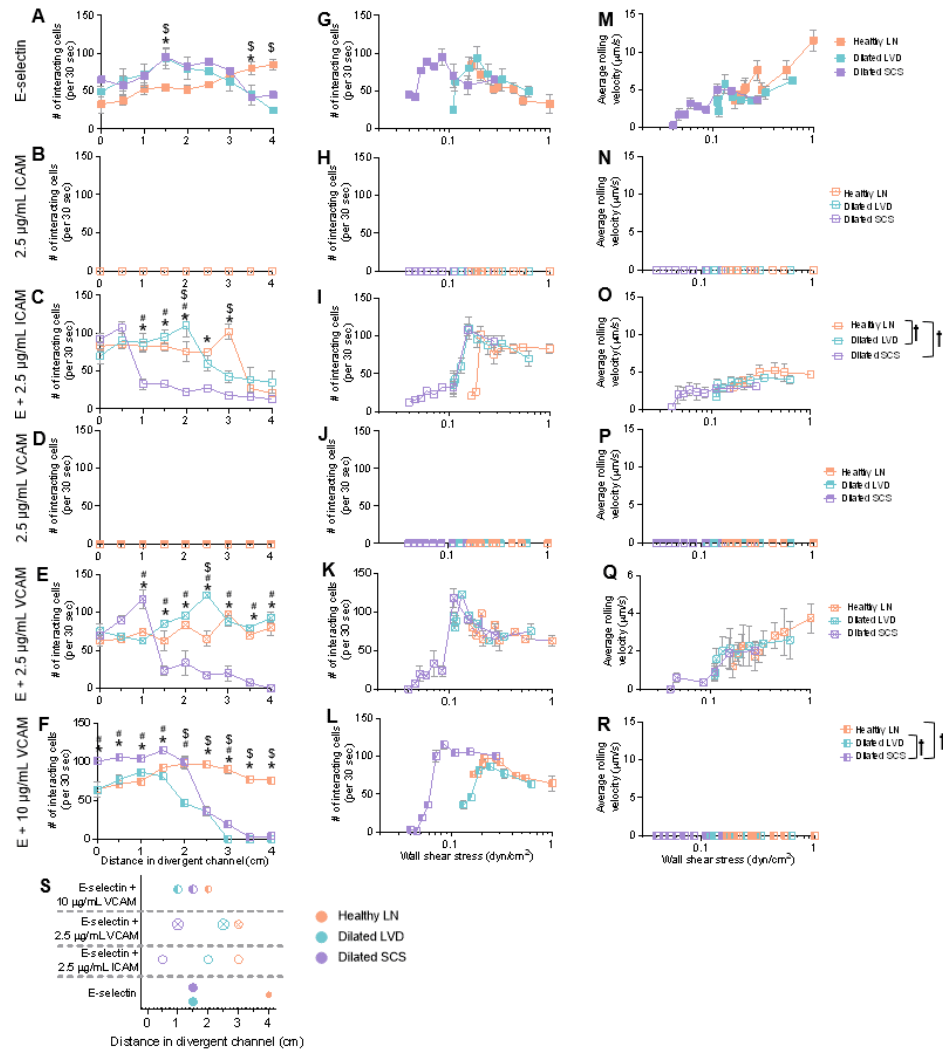


Figure 5.8. Dilation of the lymphatic vessel or the subcapsular sinus decreases the distance, but not magnitude, of maximum adhesion of monocytes in the subcapsular sinus. (A-L) The number of interacting and (M-R) the average rolling velocity of interacting THP-1 monocytes in divergent channels functionalized with (A,G,M) 2.5 µg/mL E-selectin, (B,H,N) 2.5 µg/mL ICAM, (C,I,O) 2.5 µg/mL E-selectin + 2.5 µg/mL ICAM, (D,J,P) 2.5 µg/mL VCAM, (E,K,Q) 2.5 µg/mL E-selectin + 2.5 µg/mL VCAM, or (F,L,R) 2.5 µg/mL E-selectin + 10 µg/mL VCAM. (A-F) Statistical significance by unpaired t-tests. $p < 0.05$ between: \$ healthy LN and dilated LVD, * healthy LN and dilated SCS, and # dilated LVD and dilated SCS. (G-L) Statistical significance by comparison of nonlinear regression of overlapping wall shear stress range comparing fit of number of interacting cells. † indicates $p < 0.05$. (S) Location of maximum adhesion in channel. Dot size scaled to number of interacting cells. LN denotes lymph node, LVD denotes lymphatic vessel diameter, SCS denotes subcapsular sinus. E denotes 2.5 µg/mL E-selectin.

Adhesion of PANC-1 pancreatic cancer cells, which have been shown *in vivo* to form metastatic tumors and also express numerous functional selectin, ICAM-1, and VCAM-1 ligands, including sLe^x, LFA-1, and VLA-4,^{304,305} was next explored. Like THP-1 cells, perfusion over surfaces functionalized with ICAM or VCAM alone resulted in no adhesion (Figure 5.9B,D,H,J,N,P). Notably, however, unlike THP-1 cells, PANC-1 cells also minimally adhered to E-selectin alone (Figure 5.9A,G) or E-selectin functionalized with low levels (2.5 ug/ml) of VCAM-1 (Figure 5E,K). Accordingly, minimal to no differences in the number of interacting cells (Figure 5.9A,E,G,K) and their average rolling velocities (Figure 5.9M,Q) were observed between hydrodynamic perfusion conditions using each functionalization scheme. Contrastingly, co-presentation of E-selectin with ICAM or E-selectin and higher levels (10 ug/ml) of VCAM substantially increased the number of interacting cells compared to the other functionalization schemes (Figure 5.6, 5.9C,F,I,L), while also decreasing the average rolling velocity (Figure 5.6, 5.9O,R). Furthermore, in channels co-functionalized with E-selectin and ICAM-1 or 10 ug/ml VCAM-1, the number of cells interacting in perfusion conditions modeling remodeled lymph nodes was significantly different than of quiescent lymph nodes, in both remodeled contexts as a function of channel position, though more significantly in channels co-functionalized with E-selectin and ICAM-1 or 10 ug/ml VCAM-1 in the context of a dilated afferent vessel (Figure 5.9C,F). However, overall extents of adhesion remained relatively unchanged as a function of WSS (Figure 5.9I,L) and average rolling velocities of the interacting cells were also sustained between differing hydrodynamic perfusion conditions (Figure 5.9O,R), save for at very low WSS. This suggests that PANC-1 cell adhesion is regulated most substantially or directly by both adhesion molecules presented within the

subcapsular sinus microenvironment as well as local WSS level, which serves to decrease the distance traveled into the channel before maximum adhesion is reached in dilated lymph nodes due to the low WSS levels (Figure 5.9S).

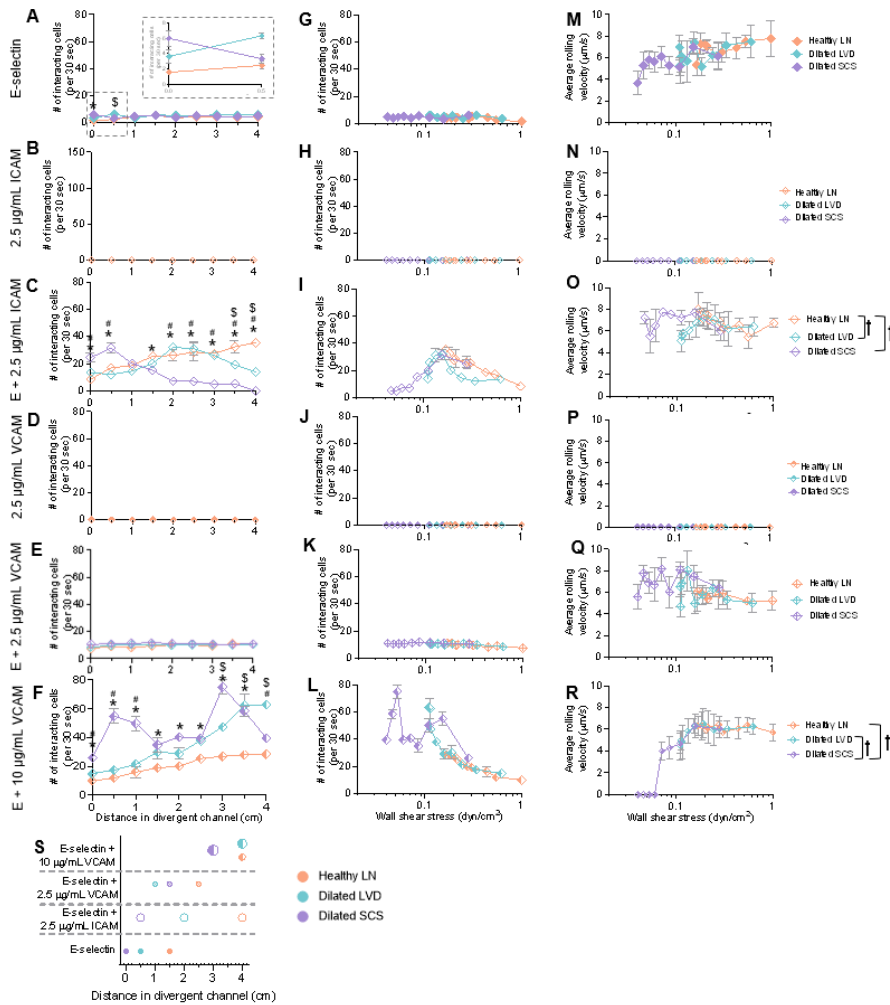


Figure 5.9. Lymphatic vessel or subcapsular sinus dilation decreases the distance in the subcapsular sinus that maximum adhesion of pancreatic cancer cells occurs while minimally altering the average rolling velocity trends. (A-L) The number of interacting and (M-R) the average rolling velocity of interacting PANC-1 cells in divergent channels functionalized with (A,G,M) 2.5 $\mu\text{g}/\text{mL}$ E-selectin, (B,H,N) 2.5 $\mu\text{g}/\text{mL}$ ICAM, (C,I,O) 2.5 $\mu\text{g}/\text{mL}$ E-selectin + 2.5 $\mu\text{g}/\text{mL}$ ICAM, (D,J,P) 2.5 $\mu\text{g}/\text{mL}$ VCAM, (E,K,Q) 2.5 $\mu\text{g}/\text{mL}$ E-selectin + 2.5 $\mu\text{g}/\text{mL}$ VCAM, or (F,L,R) 2.5 $\mu\text{g}/\text{mL}$ E-selectin + 10 $\mu\text{g}/\text{mL}$ VCAM. (A-F) Statistical significance by unpaired t-tests. $p < 0.05$ between: \$ healthy LN and dilated LVD, * healthy LN and dilated SCS, and # dilated LVD and dilated SCS. (G-L) Statistical significance by comparison of nonlinear regression of overlapping wall shear stress range comparing fit of number of interacting cells. † indicates $p < 0.05$. (S) Location of maximum adhesion in channel.

Adhesion by LS174T colon carcinoma cells, which are well studied for their adhesive properties within flow fields^{13,255,282,283} and express a variety of adhesion ligands for selectins^{80,252,306,307} and other CAMs³⁰⁸, were next evaluated.^{171,252,255,282,283,306,307} Though they adhered extensively to E-selectin (Figure 5.10A,G), LS174T cells exhibited no adhesion in flow to ICAM or VCAM alone (Figure 5.10B,D,H,J,N,P) like THP-1 and PANC-1 cells. As hypothesized, perfusion in flow experiment configurations simulating dilated lymphatic vessels and subcapsular sinuses appeared to substantially alter WSS-dependent profiles of cell adhesion (Figure 5.10A,C,E,F,G,C,K,L). However, though the extent of LS174T cell adhesion when perfused under hydrodynamic conditions mimicking quiescent and dilated afferent vessels interacted with E-selectin alone or when co-presented with VCAM varied significantly by WSS, no differences in channel position-dependent adhesion were seen (Figure 5.10A,E,F). Adhesion under conditions mimicking dilated subcapsular sinus hydrodynamic environments on the other hand did not exhibit similar channel position dependencies (Figure 5.10A,E,F). When perfused over E-selectin co-presented with ICAM, adhesion appeared highly WSS-dependent, with LS174T cell adhesion extents of dilated afferent vessel perfusion conditions closely matching trends seen in quiescent conditions. (Figure 5.10C). Perfusion under dilated sinus conditions however altered this WSS dependency (Figure 5.10I), though the channel position dependency closely matched that of dilated afferent vessel perfusion conditions (Figure 5.10C). With each functionalization scheme, measured velocities of interacting cells did not differ with respect to WSS irrespective of hydrodynamic perfusion condition (Figure 5.10M,O,Q,R). Overall, both time in flow and hydrodynamic condition, either due to the WSS level or the rate of WSS dissipation, appeared to interdependently regulate the extent

of LS174T cell adhesion whereas rolling velocity magnitude remained influenced by WSS only (Figure 5.10S).

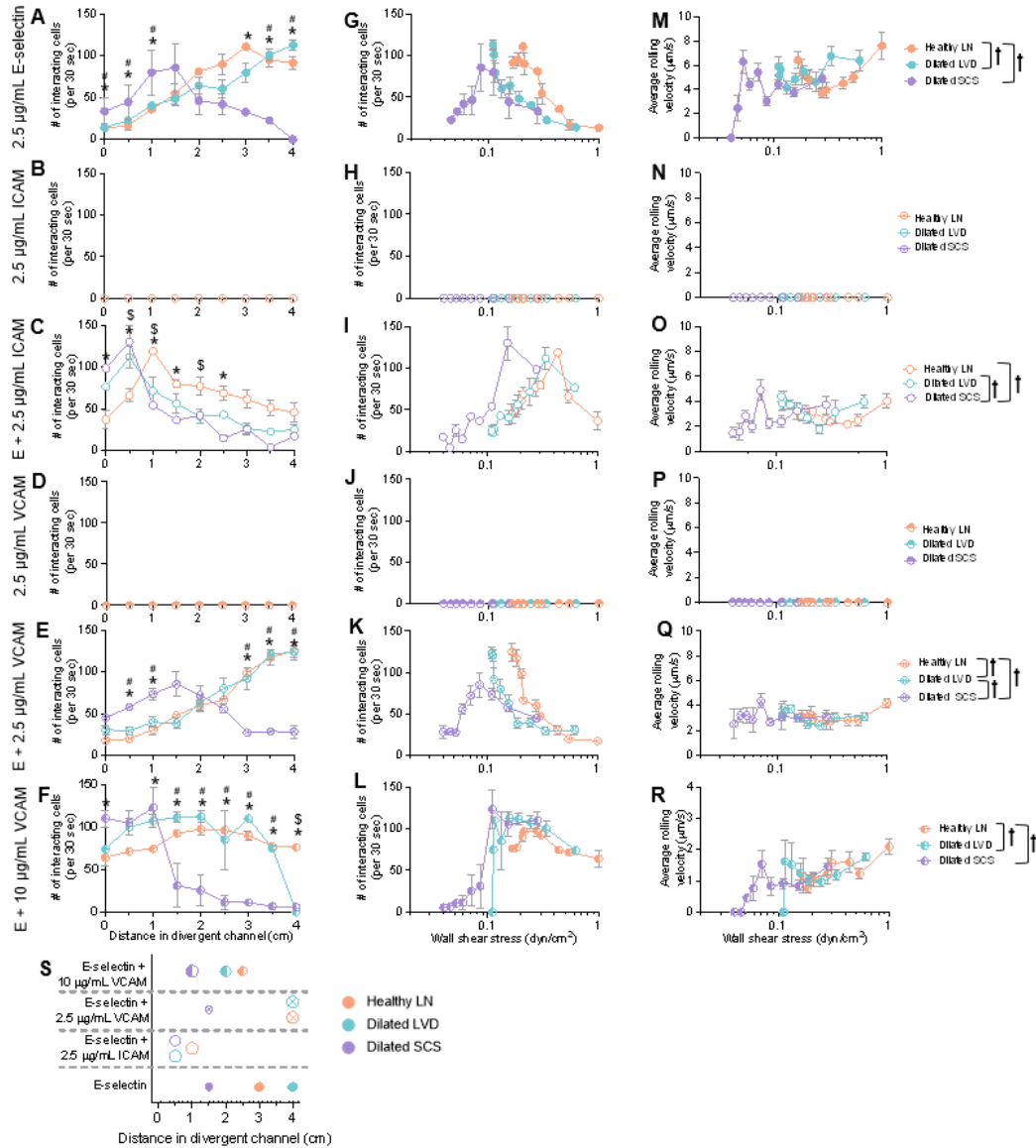


Figure 5.10. The location of maximum adhesion of colon carcinoma cells occurs earliest in lymph nodes with dilated subcapsular sinus. (A-L) The number of interacting and (M-R) the average rolling velocity of interacting PANC-1 cells in divergent channels functionalized with (A,G,M) 2.5 $\mu\text{g/mL}$ E-selectin, (B,H,N) 2.5 $\mu\text{g/mL}$ ICAM, (C,I,O) 2.5 $\mu\text{g/mL}$ E-selectin + 2.5 $\mu\text{g/mL}$ ICAM, (D,J,P) 2.5 $\mu\text{g/mL}$ VCAM, (E,K,Q) 2.5 $\mu\text{g/mL}$ E-selectin + 2.5 $\mu\text{g/mL}$ VCAM, or (F,L,R) 2.5 $\mu\text{g/mL}$ E-selectin + 10 $\mu\text{g/mL}$ VCAM. (A-F) Statistical significance by unpaired t-tests. $p < 0.05$ between: \$ healthy LN and dilated LVD, * healthy LN and dilated SCS, and # dilated LVD and dilated SCS. (G-L) Statistical significance by comparison of nonlinear regression of overlapping wall shear stress range comparing fit of number of interacting cells. † indicates $p < 0.05$. (S) Location of maximum adhesion in channel.

5.3.5 *Cell adhesivity increases when co-perfused with monocytes*

The effect of monocyte co-perfusion on LS174T cell adhesion to E-selectin in flow was assessed using a total of 100,000 LS174T cells diluted to different LS174T:THP-1 cell ratios: 3:1, 1:1, and 1:3. Co-perfusion increased both the number of interacting cells (Figure 5.11A-C) and decreased the average rolling velocity of interacting cells (Figure 5.11D-F). Notably, the WSS level at which adhesion peaked also decreased in the case of flow configurations mimicking quiescent and dilated lymphatic vessels (Figure 5.11A-B) but not dilated sinuses (Figure 5.11C).

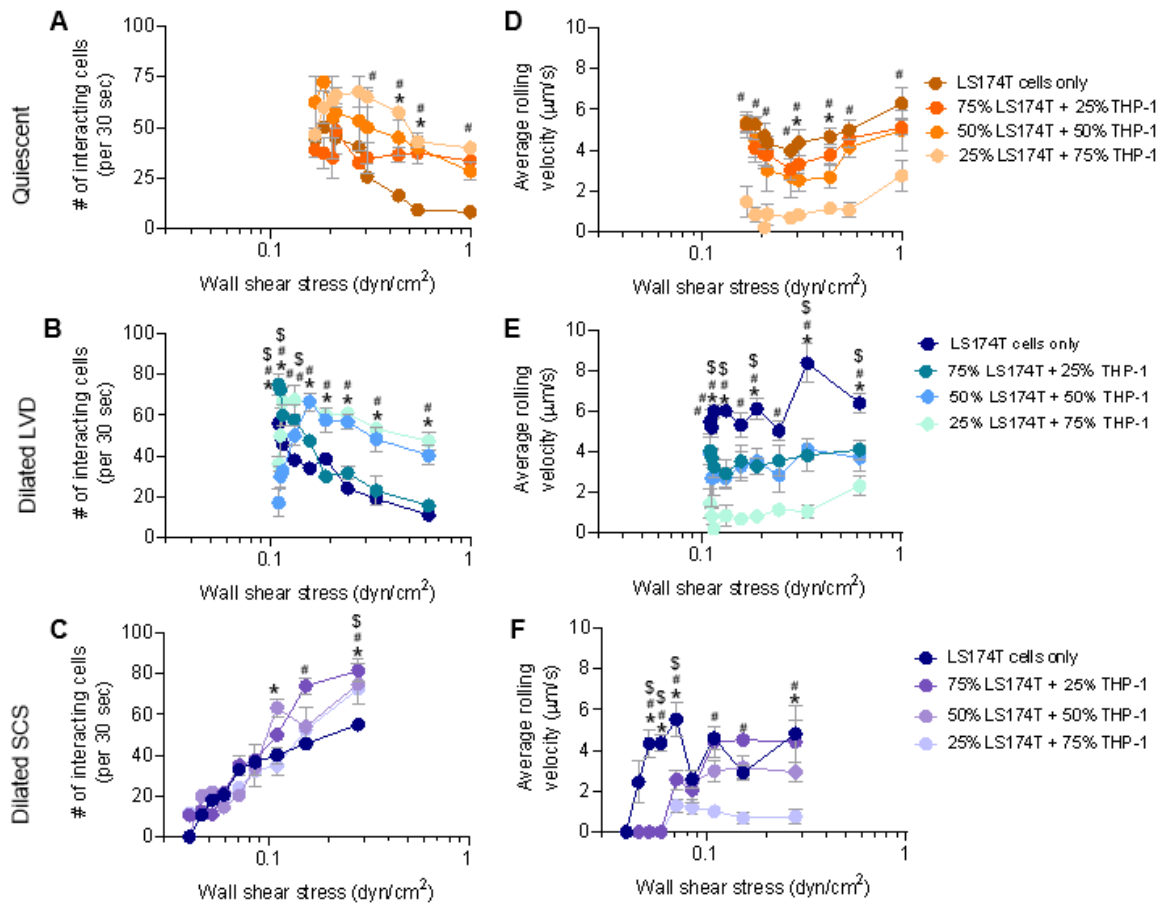


Figure 5.11. Adhesive propensity of metastatic colon carcinoma cells to E-selectin increases when co-perfused with monocytes in a manner proportional to the relative percent of monocytes. (A-C) The number of interacting LS174T cells and (E-G) the average rolling velocity of interacting LS174T cells perfused either alone or co-perfused with THP-1 monocytes at 25% THP-1: 75% LS174T, 50% THP-1: 50% LS174T, or 75% THP-1: 25% LS174T with wall shear stresses modeling a (A,D) healthy lymph node, (B,E) a dilated subcapsular sinus, or (C,F) a dilated subcapsular sinus. Channels were functionalized with 2.5 μg/mL E-selectin. (G-L) Statistical analysis by unpaired t-tests between points at each wall shear stress. $p < 0.05$ between: \$ LS174T cell pulse only vs. 25% LS174T cell pulse, * LS174T cell pulse only vs. 50% LS174T cell pulse, and # LS174T cell pulse only vs. 75% LS174T cell pulse.

When the effect of adhesive ligand co-presentation was next interrogated in the context of co-perfusion at LS174T to THP-1 ratios of 1:1, the overall extent of adhesion was uniformly equivalent, albeit extents peaked at different WSS levels in all cases, save few (Figure 5.12C, right column, 8D middle column). Specifically, changes in adhesion resulted from channel functionalization context, as monocytes increased the number of interacting cells in channels functionalized with E-selectin and ICAM-1 or moderate VCAM-1 (Figure 5.12A,C), but not high VCAM-1 (Figure 5.12E). Velocities of rolling adhesion were also on average lower for almost all tested conditions. Overall, our results revealed that co-perfusion with THP-1 cells generally enhances the adhesive propensity of LS174T cells, which substantiates previous research that has found monocytes to augment cancer cell adhesion and may provide a rationale for previous studies that have shown monocytes to increase extravasation and metastatic tumor formation in the lymph nodes *in vitro*.^{259,260}

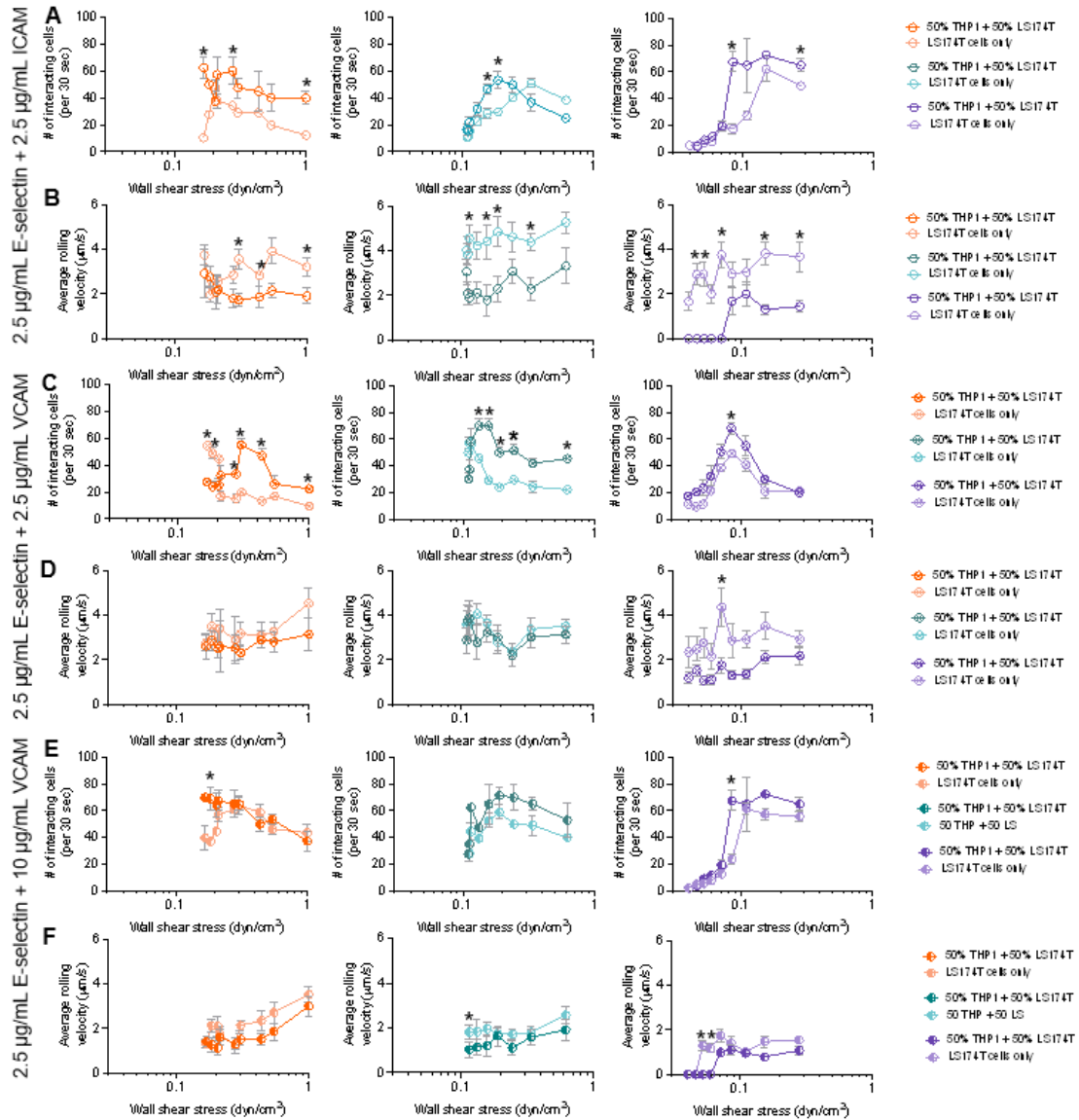


Figure 5.12. Colon carcinoma cells co-perfused with monocytes increases their adhesion behavior in lymph node models with enhanced adhesion molecule expression. The (A,C,E) number of interacting LS174T cells and (B,D,F) average rolling velocity of interacting LS174T cells perfused either alone or a cell pulse of 50% LS174T cells and 50% THP-1 monocytes with wall shear stresses modeling a healthy lymph node (orange), a dilated subcapsular sinus (blue), or a dilated subcapsular sinus (purple). Channels were functionalized with 2.5 µg/mL E-selectin + (A,B) 2.5 µg/mL ICAM-1, (C,D) 2.5 µg/mL VCAM-1, or (E,F) 10 µg/mL VCAM-1. (A-F) Perfusion of cell pulse of either 100,000 LS174T cells only or 100,000 LS174T cells + 100,000 THP-1 monocytes diluted in 125 µL of perfusion media. Statistical significance by unpaired t-tests. * indicates $p < 0.05$.

5.4 Discussion

Microfluidic-based flow systems have long been employed as *in vitro* models of the blood vasculature microenvironment to investigate biomechanical effects on the mechanisms of adhesion.^{255,282,283,309,310} This lymph node sinus microenvironment mimicking microfluidic platform thus enables *in vitro* analysis and comparison of cell adhesivity as it relates to lymphatic remodeling during inflammation or in the presence of a tumor to provide novel insights into the poorly understood but clinically significant process of lymphatic metastasis. Through the use of a divergent channel design, easily changeable perfusion flow rates, and varying channel functionalization schemes, this device was capable of mimicking quiescent lymph nodes, as well as lymph nodes that have remodeled in the presence of a tumor or inflammation through dilation of the lymphatic vessel diameter or subcapsular sinus and/or enhanced adhesion molecule expression. In so doing, videomicroscopy was used to permit the evaluation of the effects of lymphatic remodeling on the WSS-dependency and accumulation of adherent cells in physiologically relevant fluid flow. WSS magnitudes predicted by analytical solutions and COMSOL models were highly similar in magnitude to those seen within the venous circulatory system.^{35,276,299} We recognize that a limitation of our simulations and microfluidic model is that it fails to incorporate the pulsatile nature of lymphatic flow. However, given the dramatic increase in cross sectional area upon lymph entry into the lymph node, we expect flow pulsations to be minimal within the subcapsular sinus. Also, lymphatic flow rates are hypothesized to be substantially changed in disease contexts. However, given that the dependencies of WSS on sinus height are second order, we focused instead how small changes with respect to absolute sinus size could influence cell interactions within the

subcapsular space. However, given the direct proportionality and thus less sensitive dependency of WSS on lymph volumetric flow rate, results of this work could be interpreted to encompass volumetric flow rate changes in the absence of or with very small changes to subcapsular sinus dimension.

ICAM and VCAM have been implicated in metastasis by pancreatic and colon cancer cells in mice and humans. First, increased ICAM or VCAM expression correlates with enhanced colon adenocarcinoma cell adhesion to lymphatic endothelial cells *in vivo*.¹⁴⁹ Second, expression levels of ICAM and VCAM are correlated clinically with increased lymph node metastases in a variety of cancers.^{206,208,311} However, adhesion in flow by all tested cell types to ICAM and VCAM necessitated co-presentation with E-selectin, as would be expected given previous results studying cell adhesion in flow.^{301,312} This helps contribute understanding to the previous observations of E-selectin involvement in lymphatic metastasis in mouse models^{313–315} as well as the interdependency of metastasis on E-selectin expression and integrins.³¹⁶ The dependency on these adhesion molecules in the context of lymphatic metastasis has not been clearly delineated, but is supported by observations of direct correlation between the expression of these adhesion molecules and the incidence of lymph node metastasis.^{150,153} Our findings do however implicate the changes in expression of these molecules by lymphatic endothelial cells in response to altered flow states or inflammatory mediators as playing a physiological role in mediating cell infiltration into lymph nodes. In addition to facilitating immune cell homing in the context of immune response or inflammation, biochemical changes within the lymph node sinus may therefore contribute to or influence the pathway of metastatic dissemination by pancreatic and colon cancer cells. In a similar vein, adhesion by metastatic cells was

increased in a seemingly proportional manner by co-perfusion with monocytes. This is suggestive of inflammation influencing metastatic dissemination in another context. Indeed, our results indicate that co-perfusion results in activation of monocytes and cancer cells, suggesting in flow cross-talk. During co-perfusion experiments of monocytes and cancer cells, we noted the formation of large cell aggregates engaging in selectin-mediated adhesion, an observation unique to co-perfusion experiments and not seen in single cell population perfusion experiments. As such, we hypothesize that the increase in adhesion of the cancer cells may be due, at least in part, to facilitation of selectin-mediated rolling of non-adherent cancer cells by interacting monocytes, which act as an intermediary to slow down the cancer cells and initiate their adhesion, a process that has been seen by other groups.²⁶⁰ These observations also provide context as to why many groups propose single cancer cells are less efficient or unable to form metastases, as cell-cell interactions can significantly increase the adhesive and extravasation potential of metastatic cancer cells in the context of lymphatic metastasis.

The effects of lymphatic remodeling in the presence of a tumor or during inflammation may also have indirect effects on lymphocyte or cancer cell homing and extravasation in the lymph nodes by altering the tightly controlled chemotactic axis within the lymph node microenvironment which drives the regulated timing and location of lymph node infiltration.^{227,317,318} For example, CCR7 is a key chemokine receptor that directs the trafficking of lymphocytes crucial to the adaptive immune response, such as B and T cells, from the blood vessels and into the lymph nodes.³¹⁹ The ligands for CCR7 - CXCL19 and CXCL21 - are highly expressed in the inner cortex of the lymph nodes, thus promoting the migration of CCR7 expressing cells into deep portions of the lymph nodes.¹³⁵ Another

chemokine receptor, CXCR4, acts in a similar way to promote lymphocyte homing to the lymph nodes.³²⁰⁻³²³ however, our findings that biophysical and biochemical remodeling that occurs in the presence of a tumor or during states of inflammation significantly alters cell adhesion suggest that this may also influence cell homing in the context of chemotactic cues, thereby hindering the adaptive immune response. Notably, pancreatic cancer cells and colon adenocarcinoma cells also express CCR7 and CXCR4, and this expression level is directly correlated with increased lymph node metastases in patients.^{135,136,324} We hypothesize that these cancer cells may be able to harness and the CXCL19/CXCL21 gradient to continue migrating into the inner lymph node cortex after extravasating through the subcapsular sinus where they can form metastases. Furthermore, these CCR7 and/or CXCR4 expressing cancer cells may disrupt the sensitive chemokine gradient to impede chemotactic immune cell homing, prevent proper immune cell priming and maturation, and, thus, prevent an effective immune response. Concisely, given the defined chemotactic programs that drive lymphocyte and myeloid cell migration in lymph nodes from lymph, our results implicate the biophysical effects of lymph node remodeling and their influence on directing adhesion within the subcapsular sinus space as a potential axis that can regulate the mechanisms driving lymph node invasion.

5.5 Conclusion

In summary, we have developed a microfluidic system designed to recapitulate the dissipative WSS environment of the lymph node subcapsular sinus. Using this system and solutions to the WSS profile under different flow conditions, the effects of lymph node remodeling on cell adhesion were assessed. Our results indicate that biophysical changes including WSS magnitude, dissipation rate and cell transit time in flow as well as

biochemical changes such as adhesion receptor expression within the sinus lumen and the presence of lymph-borne cells synergistically contribute to the extent of adhesion that differs by cell type. Given the tight orchestration of chemotactic cues within lymph nodes to drive optimal adaptive immune responses, these findings implicate lymph node remodeling to regulate the location at which cells can optimally interact and/or within the subcapsular sinus and therefore potential mechanism of lymph node invasion.

CHAPTER 6. CONCLUDING REMARKS AND FUTURE DIRECTIONS

6.1 Conclusions

Cancer metastasis, both hematogenous and lymphatic, necessitates that circulating tumor cells extravasate through (lymphatic) endothelial cells lining the lumen of the blood vasculature or lymphatic system in a high shear microenvironment caused by dynamic fluid flow. This process is mediated, in part, by circulating tumor cells interacting with selectins presented by (lymphatic) endothelial cells in a highly orchestrated adhesion cascade, which acts to slow circulating tumor cells under hydrodynamic forces, permitting firm adhesion to the vessel wall or subcapsular sinus floor, extravasation, and the eventual formation of metastatic tumors in distant tissues or organs. Despite a basic biological understanding of selectin-mediated interactions, an outstanding problem in the field is defining and understanding the role of wall shear stress and cellular molecular profiles in initiating and sustaining selectin mediated adhesion, and the underlying causes of different abilities of disseminated tumor cells to engage in these interactions.³²⁵ Therefore, in this work, we sought to: (1) Develop an adhesion chromatography microfluidic that sorts cells based on their elution time from a selectin functionalized substrate of the flow channel to analyze attributes of cells with different adhesive phenotypes; (2) Uncouple short time- and length-scale velocity from long time- and length-scale average velocity by integrating a photoconversion system with a cell sorting adhesion chromatography platform; (3) Engineer a “lymph node sinus on-a-chip” cell adhesion microfluidic device to elucidate the effect of altered wall shear stress profiles of remodeled lymph nodes in response to tumors

in promoting immune cells and circulating tumor cell recruitment and enhancing lymphatic metastasis.

First, we engineered an integrated, parallel-plate microfluidic device to interrogate and fractionate cells based on their adhesivity to a substrate surface functionalized with adhesive ligands in a tightly controlled flow environment to elucidate associated cell-intrinsic pathways implicated in cellular adhesion. We modeled wall shear stress levels and endothelial presentation of E-selectin after the inflamed vasculature microenvironment in order to simulate *in vitro* conditions under which *in vivo* hematogenous metastasis occurs. Based on elution time from the flow channel, we collected separate fractions of cells – non-interacting and interacting – at high yields and viabilities, which enabled multiple post-perfusion analyses, including flow cytometry, *in vivo* metastasis modeling, and transcriptomic analysis. Therefore, this platform enabled the interrogation of flow-regulated cell molecular profiles, such as (co)expression levels of natively expressed selectin ligands sLe^x, CD44, and carcinoembryonic antigen, and cancer stem cell marker CD24. Additionally, this revealed that E-selectin adhesivity exhibited by metastatic human colon carcinoma cells is a transient phenotype. Facile and rapid, this methodology for unbiased, label free sorting of large populations of cells based on their adhesion in flow represents a method of studying flow-regulated adhesion *in vitro* for the identification of molecular drug targets to aid the development as anti-metastatic cancer therapeutics by enabling a system to elucidate cancer cell specific ligands that initiate slow rolling to selectins.

Second, we integrated a photoconversion cell sorting parallel-plate chromatography channel engineered in the first portion of this thesis, which enabled the measurement of

long and short time- and length-scale velocities of cells mediating adhesion in flow fields to study the mechanisms underlying adhesion to selectins by metastatic cancer cells. Through the facile enrichment of cells into subfractions of differing adhesive behaviors and a fluorescent velocity probe amenable to off-chip analysis, underlying, causal molecular profiles implicated in differing adhesive phenotypes of metastatic cancer cells were interrogated. This analytical method revealed selectin-mediated rolling adhesion was strongly associated with expression of selectin ligands, correlations that vary with ligand type and rolling velocity magnitude. Discrete selectin ligand expression profiles were also found to underlie persistent versus non-persistent adhesion on selectins, suggestive of divergent regulatory mechanisms. This integrated cell sorting and photoconversion microfluidic platform thus enabled *in vitro* analysis and comparisons of adhesive phenotypes as they relate to mechanisms of cancer cell metastasis in the context of selectin mediated adhesion, which revealed new insights into potential cancer dissemination pathways.

Finally, we engineered a lymph node “sinus-on-a-chip” adhesion microfluidic device that recapitulates the decreasing wall shear stress environment of the lymph node subcapsular sinus was engineered to interrogate the effects of wall shear stress magnitude and dissipation on human monocytic and metastatic cancer cell line adhesion. Wall shear stress levels within the microfluidic channel, which were quantified through COMSOL modeling of idealized human lymph nodes, recapitulated those of quiescent lymph nodes as well as lymph nodes that had remodeled both biophysically and biochemically due to inflammation or the presence of a tumor, which permitted the assessment of the effects of lymph node remodeling on cell adhesion. This analytical method revealed that structural

changes within the sinus and afferent lymphatic vessel alters the theoretical position at which cells can optimally interact with the floor of the subcapsular sinus, while biochemical changes through upregulation of adhesion molecules increases the overall extent of adhesion. Finally, the presence of immune cells with cancer cells further increases the adhesivity of colon carcinoma cells. implicate lymph node remodeling to regulate the location at which cells can optimally interact and/or within the subcapsular sinus and therefore potential mechanism of lymph node invasion. Concisely, this subcapsular sinus microenvironment mimicking microfluidic platform thus enables *in vitro* analysis of *in vitro* analysis and comparison of cell adhesivity as it relates to lymphatic remodeling during inflammation or in the presence of a tumor to provide novel insights into the poorly understood but clinically relevant process of lymphatic metastasis.

6.2 Contributions to the Field

Broadly, this project involves an integrated, multidisciplinary approach that combines microfluidic, biophysical, and biochemical techniques to provided fundamental insight into the basics of receptor-ligand biology and mechanisms of cancer metastasis, and in doing so, this work has contributed to numerous fields, including mechanical engineering, cancer biology, and immunology. The main contributions of this work to the scientific community is in the engineering of novel microfluidic platforms that can be used to elucidate pertinent biological problems, such as mechanisms of cancer metastasis. Although *in vivo* models may offer a more complex, physiologically relevant microenvironment to study metastatic extravasation, these platforms provide the unique capacity to probe the contributions of isolated molecules in cell adhesion in controlled microvasculature conditions. Individually, these novel systems, which have been made

available to others by publishing peer-reviewed journal articles and conference presentations, have impacted the field in the following ways.

6.2.1 Microfluidic to Interrogate Subsets of Cells with Different Average Adhesive Behavior

Chapter 3 of this work detailed the design of a cell-sorting adhesion chromatography microfluidic system that permits the collection of distinct fractions of cells based on their adhesion propensity to a functionalized substrate under hemodynamic flow mimicking microenvironments. The incorporation of a dynamic fluid flow environment to the cell-sorting microfluidic provides the unique ability to interrogate the effect of physiological shear force on the adhesive behavior of cells, something that other, static cell-sorting techniques such as bead systems or fluorescent activated cell sorting (FACS) are not capable of probing. Elucidating adhesion of cells in the context of fluid shear stress is valuable because shear stress has been implicated in promoting cancer cell adhesion during the extravasation process.^{231,326,327} For example low fluid shear stresses, such as those used here, stimulate the upregulation of mechanosensitive molecules that lead to downstream enhanced adhesion of cancer cells.³²⁸ Furthermore, collisions between adherent and free flow LS174T cells during perfusion cause the free flow cell to interact with the adherent cell leading to downstream rolling adhesion behavior of the initially free flow cell.^{255,329} Importantly, this behavior may not be observed with beads or using FACS due to the static microenvironment without the involvement of shear stress under which such sorting occurs.

Furthermore, currently, there are few methods to recover metastatic cancer cells and analyze their adhesive behavior in a high content manner. Distinctively, there are numerous advantages of this system over other methods of sorting and analysing large populations of cells (such as through the use of fluorescent-activated cell sorting). First, by incorporating high-speed videomicroscopy to the cell-sorting microfluidic, we are not only able to fractionate cells based on their average adhesive propensity, but we are also able to visualize and quantify the short time- and length-scale adhesion behavior of thousands of cells in a single experiment. Furthermore, the high-throughput nature of this system, coupled with high cell viabilities and recovery (over 80% and 90%, respectively), permits the enrichment of hundreds of thousands of cells in a single experiment, allowing facile post-perfusion analysis of the fractionated cell subsets. Notably, unlike interventional approaches that are used to study cancer cells, this system does not require a conjectural hypothesis of attributes intrinsic to adhesive propensity. Collectively, the features of this residence time-based, cell sorting adhesion microfluidic make it an ideal platform for studying biophysical and biomechanical mechanisms of long time- and length-scale cell adhesion, which can inform anti-metastatic cancer therapeutics and novel cancer cell biomarkers.

6.2.2 Integrated Microfluidic to Juxtapose Short and Long Time- and Length-Scale Adhesive Propensity

The first iteration of the cell sorting microfluidic platform describe in Chapter 3 was limited in that it quantified the average velocity of cells and permitted the collection of only two fractions of perfused cells – interacting and non-interacting. Outstandingly, however, there is also a need to interrogate not only at quantity of adhesion, but also quality

of adhesion, as metastatic cancer cells have been shown to exhibit a reduced adhesion persistence to certain cell adhesion molecules.^{13,171} Furthermore, with respect to quantity of adhesion, there is a wide distribution of average rolling velocities exhibited by metastatic cancer cells, therefore necessitating a means of sorting cells based on long time- and length-scale adhesion with greater resolution. As such, in the fourth chapter of this work, we integrated photoconversion technology, which permits the labelling of single cells based on their short time- and length-scale adhesion, with the cell sorting platform, and increased the resolution of fractionation by collecting up to three interacting cell populations. In doing so, for the first time, we were able to simultaneously quantify and compare short and long time- and length-scale adhesion of metastatic cancer cells to interrogate previous reports of reduced adhesion persistence and discern cellular molecular phenotypes that underlie persistent versus non-persistent behavior of metastatic cancer cell subsets. Succinctly, this platform improves upon former methods of interrogating metastatic cancer cell adhesion by enabling assessment of quality and quantity of adhesive behavior, and the use of such a platform can be used to identify distinguishing surface markers on highly adhesive and persistent phenotypes of cancer cells, which can be used to inform therapeutic targets that prevent extravasation of cancer cells without disrupting normal immune cell homing, or as a high-throughput method of analyzing the effect of adhesive-ligand targeting drugs or ligand knock-out on altering the rolling velocity and persistence of cells.

6.2.3 Lymph node “sinus-on-a-chip” to Elucidate Mechanisms of Lymphatic Metastasis

Chapter 5 of this work described the process of designing and implementing a lymph node “sinus-on-a-chip” microfluidic device that was incorporated with high speed videomicroscopy to visualize, quantify, and compare the adhesive behavior of monocytes

and two different metastatic cancer cell lines in models of healthy and dilated lymph nodes. While there are numerous parallel plate microfluidic devices to study the role of selectin mediated adhesion in hematogenous metastasis, similar systems to study the role of selectin mediated adhesion in lymphatic metastasis are currently lacking, despite the prominent role the lymphatics play in cancer metastasis.^{12,13,26,27,145,171} Using COMSOL to mimic lymphatic fluid flow from the afferent lymphatic vessel to the subcapsular sinus, the pathway many circulating tumor cells employ to invade the lymph node, we engineered a divergent channel design to model the wall shear stress profile that a cell infiltrating the lymph node from the afferent vessel into the subcapsular sinus would experience. Importantly, we simulated not only the conditions of a healthy lymph node, but also the conditions of a dilated subcapsular sinus and dilated afferent vessel, as well as adhesion molecule upregulation through the addition of ICAM-1 or VCAM-1, as remodelling of the lymph node often occurs in the presence of a tumor.

Unlike platforms to study metastasis through the circulatory system, this device has a decreasing wall shear stress that recapitulates the unique fluid flow profile within the lymphatic system, thereby allowing the interrogation of the effects of a decreasing wall shear stress on the adhesion mechanics and biophysical mechanisms of cells, an analysis that is not possible with current adhesion chromatography systems that mimic the microenvironment of hematogenous metastasis. Concisely, the novelty of our lymph node “sinus-on-a-chip” is that it enables, for the first time, the role of selectin-selectin ligand interactions of monocytes, cancer cells, and mixed monocyte-cancer cell populations in lymphatic extravasation to be interrogated under a variety of physiologically relevant wall shear stress and dilation conditions, which can be used to better understand the critically

under researched process of metastatic extravasation through the lymphatics, and the role of lymphatic remodelling in altering extravasation within the lymph nodes.

6.3 Future Directions

The work completed in this thesis provides new microfluidic platforms to study cancer metastasis, and these platforms will serve as the foundation for future directions of the work presented here, which should broadly focus on: (1) Verifying and optimizing microfluidic channel fabrication and functionalization, (2) increasing the breadth of cancer cell lines and adhesion molecules studied, and/or (3) implementing more complex design features into the microfluidic device to increase the accuracy of the recapitulated microenvironment under which cancer metastasis occurs.

Relevant to all work completed in this thesis, a future project should compare the coating density of surface molecules (IgG, E-selectin, ICAM-1, VCAM-1, etc.) to the actual surface density of the molecules (ie. the adsorption and functionalization density of such molecules on the substrate of the microfluidic channels). Although we have quantified the coating density of the microfluidic channels and experimentally shown that no surface molecules are shed during perfusion experiments, we have yet to quantify or estimate what the actual surface density of functionalization molecules is along the substrate of the microfluidic channel. By estimating the surface density based on the functionalization molecules affinity for the substrate/molecule with which they are adsorbed/attached to, such as the affinity of IgG Fc specific to polystyrene or the affinity of recombinant E-Selectin Fc chimera protein to IgG Fc specific, we can verify that our surface coatings are

comparable to physiological values and better compare experiments among different days or surface coating techniques.

More specifically, each aim of the thesis can be expanded with the following work:

6.3.1 Interrogating the Surface Molecule Profile of Subsets of Cells with Different Long Time- and Length-Scale Adhesive Propensities to Selectins

To date, the scope of the cell sorting microfluidic designed in this thesis focused on fractionating LS174T colon carcinoma cells over E-selectin. Notably, P- and L-selectin are also implicated in rolling adhesion during the hematogenous metastatic adhesion cascade, and therefore, a natural extension of the work presented here would include fractionating metastatic cancer cells over P- and L- selectin and comparing the cellular molecular profiles of collected interacting versus non-interacting cell subsets to elucidate cell ligands that underlie differing adhesion propensity to P- and L-selectin. This is particularly relevant when thinking about one of the objectives of the Thomas lab – to identify novel biomarkers that can be targeted for anti-cancer metastasis therapeutics – as E-, P-, and L-selectin are all known to engage selectin ligands present on the surface of metastatic cancer cells, which have the potential to be unique targets that prevent metastatic extravasation without disrupting leukocytic homing.^{24,74,185}

Furthermore, in addition to interrogating functionalization with other selectins, the microfluidic should be used to interrogate the adhesive propensities of different populations of cell lines, including cells derived from primary human tumors, and to identify distinguishing cell surface markers between the interacting and non-interacting cell subsets of these populations of cancer cells. This would permit a more thorough

understanding of the biomechanical underpinnings and cellular surface marker characteristics of long time- and length-scale selectin-mediated adhesion outside the context of LS174T cells and probe the extent of patient to patient adhesion and phenotypic variability among tumor cells. Importantly, knowledge derived from these studies could be used to identify selectin ligands that may be universally present on a variety of metastatic cancer cells, which could inform targetable markers for a widely applicable cancer therapeutic.^{24,185,330}

6.3.2 Studying the Effects of Selective Selectin Ligand Inhibition and Qualifying Cancer Stem Cell Markers

In chapter four, we presented the success of the using the integrated cell-sorting, photoconversion microfluidic platform to analyze, simultaneously, the mechanisms underlying short and long time- and length-scale adhesion and quantify the persistence of metastatic LS174T colon carcinoma cells over P-, E-, and L-selectin, particularly as it changes in response to enzymatic degradation of selectin ligands on metastatic cancer cells. As such, future work should leverage this platform to explore the effects of selective selectin-ligand inhibition on altering metastatic cancer cell adhesion and persistence. Using information gained from future work of the cell-sorting platform (as described above), which should identify additional tumor cell expressed selectin ligands implicated in adhesion across a variety of cancers and patient samples, cell populations that have the inhibition of relevant selectin ligands can be perfused through the integrated system to analyze the effectiveness of such inhibition in reducing adhesion or altering persistence. The ease of fabricating the channels, coupled with the short perfusion experiment times and wide-ranging options of post-perfusion analysis, an extensive combination of cell

populations, ligand inhibitions, and channel functionalizations can be interrogated in a high-throughput manner, permitting rapid testing of potential therapeutics, while also allowing a deeper understanding of the mechanisms by which known metabolic inhibitors that prevent metastasis work.^{81,331–333}

Moreover, the expression levels of CSC marker CD24, and coexpression levels of CD24 with other known selectin ligands, has been correlated with short and long time- and length-scale adhesion individually, but the juxtaposition of CSC marker expression as it relates to both velocity and adhesion propensity has yet to be interrogated.^{12,26} These experiments can be completed using the cell sorting, photoconversion platform, and would help complete CSC studies already completed in our lab. Additionally, given the general ambiguity in the field of cancer biology regarding common CSC markers between different cancers, the use of the platform should be extended to analyze how the expression levels of a variety of literature cited CSC markers in different metastatic cancer cell lines and patient derived tumor cells changes with regard to different adhesion propensities and persistences of collected cell fractions and/or photoconverted subsets. Together, the ideas outlined above would serve to further understand the functional effects of selectin ligands on adhesion behavior and persistence as it relates to cancer metastasis and inform a better understanding of CSC markers.

6.3.3 Enhancing the Design of the Lymph Node “Sinus-on-a-Chip” to Better Recapitulate the Lymphatic Metastasis Microenvironment

For the first time, we engineered an innovative microfluidic system to quantify the selectin-mediated adhesive behavior of cells in a physiologically relevant lymphatic

microenvironment. While this system has provided novel insight into the basic mechanisms of immune cell and circulating tumor cell extravasation through the lymphatics, it is limited in that it provides a simplistic model of the afferent lymphatic vessel and subcapsular sinus. The first iteration of the device served well to isolate only a few variables in the complex adhesion cascade, nonetheless, adding further structural details to the system will enable a deeper understanding of the biophysical and biomechanical effects of the lymphatic microenvironment and lymphatic remodeling on the ability of circulating tumor cells and immune cells to traffic and home to the lymph node. Therefore, future design iterations should be made that incorporate more structural features of the lymph node. For example, the subcapsular sinus has an array of vertical micropillars that are positioned in 6 – 20 μm intervals, dividing the space within the subcapsular sinus into smaller compartments.^{14,334} Undoubtedly, these pillars may effect fluid flow through the subcapsular sinus, and therefore could be added to the lymph node “sinus-on-a-chip” to better understand the dynamics of cell movement through the subcapsular sinus. As another example, the pulsating flow through the afferent lymphatic vessel could be modeled, as the constantly varying fluid flow may affect the presentation of selectin ligands on the surface of circulating tumor cells, as fluctuating shear forces have been observed to increase the expression of cell adhesion molecules during other physiological processes.^{297,335–340}

Additionally, thus far, due to experimental setup limitations, we have modeled the wall shear stress profile of three lymph node conditions: (1) a healthy lymph node, (2) a dilated subcapsular sinus, and (3) a dilated afferent vessel diameter. These models have provided a noteworthy first look into the effects of remodeling on cell adhesion, however, due to the prevalence of co-occurring dilation of the subcapsular sinus and afferent

lymphatic vessel, a system that is capable of modeling this scenario should be fabricated and the adhesion of metastatic and/or immune cells in the model quantified.^{137,146,239} Finally, as with future work for the other aspects of this thesis, the lymph node “sinus-on-a-chip” should be used to elucidate the adhesive behavior of different cancer cell populations, patient derived tumor cells, and other immune cells (such as B-cells or tumor associated macrophages). Specifically, studying the different adhesion mechanisms between cancers that have a tendency to metastasize to the lymph nodes versus those that do not frequently form metastatic tumors may inform differences in cell adhesive behavior that underlies the propensity of some cells to extravasate through the lymphatics, for example MDA-MB-468 cells versus 468LN cells.³⁴¹ Finally, additional co-perfusion experiments with cancer cells and monocytes should be performed to determine if monocyte augmentation of adhesion is consistent among different cancers. Collectively, extending the application of the lymph node “sinus-on-a-chip” to interrogate other cell lines and adding more lymphatic conditions to the design will serve to further bridge two main aspects of the Thomas lab – elucidating the role of the lymphatic system in cancer metastasis and understanding the biophysical and biomechanical underpinnings of cell adhesion – which may inform novel, lymph node targeting, anti-cancer metastasis therapeutics.

REFERENCES

1. Weigelt, B., Peterse, J. L. & van 't Veer, L. J. Breast cancer metastasis: markers and models. *Nat. Rev. Cancer* **5**, 591–602 (2005).
2. Lambert, A. W., Pattabiraman, D. R. & Weinberg, R. A. Emerging biological principles of metastasis. *Cell* **168**, 670–691 (2017).
3. Bendas, G. & Borsig, L. Cancer cell adhesion and metastasis: selectins, integrins, and the inhibitory potential of heparins. *Int J Cell Biol* **2012**, 676731 (2012).
4. Oh, E.-S., Seiki, M., Gotte, M. & Chung, J. Cell Adhesion in Cancer. *Int J Cell Biol* **2012**, (2012).
5. Okegawa, T., Pong, R. C., Li, Y. & Hsieh, J. T. The role of cell adhesion molecule in cancer progression and its application in cancer therapy. *Acta Biochim. Pol.* **51**, 445–457 (2004).
6. Steeg, P. S. Metastasis suppressors alter the signal transduction of cancer cells. *Nature Reviews Cancer* **3**, 55–63 (2003).
7. Hunter, K. W., Crawford, N. P. & Alsarraj, J. Mechanisms of metastasis. *Breast Cancer Research* **10**, S2 (2008).
8. Lote, H. *et al.* Carbon dating cancer: defining the chronology of metastatic progression in colorectal cancer. *Annals of Oncology* **28**, 1243–1249 (2017).

9. Thomas, S. N., Schnaar, R. L. & Konstantopoulos, K. Podocalyxin-like protein is an E-/L-selectin ligand on colon carcinoma cells: comparative biochemical properties of selectin ligands in host and tumor cells. *American Journal of Physiology-Cell Physiology* **296**, C505–C513 (2009).
10. Konstantopoulos, K. & Thomas, S. N. Cancer Cells in Transit: The Vascular Interactions of Tumor Cells. *Annual Review of Biomedical Engineering* **11**, 177–202 (2009).
11. Edwards, E. E. *et al.* P-, but not E- or L-, selectin-mediated rolling adhesion persistence in hemodynamic flow diverges between metastatic and leukocytic cells. *Oncotarget* **8**, 83585–83601 (2017).
12. Edwards, E. E., Birmingham, K. G., O’Melia, M. J., Oh, J. & Thomas, S. N. Fluorometric Quantification of Single-Cell Velocities to Investigate Cancer Metastasis. *Cell systems* **7**, 496-509.e6 (2018).
13. Oh, J., Edwards, E. E., McClatchey, P. M. & Thomas, S. N. Analytical cell adhesion chromatography reveals impaired persistence of metastatic cell rolling adhesion to P-selectin. *J. Cell Sci.* **128**, 3731–3743 (2015).
14. Das, S. *et al.* Tumor cell entry into the lymph node is controlled by CCL1 chemokine expressed by lymph node lymphatic sinuses. *J Exp Med* **210**, 1509–1528 (2013).
15. Jafarnejad, M., Woodruff, M. C., Zawieja, D. C., Carroll, M. C. & Moore, J. E. Modeling Lymph Flow and Fluid Exchange with Blood Vessels in Lymph Nodes. *Lymphat Res Biol* **13**, 234–247 (2015).

16. Li, Q. *et al.* Negative to positive lymph node ratio is a superior predictor than traditional lymph node status in stage III colorectal cancer. *Oncotarget* **7**, 72290–72299 (2016).
17. Seeberg, L. T. *et al.* Survival Impact of Primary Tumor Lymph Node Status and Circulating Tumor Cells in Patients with Colorectal Liver Metastases. *Ann Surg Oncol* **24**, 2113–2121 (2017).
18. Ouyang, Q., Chen, L., Zhao, H., Xu, R. & Lin, Q. Detecting metastasis of lymph nodes and predicting aggressiveness in patients with breast carcinomas. *J Ultrasound Med* **29**, 343–352 (2010).
19. Cho, J.-K. *et al.* Significance of Lymph Node Metastasis in Cancer Dissemination of Head and Neck Cancer. *Transl Oncol* **8**, 119–125 (2015).
20. Balsat, C. *et al.* A specific immune and lymphatic profile characterizes the pre-metastatic state of the sentinel lymph node in patients with early cervical cancer. *OncImmunity* **6**, e1265718 (2017).
21. Yoshizawa, M., Shingaki, S., Nakajima, T. & Saku, T. Histopathological study of lymphatic invasion in squamous cell carcinoma (O-1N) with high potential of lymph node metastasis. *Clin Exp Metast* **12**, 347–356 (1994).
22. Jones, D., Pereira, E. R. & Padera, T. P. Growth and Immune Evasion of Lymph Node Metastasis. *Front Oncol* **8**, 36 (2018).

23. Alitalo, A. & Detmar, M. Interaction of tumor cells and lymphatic vessels in cancer progression. *Oncogene* **31**, 4499–4508 (2012).
24. Barthel, S. R., Gavino, J. D., Descheny, L. & Dimitroff, C. J. Targeting selectins and selectin ligands in inflammation and cancer. *Expert opinion on therapeutic targets* **11**, 1473–91 (2007).
25. Natoni, A., Macauley, M. S. & O'Dwyer, M. E. Targeting Selectins and Their Ligands in Cancer. *Frontiers in oncology* **6**, 93 (2016).
26. Birmingham, K. G. *et al.* Analyzing Mechanisms of Metastatic Cancer Cell Adhesive Phenotype Leveraging Preparative Adhesion Chromatography Microfluidic. *Advanced Biosystems* **3**, 1800328 (2019).
27. Birmingham, K., Robinson, I., Edwards, E. & Thomas, S. Photoconversion and chromatographic microfluidic system reveals differential cellular phenotypes of adhesion velocity versus persistence in shear flow. *Lab on a Chip* **20**, 806–822 (2020).
28. Li, J. & King, M. R. Adhesion receptors as therapeutic targets for circulating tumor cells. *Frontiers in Oncology* **2**, 79 (2012).
29. Lech, G., Słotwiński, R., Słodkowski, M. & Krasnodębski, I. W. Colorectal cancer tumour markers and biomarkers: Recent therapeutic advances. *World J Gastroenterol* **22**, 1745–1755 (2016).

30. Geng, Y., Marshall, J. R. & King, M. R. Glycomechanics of the Metastatic Cascade: Tumor Cell–Endothelial Cell Interactions in the Circulation. *Ann Biomed Eng* **40**, 790–805 (2012).
31. Harjunpää, H., Lloret Asens, M., Guenther, C. & Fagerholm, S. C. Cell Adhesion Molecules and Their Roles and Regulation in the Immune and Tumor Microenvironment. *Front. Immunol.* **10**, (2019).
32. Chaffer, C. L. & Weinberg, R. A. A Perspective on Cancer Cell Metastasis. *Science* **331**, 1559–1564 (2011).
33. McClatchey, P. M., Hannen, E. & Thomas, S. N. Microfluidic Platforms for the Interrogation of Intravascular Cellular Trafficking Mechanisms Influenced by Hemodynamic Forces. in *Microscale Technologies for Cell Engineering* (eds. Singh, A. & Gaharwar, A. K.) 197–218 (Springer International Publishing, 2016). doi:10.1007/978-3-319-20726-1_9.
34. Papaioannou, T. G., Karatzis, E. N., Vavuranakis, M., Lekakis, J. P. & Stefanadis, C. Assessment of vascular wall shear stress and implications for atherosclerotic disease. *Int J Cardiol* **113**, 12–18 (2006).
35. Papaioannou, T. G. & Stefanadis, C. Vascular wall shear stress: basic principles and methods. *Hellenic J Cardiol* **46**, 9–15 (2005).
36. Ballermann, B. J., Dardik, A., Eng, E. & Liu, A. Shear stress and the endothelium. *Kidney International* **54**, S100–S108 (1998).

37. Osmani, N. *et al.* Metastatic Tumor Cells Exploit Their Adhesion Repertoire to Counteract Shear Forces during Intravascular Arrest. *Cell Reports* **28**, 2491-2500.e5 (2019).
38. Steeg, P. S. Metastasis suppressors alter the signal transduction of cancer cells. *Nature Reviews Cancer* **3**, 55–63 (2003).
39. Hunter, K. W., Crawford, N. P. & Alsarraj, J. Mechanisms of metastasis. *Breast Cancer Res* **10**, S2 (2008).
40. Konstantopoulos, K. & Thomas, S. N. Cancer Cells in Transit: The Vascular Interactions of Tumor Cells. *Annual Review of Biomedical Engineering* **11**, 177–202 (2009).
41. Wirtz, D., Konstantopoulos, K. & Searson, P. C. The physics of cancer: the role of physical interactions and mechanical forces in metastasis. *Nat Rev Cancer* **11**, 512–522 (2011).
42. Alon, R., Chen, S., Puri, K. D., Finger, E. B. & Springer, T. A. The Kinetics of L-selectin Tethers and the Mechanics of Selectin-mediated Rolling. *J Cell Biol* **138**, 1169–1180 (1997).
43. Puri, K. D., Finger, E. B. & Springer, T. A. The faster kinetics of L-selectin than of E-selectin and P-selectin rolling at comparable binding strength. *J. Immunol.* **158**, 405–413 (1997).

44. Rupprecht, P. *et al.* A tapered channel microfluidic device for comprehensive cell adhesion analysis, using measurements of detachment kinetics and shear stress-dependent motion. *Biomicrofluidics* **6**, 107–112 (2012).
45. Wild, M. K., Huang, M.-C., Schulze-Horsel, U., Merwe, P. A. van der & Vestweber, D. Affinity, Kinetics, and Thermodynamics of E-selectin Binding to E-selectin Ligand-1. *J. Biol. Chem.* **276**, 31602–31612 (2001).
46. Springer, T. A. Traffic signals for lymphocyte recirculation and leukocyte emigration: The multistep paradigm - ScienceDirect. *Cell* **76**, 301–314 (1994).
47. Chang, K.-C. & Hammer, D. A. Adhesive Dynamics Simulations of Sialyl-Lewisx/E-selectin-Mediated Rolling in a Cell-Free System. *Biophysical Journal* **79**, 1891–1902 (2000).
48. Vestweber, D. & Blanks, J. E. Mechanisms That Regulate the Function of the Selectins and Their Ligands. *Physiological Reviews* **79**, 181–213 (1999).
49. Ebnet, K. & Vestweber, D. Molecular mechanisms that control leukocyte extravasation: the selectins and the chemokines. *Histochem Cell Biol* **112**, 1–23 (1999).
50. Crockett-Torabi, E. Selectins and mechanisms of signal transduction. *J Leukoc Biol* **63**, 1–14 (1998).

51. Krause, D. S., Lazarides, K., Lewis, J. B., von Andrian, U. H. & Van Etten, R. A. Selectins and their ligands are required for homing and engraftment of BCR-ABL1+ leukemic stem cells in the bone marrow niche. *Blood* **123**, 1361–1371 (2014).
52. McEver, R. P. Selectins: initiators of leucocyte adhesion and signalling at the vascular wall. *Cardiovasc Res* **107**, 331–339 (2015).
53. Varki, A. Selectin ligands. *Proc Natl Acad Sci U S A* **91**, 7390–7397 (1994).
54. Cummings, R. D. & Smith, D. F. The selectin family of carbohydrate-binding proteins: structure and importance of carbohydrate ligands for cell adhesion. *Bioessays* **14**, 849–856 (1992).
55. Kiskin, N. I. *et al.* Protein mobilities and P-selectin storage in Weibel-Palade bodies. *J. Cell. Sci.* **123**, 2964–2975 (2010).
56. Collins, T., Sheppard, K.-A., Simeonidis, S. & Rose, D. W. Transcriptional Regulation of the E-Selectin Gene. in *Leukocyte Recruitment, Endothelial Cell Adhesion Molecules, and Transcriptional Control: Insights for Drug Discovery* (ed. Collins, T.) 27–53 (Springer US, 2001). doi:10.1007/978-1-4615-1565-4_2.
57. Gonzalez-Amaro, R. & Sanchez-Madrid, F. Cell adhesion molecules: selectins and integrins. *Crit Rev Immunol* **19**, 389–429 (1999).
58. Tedder, T. F., Steeber, D. A., Chen, A. & Engel, P. The selectins: vascular adhesion molecules. *FASEB J* **9**, 866–873 (1995).

59. Petruzzelli, L., Takami, M. & Humes, H. D. Structure and function of cell adhesion molecules. *Am J Med* **106**, 467–476 (1999).
60. Lorant, D. *et al.* Inflammatory roles of P-selectin. - PubMed - NCBI. *J Clin Invest* **92**, 559–570 (1993).
61. Ley, K. Functions of selectins. *Results Probl Cell Differ* **33**, 177–200 (2001).
62. Gout, S., Tremblay, P.-L. & Huot, J. Selectins and selectin ligands in extravasation of cancer cells and organ selectivity of metastasis. *Clinical & experimental metastasis* **25**, 335–44 (2008).
63. Ley, K., Laudanna, C., Cybulsky, M. I. & Nourshargh, S. Getting to the site of inflammation: the leukocyte adhesion cascade updated. *Nat Rev Immunol* **7**, 678–689 (2007).
64. Fukuda, M., Hiraoka, N. & Yeh, J.-C. C-Type Lectins and Sialyl Lewis X Oligosaccharides. *J Cell Biol* **147**, 467–470 (1999).
65. Foxall, C. *et al.* The three members of the selectin receptor family recognize a common carbohydrate epitope, the sialyl Lewis(x) oligosaccharide. *J. Cell Biol.* **117**, 895–902 (1992).
66. Horstkorte, R. & Fuss, B. Cell Adhesion Molecules. in *Basic Neurochemistry* 165–179 (Elsevier, 2012). doi:10.1016/B978-0-12-374947-5.00009-2.
67. Borsig, L. Selectins in cancer immunity. *Glycobiology* **28**, 648–655 (2018).

68. Borsig, L., Wong, R., Hynes, R. O., Varki, N. M. & Varki, A. Synergistic effects of L- and P-selectin in facilitating tumor metastasis can involve non-mucin ligands and implicate leukocytes as enhancers of metastasis. *Proceedings of the National Academy of Sciences* **99**, 2193–2198 (2002).
69. Dallas, M. R. *et al.* Divergent roles of CD44 and carcinoembryonic antigen in colon cancer metastasis. *The FASEB Journal* **26**, 2648–2656 (2012).
70. Biancone, L., Araki, M., Araki, K., Vassalli, P. & Stamenkovic, I. Redirection of tumor metastasis by expression of E-selectin in vivo. *The Journal of experimental medicine* **183**, 581–7 (1996).
71. Läubli, H. & Borsig, L. Selectins promote tumor metastasis. *Semin. Cancer Biol.* **20**, 169–177 (2010).
72. Vigl, B. *et al.* Tissue inflammation modulates gene expression of lymphatic endothelial cells and dendritic cell migration in a stimulus-dependent manner. *Blood* **118**, 205–215 (2011).
73. Läubli, H., Stevenson, J. L., Varki, A., Varki, N. M. & Borsig, L. L-Selectin Facilitation of Metastasis Involves Temporal Induction of Fut7-Dependent Ligands at Sites of Tumor Cell Arrest. *Cancer Res* **66**, 1536–1542 (2006).
74. Robinson, S. D. *et al.* Multiple, targeted deficiencies in selectins reveal a predominant role for P-selectin in leukocyte recruitment. *Proceedings of the National Academy of Sciences of the United States of America* **96**, 11452–7 (1999).

75. Zuo, Y. *et al.* Silencing L-selectin expression by siRNA attenuated metastasis of murine lymphoid neoplasm cell P388D1 to peripheral lymph nodes. *Leukemia* **21**, 180–183 (2007).
76. Rodrigues, E. & Macauley, M. S. Hypersialylation in Cancer: Modulation of Inflammation and Therapeutic Opportunities. *Cancers (Basel)* **10**, (2018).
77. Büll, C., Stoel, M. A., Brok, M. H. den & Adema, G. J. Sialic Acids Sweeten a Tumor's Life. *Cancer Res* **74**, 3199–3204 (2014).
78. Hanley, W. D., Burdick, M. M., Konstantopoulos, K. & Sackstein, R. CD44 on LS174T Colon Carcinoma Cells Possesses E-Selectin Ligand Activity. *Cancer Res* **65**, 5812–5817 (2005).
79. Zen, K. *et al.* CD44v4 Is a Major E-Selectin Ligand that Mediates Breast Cancer Cell Transendothelial Migration. *PLoS ONE* **3**, e1826 (2008).
80. Burdick, M. M. *et al.* Expression of E-selectin ligands on circulating tumor cells: cross-regulation with cancer stem cell regulatory pathways? *Front. Oncol.* **2**, (2012).
81. Hanley, W. D. *et al.* Variant isoforms of CD44 are P- and L-selectin ligands on colon carcinoma cells. *The FASEB Journal* **20**, 337–339 (2006).
82. Thomas, S. N., Zhu, F., Schnaar, R. L., Alves, C. S. & Konstantopoulos, K. Carcinoembryonic antigen and CD44 variant isoforms cooperate to mediate colon carcinoma cell adhesion to E- and L-selectin in shear flow. *The Journal of biological chemistry* **283**, 15647–55 (2008).

83. Gruszka, A. M., Valli, D., Restelli, C. & Alcalay, M. Adhesion Deregulation in Acute Myeloid Leukaemia. *Cells* **8**, (2019).
84. Muz, B. *et al.* Inhibition of P-Selectin and PSGL-1 Using Humanized Monoclonal Antibodies Increases the Sensitivity of Multiple Myeloma Cells to Bortezomib. *Biomed Res Int* **2015**, 417586 (2015).
85. Ayob, A. Z. & Ramasamy, T. S. Cancer stem cells as key drivers of tumour progression. *Journal of Biomedical Science* **25**, 20 (2018).
86. Clevers, H. The cancer stem cell: premises, promises and challenges. *Nat Med* **17**, 313–319 (2011).
87. Abdullah, L. N. & Chow, E. K.-H. Mechanisms of chemoresistance in cancer stem cells. *Clin Transl Med* **2**, 3 (2013).
88. Prieto-Vila, M., Takahashi, R., Usuba, W., Kohama, I. & Ochiya, T. Drug Resistance Driven by Cancer Stem Cells and Their Niche. *Int J Mol Sci* **18**, (2017).
89. Murayama, T. & Gotoh, N. Drug resistance mechanisms of cancer stem-like cells and their therapeutic potential as drug targets. *Cancer Drug Resist* **2**, 457–470 (2019).
90. Yeung, T. M., Gandhi, S. C., Wilding, J. L., Muschel, R. & Bodmer, W. F. Cancer stem cells from colorectal cancer-derived cell lines. *Proc Natl Acad Sci U S A* **107**, 3722–3727 (2010).
91. Pop, M. G. Stem Cell Markers in Colon Cancer. in *Basic Principles and Practice in Surgery* (IntechOpen, 2019).

92. Yan, C. *et al.* The CEA⁺/lo colorectal cancer cell population harbors cancer stem cells and metastatic cells. *Oncotarget* **7**, 80700–80715 (2016).
93. Klonisch, T. *et al.* Cancer stem cell markers in common cancers – therapeutic implications. *Trends in Molecular Medicine* **14**, 450–460 (2008).
94. Zhao, W., Li, Y. & Zhang, X. Stemness-Related Markers in Cancer. *Cancer Transl Med* **3**, 87–95 (2017).
95. Jaggupilli, A. & Elkord, E. Significance of CD44 and CD24 as Cancer Stem Cell Markers: An Enduring Ambiguity. *Clinical & developmental immunology* **2012**, 708036 (2012).
96. Li, S. & Li, Q. Cancer stem cells and tumor metastasis (Review). *Int J Oncol* **44**, 1806–1812 (2014).
97. Shiozawa, Y., Nie, B., Pienta, K. J., Morgan, T. M. & Taichman, R. S. Cancer stem cells and their role in metastasis. *Pharmacol Ther* **138**, 285–293 (2013).
98. Agliano, A., Calvo, A. & Box, C. The challenge of targeting cancer stem cells to halt metastasis. *Seminars in Cancer Biology* **44**, 25–42 (2017).
99. Dallas, M. R. *et al.* Divergent roles of CD44 and carcinoembryonic antigen in colon cancer metastasis. *FASEB J* **26**, 2648–2656 (2012).
100. Wang, Y. & Oliver, G. Current views on the function of the lymphatic vasculature in health and disease. *Genes Dev* **24**, 2115–2126 (2010).

101. Choi, I., Lee, S. & Hong, Y.-K. The new era of the lymphatic system: no longer secondary to the blood vascular system. *Cold Spring Harb Perspect Med* **2**, a006445–a006445 (2012).
102. Cueni, L. N. & Detmar, M. The lymphatic system in health and disease. *Lymphat Res Biol* **6**, 109–122 (2008).
103. Moore, J. E., Jr & Bertram, C. D. Lymphatic System Flows. *Annu Rev Fluid Mech* **50**, 459–482 (2018).
104. Suami, H. & Scaglioni, M. F. Anatomy of the Lymphatic System and the Lymphosome Concept with Reference to Lymphedema. *Semin Plast Surg* **32**, 5–11 (2018).
105. Margaris, K. N. & Black, R. A. Modelling the lymphatic system: challenges and opportunities. *Journal of The Royal Society Interface* **9**, 601–612 (2012).
106. Willard-Mack, C. L. Normal structure, function, and histology of lymph nodes. *Toxicol Pathol* **34**, 409–424 (2006).
107. Scallan, J. P., Zawieja, S. D., Castorena-Gonzalez, J. A. & Davis, M. J. Lymphatic pumping: mechanics, mechanisms and malfunction. *J Physiol* **594**, 5749–5768 (2016).
108. Louie, D. A. P. & Liao, S. Lymph Node Subcapsular Sinus Macrophages as the Frontline of Lymphatic Immune Defense. *Front Immunol* **10**, 347–347 (2019).

109. Mondor, I. *et al.* Lymphatic Endothelial Cells Are Essential Components of the Subcapsular Sinus Macrophage Niche. *Immunity* **50**, 1453-1466.e4 (2019).
110. Fujimoto, N. *et al.* Single-cell mapping reveals new markers and functions of lymphatic endothelial cells in lymph nodes. *bioRxiv* 2020.01.09.900241 (2020) doi:10.1101/2020.01.09.900241.
111. Park, S. M. *et al.* Mapping the Distinctive Populations of Lymphatic Endothelial Cells in Different Zones of Human Lymph Nodes. *PLOS ONE* **9**, e94781 (2014).
112. von Andrian, U. H. & Mempel, T. R. Homing and cellular traffic in lymph nodes. *Nature Reviews Immunology* **3**, 867–878 (2003).
113. Tewalt, E. F., Cohen, J. N., Rouhani, S. J. & Engelhard, V. H. Lymphatic endothelial cells - key players in regulation of tolerance and immunity. *Front Immunol* **3**, 305–305 (2012).
114. Alderton, G. K. Active lymph nodes. *Nature Reviews Cancer* **13**, 607–607 (2013).
115. Liao, S. & von der Weid, P. Y. Lymphatic system: an active pathway for immune protection. *Semin Cell Dev Biol* **38**, 83–89 (2015).
116. Karaman, S. & Detmar, M. Mechanisms of lymphatic metastasis. *J Clin Invest* **124**, 922–928 (2014).
117. Padera, T. P., Meijer, E. F. J. & Munn, L. L. The Lymphatic System in Disease Processes and Cancer Progression. *Annu Rev Biomed Eng* **18**, 125–158 (2016).

118. Achen, M. G. & Stacker, S. A. Molecular control of lymphatic metastasis. *Ann N Y Acad Sci* **1131**, 225–234 (2008).
119. Wong, S. Y. & Hynes, R. O. Lymphatic or hematogenous dissemination: how does a metastatic tumor cell decide? *Cell Cycle* **5**, 812–817 (2006).
120. Sleeman, J. P. The lymph node as a bridgehead in the metastatic dissemination of tumors. *Recent Results Cancer Res* **157**, 55–81 (2000).
121. Mohammed, S. I., Torres-Luquis, O., Walls, E. & Lloyd, F. Lymph-circulating tumor cells show distinct properties to blood-circulating tumor cells and are efficient metastatic precursors. *Mol Oncol* **13**, 1400–1418 (2019).
122. Yeo, K. P. & Angeli, V. Bidirectional Crosstalk between Lymphatic Endothelial Cell and T Cell and Its Implications in Tumor Immunity. *Front Immunol* **8**, 83–83 (2017).
123. Detmar, M. & Hiraoka, S. The Formation of Lymphatic Vessels and Its Importance in the Setting of Malignancy. *The Journal of Experimental Medicine* **196**, 713–718 (2002).
124. Langheinrich, M. C. *et al.* Molecular mechanisms of lymphatic metastasis in solid tumors of the gastrointestinal tract. *Int J Clin Exp Pathol* **5**, 614–623 (2012).
125. Dieterich, L. C. & Detmar, M. Tumor lymphangiogenesis and new drug development. *Advanced Drug Delivery Reviews* **99**, 148–160 (2016).
126. Yamamoto, Y. *et al.* The clinical impact of the lymph node ratio as a prognostic factor after resection of pancreatic cancer. *Anticancer Res* **34**, 2389–2394 (2014).

127. Kim, H. J. & Choi, G.-S. Clinical Implications of Lymph Node Metastasis in Colorectal Cancer: Current Status and Future Perspectives. *Ann Coloproctol* **35**, 109–117 (2019).
128. Dhar, D. K. *et al.* Metastatic lymph node size and colorectal cancer prognosis. *J Am Coll Surg* **200**, 20–28 (2005).
129. Kalnins, I. K., Leonard, A. G., Sako, K., Razack, M. S. & Shedd, D. P. Correlation between prognosis and degree of lymph node involvement in carcinoma of the oral cavity. *Am J Surg* **134**, 450–454 (1977).
130. Liu, Q., Luo, D., Li, Q., Zhu, J. & Li, X. Evaluating the Effect of Lymph Node Status on Survival in Large Colon Cancer. *Front Oncol* **8**, 602–602 (2018).
131. Abner, A. *et al.* Correlation of tumor size and axillary lymph node involvement with prognosis in patients with T1 breast carcinoma. *Cancer* **83**, 2502–8 (1998).
132. Carter, C. L., Allen, C. & Henson, D. E. Relation of tumor size, lymph node status, and survival in 24,740 breast cancer cases. *Cancer* **63**, 181–187 (1989).
133. Harrell, M. I., Iritani, B. M. & Ruddell, A. Tumor-induced sentinel lymph node lymphangiogenesis and increased lymph flow precede melanoma metastasis. *Am. J. Pathol.* **170**, 774–786 (2007).
134. Zhu, H. *et al.* CXCR2+ MDSCs promote breast cancer progression by inducing EMT and activated T cell exhaustion. *Oncotarget* **8**, (2017).

135. Zhang, L. *et al.* CCL21/CCR7 Axis Contributed to CD133+ Pancreatic Cancer Stem-Like Cell Metastasis via EMT and Erk/NF- κ B Pathway. *PLoS One* **11**, (2016).
136. Wang, L. *et al.* CCR7 regulates ANO6 to promote migration of pancreatic ductal adenocarcinoma cells via the ERK signaling pathway. *Oncol Lett* **16**, 2599–2605 (2018).
137. Stacker, S. A. *et al.* Lymphangiogenesis and lymphatic vessel remodelling in cancer. *Nature Reviews Cancer* **14**, 159–172 (2014).
138. Habenicht, L. M., Kirschbaum, S. B., Furuya, M., Harrell, M. I. & Ruddell, A. *Tumor Regulation of Lymph Node Lymphatic Sinus Growth and Lymph Flow in Mice and in Humans. YALE JOURNAL OF BIOLOGY AND MEDICINE* vol. 90 (2017).
139. Hinson, A. M. *et al.* Structural alterations in tumor-draining lymph nodes before papillary thyroid carcinoma metastasis HHS Public Access. **39**, 1639–1646.
140. Otto, B. *et al.* Molecular Changes in Pre-Metastatic Lymph Nodes of Esophageal Cancer Patients. *PLoS ONE* **9**, e102552 (2014).
141. Ji, R.-C. & Yang, L. Molecular Sciences Lymph Nodes and Cancer Metastasis: New Perspectives on the Role of Intranodal Lymphatic Sinuses. doi:10.3390/ijms18010051.
142. Sun, B. *et al.* Colorectal cancer exosomes induce lymphatic network remodeling in lymph nodes. *International Journal of Cancer* (2019) doi:10.1002/ijc.32196.

143. Garg, S. *et al.* Reirradiation for second primary or recurrent cancers of the head and neck: Dosimetric and outcome analysis. *Head Neck* **38 Suppl 1**, E961-969 (2016).
144. Karnezis, T. *et al.* VEGF-D Promotes Tumor Metastasis by Regulating Prostaglandins Produced by the Collecting Lymphatic Endothelium. *Cancer Cell* **21**, 181–195 (2012).
145. Ji, R.-C. Lymph Nodes and Cancer Metastasis: New Perspectives on the Role of Intranodal Lymphatic Sinuses. *Int J Mol Sci* **18**, (2016).
146. Qian, C.-N. *et al.* Preparing the “Soil”: The Primary Tumor Induces Vasculature Reorganization in the Sentinel Lymph Node before the Arrival of Metastatic Cancer Cells. *Cancer Res* **66**, 10365–10376 (2006).
147. Commerford, C. D. *et al.* Mechanisms of Tumor-Induced Lymphovascular Niche Formation in Draining Lymph Nodes. *Cell Reports* **25**, 3554-3563.e4 (2018).
148. Trevaskis, N. L., Kaminskas, L. M. & Porter, C. J. H. From sewer to saviour - targeting the lymphatic system to promote drug exposure and activity. *Nat Rev Drug Discov* **14**, 781–803 (2015).
149. Kawai, Y., Kaidoh, M., Yokoyama, Y. & Ohhashi, T. Pivotal roles of shear stress in the microenvironmental changes that occur within sentinel lymph nodes. *Cancer Sci.* **103**, 1245–1252 (2012).

150. Yan, J., Jiang, Y., Ye, M., Liu, W. & Feng, L. The clinical value of lymphatic vessel density, intercellular adhesion molecule 1 and vascular cell adhesion molecule 1 expression in patients with oral tongue squamous cell carcinoma. **10**, 125–130 (2014).
151. Onder, L. *et al.* Lymphatic Endothelial Cells Control Initiation of Lymph Node Organogenesis. *Immunity* **47**, 80-92.e4 (2017).
152. Miteva, D. *et al.* Transmural Flow Modulates Cell and Fluid Transport Functions of Lymphatic Endothelium | Circulation Research. *Circ Res* **106**, 920–931 (2010).
153. Schlesinger, M. & Bendas, G. Vascular cell adhesion molecule-1 (VCAM-1)--an increasing insight into its role in tumorigenicity and metastasis. *Int. J. Cancer* **136**, 2504–2514 (2015).
154. Kühnbach, C., da Luz, S., Baganz, F., Hass, V. C. & Mueller, M. M. A Microfluidic System for the Investigation of Tumor Cell Extravasation. *Bioengineering (Basel)* **5**, (2018).
155. Oh, J., Edwards, E. E., Mcclatchey, P. M. & Thomas, S. N. Analytical cell adhesion chromatography reveals impaired persistence of metastatic cell rolling adhesion to P-selectin. (2015) doi:10.1242/jcs.166439.
156. Ma, V., Middleton, K., You, L. & Sun, Y. A review of microfluidic approaches for investigating cancer extravasation during metastasis | Microsystems & Nanoengineering. *Microsyst Nanoeng* **4**, (2018).

157. Alunni-Fabbroni, M., Müller, V., Fehm, T., Janni, W. & Rack, B. Monitoring in metastatic breast cancer: is imaging outdated in the era of circulating tumor cells? *Breast Care (Basel)* **9**, 16–21 (2014).
158. Greenlee, J. D. & King, M. R. Engineered fluidic systems to understand lymphatic cancer metastasis. *Biomicrofluidics* **14**, (2020).
159. Wong, K. H. K., Truslow, J. G., Khankhel, A. H., Chan, K. L. S. & Tien, J. Artificial lymphatic drainage systems for vascularized microfluidic scaffolds. *J Biomed Mater Res A* **101**, 2181–2190 (2013).
160. Chung, M., Ahn, J., Son, K., Kim, S. & Jeon, N. L. Biomimetic Model of Tumor Microenvironment on Microfluidic Platform. *Adv Healthc Mater* **6**, (2017).
161. Lote, H. *et al.* Carbon dating cancer: defining the chronology of metastatic progression in colorectal cancer. *Ann Oncol* **28**, 1243–1249 (2017).
162. Sökeland, G. & Schumacher, U. The functional role of integrins during intra- and extravasation within the metastatic cascade. *Molecular Cancer* **18**, 12 (2019).
163. Kim, Y. J., Borsig, L., Varki, N. M. & Varki, A. P-selectin deficiency attenuates tumor growth and metastasis. *Proceedings of the National Academy of Sciences of the United States of America* **95**, 9325–30 (1998).
164. Köhler, S., Ullrich, S., Richter, U. & Schumacher, U. E-/P-selectins and colon carcinoma metastasis: first in vivo evidence for their crucial role in a clinically

- relevant model of spontaneous metastasis formation in the lung. *British journal of cancer* **102**, 602–9 (2010).
165. Thomas, S. N., Schnaar, R. L. & Konstantopoulos, K. Podocalyxin-like protein is an E-/L-selectin ligand on colon carcinoma cells: comparative biochemical properties of selectin ligands in host and tumor cells. *Am J Physiol Cell Physiol* **296**, C505–C513 (2009).
166. Baumann, P. *et al.* CD24 Expression Causes the Acquisition of Multiple Cellular Properties Associated with Tumor Growth and Metastasis. *Cancer Res* **65**, 10783–10793 (2005).
167. Läubli, H. & Borsig, L. Selectins as Mediators of Lung Metastasis. *Cancer Microenviron* **3**, 97–105 (2010).
168. Napier, S. L., Healy, Z. R., Schnaar, R. L. & Konstantopoulos, K. Selectin ligand expression regulates the initial vascular interactions of colon carcinoma cells: the roles of CD44v and alternative sialofucosylated selectin ligands. *The Journal of biological chemistry* **282**, 3433–41 (2007).
169. Alves, C. S., Yakovlev, S., Medved, L. & Konstantopoulos, K. Biomolecular characterization of CD44-fibrin(ogen) binding: distinct molecular requirements mediate binding of standard and variant isoforms of CD44 to immobilized fibrin(ogen). *J. Biol. Chem.* **284**, 1177–1189 (2009).
170. Jensen, E. C. Quantitative Analysis of Histological Staining and Fluorescence Using ImageJ. *The Anatomical Record* **296**, 378–381 (2013).

171. Edwards, E. E. *et al.* P-, but not E- or L-, selectin-mediated rolling adhesion persistence in hemodynamic flow diverges between metastatic and leukocytic cells. *Oncotarget* **8**, 83585–83601 (2017).
172. Deroulers, C. *et al.* Analyzing huge pathology images with open source software. *Diagnostic Pathology* **8**, (2013).
173. Patro, R., Duggal, G., Love, M. I., Irizarry, R. A. & Kingsford, C. Salmon provides fast and bias-aware quantification of transcript expression. *Nature Methods* **14**, 417 (2017).
174. Konstantopoulos, K., Kukreti, S. & McIntire, L. V. Biomechanics of cell interactions in shear fields. *Advanced Drug Delivery Reviews* **33**, 141–164 (1998).
175. Rutter, A., Hugenholtz, H., Saunders, J. K. & Smith, I. C. P. Classification of Brain Tumors by Ex Vivo ¹H NMR Spectroscopy. *Journal of Neurochemistry* **64**, 1655–1661 (1995).
176. Schneider, M. *et al.* Characterization of colon cancer cells: a functional approach characterizing CD133 as a potential stem cell marker. *BMC Cancer* **12**, 96 (2012).
177. Vogel, C. & Marcotte, E. M. Insights into the regulation of protein abundance from proteomic and transcriptomic analyses. *Nat. Rev. Genet.* **13**, 227–232 (2012).
178. Zhang, M. *et al.* Evidence for the importance of post-transcriptional regulatory changes in ovarian cancer progression and the contribution of miRNAs. *Scientific Reports* **7**, 8171 (2017).

179. Zhong, L., Huot, J. & Simard, M. J. p38 activation induces production of miR-146a and miR-31 to repress E-selectin expression and inhibit transendothelial migration of colon cancer cells. *Scientific Reports* **8**, 2334 (2018).
180. Zhong, L., Simoneau, B., Huot, J. & Simard, M. J. p38 and JNK pathways control E-selectin-dependent extravasation of colon cancer cells by modulating miR-31 transcription. *Oncotarget* **8**, 1678–1687 (2016).
181. Zhang, Y., Wu, M., Han, X., Wang, P. & Qin, L. High-throughput, label-free isolation of cancer stem cells based on cell adhesion capacity. *Angew Chem Int Ed Engl* **54**, 10838–10842 (2015).
182. Tran, R. *et al.* Microfluidic Transduction Harnesses Mass Transport Principles to Enhance Gene Transfer Efficiency. *Molecular Therapy* **25**, 2372–2382 (2017).
183. Weigelt, B., Peterse, J. L. & van't Veer, L. J. Breast cancer metastasis: markers and models. *Nature Reviews Cancer* **5**, 591–602 (2005).
184. Lech, G., Słotwiński, R., Słodkowski, M. & Krasnodębski, I. W. Colorectal cancer tumour markers and biomarkers: Recent therapeutic advances. *World Journal of Gastroenterology* **22**, 1745 (2016).
185. Natoni, A., Macauley, M. S. & O'Dwyer, M. E. Targeting Selectins and Their Ligands in Cancer. *Frontiers in oncology* **6**, 93 (2016).

186. Sleeboom, J. J. F., Eslami Amirabadi, H., Nair, P., Sahlgren, C. M. & den Toonder, J. M. J. Metastasis in context: modeling the tumor microenvironment with cancer-on-a-chip approaches. *Disease models & mechanisms* **11**, dmm033100 (2018).
187. Greenberg, A. W. & Hammer, D. A. *Cell Separation Mediated by Differential Rolling Adhesion*. (2001).
188. Cheung, L. S.-L. *et al.* Kinematics of Specifically Captured Circulating Tumor Cells in Bio-Functionalized Microchannels. *Journal of Microelectromechanical Systems* **19**, 752–763 (2010).
189. Malandrino, A., Kamm, R. D. & Moeendarbary, E. In Vitro Modeling of Mechanics in Cancer Metastasis. *ACS Biomaterials Science & Engineering* **4**, 294 (2018).
190. Moeendarbary, E. & Harris, A. R. Cell mechanics: principles, practices, and prospects. *Wiley interdisciplinary reviews. Systems biology and medicine* **6**, 371–88 (2014).
191. Seeberg, L. T. *et al.* Survival Impact of Primary Tumor Lymph Node Status and Circulating Tumor Cells in Patients with Colorectal Liver Metastases. doi:10.1245/s10434-017-5818-2.
192. Stein, T. N. & Berger, M. R. Quantification of liver metastases from LS174T human colorectal cancer cells in nude rats by PCR. *Anticancer research* **19**, 3939–45.
193. Thomas, S. N., Schnaar, R. L. & Konstantopoulos, K. Podocalyxin-like protein is an E-/L-selectin ligand on colon carcinoma cells: comparative biochemical properties of

- selectin ligands in host and tumor cells. *American Journal of Physiology-Cell Physiology* **296**, C505–C513 (2009).
194. Dimitroff, C. J., Lee, J. Y., Fuhlbrigge, R. C. & Sackstein, R. A distinct glycoform of CD44 is an L-selectin ligand on human hematopoietic cells. *Proceedings of the National Academy of Sciences of the United States of America* **97**, 13841–6 (2000).
195. M Burdick, M., McCaffery, J., Kim, Y., Bochner, B. & Konstantopoulos, K. Colon carcinoma cell glycolipids, integrins, and other glycoproteins mediate adhesion to HUVECs under flow. *American journal of physiology. Cell physiology* **284**, C977-87 (2003).
196. Burdick, M. M., Chu, J. T., Godar, S. & Sackstein, R. HCELL is the major E- and L-selectin ligand expressed on LS174T colon carcinoma cells. *The Journal of biological chemistry* **281**, 13899–13905 (2006).
197. Beckman Anderson Fellow, M., Patterson, G. H. & Lippincott-Schwartz, J. A Photoactivatable GFP for Selective Photolabeling of Proteins and Cells. *Proc. Natl. Acad. Sci. U.S.A* **293**, 727 (1999).
198. Patterson, G. H. & Lippincott-Schwartz, J. Selective photolabeling of proteins using photoactivatable GFP. *Methods* **32**, 445–450 (2004).
199. Mitchell, M. J. & King, M. R. Computational and experimental models of cancer cell response to fluid shear stress. *Frontiers in Oncology* vol. 3 MAR (2013).

200. Konstantopoulos, K., Kukreti, S. & McIntire, L. V. Biomechanics of cell interactions in shear fields. *Advanced Drug Delivery Reviews* vol. 33 141–164 (1998).
201. Burdick, M. M., McCaffery, J. M., Kim, Y. S., Bochner, B. S. & Konstantopoulos, K. Colon carcinoma cell glycolipids, integrins, and other glycoproteins mediate adhesion to HUVECs under flow. *American Journal of Physiology-Cell Physiology* **284**, C977–C987 (2003).
202. Li, S.-S. *et al.* Sialyl Lewisx-P-selectin cascade mediates tumor–mesothelial adhesion in ascitic fluid shear flow. *Nature Communications* **10**, 2406 (2019).
203. Tchamitchi, M. H., Smith, † C Wayne & Mariscalco, M. M. *Neonatal neutrophil interaction with P-selectin: contribution of P-selectin glycoprotein ligand-1 and sialic acid.* doi:10.1002/jlb.67.1.73.
204. Shiozaki, K., Yamaguchi, K., Takahashi, K., Moriya, S. & Miyagi, T. Regulation of sialyl Lewis antigen expression in colon cancer cells by sialidase NEU4. *The Journal of biological chemistry* **286**, 21052–61 (2011).
205. von Andrian, U. H. *et al.* L-selectin mediates neutrophil rolling in inflamed venules through sialyl LewisX-dependent and -independent recognition pathways. *Blood* **82**, 182–191 (1993).
206. Pai, R. K. *et al.* Pattern of lymph node involvement and prognosis in pancreatic adenocarcinoma: direct lymph node invasion has similar survival to node-negative disease. *Am. J. Surg. Pathol.* **35**, 228–234 (2011).

207. You, M. S. *et al.* Lymph node ratio as valuable predictor in pancreatic cancer treated with R0 resection and adjuvant treatment. *BMC Cancer* **19**, 952 (2019).
208. Fortea-Sanchis, C., Martínez-Ramos, D. & Escrig-Sos, J. The lymph node status as a prognostic factor in colon cancer: comparative population study of classifications using the logarithm of the ratio between metastatic and nonmetastatic nodes (LODDS) versus the pN-TNM classification and ganglion ratio systems. *BMC Cancer* **18**, (2018).
209. Kim, H. J. & Choi, G. Clinical Implications of Lymph Node Metastasis in Colorectal Cancer: Current Status and Future Perspectives. *Ann Coloproctol* **35**, 109–117 (2019).
210. Liu, X. *et al.* Analysis of Lymph Node Metastasis Correlation with Prognosis in Patients with T2 Gastric Cancer. *PLoS One* **9**, (2014).
211. Wong, S. Y. & Hynes, R. O. Lymphatic or Hematogenous Dissemination: How Does a Metastatic Tumor Cell Decide? *Cell Cycle* **5**, 812–817 (2006).
212. Karaman, S. & Detmar, M. Mechanisms of lymphatic metastasis. *J. Clin. Invest.* **124**, 922–928 (2014).
213. Carr, I. Lymphatic metastasis. *Cancer Metastasis Rev.* **2**, 307–317 (1983).
214. Farnsworth, R. H., Achen, M. G. & Stacker, S. A. The evolving role of lymphatics in cancer metastasis. *Current Opinion in Immunology* **53**, 64–73 (2018).
215. Makkouk, A. & Weiner, G. J. Cancer Immunotherapy and Breaking Immune Tolerance: New Approaches to an Old Challenge. *Cancer Res* **75**, 5–10 (2015).

216. Vinay, D. S. *et al.* Immune evasion in cancer: Mechanistic basis and therapeutic strategies. *Seminars in Cancer Biology* **35**, S185–S198 (2015).
217. Fontebasso, Y. & Dubinett, S. M. Drug Development for Metastasis Prevention. *Crit Rev Oncog* **20**, 449–473 (2015).
218. Fendt, S.-M. Is There a Therapeutic Window for Metabolism-Based Cancer Therapies? *Front Endocrinol (Lausanne)* **8**, (2017).
219. Huang, B. *et al.* Active targeting of chemotherapy to disseminated tumors using nanoparticle-carrying T cells. *Sci Transl Med* **7**, 291ra94 (2015).
220. Moore, J. E. & Bertram, C. D. Lymphatic System Flows. *Annu Rev Fluid Mech* **50**, 459–482 (2018).
221. Brown, M. *et al.* Lymph node blood vessels provide exit routes for metastatic tumor cell dissemination in mice. *Science* **359**, 1408–1411 (2018).
222. Jeong, K. *et al.* FAK inhibition reduces metastasis of $\alpha 4$ integrin-expressing melanoma to lymph nodes by targeting lymphatic VCAM-1 expression. *Biochem. Biophys. Res. Commun.* **509**, 1034–1040 (2019).
223. Lee, Y.-C. *et al.* Targeting Constitutively Activated $\beta 1$ Integrins Inhibits Prostate Cancer Metastasis. *Mol Cancer Res* **11**, 405–417 (2013).
224. P, F. & Ja, V. Integrins in tumor angiogenesis and lymphangiogenesis. *Methods Mol Biol* **757**, 471–486 (2012).

225. Cohen, S., Haimovich, J. & Hollander, N. Anti-idiotypic × Anti-LFA-1 Bispecific Antibodies Inhibit Metastasis of B Cell Lymphoma. *The Journal of Immunology* **170**, 2695–2701 (2003).
226. Kawai, Y., Kaidoh, M., Yokoyama, Y., Sano, K. & Ohhashi, T. Chemokine CCL2 facilitates ICAM-1-mediated interactions of cancer cells and lymphatic endothelial cells in sentinel lymph nodes. *Cancer Sci.* **100**, 419–428 (2009).
227. Weitzenfeld, P. *et al.* Chemokine axes in breast cancer: factors of the tumor microenvironment reshape the CCR7-driven metastatic spread of luminal-A breast tumors. *Journal of Leukocyte Biology* **99**, 1009–1025 (2016).
228. Zhou, J. *et al.* The Role of Chemoattractant Receptors in Shaping the Tumor Microenvironment. *BioMed Research International* <https://www.hindawi.com/journals/bmri/2014/751392/> (2014)
doi:<https://doi.org/10.1155/2014/751392>.
229. Sleeman, J. P., Nazarenko, I. & Thiele, W. Do all roads lead to Rome? Routes to metastasis development. *International Journal of Cancer* **128**, 2511–2526 (2011).
230. Mitchell, M. J. & King, M. R. Computational and Experimental Models of Cancer Cell Response to Fluid Shear Stress. *Front Oncol* **3**, (2013).
231. Huang, Q. *et al.* Fluid shear stress and tumor metastasis. *Am J Cancer Res* **8**, 763–777 (2018).

232. Hagihara, T. *et al.* Hydrodynamic stress stimulates growth of cell clusters via the ANXA1/PI3K/AKT axis in colorectal cancer. *Sci Rep* **9**, 20027 (2019).
233. Lee, H. J. *et al.* Fluid shear stress activates YAP1 to promote cancer cell motility. *Nature Communications* **8**, 14122 (2017).
234. Planas-Paz, L. & Lammert, E. Mechanosensing in Developing Lymphatic Vessels. *Advances in anatomy, embryology, and cell biology* **214**, 23–40 (2014).
235. Achen, M. G. & Stacker, S. A. Molecular control of lymphatic metastasis. *Ann. N. Y. Acad. Sci.* **1131**, 225–234 (2008).
236. Habenicht, L. M., Kirschbaum, S. B., Furuya, M., Harrell, M. I. & Ruddell, A. Tumor Regulation of Lymph Node Lymphatic Sinus Growth and Lymph Flow in Mice and in Humans. *Yale J Biol Med* **90**, 403–415 (2017).
237. Hinson, A. M. *et al.* Structural alterations in tumor-draining lymph nodes before papillary thyroid carcinoma metastasis. *Head Neck* **39**, 1639–1646 (2017).
238. Otto, B. *et al.* Molecular Changes in Pre-Metastatic Lymph Nodes of Esophageal Cancer Patients. *PLoS One* **9**, (2014).
239. Sun, B. *et al.* Colorectal cancer exosomes induce lymphatic network remodeling in lymph nodes. *Int. J. Cancer* **145**, 1648–1659 (2019).
240. West, H. & Jin, J. Lymph Nodes and Lymphadenopathy in Cancer. *JAMA Oncol* **2**, 971 (2016).

241. Rohner, N. A. *et al.* Lymph node biophysical remodeling is associated with melanoma lymphatic drainage. *FASEB J* **29**, 4512–4522 (2015).
242. Swartz, M. A. & Lund, A. W. Lymphatic and interstitial flow in the tumour microenvironment: linking mechanobiology with immunity. *Nat. Rev. Cancer* **12**, 210–219 (2012).
243. Miyaji, K. *et al.* The stiffness of lymph nodes containing lung carcinoma metastases: a new diagnostic parameter measured by a tactile sensor. *Cancer* **80**, 1920–1925 (1997).
244. Paszek, M. J. *et al.* Tensional homeostasis and the malignant phenotype. *Cancer Cell* **8**, 241–254 (2005).
245. Riedel, A., Shorthouse, D., Haas, L., Hall, B. A. & Shields, J. Tumor-induced stromal reprogramming drives lymph node transformation. *Nat. Immunol.* **17**, 1118–1127 (2016).
246. Webster, B. *et al.* Regulation of lymph node vascular growth by dendritic cells. *J. Exp. Med.* **203**, 1903–1913 (2006).
247. Pan, W.-R., Roux, C. M. le, Levy, S. M. & Briggs, C. A. The morphology of the human lymphatic vessels in the head and neck. *Clinical Anatomy* **23**, 654–661 (2010).
248. Seidl, M. *et al.* Morphology of Immunomodulation in Breast Cancer Tumor Draining Lymph Nodes Depends on Stage and Intrinsic Subtype. *Scientific Reports* **8**, 1–12 (2018).

249. McLaughlin, R. A. *et al.* Imaging of Human Lymph Nodes Using Optical Coherence Tomography: Potential for Staging Cancer. *Cancer Res* **70**, 2579–2584 (2010).
250. Haley, P. J. The lymphoid system: a review of species differences. *J Toxicol Pathol* **30**, 111–123 (2017).
251. Treuting, P. M. *et al.* *Comparative Anatomy and Histology: A Mouse and Human Atlas (Expert Consult)*. (Academic Press, 2012).
252. Hanley, W. D. *et al.* Variant isoforms of CD44 are P- and L-selectin ligands on colon carcinoma cells. *The FASEB Journal* **20**, 337–339 (2006).
253. Thomas, S. N., Zhu, F., Schnaar, R. L., Alves, C. S. & Konstantopoulos, K. Carcinoembryonic antigen and CD44 variant isoforms cooperate to mediate colon carcinoma cell adhesion to E- and L-selectin in shear flow. *J. Biol. Chem.* **283**, 15647–15655 (2008).
254. Napier, S. L., Healy, Z. R., Schnaar, R. L. & Konstantopoulos, K. Selectin Ligand Expression Regulates the Initial Vascular Interactions of Colon Carcinoma Cells: The Roles of CD44V and Alternative Sialofucosylated Selectin Ligands. *Journal of Biological Chemistry* **282**, 3433–3441 (2006).
255. Edwards, E. E., Birmingham, K. G., O’melia, M. J., Oh, J. & Thomas, S. N. Fluorometric Quantification of Single Cell Velocities to Investigate Cancer Metastasis. *Cell Sys* **7**, 496–509 (2018).

256. Muller, W. A. New Mechanisms and Pathways for Monocyte Recruitment. *J Exp Med* **194**, f47–f52 (2001).
257. Hampton, H. R. & Chtanova, T. Lymphatic Migration of Immune Cells. *Front Immunol* **10**, (2019).
258. Ingersoll, M. A., Platt, A. M., Potteaux, S. & Randolph, G. J. Monocyte trafficking in acute and chronic inflammation. *Trends Immunol.* **32**, 470–477 (2011).
259. Häuselmann, I. *et al.* Monocyte Induction of E-Selectin-Mediated Endothelial Activation Releases VE-Cadherin Junctions to Promote Tumor Cell Extravasation in the Metastasis Cascade. *Cancer Res.* **76**, 5302–5312 (2016).
260. Evani, S. J., Prabhu, R. G., Gnanaruban, V., Finol, E. A. & Ramasubramanian, A. K. Monocytes mediate metastatic breast tumor cell adhesion to endothelium under flow. *FASEB J* **27**, 3017–3029 (2013).
261. Weledji, E. P., Enoworock, G., Mokake, M. & Sinju, M. How Grim is Pancreatic Cancer? *Oncol Rev* **10**, (2016).
262. Wong, S. L. Lymph Node Counts and Survival Rates After Resection for Colon and Rectal Cancer. *Gastrointest Cancer Res* **3**, S33–S35 (2009).
263. Kikuchi, R., Sukhbaatar, A., Sakamoto, M., Mori, S. & Kodama, T. A model system for studying superselective radiotherapy of lymph node metastasis in mice with swollen lymph nodes. *Clinical and Translational Radiation Oncology* **20**, 53–57 (2020).

264. Takeda, K., Mori, S. & Kodama, T. Study of fluid dynamics reveals direct communications between lymphatic vessels and venous blood vessels at lymph nodes of mice. *Journal of Immunological Methods* **445**, 1–9 (2017).
265. Blatter, C. *et al.* In vivo label-free measurement of lymph flow velocity and volumetric flow rates using Doppler optical coherence tomography. *Scientific Reports* **6**, 1–10 (2016).
266. Dadiani, M. *et al.* Real-time Imaging of Lymphogenic Metastasis in Orthotopic Human Breast Cancer. *Cancer Res* **66**, 8037–8041 (2006).
267. Singh, R. & Choi, B. K. Siglec1-expressing subcapsular sinus macrophages provide soil for melanoma lymph node metastasis. *eLife* **8**, e48916 (2019).
268. Nakashima, H., Terabe, M., Berzofsky, J., Husain, S. & Puri, R. A Novel Combination Immunotherapy for Cancer by IL-13R 2-Targeted DNA Vaccine and Immunotoxin in Murine Tumor Models. *Journal of immunology (Baltimore, Md. : 1950)* **187**, 4935–46 (2011).
269. Kikuchi, S. *et al.* Biological Ablation of Sentinel Lymph Node Metastasis in Submucosally Invaded Early Gastrointestinal Cancer. *Molecular Therapy* **23**, 501–509 (2015).
270. Burton, J. B. *et al.* Adenovirus-mediated gene expression imaging to directly detect sentinel lymph node metastasis of prostate cancer. *Nature Medicine* **14**, 882–888 (2008).

271. Nakayama, A., Ogawa, A., Fukuta, Y. & Kudo, K. Relation between lymphatic vessel diameter and clinicopathologic parameters in squamous cell carcinomas of the oral region. *Cancer* **86**, 200–206 (1999).
272. Lund, A. W., Medler, T. R., Leachman, S. A. & Coussens, L. M. Lymphatic Vessels, Inflammation, and Immunity in Skin Cancer. *Cancer Discov* **6**, 22–35 (2016).
273. Shen, C.-N. *et al.* Lymphatic vessel remodeling and invasion in pancreatic cancer progression. *EBioMedicine* **47**, 98–113 (2019).
274. Ozasa, R., Ohno, J., Iwahashi, T. & Taniguchi, K. Tumor-induced lymphangiogenesis in cervical lymph nodes in oral melanoma-bearing mice. *Journal of Experimental & Clinical Cancer Research* **31**, 83 (2012).
275. Sweetey, S. V. & Narayankar, A. S. Evaluation of lymph node ratio and morphologic patterns of nodal reactive hyperplasia in primary organ malignancy. *Indian Journal of Pathology and Microbiology* **62**, 216 (2019).
276. Fujiwara, M. *et al.* Measurement of cutaneous lymphatic flow rates in patients with skin cancer: area extraction method. *The Journal of Dermatology* **41**, 498–504 (2014).
277. Lachance, P.-A., Hazen, A. & Sevick-Muraca, E. M. Lymphatic Vascular Response to Acute Inflammation. *PLoS One* **8**, (2013).
278. Weitman, E. S. *et al.* Obesity impairs lymphatic fluid transport and dendritic cell migration to lymph nodes. *PLoS ONE* **8**, e70703 (2013).

279. Jakubzick, C. *et al.* Minimal differentiation of classical monocytes as they survey steady-state tissues and transport antigen to lymph nodes. *Immunity* **39**, 599–610 (2013).
280. Leirião, P., Fresno, C. del & Ardavin, C. Monocytes as effector cells: Activated Ly-6Chigh mouse monocytes migrate to the lymph nodes through the lymph and cross-present antigens to CD8⁺ T cells. *European Journal of Immunology* **42**, 2042–2051 (2012).
281. Guo Junke *et al.* Exact Solution to Navier-Stokes Equation for Developed Radial Flow between Parallel Disks. *Journal of Engineering Mechanics* **143**, 04017026 (2017).
282. Birmingham, K. G., Robinson, I. E., Edwards, E. E. & Thomas, S. N. Photoconversion and chromatographic microfluidic system reveals differential cellular phenotypes of adhesion velocity versus persistence in shear flow. *Lab Chip* (2020) doi:10.1039/c9lc00923j.
283. Birmingham, K. G. *et al.* Analyzing Mechanisms of Metastatic Cancer Cell Adhesive Phenotype Leveraging Preparative Adhesion Chromatography Microfluidic. *Advanced Biosystems* **3**, 1800328 (2019).
284. Hoshida, T. *et al.* Imaging steps of lymphatic metastasis reveals that vascular endothelial growth factor-C increases metastasis by increasing delivery of cancer cells to lymph nodes: therapeutic implications. *Cancer Res.* **66**, 8065–8075 (2006).

285. Turner, V. M. & Mabbott, N. A. Structural and functional changes to lymph nodes in ageing mice. *Immunology* **151**, 239–247 (2017).
286. Ohtani, O. & Ohtani, Y. Structure and function of rat lymph nodes. *Arch. Histol. Cytol.* **71**, 69–76 (2008).
287. Lund, H., Boysen, P., Åkesson, C. P., Lewandowska-Sabat, A. M. & Storset, A. K. Transient Migration of Large Numbers of CD14⁺⁺ CD16⁺ Monocytes to the Draining Lymph Node after Onset of Inflammation. *Front. Immunol.* **7**, (2016).
288. Maletto, B. A. *et al.* Presence of neutrophil-bearing antigen in lymphoid organs of immune mice. *Blood* **108**, 3094–3102 (2006).
289. Harmsen, A. G., Muggenburg, B. A., Snipes, M. B. & Bice, D. E. The role of macrophages in particle translocation from lungs to lymph nodes. *Science* **230**, 1277–1280 (1985).
290. León, B., López-Bravo, M. & Ardavín, C. Monocyte-derived dendritic cells formed at the infection site control the induction of protective T helper 1 responses against *Leishmania*. *Immunity* **26**, 519–531 (2007).
291. Randolph, G. J., Inaba, K., Robbiani, D. F., Steinman, R. M. & Muller, W. A. Differentiation of phagocytic monocytes into lymph node dendritic cells in vivo. *Immunity* **11**, 753–761 (1999).
292. Shi, C. & Pamer, E. G. Monocyte recruitment during infection and inflammation. *Nat. Rev. Immunol.* **11**, 762–774 (2011).

293. Segal, L. *et al.* PAR-3 Knockdown Enhances Adhesion Rate of PANC-1 Cells via Increased Expression of Integrin α v and E-Cadherin. *PLoS One* **9**, (2014).
294. Gradiz, R., Silva, H. C., Carvalho, L., Botelho, M. F. & Mota-Pinto, A. MIA PaCa-2 and PANC-1 – pancreas ductal adenocarcinoma cell lines with neuroendocrine differentiation and somatostatin receptors. *Scientific Reports* **6**, 1–14 (2016).
295. Emir, E. *et al.* Predicting Response to Radioimmunotherapy from the Tumor Microenvironment of Colorectal Carcinomas. *Cancer research* **67**, 11896–905 (2008).
296. Delitto, D. *et al.* Human pancreatic cancer xenografts recapitulate key aspects of cancer cachexia. *Oncotarget* **8**, 1177–1189 (2016).
297. Walpola Piyal L., Gotlieb Avrum I., Cybulsky Myron I. & Langille B. Lowell. Expression of ICAM-1 and VCAM-1 and Monocyte Adherence in Arteries Exposed to Altered Shear Stress. *Arteriosclerosis, Thrombosis, and Vascular Biology* **15**, 2–10 (1995).
298. Atarashi, K., Hirata, T., Matsumoto, M., Kanemitsu, N. & Miyasaka, M. Rolling of Th1 cells via P-selectin glycoprotein ligand-1 stimulates LFA-1-mediated cell binding to ICAM-1. *J. Immunol.* **174**, 1424–1432 (2005).
299. Berendam, S. J. *et al.* Comparative Transcriptomic Analysis Identifies a Range of Immunologically Related Functional Elaborations of Lymph Node Associated Lymphatic and Blood Endothelial Cells. *Front Immunol* **10**, 816 (2019).

300. Rebhun, R. B. *et al.* Constitutive Expression of the $\alpha 4$ Integrin Correlates with Tumorigenicity and Lymph Node Metastasis of the B16 Murine Melanoma. *Neoplasia* **12**, 173–182 (2010).
301. Burns, M. P. & DePaola, N. Flow-conditioned HUVECs support clustered leukocyte adhesion by coexpressing ICAM-1 and E-selectin. *American Journal of Physiology-Heart and Circulatory Physiology* **288**, H194–H204 (2005).
302. Kong, D.-H., Kim, Y. K., Kim, M. R., Jang, J. H. & Lee, S. Emerging Roles of Vascular Cell Adhesion Molecule-1 (VCAM-1) in Immunological Disorders and Cancer. *Int J Mol Sci* **19**, (2018).
303. Eniola, A. O., Willcox, P. J. & Hammer, D. A. Interplay between rolling and firm adhesion elucidated with a cell-free system engineered with two distinct receptor-ligand pairs. *Biophys. J.* **85**, 2720–2731 (2003).
304. Kate, M., Hofland, L., van Koetsveld, P., Jeekel, J. & Eijck, C. Pro-Inflammatory Cytokines Affect Pancreatic Carcinoma Cell. Endothelial Cell Interactions. *JOP : Journal of the pancreas* **7**, 454–64 (2006).
305. Fan, Y. *et al.* Leptin signaling enhances cell invasion and promotes the metastasis of human pancreatic cancer via increasing MMP-13 production. *Oncotarget* **6**, 16120–16134 (2015).
306. Dallas, M. R. *et al.* Divergent roles of CD44 and carcinoembryonic antigen in colon cancer metastasis. *FASEB J* **26**, 2648–2656 (2012).

307. Thomas, S. N., Zhu, F., Schnaar, R. L., Alves, C. S. & Konstantopoulos, K. Carcinoembryonic Antigen and CD44 Variant Isoforms Cooperate to Mediate Colon Carcinoma Cell Adhesion to E- and L-selectin in Shear Flow. *J Biol Chem* **283**, 15647–15655 (2008).
308. Paschos, K. A., Canovas, D. & Bird, N. C. The engagement of selectins and their ligands in colorectal cancer liver metastases. *J Cell Mol Med* **14**, 165–174 (2010).
309. Köhler, S., Ullrich, S., Richter, U. & Schumacher, U. E-/P-selectins and colon carcinoma metastasis: first in vivo evidence for their crucial role in a clinically relevant model of spontaneous metastasis formation in the lung. *Br. J. Cancer* **102**, 602–609 (2010).
310. Sleeboom, J. J. F., Amirabadi, H. E., Nair, P., Sahlgren, C. M. & Toonder, J. M. J. den. Metastasis in context: modeling the tumor microenvironment with cancer-on-a-chip approaches. *Disease Models & Mechanisms* **11**, (2018).
311. Sökeland, G. & Schumacher, U. The functional role of integrins during intra- and extravasation within the metastatic cascade. *Molecular Cancer* **18**, 12 (2019).
312. Prabhakarandian, B., Goetz, D. J., Swerlick, R. A., Chen, X. & Kiani, M. F. Expression and functional significance of adhesion molecules on cultured endothelial cells in response to ionizing radiation. *Microcirculation* **8**, 355–364 (2001).
313. Shaker, O. G., Ay El-Deen, M. A., Abd El-Rahim, M. T. & Talaat, R. M. Gene expression of E-selectin in tissue and its protein level in serum of breast cancer patients. *Tumori* **92**, 524–530 (2006).

314. Zhu, T., Hu, X., Wei, P. & Shan, G. Molecular background of the regional lymph node metastasis of gastric cancer (Review). *Oncology Letters* **15**, 3409–3414 (2018).
315. Steele, M. Pancreatic Cancer Invasion of the Lymphatic Vasculature and Contributions of the Tumor Microenvironment: Roles for E-selectin and CXCR4. *Theses & Dissertations* (2016).
316. Alexiou, D. *et al.* Clinical significance of serum levels of E-selectin, intercellular adhesion molecule-1, and vascular cell adhesion molecule-1 in gastric cancer patients. *Am. J. Gastroenterol.* **98**, 478–485 (2003).
317. Chow, M. T. & Luster, A. D. Chemokines in Cancer. *Cancer Immunol Res* **2**, 1125–1131 (2014).
318. Marcuzzi, E., Angioni, R., Molon, B. & Calì, B. Chemokines and Chemokine Receptors: Orchestrating Tumor Metastasis. *Int J Mol Sci* **20**, (2018).
319. Förster, R., Davalos-Missslitz, A. C. & Rot, A. CCR7 and its ligands: balancing immunity and tolerance. *Nature Reviews Immunology* **8**, 362–371 (2008).
320. Patrussi, L. *et al.* Enhanced Chemokine Receptor Recycling and Impaired S1P1 Expression Promote Leukemic Cell Infiltration of Lymph Nodes in Chronic Lymphocytic Leukemia. *Cancer Res.* **75**, 4153–4163 (2015).
321. López-Giral, S. *et al.* Chemokine receptors that mediate B cell homing to secondary lymphoid tissues are highly expressed in B cell chronic lymphocytic leukemia and

- non-Hodgkin lymphomas with widespread nodular dissemination. *Journal of Leukocyte Biology* **76**, 462–471 (2004).
322. Okada, T. *et al.* Chemokine Requirements for B Cell Entry to Lymph Nodes and Peyer's Patches. *J Exp Med* **196**, 65–75 (2002).
323. Kodama, J. *et al.* Association of CXCR4 and CCR7 chemokine receptor expression and lymph node metastasis in human cervical cancer. *Annals of Oncology* **18**, 70–76 (2007).
324. Schimanski, C. C. Effect of Chemokine Receptors CXCR4 and CCR7 on the Metastatic Behavior of Human Colorectal Cancer. *Clinical Cancer Research* **11**, 1743–1750 (2005).
325. Guan, X. Cancer metastases: challenges and opportunities. *Acta Pharmaceutica Sinica B* **5**, 402–418 (2015).
326. Hyler, A. R. *et al.* Fluid shear stress impacts ovarian cancer cell viability, subcellular organization, and promotes genomic instability. *PLoS One* **13**, (2018).
327. Follain, G. *et al.* Fluids and their mechanics in tumour transit: shaping metastasis. *Nature Reviews Cancer* **20**, 107–124 (2020).
328. Paddillaya, N. *et al.* Biophysics of Cell-Substrate Interactions Under Shear. *Front Cell Dev Biol* **7**, (2019).

329. Burdick, M. M. & Konstantopoulos, K. Platelet-induced enhancement of LS174T colon carcinoma and THP-1 monocytoid cell adhesion to vascular endothelium under flow. *Am. J. Physiol., Cell Physiol.* **287**, C539-547 (2004).
330. Martin, E. W., Malgor, R., Resto, V. A., Goetz, D. J. & Burdick, M. M. Dynamic biochemical tissue analysis detects functional selectin ligands on human cancer tissues. *Sci Rep* **9**, 8511–8511 (2019).
331. Borsig, L. *et al.* Heparin and cancer revisited: mechanistic connections involving platelets, P-selectin, carcinoma mucins, and tumor metastasis. *Proc. Natl. Acad. Sci. U.S.A.* **98**, 3352–3357 (2001).
332. Ramos, C. L. *et al.* Functional Characterization of L-Selectin Ligands on Human Neutrophils and Leukemia Cell Lines: Evidence for Mucinlike Ligand Activity Distinct From P-Selectin Glycoprotein Ligand-1. *Blood* **91**, 1067–1075 (1998).
333. Patel, M. S., Miranda-Nieves, D., Chen, J., Haller, C. A. & Chaikof, E. L. Targeting P-selectin glycoprotein ligand-1/P-selectin interactions as a novel therapy for metabolic syndrome. *Transl Res* **183**, 1–13 (2017).
334. Zhang, Y. *et al.* Migratory and adhesive cues controlling innate-like lymphocyte surveillance of the pathogen-exposed surface of the lymph node. *eLife* **5**, e18156 (2016).
335. Hansen, R. R. *et al.* High content evaluation of shear dependent platelet function in a microfluidic flow assay. *Ann Biomed Eng* **41**, 250–262 (2013).

336. Nomura, S. *et al.* High-shear-stress-induced activation of platelets and microparticles enhances expression of cell adhesion molecules in THP-1 and endothelial cells. *Atherosclerosis* **158**, 277–287 (2001).
337. Sato, M. *et al.* Microcirculation-on-a-Chip: A Microfluidic Platform for Assaying Blood- and Lymphatic-Vessel Permeability. *PLoS ONE* **10**, e0137301 (2015).
338. Santos, A., Bakker, A. D., Zandieh-Doulabi, B., Semeins, C. M. & Klein-Nulend, J. Pulsating fluid flow modulates gene expression of proteins involved in Wnt signaling pathways in osteocytes. *Journal of Orthopaedic Research* **27**, 1280–1287 (2009).
339. Mondy J. Sheppard *et al.* Platelet-Derived Growth Factor Ligand and Receptor Expression in Response to Altered Blood Flow In Vivo. *Circulation Research* **81**, 320–327 (1997).
340. Walshe, T. E., O'Brien, C. & Cahill, P. A. Notch Signaling in Co-Cultured Endothelial & Pericyte Cells Exposed to Pulsatile Flow. *Investigative Ophthalmology & Visual Science* **46**, 4654–4654 (2005).
341. Vantyghem, S. A. *et al.* A New Model for Lymphatic Metastasis: Development of a Variant of the MDA-MB-468 Human Breast Cancer Cell Line that Aggressively Metastasizes to Lymph Nodes. *Clin Exp Metastasis* **22**, 351–361 (2005).